Advanced Applications of Hydrogen and Engineering Systems in the Automotive Industry

Edited by Luigi Cocco and Muhammad Aziz

Advanced Applications of Hydrogen and Engineering Systems in the Automotive Industry

Edited by Luigi Cocco and Muhammad Aziz
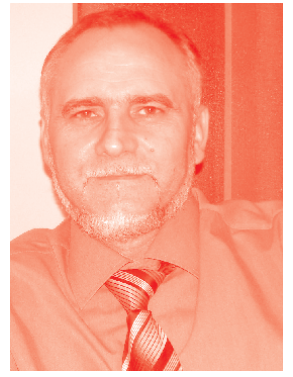
IntechOpen

Supporting open minds since 2005

Notice
Statements and opinions expressed in the chapters are these of the individual contributors and not necessarily those of the editors or publisher. No responsibility is accepted for the accuracy of information contained in the published chapters. The publisher assumes no responsibility for any damage or injury to persons or property arising out of the use of any materials, instructions, methods or ideas contained in the book.

We are IntechOpen,
the world's leading publisher of Open Access books
Built by scientists, for scientists

5,200+
Open access books available

129,000+
International authors and editors

155M+
Downloads

156
Countries delivered to

Our authors are among the
Top 1%
most cited scientists

12.2%
Contributors from top 500 universities

Interested in publishing with us?
Contact book.department@intechopen.com

Numbers displayed above are based on latest data collected.
For more information visit www.intechopen.com

Meet the editors

Dr. Luigi Cocco is a professional engineer with fifteen years of experience in the automotive industry. He worked in the Electrical and Electronic R&D and Supply Quality departments of racing/luxury/premium Italian vehicle manufacturers, such as Ferrari F1 Team, Automobili Lamborghini, and Maserati. Currently, he is Head of Global Value Optimization for Passive Safety, Active Chassis and ADAS systems for all former FCA brands. After obtaining a master's degree in Telecommunication Engineering, Dr. Cocco obtained a Ph.D. in Information Engineering. Since 2019, he has been a member of the Coordination Board of MotorVehicle University of Emilia-Romagna (MUN-ER). He has published several papers and three books: *Modern Metrology Concerns* (2012), *New Trends and Developments in Metrology* (2016), and *Standards, Methods, and Solutions of Metrology* (2018).

Dr. Muhammad Aziz is currently an Associate Professor at the Institute of Industrial Science, The University of Tokyo, Tokyo, Japan. He received a BEng, MEng, and DEng in Mechanical Engineering from Kyushu University, Japan, in 2004, 2006, and 2008, respectively. His research interests include power generation, renewable energy utilization, process modeling, smart grids, electric vehicles, batteries, and hydrogen production and utilization. He has published more than 125 peer-reviewed journals, 22 books and book chapters, and more than 200 proceedings. In addition, Dr. Aziz is also an active reviewer for more than sixty distinguished journals related to energy research.

Contents

Preface

The development of technologies in the transportation sector covers a broad range of aspects, including reliability, safety, comfort, energy efficiency, economy, and environment. Moreover, the automobile business is tremendously peculiar due to several strict requirements regarding functional reliability, safety standards, comfort level, high-volume production, and environmental limits. In addition, the industry is experiencing a disruptive evolution of modern vehicle research and design: electrification, connectivity, and autonomous driving.

Clean and environmentally friendly transportation systems are urgently needed, due to the huge amounts of energy they currently use and the CO_2 emissions they produce. Among potential secondary energy sources, hydrogen is considered very promising in terms of efficiency, cleanliness, and technological options for production, storage, and utilization. In transportation systems, it has been predicted that electricity and hydrogen will dominate the fuel supply for vehicles.

This book is organized into two sections. The first section deals with automotive engineering systems, while the second section discusses the potential of hydrogen as a clean and carbon-free energy source in the transportation sector.

The first section of the book provides a robust focus on automotive engineering, including new proposals and the latest trends about some road vehicle systems/sub-systems. Each chapter in this section presents a rigorous analysis or a new solution; professional and academic readers will appreciate both the theory dissertation and the industrial application.

The first section "Automotive Engineering Systems" includes five chapters:

Chapter "Hybrid Steering Systems for Automotive Applications," presents a new type of small power hybrid steering system dedicated to some types of heavy mobile robots. It also includes research results on the static and dynamic performances of hybrid electrohydraulic servomechanisms. The new concept was generated by the needs of modern aerospace technology called "flight by wire." The new wave of autonomous driving generated many combinations of electric and hydraulic components and the authors focus on the accuracy of the hybrid steering system of an articulated tractor.

The chapter "New Robust Control Design of Brake-by-Wire Actuators" discusses the control design of three different brake-by-wire actuators. After modeling the actuators adopting the bond graphs method, a cascaded control architecture is used to control these active systems via the Youla parameterization technique. A one-wheel model is used to compare these brake-by-wire systems in terms of stopping distance and actuator efforts and energy usage. The chapter also introduces the design of disturbance rejections for each loop.

The chapter "Role of Bearings in New Generation Automotive Vehicles: Powertrain", explains the main activities to obtain high-performance bearings, such as correct

selection of materials, manufacturing technologies, design-optimized geometries, sealing, lubrication, and application. Bearings are essential to achieve some modern automobiles' performance targets (maximum vehicle uptime, utilization, and better total cost of ownership); furthermore, they have a crucial role in powertrain health monitoring.

The chapter "Generation and Relaxation of Residual Stresses in Automotive Cylinder Blocks", studies the relaxation of residual stresses and their correlation to aging temperature and aging time. Particularly, for I4 and V-6 engine blocks, there is refinement in microstructure due to the increase in solidification rate along the cylinder length. Solution heat treatment and freezing lead to the maximum amount of residual stress relaxation where 50 percent of the residual stresses are reduced after the solution heat treatment step. Relaxation of residual stresses depends on the geometry and size of the workpiece.

The chapter "Quality and Trends of Automotive Fuels", analyzes the combustion for the most used fuels: gas oil and gasoline. Due to different combustion requirements, the fundamental properties of both fuels are examined. In addition, with the advent of various renewable components in both fuels, new trends are emerging for both fuel quality assessments, as these are molecularly distinct from their crude oil counterparts.

The second section "Hydrogen in the Future Transportation System" focuses on several interesting and cutting-edge topics describing several issues in the following chapters:

The chapter "Light Weight Complex Metal Hydrides for Reversible Hydrogen Storage", investigates complex metal hydrides involving lightweight elements or compounds for reversible hydrogen storage. The complex hydrides are prepared via an inexpensive solid-state mechano-chemical process under a reactive atmosphere at ambient temperatures. The structural, microstructural, surface, and other physicochemical behaviors of these lightweight complex metal hydrides are analyzed and discussed.

The chapter "Hydrogen Storage: Materials, Kinetics and Thermodynamics", describes hydrogen storage and its impact on the envisaged green environment. Moreover, graphene and borohydrides hydrogen storage materials are also reviewed extensively along with the kinetic models thereof. Furthermore, the chapter discusses the reaction mechanism of graphene nanocomposites.

The chapter "Hydrogen Fuel Cell Implementation for the Transportation Sector", discusses the application of a fuel cell in the transportation sector. It reviews the status of projected fuel cell electric vehicles (FCEVs) and considers the factors influencing the commercialization of FCEVs, including the importance of fuel cells for electric vehicles. It also examines degradation diagnoses using accelerated stress test procedures, FCEV hybridization, and the contribution of an energy storage device for charging these vehicles. The chapter also includes case studies relating to material degradation occurring from driving behavior. Finally, the chapter describes the importance of energy storage to support the growth of electric vehicle technologies, especially the integration of vehicles and the grid.

The chapter "Quantum Calculations to Estimate the Heat of Hydrogenation Theoretically", deals with the calculation and analysis of standard enthalpies of

hydrogenation of twenty-nine unsaturated hydrocarbon compounds in the gas phase by CCSD(T) theory. Geometries of reactants and products are optimized at the M06-2X/6-31g(d) level. The mean absolute deviations of the enthalpies of hydrogenation between the calculated and experimental results range from 8.8 to 3.4 kJ mol-1 based on the comparison between the calculation and experimental results. In addition, a very good linear correlation between experimental and calculated enthalpies of hydrogenation is obtained.

Our appreciation goes to all authors for their valuable contributions. The first editor would also like to thank his niece Maria Sofia for her motivating liveliness. The second editor would like to express his appreciation for his family, especially his wife and children.

Luigi Cocco, Ph.D.
Maserati S.p.A.,
Modena, Italy

Muhammad Aziz, Dr. Eng.
Institute of Industrial Science,
The University of Tokyo,
Tokyo, Japan

Section 1

Automotive Engineering Systems

Chapter 1

Hybrid Steering Systems for Automotive Applications

Nicolae Vasiliu, Daniela Vasiliu, Constantin Drăgoi,
Constantin Călinoiu and Toma Cojocaru-Greblea

Abstract

The paper presents the results of the researches performed in order to find out the static and dynamic performances of some recent types of hybrid electrohydraulic servomechanisms. The new concept was generated by the needs of the modern aerospace technology called "flight by wire", directed to the use of compact actuators composed mainly by a brushless motor driving a hydrostatic pump connected in a close loop with a hydraulic cylinder. The numerical simulations performed with Simcenter Amesim language pointed out the possibility of saving a lot of energy with this new concept, already used on civil airplanes and fighters. The new wave of autonomous driving generated a lot of combinations of electric and hydraulic components, according the peculiarities of applications. The authors studied the accuracy of the hybrid steering system of an articulated tractor based on a digital industrial servo valve combined with an ORBITROL standard unit. The structure of the last generation of the trucks hybrid steering systems was also studied, taking into account the real performances of each component. Finally, the effect of the strong penetration of the hybrid servo systems in the automotive manufacturing systems is assessed.

Keywords: energy saving, hybrid electrohydraulic servo systems, modeling, simulation, experimental validation

1. Introduction

The classical electrohydraulic servomechanisms, which include different types of high-speed two or three-stages servo valves (with flapper - nozzles, jet - pipes or piezo ceramic actuators) are still widely used in high performance control systems due to their very high dynamics reaching even 1000 Hz. However, the complex and expensive maintenance program, and the low overall energy efficiency due to the lamination of the fluid are strong drawbacks. The maximum efficiency of a classical hydraulic position servo system is lower than 65%. Consequently, all the advanced fluid control systems include oil coolers, and use special synthetic fluids for wide temperature ranges. In spite of these peculiarities, the modern servo valves offer minor time constants, which allow a high positioning accuracy. In the recent evolution of the electrohydraulic servo systems two important structural improvements can be pointed out:

a. The replacement of the classical servo valves by proportional directional flow control valves in different industrial applications (Rexroth, from 1989).
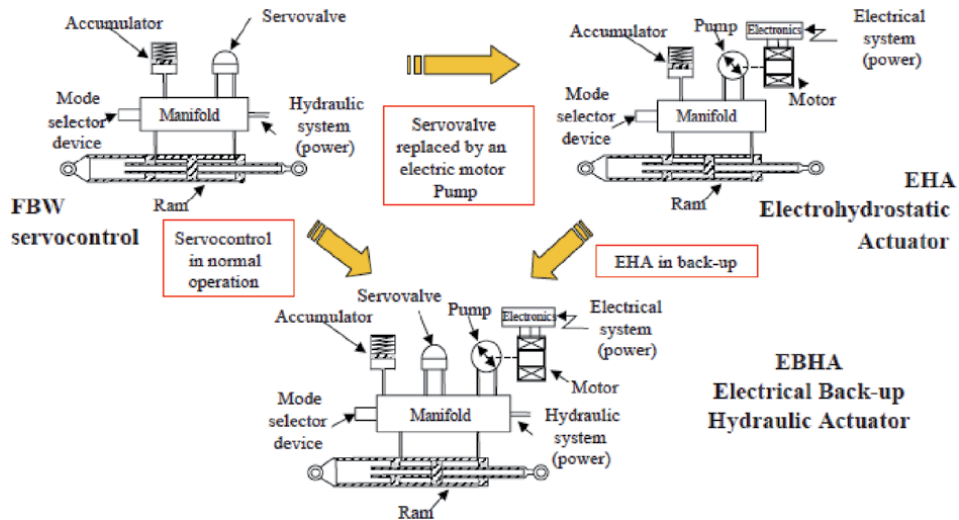
Figure 1.
Symmetrical structures of classical and hybrid electrohydraulic servos.

a)   b)
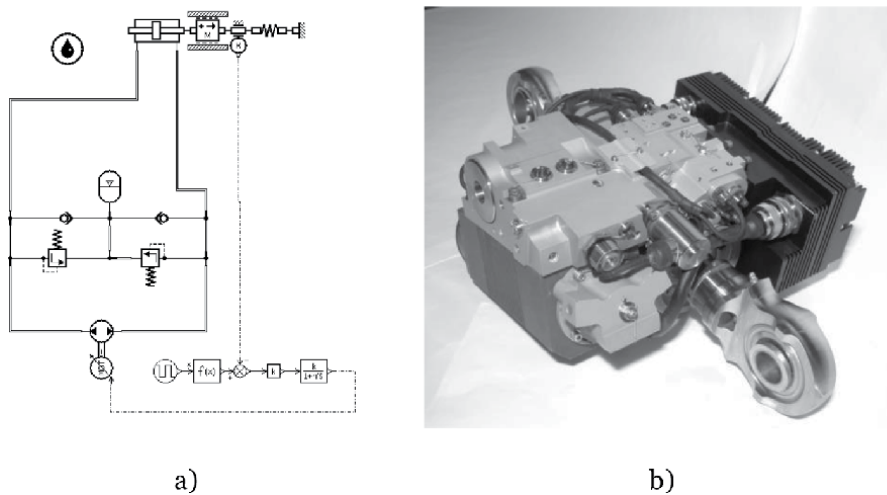
Figure 2.
Structure of a hybrid servomechanism designed for actuating the ailerons of A380: (a) Basic hydraulic diagram; (b) Main view of assembly.

b. The replacement of any kind of servo valves by a bidirectional reversible volumetric pump driven with a brushless motor controlled by power electronics (Airbus, from 2005). This evolution is presented in **Figure 1** for symmetric actuators [1, 2]. **Figure 2** shows the hydraulic diagram, and the main view of A380 ailerons servos [1, 2].

2. Dynamics of a basic hybrid servomechanism

The assessment of the static and dynamic behavior of a hybrid servomechanism was performed by numerical simulation using Simcenter Amesim language

produced by SIEMENS PLM Software [3, 4]. The simplified simulation network is shown in **Figure 2a**. The real hydro mechanical diagram of the system, proposed by Prof. J.-Ch. Mare in 2013 [5], shows a much more complex mechatronic system, with a mode selector (active or damping), a differential pressure transducer for the main loop, a rudder angle transducer, some hydraulic resistances modeling the system leakages etc. (**Figures 3** and **4**).

The core of the system is simple, but the whole assembly looks like a F1 hydraulic system with nine complex control loops: Power Steering, Gearshift Clutch, Differential, and Reverse gear, DRS, Brake by Wire, Throttle Inlet valves, and Turbo Wastegate. All of them are supplied in close loop by a single Parker swash plate axial pistons pump, pressure compensated! [6].

A simple design [5] based on a DC motor driving a gear pump, and a hydraulic cylinder can reveal both good enough dynamic performances, and some design
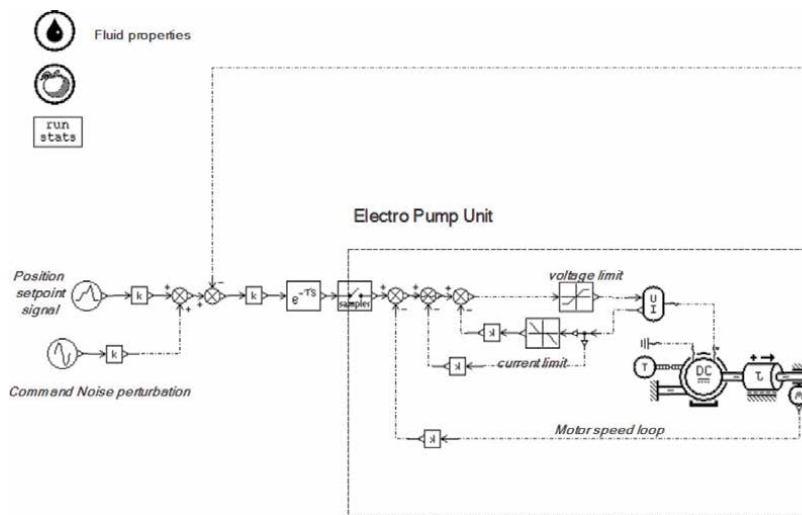
Figure 3.
Electric drive system and the position loop controller.
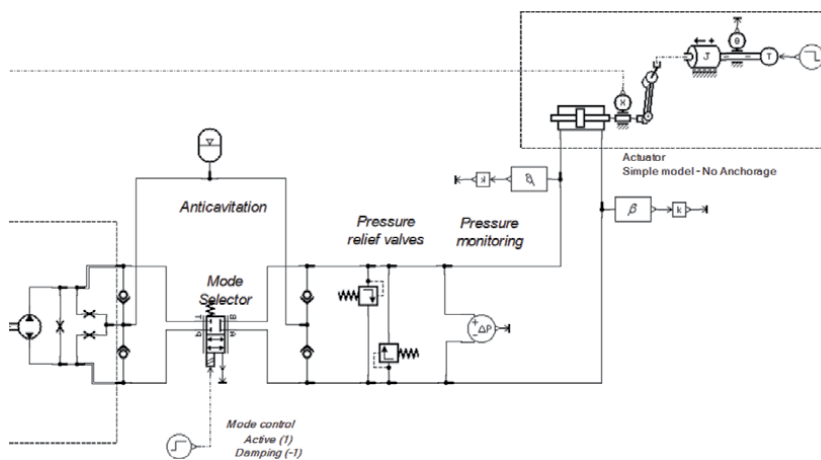
Figure 4.
Hydraulic section of a complete hybrid servomechanism.

problems involved in the lifetime of a hybrid servomechanism. The time constant can be easy found using a small voltage step input, for obtaining a piston displacement of 1.0 cm from a stroke of 2.5 cm. A reasonable force step input applied on the hydraulic cylinder piston rod can show the system capability to reject common disturbances. Both events were simulated with Simcenter Amesim language for a pump of 1 cc3/rev, reaching 9000 rev/min and 250 bar, driven by a small DC motor of 25 Nm at 270 V and 45 A, with shaft speed sensors used to allow the speed control. The results are presented on the same diagram from **Figure 5**. The time constant of the electro pump is less than 0.25 s, and the piston final position is reached in less than 0.7 s. A piston sudden load variation of 40,000 N generates a drift of about 20% from the nominal value 0f about 80,000N.

Figures 6–8 show the evolution of the main parameters of the pump during the studied transient.

A sudden aerodynamic load on the aileron can generate a short cavitation period in the suction line of the pump. This dangerous event is avoided by loading the

a)

b)
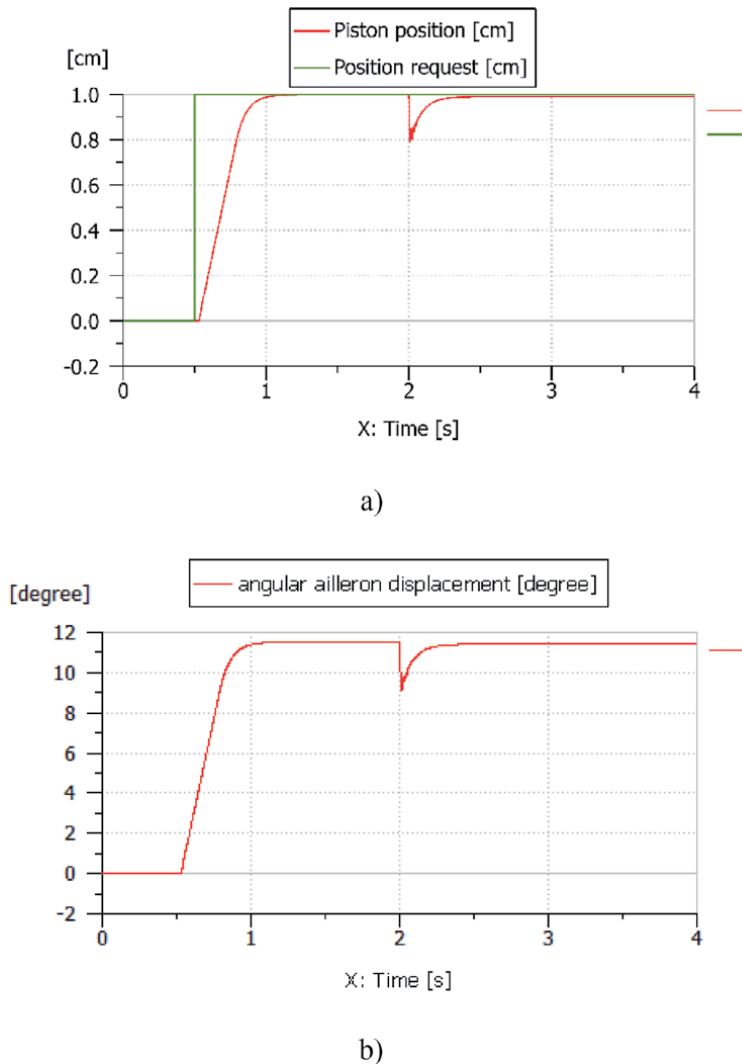
Figure 5.
Dynamic response for a common position request followed by the rejection of a sudden aerodynamic load: (a) Position request and the piston sliding position; (b) Aileron angular position as a function of time.
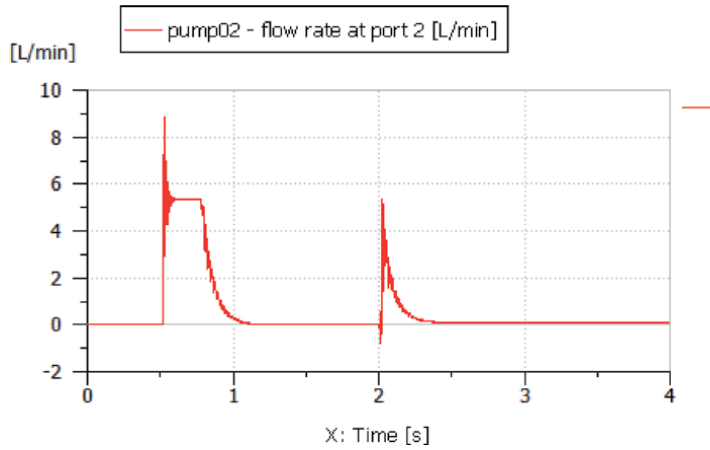
Figure 6.
Pump flow rate evolution during the studied transient.
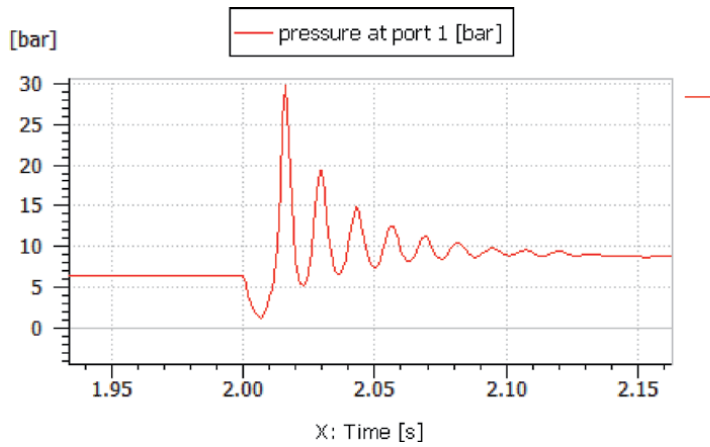
Figure 7.
Pressure in the suction port at the beginning of the aerodynamic load.
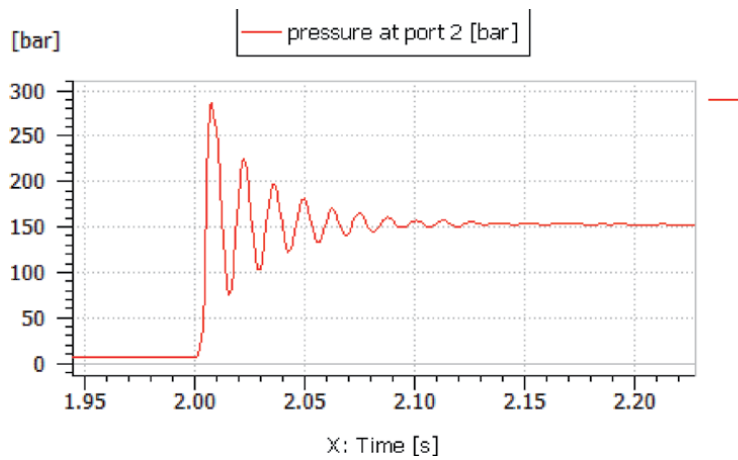
Figure 8.
Pump delivery pressure evolution during the studied load transient.

hydraulic accumulator with nitrogen at 5-6 bar. The compensation of the aerody-namic load applied on the aileron needs a remnant voltage on the armature winding, and a corresponding current (**Figures 9** and **10**). However, the energy needed for the studied operation cycle is very low (less than 120 J).

It is useful to study the frequency response of a basic hybrid servomechanism. This task can easy be accomplished using the "transfer meter" block from the "control library" of Simcenter Amesim (**Figure 11**). A typical result (**Figure 12**) shows a normal behavior for small amplitude input signals: (a) low auto-oscillation risk; (b) lower, but dynamic good enough performance for practice.

The studied dynamic model, even simple, gives an overview of the wide facili-ties of the behavioral analysis by simulation. However, in reality, some parts of the system should be better considered to get a more predictive representation. Much more, the experimental validation of each new component needs a lot of experi-mental researches. The history of the high tech electro hydraulic manufacturers has shown a huge effort of fine-tuning and implementing new generations of compo-nents and systems [7–9]. Dominque van den Bossche [2] summarized some of developing stages of this process in close connection with the possible dangerous situations, which can occur in any flight control systems. Specific maintenance programs have to be implemented in all manufacturing process related to the automotive engineering.
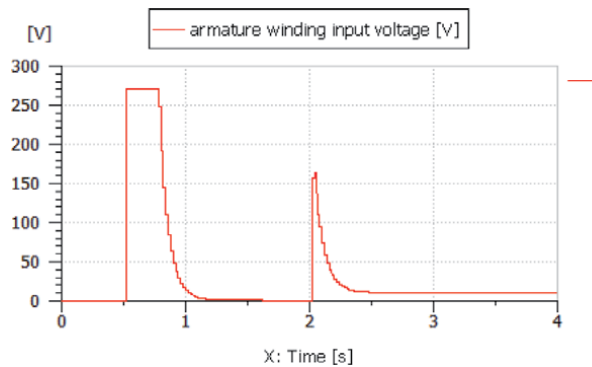
Figure 9.
Variation of the input voltage applied to the armature winding.
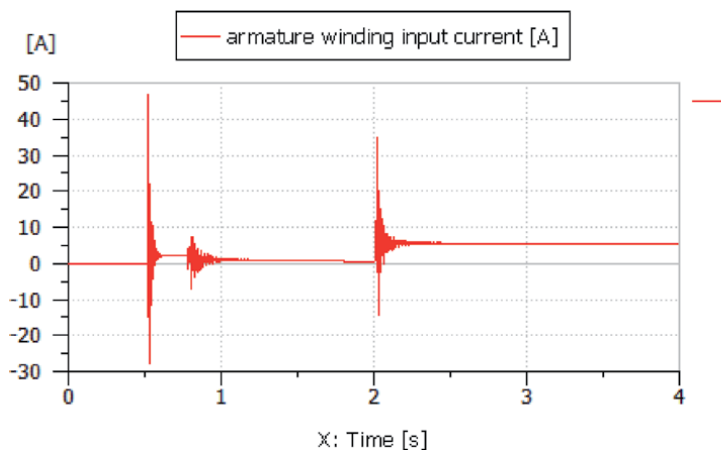
Figure 10.
Variation of the input current in the armature winding.
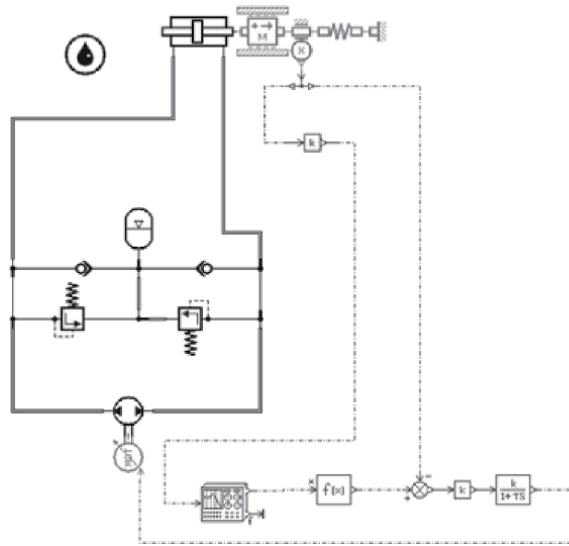
Figure 11.
Simulation network for servomechanism frequency response.
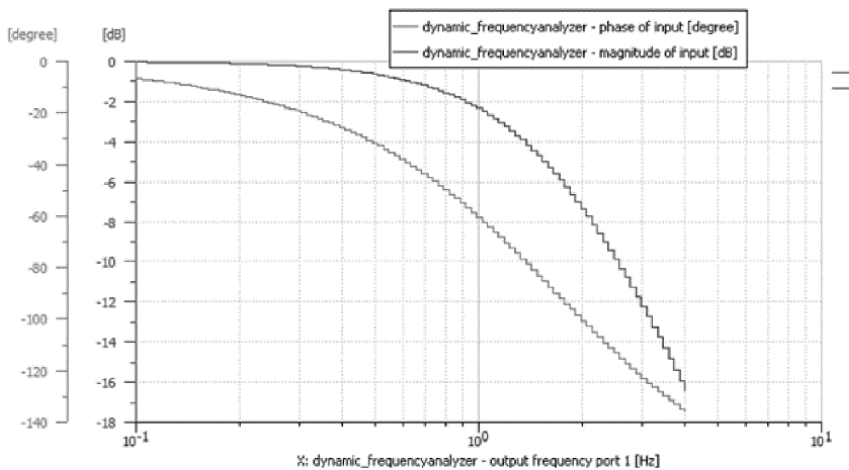
Figure 12.
Frequency response of a symmetric hybrid servomechanism.

The new generation of mechatronic simulation languages reduced drastically this effort. The use of the Real Time Simulation with Hardware In-The-Loop accelerated this process [10–13]. For example, Amesim models can be imported in LabVIEW real time platforms in order to simulate the automotive systems using the general software platform from **Figure 13** [10].

A successful hardware implementation of this concept is presented in **Figure 14**, in order to speed up the design of the new automotive control programs.

The RT simulations with Amesim are frequently used for tailoring different applications of the electrohydraulic hybrid servomechanisms. For example, the complex steering systems of "Self-Propelled Modular Transporter" as that designed by Mammoet [14] need a RTS of all the path followed during the process. The independent propulsion and steering axles are regarded as "super component" in the simulation network of such a complex vehicle. The RTS platform from
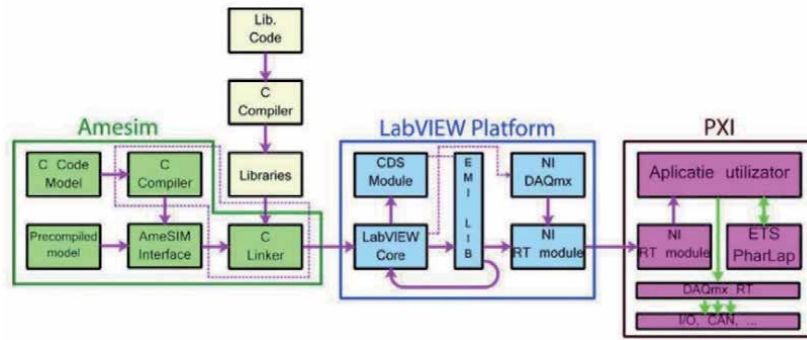
Figure 13.
RTS Platform of Amesim models in LabVIEW RT environment [10]

Figure 14.
RTS test platform created in the Fluid Power Laboratory of U.P.B. for automotive electric transmissions [11]

Figure 15, designed by the authors allow the validation of the Amesim simulations for different configurations of complex servomechanisms [12, 13].

3. Hybrid steering servomechanisms for tractors

3.1 Modern trends in autonomous driving systems

A modern trend in the agriculture is about making farming processes more accurate, efficient, and sustainable with advanced satellite navigation systems (like

Figure 15.
RTS platform for different complex hybrid servomechanisms.

GPS) and Information Technology (ITC). Precision Farming is raising the agriculture to a new level: doing the right thing, in the right place, the right way, at the right time in the field. Apart from satellite navigation systems, Precision Farming makes use of a number of other key technologies [15, 16]. They include automated steering systems, which take over specific driving tasks like auto - steering, overhead turning, following field edges and overlapping of rows. On tractors, combine harvesters, maize harvesters and other simulate vehicles there is often a need for electrically actuated steering to make automatic GPS controlled steering possible. In addition, manual steering with variable ratio is an often-wanted feature to improve productivity and driver comfort. For this purpose, Sauer-Danfoss [17, 18] has developed a combined steering unit and electro hydraulic steering valve
(**Figures 16–18**) named OSPE: OSP for normal manual steering wheel activated

Figure 16.
Hybrid steering module OSPE including both hydromechanical OSP and electrohydraulic proportional servovalve PVE (Sauer Danfoss).
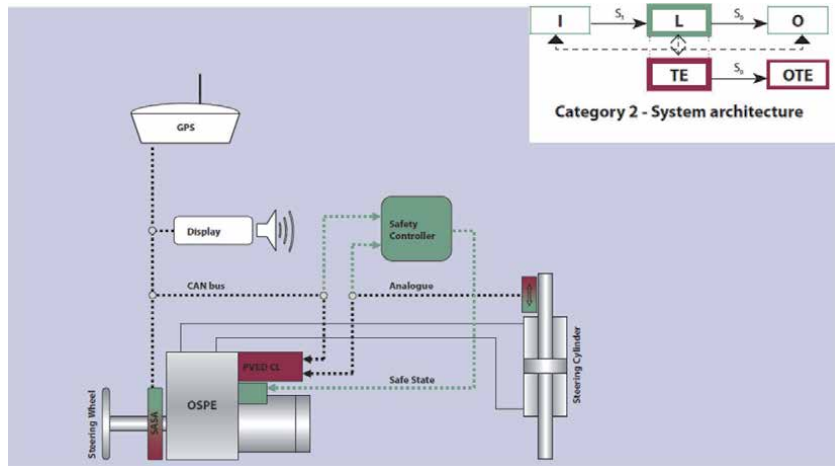
Figure 17.
Hybrid steering system for tractors [17, 18].
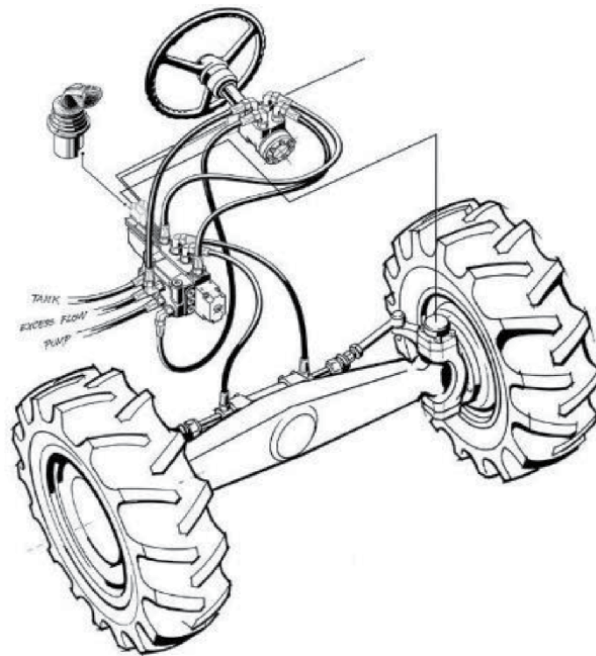
Figure 18.
Electrical and mechanical complex pilot operated steering valve [13].

steering and E for electro hydraulic steering activated by electrical input signal either from GPS or vehicle controller or from steering wheel sensor (SASA) for variable steering ratio. In variable steering mode, the electro hydraulic valve part adds flow to the metered out flow from the steering unit part of the OSPE. This combination has built in safety function in form of cut off valve, which makes unintended steering from Electro hydraulic valve part impossible. So OSPE is the right steering element to build up steering system with very high safety level and so to be able to fulfill legislations demands like e.g. in EU Machinery Directive 2006/42/EC.

Figure 19.
The driving cabin of a modern tractor.

On different kind of heavy mobile equipment, as tractors, mobile cranes, self-propelled modular transporter like Mammoet and dedicated mobile systems like fire trucks there is often need for electrically controlled steering either in the form of a joystick, or fully automatic wireless. For such applications Sauer-Danfoss has developed the pilot operated steering valve type EHPS, which covers a wide range of flows by different geometrical spool flow gain (**Figure 18**).

The above systems turn any tractor in a friendly environment for driver. John Deere [19] gives modern examples of ergonomic cabin of the tractor type 8400R (**Figure 19**).

3.2 Options for a new hybrid steering system

There are some initial decisions to make in order to design a hybrid steering system for any kind of mobile equipment. First, the new system has to allow the human operator to drive himself the equipment anytime i.e. to have the highest priority. Second, the new control system has to be stable and to preserve the accuracy of the previous one under any operation condition. The electrical component strongly depends on the electric power supply, rising real problems from the security point of view. Some electrical power supply systems can reduce the risk of the electrical systems failure. The main problem is to use the same steering cylinders with two kinds of hydraulic metering valves. Both of them need to have close center, or to be isolated upon the request of the driver by an additive directional valve. The relative small fuel consumption introduced by an open center ORBITROL hydraulic steering units can be preserved by driving the input with an electric actuator like a stepping motor with 100-200 pulses/revolution. This option needs a special design of the stepping motor in order to insert it into a steering column. On the other hand, the use of an open center flow valve leads to a poor tracking ability that increases with the steering wheel speed [17]. A typical steady state diagram of such a hydro mechanical feedback steering unit shows a small force capability for high turning speeds. The modern product range has to cover applications of all types of mobile equipment.

This section presents the structure and the performance of a new electro hydraulic steering system for articulated mobile equipment remote controlled. The new concept was designed and tested in the Fluid Power Systems of the University "POLITEHNICA" of Bucharest in order to point out the accuracy and the stability of a control solution based on a dual input (digital and analog) IAC-R REXROTH valve

(**Figure 20**), and a single OBE analog input valve of the same size [20]. The software is individually tailored for the different configurations and combinations of the IAC-R valve by standard parameters set in the factory. Settings for the closed-loop and control parameters are done via the bus interface. Several characteristics define the last generation of electro hydraulic control: fully digitized valve and axis control electronics; position and force control of hydraulic axes directly in the valve; various controller functions available (pressure/flow rate, position and alternating control); input of set points, configuration and diagnosis via field bus (depending on the type via CANopen or Provirus DP). Additional analog set point interface can be used as an alternative to set point input via field bus, but the electromagnetic interferences can create serious troubles, which need safety requirements according ISO 26262.

The CANbus type of controller area network is best suited for multipoint, long range cabling in high electromagnetic interferences areas where analog feedback signals may fail. This new type of control is widely used in military, automotive and aerospace simulating platforms or other systems where accuracy is very important. The behavior of the servovalve in a digital position-closed loop was identified by the aid a special test platform, which includes a strong elastic component, and a variable mass load (**Figures 21** and **22**).
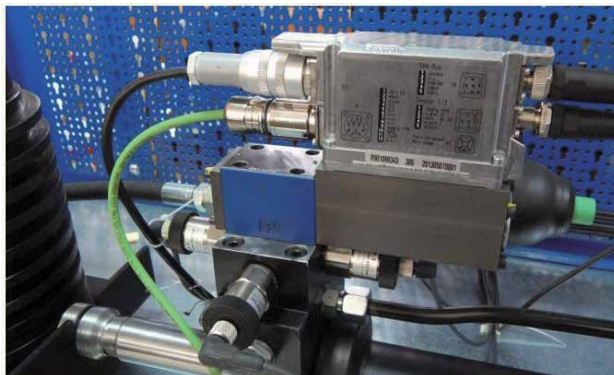
Figure 20.
High-response valve with integrated digital axis controller (IAC-R) and field bus interface (REXROTH)
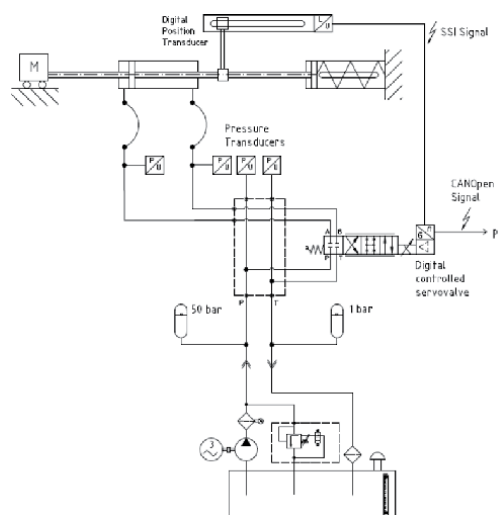
Figure 21.
Hydraulic diagram of the platform for testing digital servovalves.

Figure 22.
Test platform for identifying the digital servovalve performance [17].

A magnetostrictive digital displacement transducer with SSI interface was used for the load. Position reference is set though CANopen bus, and the control algorithm is a PID made with the OBE of the digital servo valve. The reference value for the digital test was generated with the application provided by the manufacturer and sent with a USB<->CANopen adapter. The positioning accuracy depends on the friction force of the steering cylinder as a function of speed (**Figure 23**).

Figure 24 shows a typical response of a servomechanism with P controller. The response time of the digital servovalve is very small: about 2 ms for a 10% input signal. Consequently, the frequency response is very fast (**Figure 25**).

The system performances were identified using a forestry articulated tractor (**Figure 26**) designed as prototype by the research department of the Romanian company "PROMEX" from Brăila [22]. The front chassis was locked, leaving free the back one to rotate on a circular raceway (**Figure 27**). The tractor steering system was studied by the aid of a rotary hydraulic motor controlled in closed loop by a servovalve (**Figure 28**). Then, the steering amplifier was replaced by the servovalve itself.

Usually, the control valve of the ORBITROL hydraulic steering unit is designed with open center for reducing both fuel consumption and steering mechanical
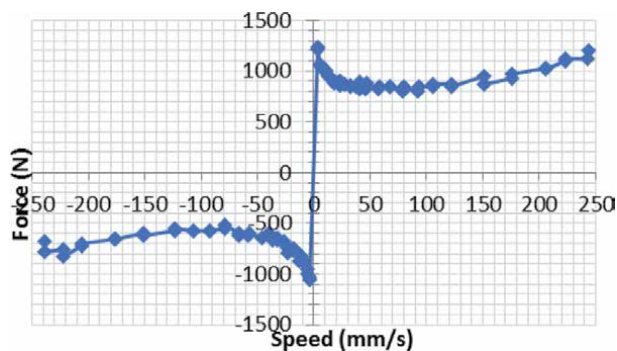
Figure 23.
Friction force of the steering cylinder as a function of speed [21].
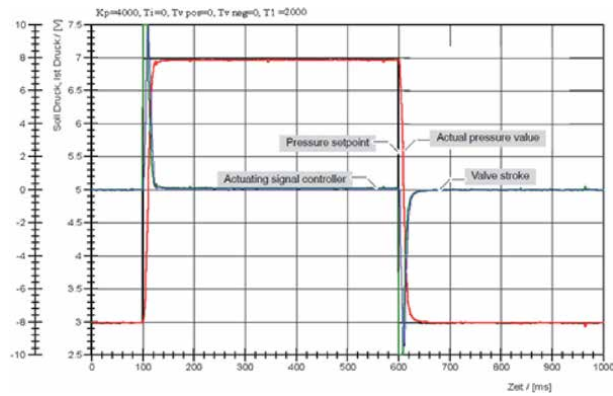
Figure 24.
Typical response of the servomechanism for a P controller with KP = 4.
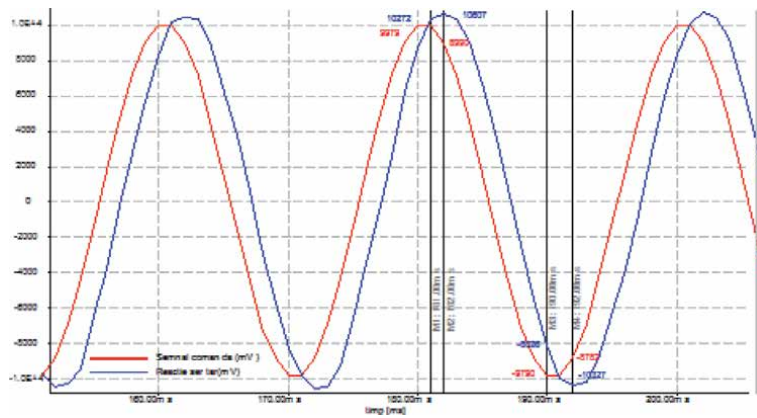
Figure 25.
Frequency response of the servovalve spool position for a sine input of 1.0 V at 50 Hz (given by CANopen).

Figure 26.
Overall view of the articulated full hydraulic tractor.

shocks. The "price" of these gains is a big backlash (**Figures 29** and **30**) which increases with the input frequency [23].

The direct control of the steering angle by a servovalve needs a constant pressure supply but avoids the backlash (**Figures 31** and **32**). However, the hysteresis
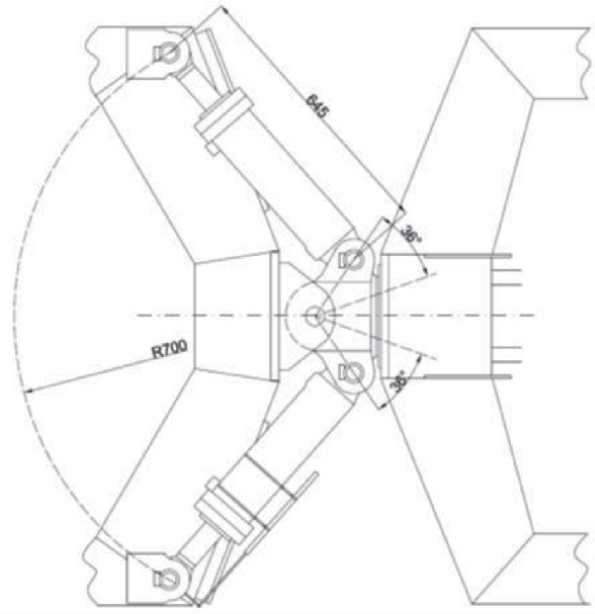
Figure 27.
Plain view of the steering hydraulic cylinders with position transducer.
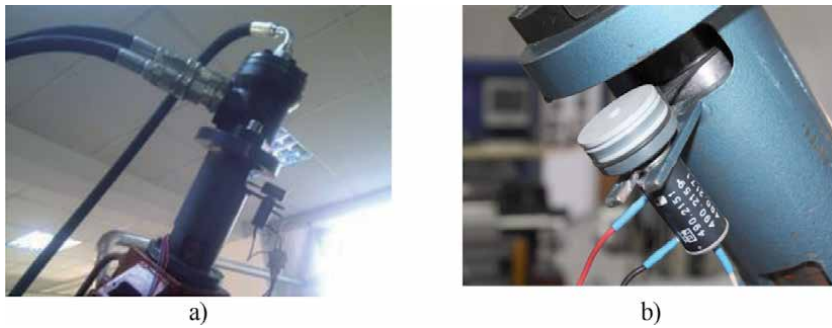
Figure 28.
Hybrid steering servo system driven by an ORBIT motor in close loop: (a) driving system view; (b) rotary feedback potentiometer driven by the motor.
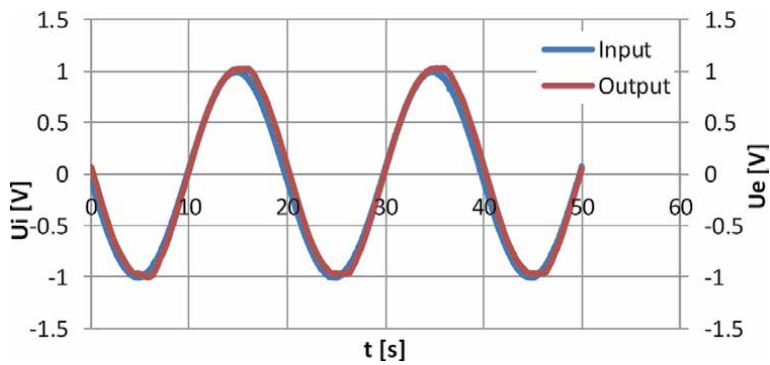
Figure 29.
Steering system response when ORBITROL unit is driven by a hydraulic motor (Ui = 1.0 V; f = 0,05 Hz).
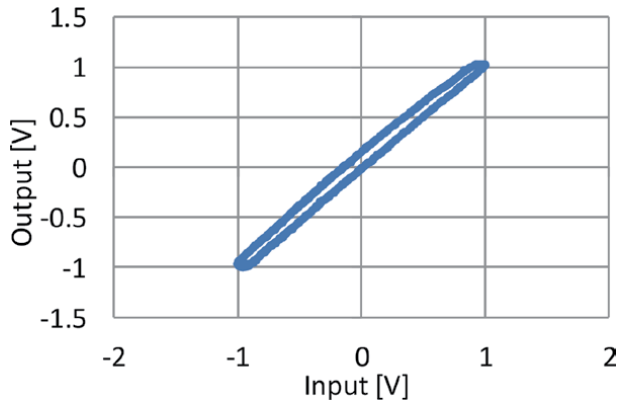
Figure 30.
Steering system steady state characteristics when ORBITROL unit is driven by a hydraulic motor (Ui = 1.0 V; f = 0.05 Hz).
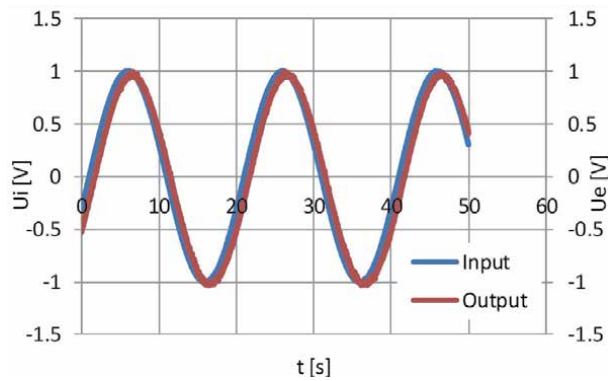
Figure 31.
Steering system frequency response when cylindres are driven by a servovalve (Ui = 1.0 V; f = 0,05 Hz; p_s = 100 bar).

increases with the input frequency. The normal friction forces inside the hydraulic cylinders increase the nonlinearity of the steady state characteristics.

The steering process quality can be improved by increasing the pressure supply, reducing the length of the hoses, and the servovalve gain around the null.
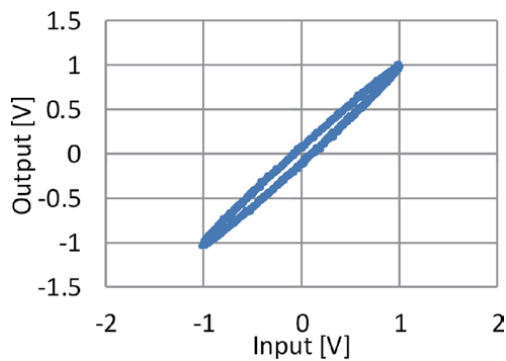
Figure 32.
Steady state characteristics for Ui = 1V, f = 0.05 Hz and p_s = 100 bar.

A common stepping motor with battery-less multi-turn absolute encoder can be regarded as a possible electromechanical interface in the ORBITROL steering system, but the size and the weight are too large for the normal input torque (about 10 Nm).

4. Hybrid steering systems for trucks and buses

The high-speed trucks and buses offer an important field of applications to the hybrid servo systems. However, the linear mechanical feedback of the classical steering box is still used in modern front axles with independent suspension arms (**Figure 33**) [24].

A hybrid effect can be introduced by a brushless servomotor placed on the steering column, or in a mixing box SC, in series with the torsion bar, under the shape of a module with two inputs, which controls the rotary valve (**Figure 34**).

The rotary valve opening has a high frequency oscillations (**Figure 35a**), but the steering process remains continuous (**Figure 35b**).

The basic rotary steering box of the trucks and buses has the same structure as the linear one, the only difference coming from the feedback: the piston motion is fed back to the torsion bar with a ball screw (**Figure 36**). A brushless motor placed in series with the input shaft can control the motion of the rotary valve (**Figure 37**).

The brushless motor controls the torsion bar by a complex torque and angle sensor composed by Hall sensors and a rotary inductive wheel (**Figure 38**).
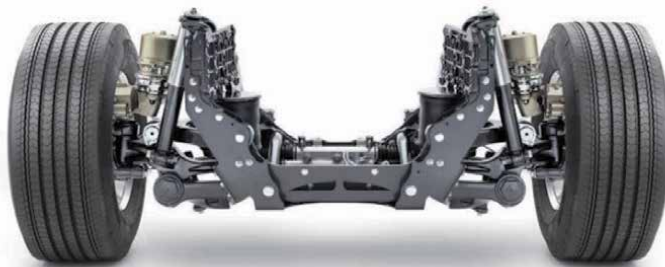
Figure 33.
Front axle of a modern truck with linear steering box.
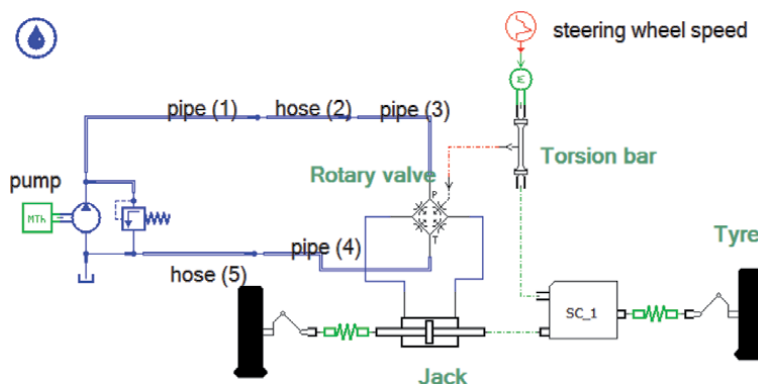
Figure 34.
Simcenter Amesim simulation of a hybrid linear steering box [25].
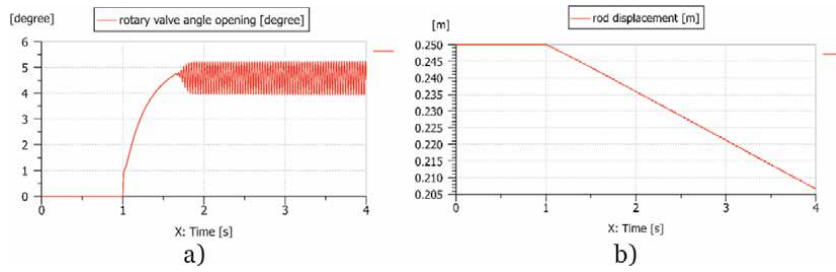
Figure 35.
Valve opening and rod displacement for a hydraulic steering system [4]: (a) rotary valve angle opening [degree]; (b) rod displacement [m].
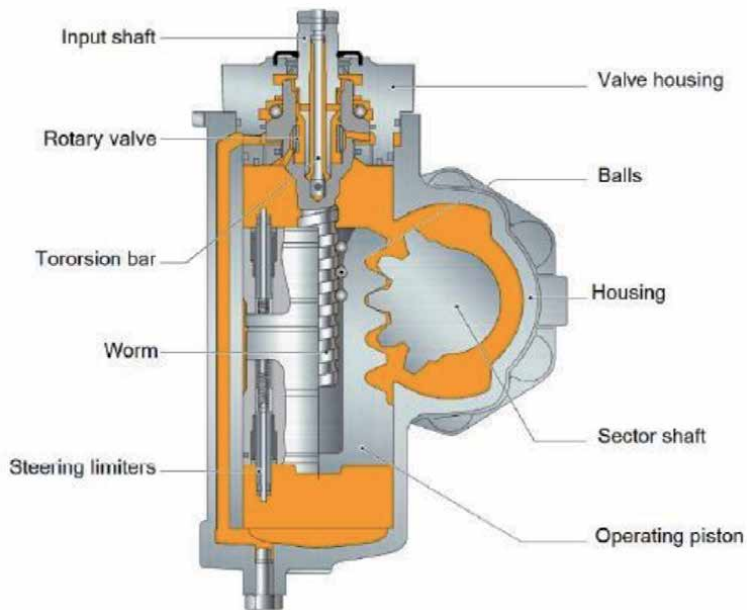
Figure 36.
Steering box with ball screw feedback [22].

Figure 37.
Hybrid steering box [26].
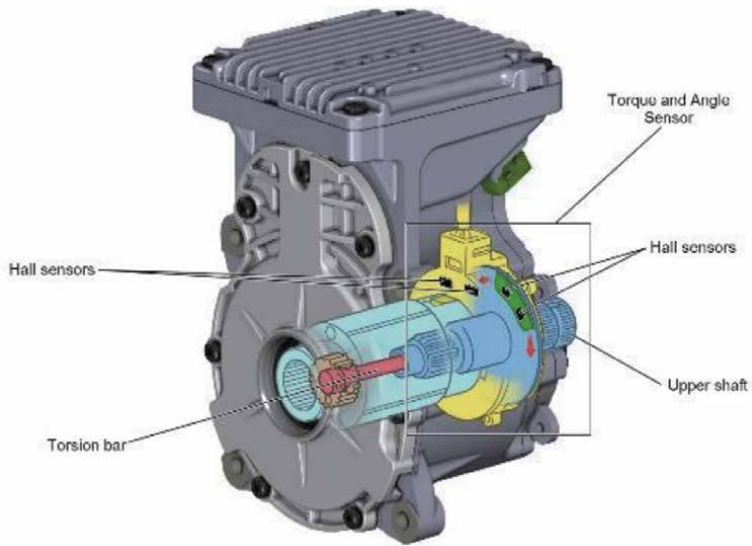
Figure 38.
Brushless motor with complex control functions [26].
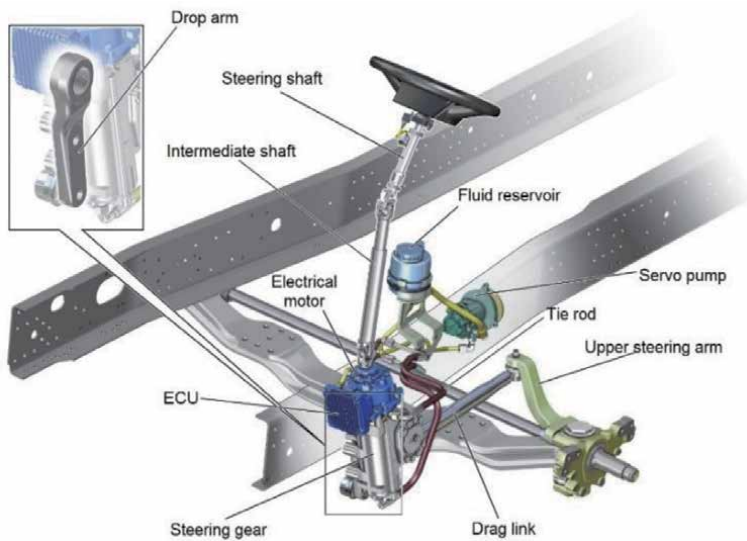
Figure 39.
Components of the hybrid steering system placed in a Volvo truck [26].

A general view of the hybrid system of a Volvo truck shows the minimum changes needed in the standard version of the car for introducing the hybrid feature (**Figure 39**).

The HYDRAPULSE Company from U.S.A. introduced a special kind of hybrid driving system. EHSU is a ruggedized electric hydraulic steering pump (electro-hydraulic) unit with integrated motor, controller, and closed-loop feedback that is specifically designed for mobile steering assist and e-steering applications. The EHSU (**Figure 40**) is available in both high and low voltage models and a variety of pump displacements and power levels. There is no electrical feedback from the steering arm! [27].
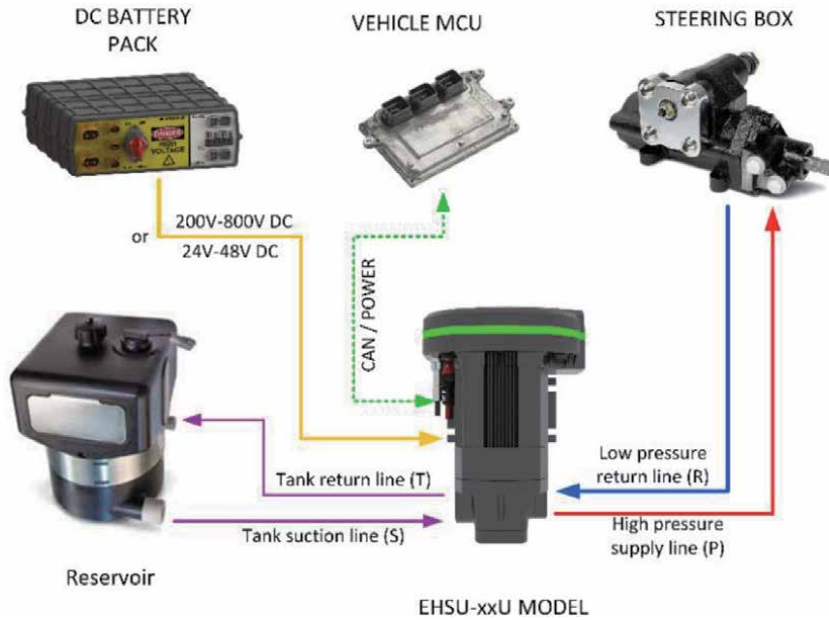
Figure 40.
Electrohydraulic hybrid steering systems without direct feedback.

5. Conclusions and future research

The basic hydrostatic transmission, composed by a volumetric pump and a hydraulic cylinder remains the most simple, compact and light mechanism for generating any force. The combination between a brushless motor, with digital driver, and a ball screw connected in close position loop became already the best driving system for small inertial loads, but the upper limit of the force remains low. The hybrid combination between a brushless motor and a hydrostatic transmission composed mainly by a high-speed pump, and a linear servomotor offers the best performances with the smallest weight and reduced dimensions. In the last decade,
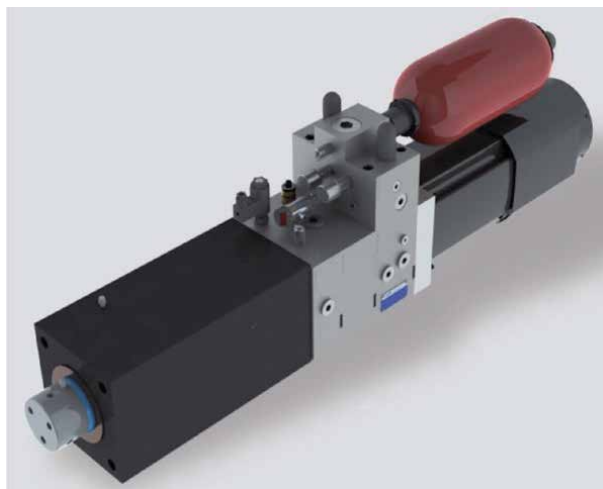
Figure 41.
Voith industrial digital hybrid servomechanism [28].

a significant progress was achieved in promoting this new generation of compact actuators in all the modern industrial manufacturing process, different kind of steering system for airplanes, ships, trucks, the control systems for engines, turbines, ships, trucks etc. (**Figures 41** and **42**). The author's team created a new type of small power hybrid steering system dedicated to some type of heavy mobile robots. **Figure 43** presents a part of the test platform of the servopump [30]. A FPGA controller was designed for controlling the whole system. The exposure of the experimental results overcomes the frame of this paper.

However, some information about the components of the test bench built in the frame of the University POLITEHNICA of Bucharest can be useful for a better understanding of the design problems. An AC Servo Motor & Driver, MINAS A6 series produced in 2016 by Panasonic Corporation Motor Business Division was chosen for driving a reversible high-pressure gear pump XR012 from Vivolo Corporation.

A PXI industrial device from NI Corporation [20] controls the assembly by the aid of the LabVIEW real time environment. The hydraulic cylinder, designed by the authors for high mechanical efficiency, includes a tension and compression load cell Model 2712 – 500 from Sensy Company from Belgium; two pressure sensors type 7768202 from VIKA Company, and a linear displacement transducer type MLS130-200-R-N from Penny & Giles Company. Hydac Group and Bosch Rexroth Group supplied the hydraulic circuit components. After the first series of performance test, a cheaper dedicated controller was designed, and successfully tuned (**Figure 44**).

Figure 42.
Rexroth industrial digital hybrid servomechanism [29].

Figure 43.
Servopump for hybrid servomechanisms designed in the Fluid Power Systems Laboratory of U.P.B. [30].
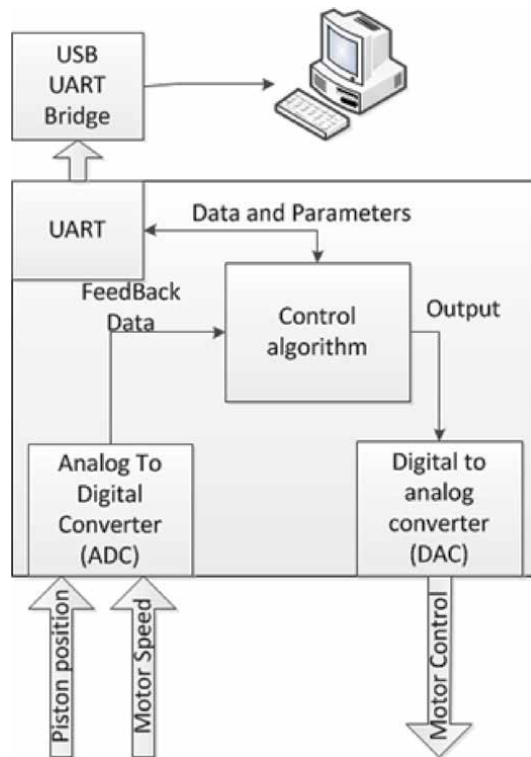
Figure 44.
Architecture of a configurable embedded controller for hybrid automotive servomechanisms [30].

Anyway, the road to a mature industrial design will be a long one, and according to Dirk Hartmann and Herman Van der Auweraer from Siemens Corporation, it must pass through all the stages of the modern manufacturing process called now Digital Twins [31].

Acknowledgements

Author details

Nicolae Vasiliu*, Daniela Vasiliu, Constantin Drăgoi, Constantin Călinoiu
and Toma Cojocaru-Greblea
University POLITEHNICA of Bucharest, Bucharest, Romania

*Address all correspondence to: nicolae.vasiliu@upb.ro

IntechOpen

References

[1] Xavier Le tron, A380 Flight Controls overview, Presentation at Hamburg University of Applied Sciences, 27 September 2007, http://hamburg.dglr.de.

[2] Dominque van den Bossche, The A380 Flight Control Electrohydrostatic Actuators, Achievements and Lessons Learnt. In "Proceedings of the 25th International Congress of the Aeronautical Sciences", Hamburg, Germany, 3–September 2006, pp. 1–8.

[3] Siemens PLM Software, Simcenter Amesim, Leuven, 2013. Available from: https://www.plm.automation.siemens.com/global/en/products/simcenter/simcenter-amesim.html.

[4] Vasiliu N, Vasiliu D, Călinoiu C, Puhalschi R. Simulation of Fluid Power Systems with Simcenter Amesim, CRC Press, Taylor &Francis Group, 978-1-4822-5355-9, Boca Raton, FL, USA, 2018.

[5] Mare J-Ch. Aerospace Actuators 3, ISTE&WILEY, 978-1-84821-943-4, 2018, Hoboken, NJ 07030, USA.

[6] Scarborough C. The fundamentals of Formula 1 hydraulic systems explained, Motorsport Technology, Available online: The%20fundamentals%20of%20Formula%201%20hydraulics%20systems%20explained%20-%20Motorsport%20Technology.html.

[7] Parker, H. Compact EHA—Electro-Hydraulic Actuators for High Power Density Applications. 2013. Available online: https://goo.gl/t2FMw2.

[8] Rexroth, B. Advantages of Electrification and Digitalization Technology for Hydraulics. 2018. Available online: https://goo.gl/4G6Jxn.

[9] Padovani D., Ketelsen S., Hagen D. and Schmidt L. A Self-Contained Electro-Hydraulic Cylinder with Passive Load-Holding Capability. Energies 2019, 12(2), https://doi.org/10.3390/en12020292.

[10] Vasiliu, C. Real Time Simulation of the Automotive Electrical Transmissions. [PhD thesis]. University POLITEHNICA of Bucharest; 2011.

[11] Vasiliu, C., Vasile N. Innovative HIL Architecture for Electric Powertrain Testing, U.P.B. Sci. Bull., Series C, Vol. 74, Iss. 2, 2012, ISSN 1454-234x.

[12] Puhalschi, R.C. Modeling and Real Time Simulation of the Energy Control Systems. [PhD thesis]. University POLITEHNICA of Bucharest; 2013.

[13] Puhalschi, R., Vasiliu D., Ion Guță D. D., Mihalescu B. Concurrent Engineering by Hardware-in-the-loop Simulation with R-T Workshop, 18th European Concurrent Engineering Conference - ECEC'2012, JW Marriott Hotel, Bucharest, Romania, April 18-20, p.27-31, 2012, EUROSYS-ETI Publication, ISBN: 978-90-77381-71-7, EAN: 9789077381717.

[14] https://www.mammoet.com/cases/year-round-construction-in-the-arctic/

[15] CEMA-European Agricultural Machinery Association, Precision Farming and Digital Farming. Available online: https://www.cemaagri.org/index.php?option=com_content&view=category&id=10&Itemid=152www.cema-agri.org/EuropeanAgriculturalMachinery.

[16] EU Machinery Directive 2006/42/EC. Available online: https://eur-lex.europa.eu/legal-content/EN/TXT/?uri=CELEX:32006L004.

[17] Danfoss. OSPE Steering Valve, Technical Information, July 2020. Available online:https://assets.danfoss.com/documents/DOC348562964075/DOC34856296407.pdf

[18] Danfoss. Technical Information, EHPS Steering Valve, PVE Actuation Module, OSPCX CN Steering Unit. May 2015. Available online: https://assets.danfoss.com/documents/DOC152886484673/DOC152886484673.pdf

[19] John Deere tractors Series 8400R. Technical Specification. 2020. Available online: https://www.deere.com/en/tractors/4wd-track-tractors/

[20] Bosch-Rexroth. 2006. IAC-R valve Operating manual (with CANopen)", RE 29090-B-01/06.05.

[21] Ganziuc Al. Electrohydraulic Servomechanisms with high Immunity Level [PhD thesis]. University POLITEHNICA of Bucharest; 2013.

[22] Aramă Șt. 1984. Articulate forestry tractor with integral hydrostatic transmission. Romanian Patent 80,316.

[23] Irimia P.C. Researches on the power management of the off-road vehicles [PhD thesis]. University POLITEHNICA of Bucharest; 2015.

[24] Volvo Bus Corporation. VDS – Volvo dynamic steering. BED 00791.15.10 EN.

[25] Vasile L.N. Researches on the automotive hydraulic steering systems. [PhD thesis]. University POLITEHNICA of Bucharest; 2005.

[26] Volvo Truck Corporation. VOLVO FH16 Technical Guide. 2016.

[27] Terzo Power Systems. Electro-Hydraulic Steering Units. 2020. Available online: https://terzopower.com/hydrapulse-ehsu/

[28] https://www.voithturbo.com/hydraulic-systems.

[29] https://www.boschrexroth.com/en/xc/company/press/index2-31936.

[30] Cojocaru-Greblea T. Researches on the automotive hybrid steering systems. [PhD thesis]. University POLITEHNICA of Bucharest; 2020.

[31] Hartmann D, Van der Auweraer H. Digital Twins. arXiv:2001.09747v1 [cs.CY] 3 Jan 2020.

Chapter 2

New Robust Control Design of Brake-by-Wire Actuators

Ehsan Arasteh and Francis Assadian

Abstract

This chapter discusses control design of three different brake-by-wire actuators. The brakes studied include an Electro-Hydraulic brake with pressure modulation for wheel slip control, and two different Electro-Mechanical Brake configurations that directly use electric motors to control the movement of the caliper for wheel slip control. After modeling the actuators with the use of bond graphs, a cascaded control architecture is used to control these active systems. Individual controllers are designed using Youla robust control design method. Then, a feed-forward disturbance rejection is designed and added to the loops and its effectiveness is analyzed. Finally, a one-wheel model is used to compare these brake-by-wire systems in terms of stopping distance and actuator efforts.

Keywords: brake-by-wire, electro-hydraulic brake, robust control, electro-mechanical brake, disturbance rejection

1. Introduction

X-By-Wire technologies are the future of the automotive industry due to an increasing demand for electrification and fuel efficiency. Their electronic architectures and interface also make them a great candidate for autonomous and hybrid electric/electric vehicles. Among all the necessary by-wire technologies, brake-by-wire systems are a priority due to their safety-critical nature role in the vehicle [1, 2].

Brake-by-wire systems can reduce component weight and allow the actuators to consume energy only when required by blending both regenerative braking and friction braking. This can minimize fuel consumption and CO_2 emissions. Using sensors and control methods, caliper drag can be eliminated by making brake-by-wire technology even more energy efficient. Individual wheel braking and faster activation time can be combined with the vehicle's ECS system to make the vehicle safer. The reliability of new actuators and the risk and cost associated with deploying new brake technologies are the main hurdles of brake-by-wire systems becoming a popular choice for the automotive manufacturers [3, 4].

Brake systems are categorized into wet and dry brakes. Wet brakes employ fluids for their operation, and dry brakes are usually purely mechanical systems. Electro-hydraulic brake systems are a type of wet brakes where their pressure is modified using pressure modulators that can be controlled electronically. The pressure source can be packaged in one centralized location for all four wheels like Bosch's first electro-hydraulic brake system [5], or it can be local to each wheel like

MKC-l from Continental [6] (local Electro-hydraulic brakes). Dry brakes can also be realized in a few different configurations. There is an electro-mechanical brake that utilizes a small motor, planetary gear set and a roller-screw to move the brake pad [7–13]. However, this type of brake requires a 42 Volt motor to operate and consumes a lot of energy [3]. Electronic-wedge brakes on the other hand, uses a wedge mechanism to create a system that draws the wedge pad inside the brake; therefore, requiring less energy to operate [13–21]. Vienna Engineering also came up with a similar idea that uses a crank-shaft mechanism that reduces the complexity of reduction gears and roller screws [22–25].

Purely dry brakes such as Electronic Wedge and VE brakes, are going to be costlier that Electro-Hydraulic brakes since they are newer technologies and require more research and development to productionize. On the other hand, EHB has already been in the market for a while. The other challenge for purly dry brakes is reliability since they have more electronic components and they all need to reliably perform in a harsh environment near the brake where vibration, shock and high temperatures can have significant impact [3].

In this work, we have chosen to study Electro-Hydraulic (EHB), Electro-Mechanical (EMB) and Electronic Wedge Brakes (EWB). We will start by modeling the brakes using bond graph in Section 2. Bond graph is graphical representation method to model dynamical systems that utilizes flow of energy. It is an easy and intuitive way to model physical systems especially the ones that are in the multi-energy domain (e.g. Electro-Mechanical, Electro-Hydraulic). Readers can take a look at [26] for further readings on bond graphs.

After modeling the actuators, we will design the controllers using Youla Paramerization technique. Finally, we will add disturbance rejection and compare results for EMB and EWB controllers and show their effectiveness. The purpose of this book chapter is to show the process of modeling of three different brake-by-wire actuators and designing their robust controllers using Youla paramerization.

2. System modeling

In this section, we discuss the schematics, bond graphs, and the equations of motion based on the bond graphs for each brake system. All the actuator models include a one-wheel vehicle model that is represented in **Figure 1**. It includes a moving wheel with a rotational inertia connected to a point mass. This simple dynamic model is very useful for preliminary studies of brake actuators and algorithms (such as ABS and TCS) and is easy to implement on the test rig. This simple
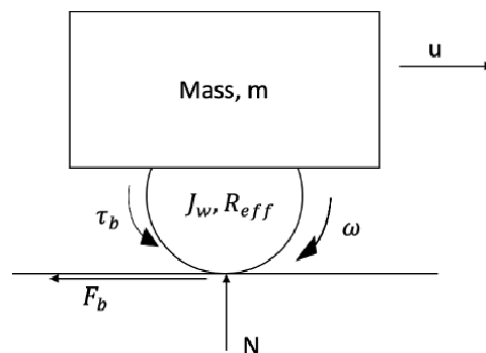
Figure 1.
One-wheel vehicle model used to analyze the brake actuator behaviors.

model is only utilized to study longitudinal dynamic effects in the vehicle. This model suffices for studying most of the brake-by-wire actuators and ABS technologies since it focuses on the longitudinal dynamics of the vehicle. Higher fidelity vehicle models, which include lateral dynamics, such as bicycle model and extended bicycle model will be considered in the future, once the preliminary comparisons of different actuators are studied and revealed using this simple model [25, 27–30]. The bond graph of this model is included in **Figure 2**.

State equations for this model are as follows

$$\dot{p}_\omega = J_w\dot{\omega} = F_bR_{eff} - \tau_b - B\omega \qquad (1)$$

$$\dot{p}_u = m\dot{u} = -F_b \qquad (2)$$

Where u is forward velocity, ω is wheel angular velocity, τ_b is braking torque, F_b is braking force, N is normal force, B is bearing friction coefficient, R_{eff} is effective wheel radius, p_ω is the angular momentum of the wheel, and p_u is the vehicle's momentum. For the braking force modeling, the Burckhardt tire model is chosen in which the coefficient of friction (μ) is a function of the longitudinal slip (λ) (Eq. 4) and the longitudinal slip is defined in Eq. 3 [31, 32].

$$\lambda = \frac{u - \omega R_{eff}}{|u|} \qquad (3)$$

$$F_b = \mu(\lambda) \cdot N = \left[c_1\left(1 - e^{-c_2\lambda}\right) - c_3\lambda\right] \cdot N \qquad (4)$$

where N is the normal force. The state equations describing the one-wheel model will always be present in all brake type models since the vehicle model will stay the same.

2.1 Electro-hydraulic brake actuator

The schematic of an electro-hydraulic brake (EHB) actuator is presented in **Figure 3**. It includes a hydraulic pipe which carries the hydraulic fluid with the pressure input (P_{in}) to a cylinder chamber, which in turn changes this pressure into the movement of the brake pad. Therefore, the brake pad movement results in stopping the brake disk from moving [33].

The bond graph model is derived based on the schematic in **Figure 3**. The input is modulated pressure, and this pressure is an input to the hydraulic line, where, by using a transformer, it results in the brake pad movement (the pressure reservoir and the motor that modulates the pressure are not included in the model and will be added in the future studies). The interaction between the brake pad and the wheel is modeled with a stiffness (k_{cal}). Brake torque is also modeled by a modulated resistance which changes with the displacement of the brake pad.

State equations (Eq. 5–8) are derived based on the bond graph in **Figure 4**.
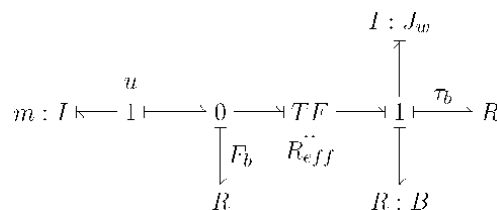
Figure 2.
One-wheel bond graph.
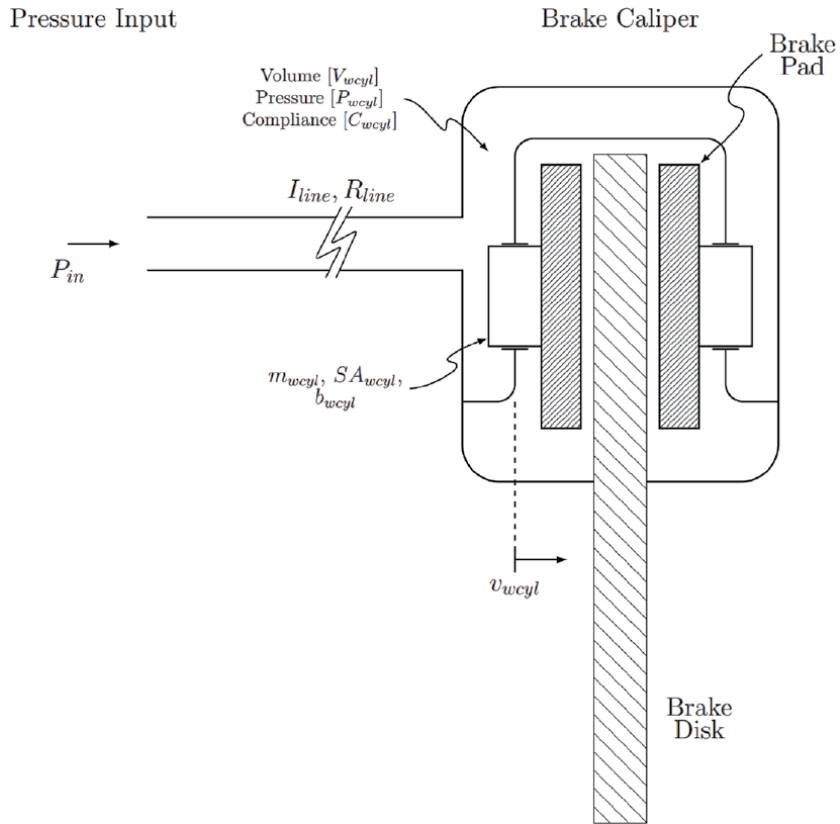
Figure 3.
Electro-hydraulic brake actuator (EHB) schematics [33].
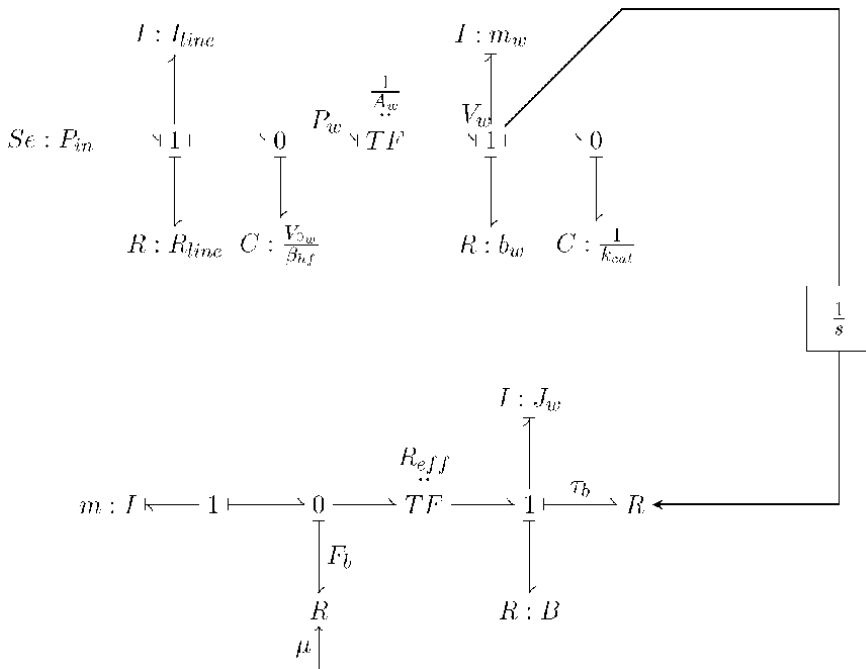
Figure 4.
EHB bond graph.

$$\dot{p}_{line} = P_{in} - R_{line}\frac{p_{line}}{I_{line}} - q_w\frac{\beta_{hf}}{V_{0_w}} \tag{5}$$

$$\dot{q}_w = \frac{p_{line}}{I_{line}} - A_w\frac{p_w}{m_w} \tag{6}$$

$$\dot{p}_w = A_wq_w\frac{\beta_{hf}}{V_{0_w}} - b_w\frac{p_w}{m_w} - q_{cal}k_{cal} \tag{7}$$

$$\dot{q}_{cal} = \frac{p_w}{m_w} \tag{8}$$

Where $R_{line}, p_{line}, I_{line}, \beta_{hf}, V_{0_w}, A_w, p_w, V_w$, and q_{cal} are hydraulic line resistance, hydraulic line pressure, line inertia, bulk modulus, volume of cylinder chamber, surface area of the piston, pressure on the brake pad, velocity of the brake pad, and brake pad position, respectively. The brake torque is calculated using Eq. 9.

$$\tau_b = \begin{cases} 2\mu_{cal}r_{eff}k_{cal}(x_{cal} - x_0) \ , & \text{if } x_{cal} \geq x_0 \\ 0, & \text{otherwise} \end{cases} \tag{9}$$

Where $\mu_{cal}, r_{eff}, x_{cal}$, and x_0 are brake friction coefficient between the pad and the wheel, brake pad effective radius, brake pad position (same as q_{cal}), and brake clearance, respectively. Eqs. 5–9 along with Eqs. 1–4 present the state equations for this brake system [29].

2.2 Electro-mechanical brake actuator

Figure 5 shows a schematic of an electro-mechanical brake actuator. It consists of an electric motor, planetary gear set, ball screw, piston, brake pad, and floating caliper to oppose the brake pad. In this actuator, the motor's rotational motion becomes the brake pad's movement through one (or more) planetary gear sets and a ball screw mechanism. This movement will then create a clamp force given by F_{cl} in **Figure 5** [10, 34].

Figure 6 illustrates the bond graph model for an electro-mechanical brake actuator (EMB). The input to the system is voltage (V_{in}) to the motor. The motor includes an inductance (L_m) and a resistance (R_m). The motor's current is proportional to a torque on the shaft and this proportionality is modeled by a gyrator (with K_t representing the motor constant). The shaft has a rotational inertia (J_m). The resistance that exists inside the planetary gear set, the ball-screw mechanism and the motor shaft is lumped together and modeled by an R-element. This resistance element is explained more in the next section.
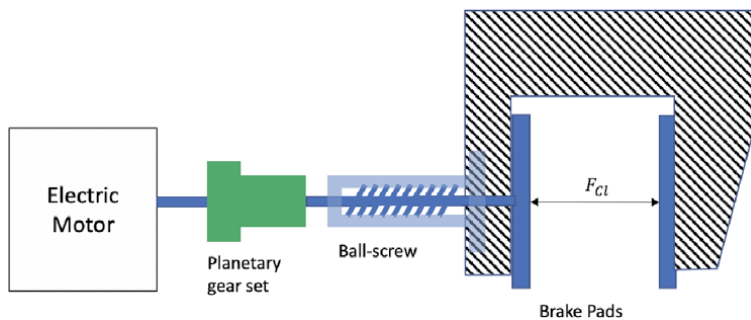
Figure 5.
EMB Schematics (adapted from [34, 35]).
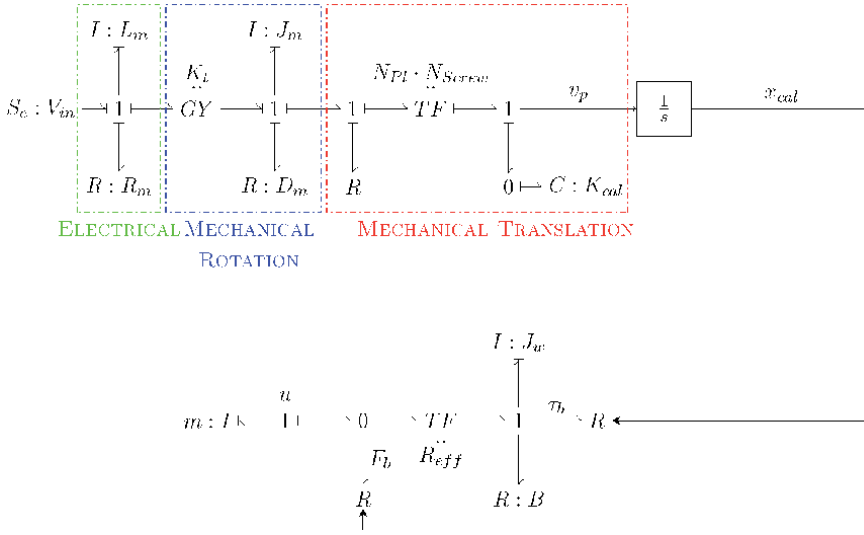
Figure 6.
EMB's bond graph.

The transformer is then used for the planetary gear set ratio (N_{pl}) and the ball-screw mechanism lead ratio (N_{Screw}). And finally, the interaction between the brake pad and the wheel is modeled with a stiffness similar to the one in the electro-hydraulic brake system's bond graph (K_{cal}).

Based on the bond graph in **Figure 6**, the state equations are presented in Eqs. 10–12. Also, the brake torque is calculated similar to the EHB actuator using Eq. 9.

$$\dot{I}_m = \frac{1}{L_m} \left(V_{in} - R_m \cdot I_m - K_t \cdot \omega_m \right) \tag{10}$$

$$\dot{\omega}_m = \frac{1}{J_m} \left(K_t \cdot I_m - D_m \cdot \omega_m - \tau_f - N_p \cdot N_s \cdot K_{cal} \cdot max \left(x_{cal} - x_0, 0 \right) \right) \tag{11}$$

$$\dot{X}_{cal} = N_s \cdot N_p \cdot \omega_m \tag{12}$$

The lumped friction torque (τ_f) is modeled using Karnopp friction with the Coulomb friction torque (τ_c) and maximum stiction torque (τ_s) having an affine relationship with the clamp force (F_{cl}). The area around zero of the motor rotational velocity is given by $d\omega$, and ω_m is the motor's rotational velocity and τ_{pl_0} is the friction torque when the shaft is not moving. C and G are constants that can be acquired using experimental results [10, 36].

$$\tau_f = \begin{cases} \tau_c \cdot \text{sign}(\omega_m) + b_v \cdot \omega_m & |\omega_m| \geq d\omega \\ \min \left(|\tau_{pl_0}|, \ \tau_s|| \right) \cdot \text{sign}\left(\tau_{pl_0} \right) & \text{else} \end{cases} \tag{13}$$

$$\tau_c = C + G \cdot F_{cl} \tag{14}$$

2.3 Electronic wedge brake actuator

We can draw the schematic for the wedge and the caliper in **Figure 7**. The motor's rotational velocity is being translated through a planetary gear set (not shown in the schematic) and a roller screw to a linear force on the wedge. Motor
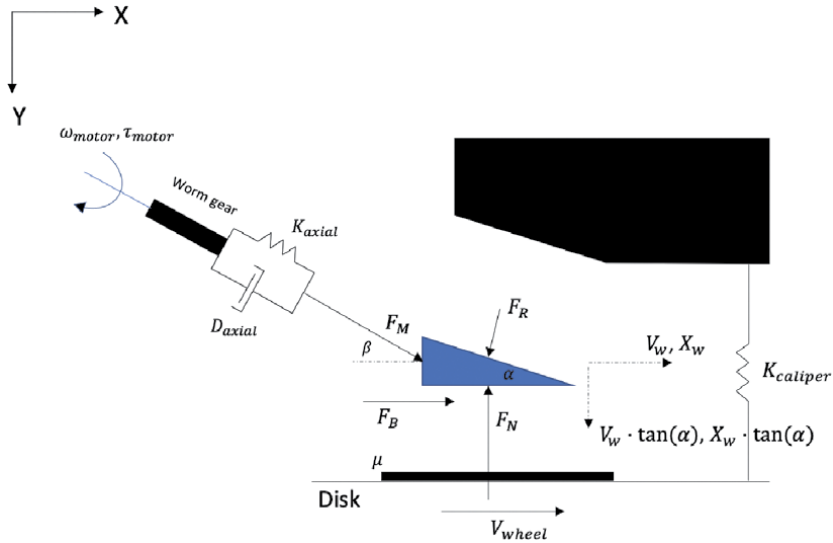
Figure 7.
EWB schematics.

shaft's axial stiffness and resistance is also added to the system. $K_{caliper}$ represents the stiffness of the caliper itself the stiffness between the wedge and the disk.

If we write the force equations for the wedge brake, we can get X-direction:

$$m_w \dot{V}_w = F_M \cos \beta + F_B - F_R \sin \alpha \qquad (15)$$

Y-direction:

$$m_w \dot{V}_w \tan (\alpha) = F_M \sin \beta - F_N + F_R \cos \alpha \qquad (16)$$

And for the disk surface, we can write

$$F_N = K_{Ca1} \cdot X_w \tan (\alpha) \qquad (17)$$

By rearranging Eqs. 15–17, we can remove the reaction force in the equations and write Eq. 18. We have incorporated Eq. 18 into the bond graph using 3 transformers.

$$\dot{V}_W = \frac{1}{m_W(1 + \tan^2 \alpha)} \left(\frac{1}{\cos \alpha} F_M + (\mu_{cal} - \tan \alpha) \tan \alpha (K_{cal}) \cdot X_w \right) \qquad (18)$$

Figure 8 represents the bond graph of the electronic wedge brake. The input to the system is motor voltage. The electric motor section remains the same as discussed in the previous sections. The transformer includes the roller-screw's lead ratio $\left(\frac{L}{2\pi} \right)$ and the planetary gear set's gear ratio (N). For the sake of simplicity, we assume, $\alpha = \beta$. F_B is the brake force that can be calculated from the relative velocity between the caliper and the wheel; however, since the wheel's velocity is much faster than the caliper's velocity, for the sake of simplicity, we assume that it would only be a function of caliper's movement. Finally, the transformer gains Tl, T2, and T3, based on Eq. 18, will become Eqs. 19–21.

$$T_1 = \frac{1}{\cos \alpha} \cdot \frac{1}{1 + \tan^2 \alpha} = \cos (\alpha) \qquad (19)$$
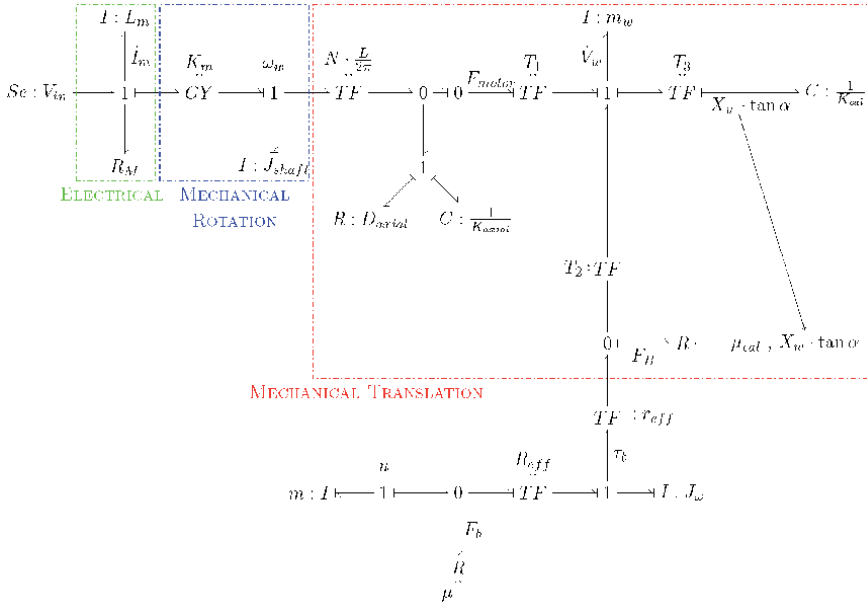
Figure 8.
EWB's Bond Graph.

$$T_2 = \frac{1}{1 + \tan^2 \alpha} \tag{20}$$

$$T_3 = \frac{\tan \alpha}{1 + \tan^2 \alpha} \tag{21}$$

Based on the bond graph, the equations of motion for the wedge brake are provided by Eqs. 22–28. Brake Torque is also calculated the same as other actuators.

$$\dot{i}_m = \frac{1}{L_m} \left(V_{in} - i_m \cdot R_m - K_m \cdot \omega_m \right) \tag{22}$$

$$\dot{q}_{ax} = LN\omega - \frac{V_w}{\cos(\alpha)} \tag{23}$$

$$F_m = K_{ax} q_{ax} + D_{ax} \dot{q}_{ax} \tag{24}$$

$$\dot{\omega} = \frac{1}{J_m} \{ K_m i_m - D_m \cdot \omega - L \cdot N \cdot F_m \} \tag{25}$$

$$\dot{V}_w = \frac{1}{M_w (1 + \tan^2(\alpha))} \{ \frac{F_m}{\cos(\alpha)} + (K_{cal} \cdot X_w \cdot \tan(\alpha)(\mu_{cal} - \tan(\alpha))) \} \tag{26}$$

$$\dot{X}_w = V_w \tag{27}$$

$$F_b = \mu_{cal} K_{cal} X_w \tan(\alpha) \tag{28}$$

3. Control strategy

In this section, we discuss the control strategy for each brake actuator. For each of the brake actuators, a transfer function is obtained using the linearized equations of motion provided in the previous sections (all the nonlinearities in the frictions and caliper stiffness are linearized). Controllers in each case are designed using Youla-Kucera parameterization, which we will discuss in details in this section. This

control strategy ensures internal stability, robustness, and reference tracking of the closed-loop system.

In the electro-hydraulic brake actuator, the pressure is the input and the output is brake force $\left(G_p = \frac{F_b}{P_{in}}\right)$. A controller was designed around the plant to follow a specific brake reference force. In practice, we would need to either estimate the brake force (or brake torque) or use a sensor to acquire that information [29]. For the electro-mechanical and electronic-wedge brakes, a cascaded control scheme is used. The schematics of these control architectures are shown in **Figures 9** and **10** [8, 10]. In the cascaded control scheme, each inner closed-loop system is a new plant for the outer loop controller design. In this case, for the first loop, the input is the motor's voltage and the output is the motor's current. For the second loop, the input is the motor's current and the output is the motor's angular velocity. Lastly, for the most outer loop, the input is the motor's angular velocity and the output is clamping force (the normal force that clamps the wheel). Cascaded control increase performance and robustness of systems with relatively more nonlinearities. Hence, the controllers for the EMB and EWB were designed using cascaded control since they have more non-linearities (e.g. mechanical friction) than the standard EHB. The current and angular velocity of the shaft can be directly measured while the clamp force requires to either be estimated or measured using a force sensor. Additionally, each loop has a disturbance which we will ignore in the first part of the control design. Later, we will use a disturbance rejection scheme to mitigate the effect of these disturbances.

3.1 Robust control design using Youla parameterization

Youla parameterization is a robust control technique that allows for shaping the desired closed-loop transfer function (T), known as complimentary sensitivity transfer function, while ensuring internal stability, disturbance rejection at low frequency, and sensor noise and unmodeled disturbance rejections at high frequencies. The main
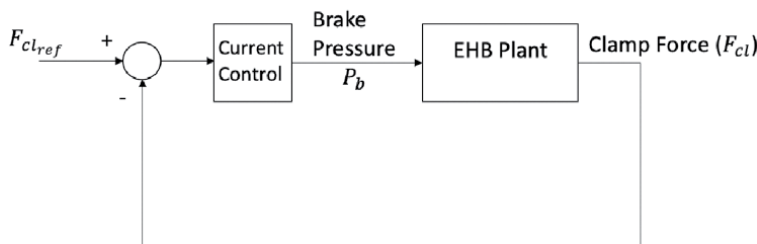
Figure 9.
Overall control architecture of EHB actuator.
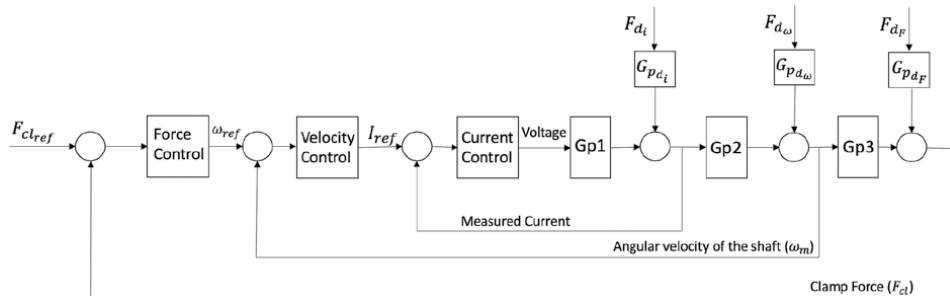
Figure 10.
Overall control architecture of EMB and EWB actuators.

idea is to shape the closed-loop transfer function (T) with a transfer function called Youla (Y(s)), which when multiplied by the plant transfer function (G_p) would become the closed loop transfer function (Eq. 29). To have a good tracking performance at steady-state, T(s) should be one in magnitude at low frequencies, it should be small in magnitude at high frequencies to ensure high frequency disturbance rejection.

$$T(s) = G_p(s) \cdot Y(s) \tag{29}$$

Therefore, according to Eq. 29, we can shape the closed-loop transfer function (provided that we meet the interpolation conditions, for ensuring internal stability, mentioned below). It is worth noting that Youla transfer function is related to the actuator effort so having a low magnitude Youla especially at high frequencies would keep the actuator effort low.

The closed loop transfer function (T(s)) is complementary to the sensitivity transfer function (S(s)) and the vector sum of these two transfer functions as given by (Eq. 30) is known as algebraic constraint. Therefore, this sensitivity transfer function should be small at low frequencies (to reject low frequency disturbances) and equal to one in magnitude at high frequencies due to the algebraic constraint.

$$S(s) = 1 - T(s) \tag{30}$$

If G_p is stable, the feedback loop would be internally stable if and only if Y(s) is selected to be stable. When G_p is not stable, $Y(s)$, $S(s)$, $T(s)$, and G_pS must all be stable to make the feedback loop internally stable. Therefore, to meet these conditions if there is an unstable pole (α_p) repeated n times in the plant (G_p), Eqs. 31 and 32, which are the interpolation conditions, have to be met (If the unstable pole is not repeated, Eq. 31 would suffice to meet the interpolation conditions).

$$T(\alpha_p) = 1, \quad S(\alpha_p) = 0 \tag{31}$$

$$\frac{d^k T}{ds^k}(\alpha_p) = 0, \quad \frac{d^k S}{ds^k}(\alpha_p) = 0, \quad For \quad 1 \le k \le n \tag{32}$$

For a non-minimum phase zero (α_z) repeated n time, zeros in the RHP (Right Half Plane), the interpolation conditions are given by Eqs. 33 and 34. If the unstable zero is not repeated, Eq. 33 is the only interpolation condition that has to be met [37].

$$S(\alpha_z) = 1, \quad T(\alpha_z) = 0 \tag{33}$$

$$\frac{d^k S}{ds^k}(\alpha_z) = 0, \quad \frac{d^k T}{ds^k}(\alpha_z) = 0, \quad For \quad 1 \le k \le n \tag{34}$$

If all the conditions above are met, then we can obtain the controller using Eq. 35.

$$G_c(s) = Y(s) \cdot S(s)^{-1} \tag{35}$$

In the following subsections, we discuss the controller design for the proposed brake actuators using the above strategy known as Youla parameterization.

3.2 EHB Youla control design

For the first step, we should acquire EHB's plant transfer function from the pressure input to the clamp force exerted on the wheel, which can be derived from Eqs. 5–9. However, using bond graph and equivalent mass (m_{Eq}) and resistance

(b_{Eq}), we can further simplify the equations and the transfer function to a lower degree. The equivalent mass and resistance are defined in the Eqs. 36 and 37 [33].

$$m_{Eq} = m_w + A_w^2 \cdot I_{line} \tag{36}$$

$$b_{Eq} = b_w + A_w^2 \cdot R_{line} \tag{37}$$

The transfer function from the input pressure to the clamp force can be written as (Eq. 38).

$$G_{P_{EHB}} = \frac{F_{cl}}{P_{in}} = \frac{k_{cal} \cdot A_w}{m_{Eq}s^2 + b_{Eq}s + k_{cal}} \tag{38}$$

Since the plant is stable and does not contain any unstable poles or non minimum phase zeros, no interpolation conditions need to be satisfied except selecting a stable Youla transfer function. We have selected this transfer function such that all of the plant's poles are canceled in order to freely shape the closed loop transfer function $T(s)$ and then compute this closed loop transfer function from Eq. 29. We choose the closed loop transfer function to be a second order Butterworth filter (Eq. 40) since this filter shape is optimal and we can freely choose the bandwidth and crossover frequencies. Additionally, we can add a low pass filter to Youla parameter to force it to be small in magnitude at high frequencies as we mentioned in the Section 3.1. This will result in Eqs. 39 and 40. By having T and Y, we can compute the controller using Eqs. 30 and 35. Since this process is the same in all the control designs, from now on, we only calculate Y and T for each loop. The sensitivity transfer function, S, can be computed from T (Eq. 30) and the controller transfer function, (G_c), can be computed using Eq. 35.

$$Y_{EHB} = G_{P_{EHB}}^{-1} \cdot \frac{\omega_n^2}{s^2 + 2\omega_n\xi \cdot s + \omega_n^2} \cdot \frac{W_1}{s + W_1} = \frac{\omega_n^2}{k_{cal} \cdot A_w} \cdot \frac{m_{Eq}s^2 + b_{Eq}s + k_{cal}}{s^2 + 2\omega_n\xi \cdot s + \omega_n^2} \frac{W_1}{s + W_1} \tag{39}$$

$$T_{EHB} = \frac{\omega_n^2}{s^2 + 2\omega_n\xi \cdot s + \omega_n^2} \cdot \frac{W_1}{s + W_1} \tag{40}$$

We now have two control parameters to tune: ω_n, and W_1 (ξ is selected to be $\frac{1}{\sqrt{2}}$ for a second order Butterworth filter). We can choose the natural frequency of the Butterworth filter (ω_n) based on the closed loop bandwidth requirement. In addition, using rule of thumb, we select W_1 to be at least five times bigger that the closed loop bandwidth so that the pole location associated with this transfer function would have no impact on the closed loop bandwidth. **Figure 11** shows a Bode magnitude plot of the T, S and Y based on the proposed control design.

Figure 12 shows the time response of the EHB closed and open loops. The open-loop pressure input is 3.2 kPa (this is chosen to generate the same steady-state results as the closed-loop controller) and the closed-loop is set to follow a 8 kN clamp force target. As shown in **Figure 12**, the controller is capable of following the target well and eliminates the open-loop overshoot.

3.3 EMB Youla control design

Since we have a cascaded control strategy for the EMB actuator, we are required to design three controllers. We start from the inner loop (current control), and the second loop (angular velocity of the shaft), and lastly we make our way up to the most outer loop which is clamp force control.
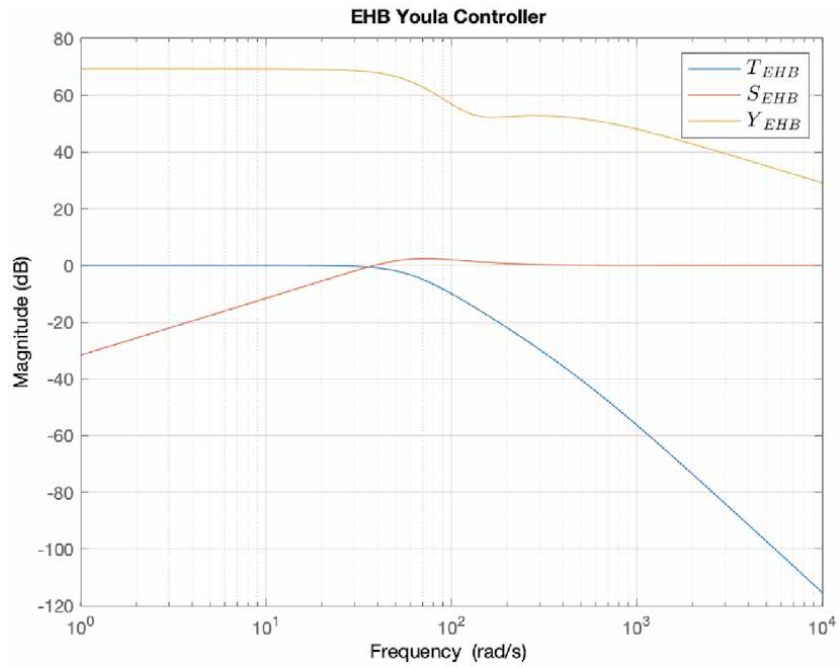
Figure 11.
EHB's designed closed-loop transfer function (T), Youla transfer function (Y), and sensitivity transfer function (S).
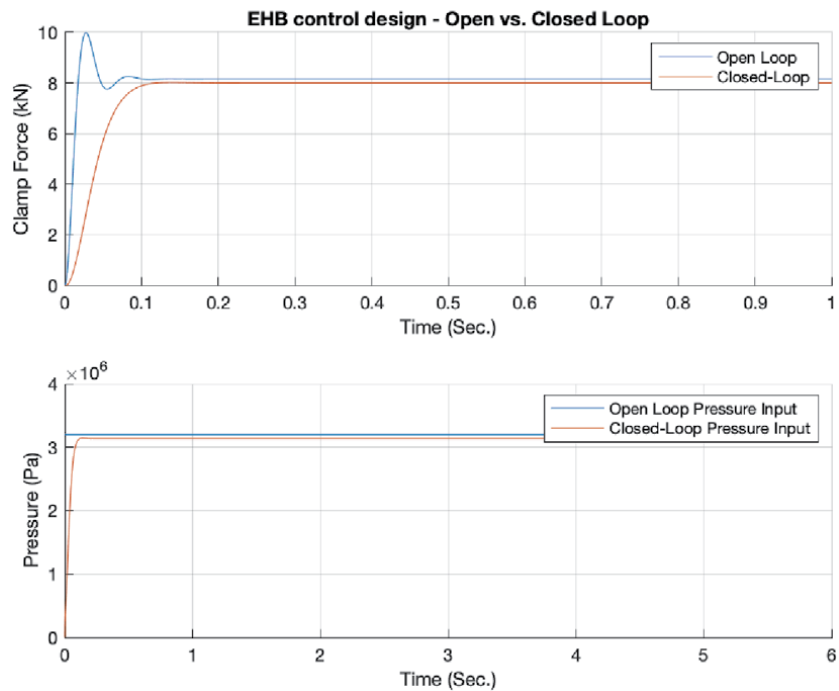
Figure 12.
EHB's controller results - closed loop vs. open loop.

Using Eq. 10, we can calculate the transfer function from the voltage input to the output current. However, we are regarding the last term in the equation $(K_t \cdot \omega_m)$ as a disturbance. The idea is to divide the bond graph into three separate blocks and control each block using the cascaded control strategy. This approach would make the design simpler and more intuitive so that any inputs from other blocks are regarded as disturbances. In this case, the input signal from the gyrator in **Figure 6** is regarded as a disturbance. We can then write the transfer function as Eq. 41.

$$G_{p_{EMB}} = \frac{I_m}{V_{in}} = \frac{\frac{1}{L_m}}{s + \frac{R_m}{L_m}} \tag{41}$$

Since $G_{p_{EMB}}$ has no unstable pole and non-minimum phase zero, we can cancel all the plant poles and create the desired closed loop response. However, canceling all the poles would result in a bigger magnitude of Youla transfer function; therefore, higher actuation effort. Since we want to keep the actuator effort as low as possible, we are going to only use a low-pass filter for Youla transfer function. In this design, we select the Youla transfer function such that the closed loop transfer function T has the same bandwidth as the original plant. The selected Youla transfer function is given by Eq. 42. Based on Y_{EMB_1}, we can compute T_{EMB_1} which is shown in Eq. 43. Another important note, when designing cascaded controllers, is that the closed-loop bandwidth of the inner loop has to be always faster than its outer loop. This ensures that the inner loop follows any command changes of the outer loop and hence, the overall closed loop stability is not compromised.

$$Y_{EMB_1} = \frac{1}{G_{p_{EMB_1}}(0)} \cdot \frac{W_1}{s + W_1} = R_m \cdot \frac{W_1}{s + W_1} \tag{42}$$

$$T_{EMB_1} = R_m \cdot \frac{W_1}{s + W_1} \cdot \frac{1}{L_m s + R_m} \tag{43}$$

Figure 13a shows that the magnitude of Youla transfer function reduces at high frequency while T and S have their desired shapes.

The controller for the second loop will be designed next. In this case, the new plant to is the inner loop closed-loop transfer function (T_{EMB}) multiplied by the transfer function from the second block open loop related to the dynamics of angular velocity of the shaft. The dynamics of the second block can be derived from Eq. 11 by considering the last term as the disturbance and substituting the nonlinear friction with a linear one $(\tau_f = D_m \cdot \omega_m)$. This results in Eq. 44, and transfer functions Y_{EMB2} and T_{EMB2} are given by Eqs. 45 and 46 respectively.

$$G_{EMB_2} = T_{EMB_1} \cdot \frac{\omega_m}{I_m} = T_{EMB_1} \cdot \frac{\frac{K_t}{J_m}}{s + \frac{D_m}{J_m}} \tag{44}$$

$$Y_{EMB_2} = \frac{1}{G_{EMB_2}(0)} \cdot \frac{W_2}{s + W_2} = \frac{D_m}{K_t} \cdot \frac{W_2}{s + W_2} \tag{45}$$

$$T_{EMB_2} = D_m \cdot \frac{W_2}{s + W_2} \cdot \frac{W_1}{s + W_1} \cdot \frac{1}{J_m s + D_m} \cdot \frac{R_m}{L_m s + R_m} \tag{46}$$

For the last loop, the transfer function from ω_m to F_{Cl}, the same procedure as the last loop is utilized to compute the open loop transfer function (Eq. 47). As shown in Eq. 47, there is a pole at zero. This pole must be canceled by Youla transfer function to meet the interpolation conditions $(T(0) = 1$ and $S(0) = 0)$, hence,
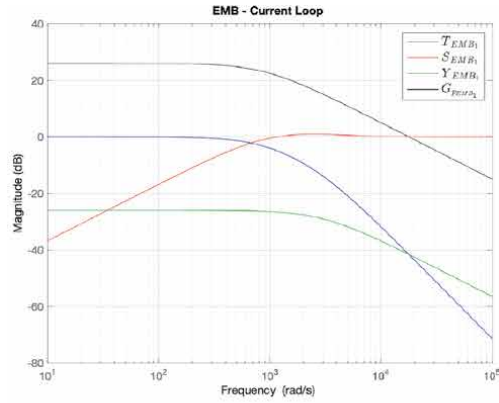
(a)
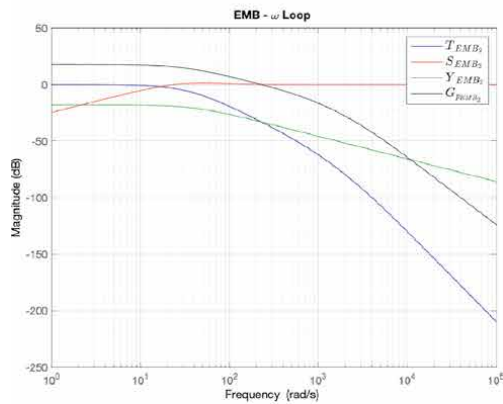
(b)
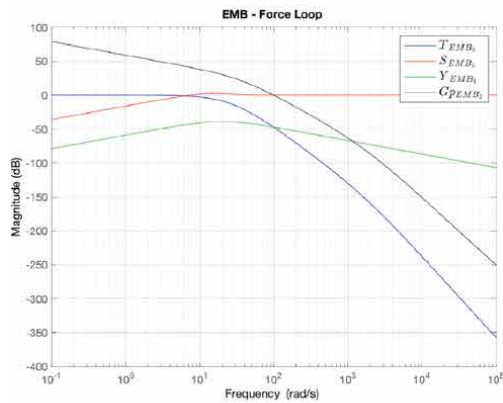
(c)

Figure 13.
EMB's designed closed-loop transfer function (T), Youla transfer function (Y), and sensitivity transfer function (S) for the current, ω and force control loop. (a) Current control bodes, (b) angular velocity control bodes, and (c) force control bodes.

to ensure internal stability. Finally, the transfer functions Y_{EMB2} and T_{EMB2} are given by Eqs. 48 and 49 respectively. The Bode plots are equivalently shown in **Figure 13b** and **c**.

$$G_{EMB_3} = T_{EMB_2} \cdot \frac{F_{cal}}{\omega_m} = T_{EMB_2} \cdot \frac{K_{cal} \cdot N_s \cdot N_p}{s} \tag{47}$$

$$Y_{EMB_3} = \frac{s}{G_{EMB_3} \cdot s(0)} \left(\frac{W_3}{s + W_3}\right)^2 = \frac{s}{K_{cal} \cdot N_s \cdot N_p} \cdot \left(\frac{W_3}{s + W_3}\right)^2 \tag{48}$$

$$T_{EMB_3} = G_{EMB_3} \cdot Y_{EMB_3} = \left(\frac{W_3}{s + W_3}\right)^2 \cdot \frac{W_2}{s + W_2} \cdot \frac{W_1}{s + W_1} \cdot \frac{D_m}{J_m s + D_m} \frac{R_m}{L_m s + R_m} \tag{49}$$

3.4 EWB Youla control design

For this actuator, we follow the same procedure as the EMB and Eqs. 50–58 are the results of this control design process. **Figure 14** shows the magnitude Bode plots of the closed loop transfer functions for the current, angular velocity of the shaft, and clamp force, respectively.

$$G_{p_{EWB_1}} = \frac{I_m}{V_{in}} = \frac{\frac{1}{L_m}}{s + \frac{R_m}{L_m}} \tag{50}$$

$$Y_{EWB_1} = \frac{1}{G_{p_{EWB_1}}(0)} \cdot \frac{W_1}{s + W_1} = R_m \cdot \frac{W_1}{s + W_1} \tag{51}$$

$$T_{EWB_1} = R_m \cdot \frac{W_1}{s + W_1} \cdot \frac{1}{L_m s + R_m} \tag{52}$$

$$G_{EWB_2} = T_{EWB_1} \cdot \frac{\omega_m}{I_m} = T_{EWB_1} \cdot \frac{\frac{K_t}{J_m}}{s + \frac{D_m}{J_m}} \tag{53}$$

$$Y_{EWB_2} = \frac{1}{G_{EWB_2}(0)} \cdot \frac{W_2}{s + W_2} = \frac{D_m}{K_t} \cdot \frac{W_2}{s + W_2} \tag{54}$$

$$T_{EWB_2} = D_m \frac{W_2}{s + W_2} \frac{W_1}{s + W_1} \frac{1}{J_m s + D_m} \frac{R_m}{L_m s + R_m} \tag{55}$$

$$G_{EWB_3} = T_{EWB_2} \frac{F_{cal}}{\omega_m} = T_{EWB_2} \cdot K_{cal} \cdot \sin(\alpha) \frac{L \cdot N}{2\pi} \cdot \frac{1}{s} \cdot \frac{D_{ax}s + K_{ax}}{m_w s^2 + D_{ax}s + K_{cal}\sin^2\alpha + K_{ax}} \tag{56}$$

$$Y_{EWB_3} = \frac{s}{G_{EWB_3} \cdot s(0)} \cdot \left(\frac{W_3}{s + W_3}\right)^2 = \frac{2\pi \cdot \left(K_{cal} \cdot \sin^2\alpha + K_{ax}\right)}{K_{cal} \cdot L \cdot N \cdot K_{ax}\sin\alpha} \cdot s \cdot \left(\frac{W_3}{s + W_3}\right)^2 \tag{57}$$

$$T_{EWB_3} = Y_{EWB_3} \cdot G_{EWB_3}$$

$$= \left(\frac{W_3}{s + W_3}\right)^2 \frac{W_2}{s + W_2} \frac{W_1}{s + W_1} \cdot$$

$$\frac{D_m}{J_m s + D_m} \cdot \frac{R_m}{L_m s + R_m} \cdot \frac{K_{cal}\sin^2\alpha + K_{ax}}{K_{ax}} \cdot \frac{D_{ax}s + K_{ax}}{m_w s^2 + D_{ax}s + K_{cal}\sin^2\alpha + K_{ax}} \tag{58}$$

3.5 Disturbance rejection

In our previous cascaded control strategy, we ignored the disturbance terms in each loop. However, these disturbance still have a negative impact on each loop's performance. Therefore, we are interested in looking at how each of these
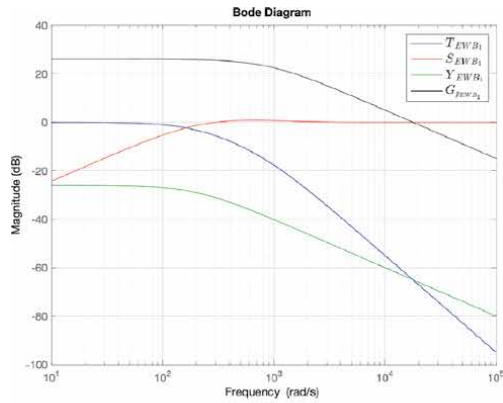
(a)
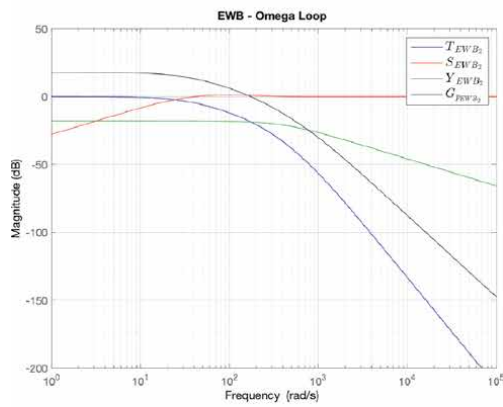
(b)
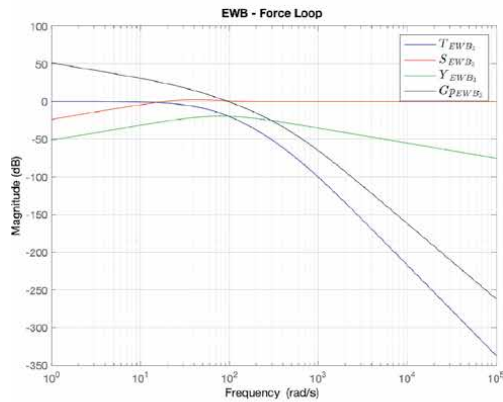
(c)

Figure 14.
EWB's designed closed-loop transfer function (T), Youla transfer function (Y), and sensitivity transfer function (S) for the current, angular velocity of the shaft, and force control loop. (a) Current control bodes, (b) angular velocity control bodes, and (c) force control bodes.

disturbances play a role in the loop. To analyze the effect of disturbances, we need to obtain the disturbance input to the loop output transfer function in each case. This would also help in design a feed-forward disturbance rejection to mitigate the negative effect of disturbances on the output and actuator effort. **Figure 10** shows a

block diagram where the disturbances in the cascaded control loop are given. To mitigate the effect of disturbance in each loop, a feed-forward term is added to reject these disturbances, as shown in **Figure 15**. For the sake of simplicity, the disturbance rejections have not been shown in all the cascaded loops. This disturbance rejection technique can be used wherever the disturbance can be estimated as these disturbance signals cannot be directly measured. Since the estimation might be computationally expensive and not very accurate at times, we should only use disturbance rejection wherever there is a great negative impact on closed loop the performance or on the actuator effort. The effect of the disturbance rejection is shown in Eq. 59 by additional term $-G_{p_d}G_p^{-1}S$

$$u = \left(-G_{p_d} \cdot G_p^{-1}S - Y \cdot G_{p_d} \right) \cdot F_d + Y \cdot r \tag{59}$$

Figure 16 shows the time response of the current loop for a step function of 5 A. As shown, the disturbance rejection has a faster response while maintaining the same level of actuation. It has slightly increases the actuator effort; however, since the closed loop time response with the disturbance rejection is faster, the feedback control loop bandwidth can be reduced to produce the similar time response
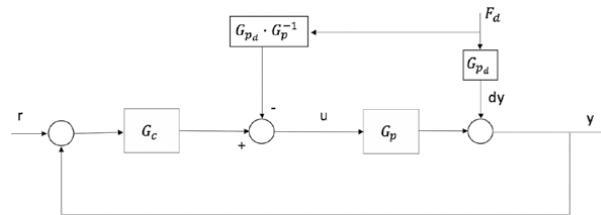
Figure 15.
Block diagram of disturbance rejection scheme used in the cascaded controller loops for EMB/EWB.
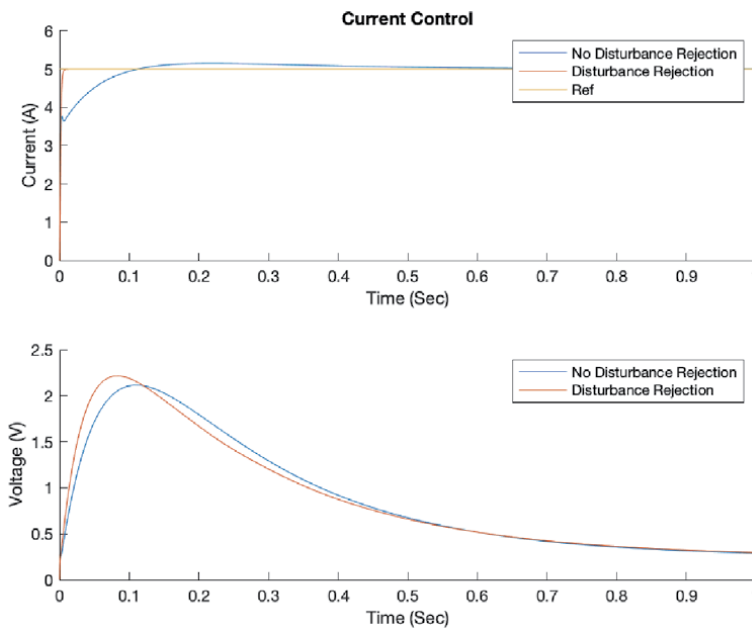
Figure 16.
EMB's current control step time response with and without the disturbance rejection.
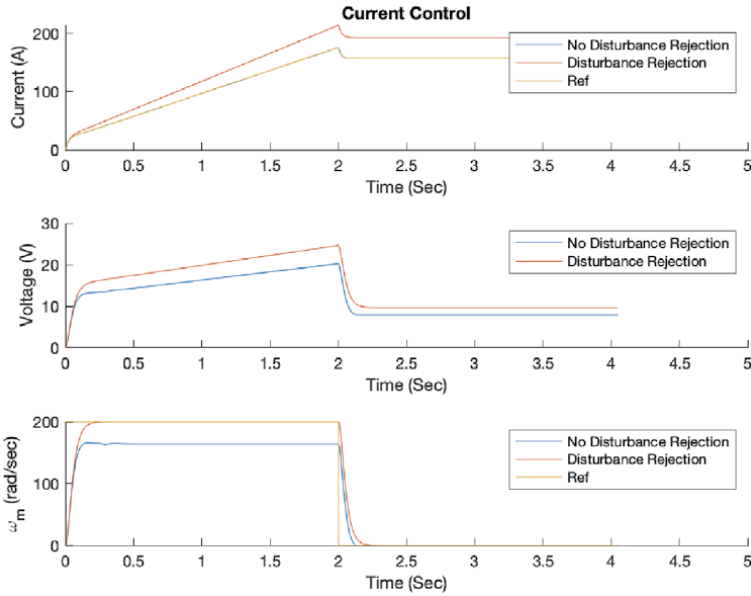
Figure 17.
EMB's angular velocity control pulse response with and without the disturbance rejection.

without the feed-forward term. This way we can reduce the actuation effort. **Figure 17** shows the response of the second loop to a pulse function of 200 $\frac{rad}{sec}$ including the current disturbance rejection capability. This shows that disturbance rejection has a big effect on the steady-state value. Finally, **Figure 18**, shows the result of the actuator's response for a 10-kN clamp force reference. As discussed, when the disturbance rejection scheme is utilized, the closed loop response of the EMB actuator is faster (0.35 seconds vs. 0.8 seconds) while maintaining around the same level of actuation. It should be noted that all the time response simulations are based on nonlinear models. Nonlinearity includes both frictions and actuator
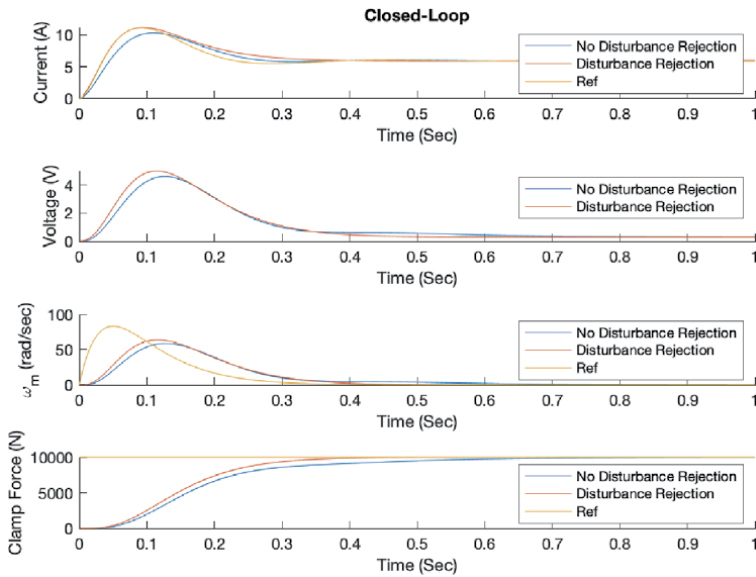
Figure 18.
EMB's closed-loop response over a step function with and without the disturbance rejection.
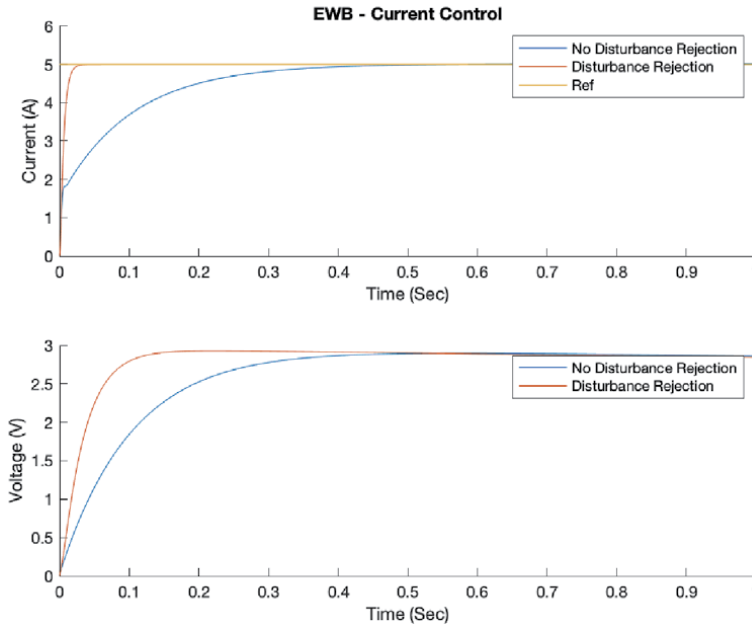
Figure 19.
EWB's current control step time response with and without the disturbance rejection.

saturation limits on the caliper for EMB actuator and only saturation limits for EWB actuator. Future studies will include addition of non-linear frictions to EWB.

Figures 19–21 show the results for the EWB actuator disturbance rejection performances. As shown in **Figure 19**, the disturbance rejection has a great impact on the current control responsiveness while maintaining the same amount of voltage. However, **Figures 20** and **21** show that the second and third loop's disturbance rejections do not have much of impacts on the either closed- loop responses or
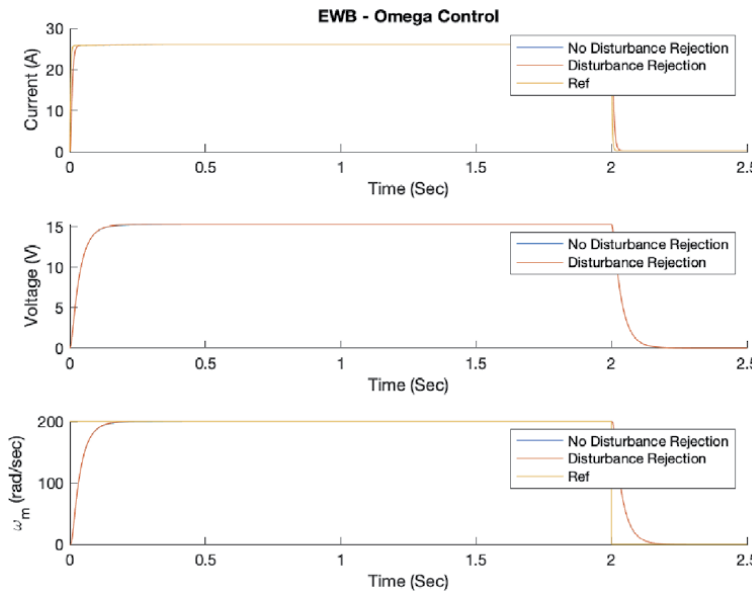
Figure 20.
EWB's angular velocity control pulse response with and without the disturbance rejection.
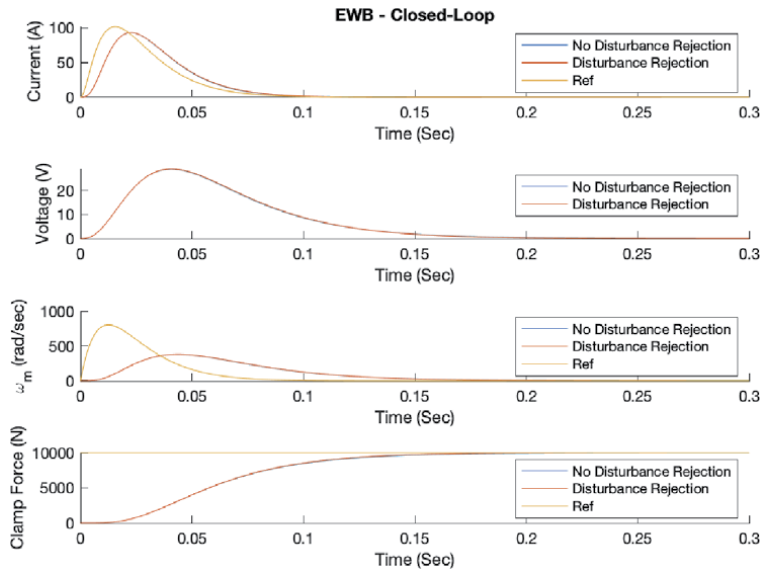
Figure 21.
EWB's closed-loop response over a step function with and without the disturbance rejection.

actuator efforts; therefore, it is recommended, in this case, to only use the current control feedforward disturbance rejection capability and abandon the other disturbance rejections in the second and the third loops.

4. Conclusions

In this chapter, we modeled three different friction brake-by-wire actuators using bond graph method. We then designed closed loop feedback controllers for each actuator using Youla parameterization technique. For the EMB and EWB actuators, we used a cascaded control strategy. Additionally, we designed disturbance rejections for each of their loops. The results of these disturbance rejections were discussed and it was found that EHB has a fastest response compared with the EMB and EWB actuators. However, this comes at higher cost due to addition of hydraulic lines and modules. When comparing the EMB and EWB actuators, based on the given current tuning, EWB has a faster response than the EMB, however, EWB also requires a higher actuator effort. Further investigation is required, by simultaneous optimization of actuators' physical systems including their control parameters, to have a better comparative analysis of the proposed actuators.

Other future studies will include more complex models where additional of some missing physical components (such as hydraulic pump, accumulator, and hydraulic build and dump valves) would be necessary to improve the accuracy of our comparative results. Additionally, a reference trajectory generator can be added, such as [38], to compare the performance of the proposed actuators during an ABS maneuver.

Acknowledgements

Author details

Ehsan Arasteh* and Francis Assadian
University of California, Davis, USA

*Address all correspondence to: earasteh@ucdavis.edu

IntechOpen

References

[1] Yuan Y, Zhang J, Li Y, Lv C. Regenerative Brake-by-Wire System Development and Hardware-in-Loop Test for Autonomous Electrified Vehicle. Available from: https://www.sae.org/content/2017-01-0401/.

[2] Sinha P. Architectural Design and Reliability Analysis of a Fail-Operational Brake-by-Wire System from ISO 26262 Perspectives;96(10):1349–1359. Available from: https://linkinghub.elsevier.com/retrieve/pii/S095183201100041X.

[3] Gombert BDM, Schautt M, Roberts RP. The Development of Alternative Brake Systems. In: Crolla D, Foster DE, Kobayashi T, Vaughan N, editors. Encyclopedia of Automotive Engineering. John Wiley & Sons, Ltd;. p. 1–11. Available from: http://doi.wiley.com/10.1002/9781118354179.auto025.

[4] Bob Chabot. Brake to the Future; pp. 18–24. Available from: https://www.motor.com/magazine-summary/brake-to-the-future.

[5] Hofmann D, Binder J, Pfau M, Schunck E. Hydraulic brake system for a vehicle. Google Patents; 2000. US Patent 6,149,247.

[6] Feigel HJ. Integrated Brake System without Compromises in Functionality; 114(7–8):46–50. Available from: http://link.springer.com/10.1007/s38311-012-0192-y.

[7] Cheon JS. Brake By Wire System Configuration and Functions Using Front EWB (Electric Wedge Brake) and Rear EMB (Electro-Mechanical Brake) Actuators;. Available from: https://www.sae.org/content/2010-01-1708/.

[8] Line C, Manzie C, Good M. Control of an Electromechanical Brake for Automotive Brake-By-Wire Systems with an Adapted Motion Control Architecture;. Available from: http://papers.sae.org/2004-01-2050/.

[9] Yamasaki T, Eguchi M, Makino Y. Development of an Electromechanical Brake; p. 9.

[10] Line C, Manzie C, Good MC. Electromechanical Brake Modeling and Control: From PI to MPC;16(3):446–457. Available from: http://ieeexplore.ieee.org/document/4475522/.

[11] Schwarz R, Isermann R, Böhm J, Nell J, Rieth P. Modeling and Control of an Electromechanical Disk Brake;. Available from: http://papers.sae.org/980600/.

[12] Line C, Manzie C, Good M. ROBUST CONTROL OF AN AUTOMOTIVE ELECTROMECHANICAL BRAKE;40(10):579–586. Available from: https://linkinghub.elsevier.com/retrieve/pii/S1474667015319765.

[13] Sakamoto T, Hirukawa K, Ohmae T. Cooperative Control of Full Electric Braking System with Independently Driven Four Wheels. In: 9th IEEE International Workshop on Advanced Motion Control, 2006. IEEE;. p. 602–606. Available from: http://ieeexplore.ieee.org/document/1631728/.

[14] Hartmann H, Schautt M, Pascucci A, Gombert B. eBrake® - The Mechatronic Wedge Brake;. p. 2002–01–2582. Available from: https://www.sae.org/content/2002-01-2582/.

[15] Fox J, Roberts R, Baier-Welt C, Ho LM, Lacraru L, Gombert B. Modeling and Control of a Single Motor Electronic Wedge Brake;. Available from: https://www.sae.org/content/2007-01-0866/.

[16] Han K, Kim M, Huh K. Modeling and Control of an Electronic Wedge

Brake;226(10):2440–2455. Available from: http://journals.sagepub.com/doi/10.1177/0954406211435584.

[17] Che Hasan MH, Khair Hassan M, Ahmad F, Marhaban MH. Modelling and Design of Optimized Electronic Wedge Brake. In: 2019 IEEE International Conference on Automatic Control and Intelligent Systems (I2CACIS). IEEE;. p. 189–193. Available from: https://ieee xplore.ieee.org/document/8825045/.

[18] Cheon JS, Kim J, Jeon J. New Brake By Wire Concept with Mechanical Backup;5(4):1194–1198. Available from: https://www.sae.org/content/2012-01-1800/.

[19] Emam MAA, Emam AS, El-Demerdash SM, Shaban SM, Mahmoud MA. Performance of Automotive Self Reinforcement Brake System;1(1):7.

[20] Ahmad F, Hudha K, Mazlan S, Jamaluddin H, Aparow V, Yunos MM. Simulation and Experimental Investigation of Vehicle Braking System Employing a Fixed Caliper Based Electronic Wedge Brake;94(4):327–340. Available from: http://journals.sagepub.com/doi/10.1177/0037549717733805.

[21] Ho LM, Roberts R, Hartmann H, Gombert B. The Electronic Wedge Brake - EWB;. Available from: https://www.sae.org/content/2006-01-3196/.

[22] Putz MH, Wunsch C, Morgan J, Schiffer M, Brugger J. Energy and Timing Advantages of Highly Non-Linear EMB Actuation;. Available from: https://www.sae.org/content/2013-01-2067/.

[23] Putz MH, Wunsch C, Schiffer M, Peternel J. Test Results of A Sensor-Less, Highly Nonlinear Electro-Mechanical Brake;. Available from: https://www.sae.org/content/2014-01-2541/.

[24] Putz MH, Wunsch C, Morgan J. The VE Electro-Mechanical Car Brake for

Windmills (and Railways);. Available from: https://www.sae.org/content/2012-01-1796/.

[25] Putz MH. VE Mechatronic Brake: Development and Investigations of a Simple Electro Mechanical Brake;. Available from: https://www.sae.org/content/2010-01-1682/.

[26] Karnopp D, Margolis DL, Rosenberg RC. System Dynamics: Modeling and Simulation of Mechatronic Systems. 5th ed. Wiley;.

[27] Yi J, Alvarez L, Horowitz R, de Wit CC. Adaptive Emergency Braking Control Using a Dynamic Tire/Road Friction Model. In: Proceedings of the 39th IEEE Conference on Decision and Control (Cat. No.00CH37187). vol. 1. IEEE;. p. 456–461. Available from: http://ieeexplore.ieee.org/document/912806/.

[28] Anwar S. An Anti-Lock Braking Control System for a Hybrid Electromagnetic/Electrohydraulic Brake-by-Wire System. In: Proceedings of the 2004 American Control Conference. IEEE;. p. 2699–2704 vol.3. Available from: https://ieeexplore.ieee.org/document/1383873/.

[29] Loyola J, Assadian F. An Investigation Into New ABS Control Strategies;9(2):869–876. Available from: https://www.sae.org/content/2016-01-1639/.

[30] Filipozzi L, Assadian F, Kuang M, Johri R, Alcantar JV. An Investigation into the Traction and Anti-Lock Braking System Control Design. In: SAE Technical Paper. SAE International; 2020. Available from: https://doi.org/10.4271/2020-01-0997.

[31] Burckhardt, Manfred. Fahrwerktechnik: Radschlupf-Regelsysteme. Vogel-Verlag, Wurtzburg.

[32] Canudas de Wit C, Horowitz R, Tsiotras P. Model-Based Observers for

Tire/Road Contact Friction Prediction. In: Nijmeijer H, Fossen TI, editors. New Directions in Nonlinear Observer Design. vol. 244 of Lecture Notes in Control and Information Sciences. Springer London;. p. 23–42. Available from: http://link.springer.com/10.1007/BFb0109919.

[33] Loyola J. An investigation into new ABS control strategies; 2017.

[34] Wang N, A Kaganov aAK S Code. Actuating Mechanism and Brake Assembly [patent;](WO 2005/124180 A1):13.

[35] Ahn JK, Jung KH, Kim DH, Jin HB, Kim HS, Hwang SH. Analysis of a Regenerative Braking System for Hybrid Electric Vehicles Using an Electro-Mechanical Brake;10(2):229–234. Available from: http://link.springer.com/10.1007/s12239-009-0027-z.

[36] Karnopp D. Computer Simulation of Stick-Slip Friction in Mechanical Dynamic Systems;107(1):100–103. Available from: https://asmedigitalcollection.asme.org/dynamicsystems/article/107/1/100/400601/Computer-Simulation-of-StickSlip-Friction-in.

[37] Assadian F, Mallon K. Robust Control: Youla Parameterization Approach. JOHN WILEY; 2020.

[38] Arasteh E, Assadian F, Filipozzi L. Algorithm to Generate Target for Anti-Lock Braking System Using Wheel Power;2:6.

Role of Bearings in New Generation Automotive Vehicles: Powertrain

Maruti Khaire

Abstract

Modern Automobile powertrain's technology is transforming to enable "connected, autonomous, shared and electric" (CASE). Modern automobiles are targeting to achieve the maximum vehicle uptime, utilization, and better total cost of ownership (TCO). Bearing is a vital component (sub-system) to achieve modern automobile's performance targets. Bearings plays important role of performance enhancement of all the rotating parts in systems by carrying the load and facilitating transfer of torque. Bearings achieve its performance via correct selection of materials, manufacturing technologies, design optimized geometries, sealing, lubrication in addition to application specific features. In modern automobile passenger comfort is key consideration and role of bearing is critical to achieve lower system noise. This chapter focuses on building awareness of the bearing technical requirements for different aggregates and means to achieve the requirements for modern automobiles. Summary of 11,300 patent's titles and customer voice analysis suggest the bearing development focus areas direction which are covered in this chapter. This chapter also introduces bearing technology research focus areas like reliability improvement, power-dense solutions, integrated functions, friction optimization, sealing/lubrication solutions, adoption of sensors, and also special application-specific eMotors bearings. Modern electronic technologies integrated with bearings are performing the critical role of powertrain health monitoring in the vehicle. However, bearings are having furthermore potential to contribute and enhance the performance of modern automobiles in near future.

Keywords: electric vehicles, bearings, power-dense, sensorization, NVH, capacities, integrated functions, friction, electric insulations

1. Introduction

Modern automobiles have made a significant contribution to the growth of society and humankind. Automobile vehicles and power train technology refined over the century of focused hard work by automobile engineering and scientist. Modern internal combustion engine propelled automobiles have satisfied multiple needs humankind in everyday life. It is difficult to imagine a world without automobiles in the present time [1]. The contribution of bearing to enhance the performance of automobiles is also immense. Bearings play's a critical role in the enhancement of any rotating systems performance by bearing loads and facilitating the load transfer

with minimum friction in addition to other functions. All rotating components of automobile systems require bearings to do its functions appropriately. Bearings improve the performance of the automobiles by supporting heavy loads and reducing friction. Major automobile sub-systems where bearings are implemented are internal combustion engines, transmissions, wheels, steering, pumps, and other electrical systems.

However, the popularity of automobiles, population density in the urban areas as well as rapidly growing urbanization has negatively impacted the environment. It raised health-related concerns to humans as well as other habitats. Internal combustion engines played the critical role of being prime mover for automobiles however, it is also a major source of pollution in urban areas due to the burning of fossil fuels and its by-products like CO_2, NOx, etc. In recent times focus on emission control from regularity bodies, country specific laws are increasing which is pushing researchers to look for solutions beyond internal combustion engines. In recent times electric powertrains, hybrid powertrains have already proven to be the strong alternatives to conventional engines.

1.1 Mega trends in automotive industry

Present time, the global automobile industry is focusing on clean transportation solutions including hybrid and battery electric drives. Automobiles are typically considered person-driven, personal transportation internal combustion engine (fossil fuel) propelled and independently operated transportation medium. In present times automobiles (passenger vehicles) are majorly part of personal transportation, however, incoming times the way automobiles are being utilized in practice is transforming toward shared mobility, autonomous vehicles.

The automobile industry is experiencing a major technology shift. Connected, Autonomous, Shared, and Electrified (CASE) are major technology trends in the automobile utilization and technology development (**Figure 1**).

Shared mobility is more of productive utilization of vehicle and related technology which connects vehicle or operator via internet-based communication for sharing the vehicle. Basically, vehicle ownership and utilization are extended for more productive utilization vehicle. Modern information technology, internet, and availability of electronic hardware making it feasible to ensure vehicle to vehicle, vehicle to device communication, and improve vehicle utilization to improve the uptime of vehicles. Modern automobiles are expected to utilize to its maximum potential, so it is becoming imperative to monitor the health of the system in real-time.
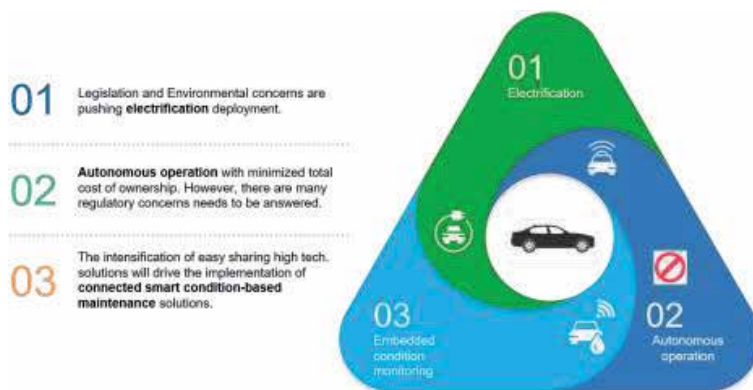
Figure 1.
Mega trends in automobile industry.

The electrification of the powertrain is another megatrend in the automobile industry. The electric vehicle powertrain is a major shift from fossil fuel-based prime mover (engine) to battery operated electric motors as a prime mover. Electrified vehicles are more efficient, less polluting making it a more transportation friendly solution. Electrification of powertrains is a major technology shift in which the propulsion of vehicles needs a lesser number of rotating parts as well as it simplifies the complete powertrain. Electric powertrains operate at lower cost as well.

In the present time, commuting to work in dense traffic is putting additional stress on vehicle operators and waste of precious productive time. Autonomous operation is the solution to these new challenges. Automobiles are using more electronics hardware than ever before due to these added functionalities. Driver assisted operation as well as complete autonomous drive powertrains are implemented in practice in modern automobiles. Real-time health monitoring of vehicle is important for the trouble-free operation as well as the safety of passengers in modern era vehicles.

As the automobile powertrain technologies are changing it is also percolating to critical components/subsystems like bearing. Modern vehicle bearings are far refined and technologically superior compare to traditional automobiles bearings. They are having multiple additional functionalities over the primary bearing functions. This chapter is about understanding the role of bearings in modern automobiles vehicles to achieve the mega technology shift in the automobile industry. The subsequent text introduces bearing technology research focus areas like reliability improvement, power-dense solutions, integrated functions, friction optimization, sealing/lubrication solutions [2], adoption of sensors, and also special application-specific eMotors bearings.

1.2 Modern automobiles powertrains and its significance

Modern automobile powertrains are working on the same engineering principles however, they are having far superior performance compare former powertrains. Modern powertrains are an integrated mechanical, electrical and electronics system to achieve the objective of lesser emission, better fuel efficiency, and higher overall efficiency. The modern powertrain can be classified into two major categories: Hybrid powertrain and battery electric powertrain.

Hybrid powertrains are having dual power sources like internal combustion engine and motor + battery arranged in multiple layouts like parallel, series, balanced, etc.

Figure 2 is a typical layout of a hybrid powertrain. It can be observed in the figure that the complete powertrain is having all the systems of a conventional powertrain including an internal combustion engine, transmissions and additionally it is also having a battery and motor to support the vehicle propulsion.

In a hybrid powertrain number of bearings are more compare to the conventional powertrain. The bearings are used in the engine, transmission, motors, and transfer case. The hybrid powertrains are having more rotating parts however, this powertrain runs efficiently as all special events in operations like peak power requirements are fulfilled by the battery powered electric motor.

Full battery-electric vehicle powertrains are simpler in construction and having lesser rotating components. Battery electric vehicle powertrains are also having multiple configurations like traction motor + transmission, independent in-wheel motors for each wheel, etc.

Figure 3 is a typical layout of a battery-electric powertrain, in which it is having a floor-mounted battery pack and traction motor drive for driving the wheels. Compare to conventional ICE vehicles this layout is simple and efficient. A lesser

Figure 2.
Typical hybrid powertrain layout [3].

Figure 3.
Typical full battery electric powertrain layout [4].

number of rotating parts means there are lesser possibilities of parts damage due to wear and tear and hence the system life is higher. This is one of the reasons Battery Electric vehicles are claimed to have higher life as well as OEMs offers longer warranty period. However, electric vehicles are having other challenges like higher speed, higher operating temperatures of parts, and risk of fire due electric system. It is important to mention here that batteries used in electric vehicles need proper cooling to operate at prescribed temperature limit to have extending time for battery discharge as well as minimizing other risks.

Refer **Figure 4**, which is indicating the battery packs construction in battery electric vehicles and its stacking, connection to electric motors.

Figure 4.
Typical battery pack in battery-electric powertrain [5].

1.3 Different types of powertrains

In the previous section, two main types of the modern powertrain are discussed i.e. hybrid power train and full battery-electric powertrains.

In this section, a comparison of different types of powertrains is presented (refer **Figures 5–7**).

Multiple parameters influence the selection of the powertrains types to implement in the vehicle such as vehicle operating range, power requirements, charging time, cost, availability of access to charging infrastructure, etc.

Battery electric vehicles powertrains (refer **Figure 5**) are comparatively simples in the structure. These vehicles operate very efficiently. However, they need significant time for the recharging so the vehicle will be down until it recharges. It is expensive to increase vehicle travel distance range mainly due to battery prices.

A hybrid power train (refer **Figure 6**) utilizes the current powertrain configuration and adds the battery/emotors to enhance the performance of the powertrain as well as extend the operating range by improving the fuel efficiency of the internal combustions' engine. It does not require an exclusive charging infrastructure as it primarily runs on fossil fuels. However, this powertrain does have emission-related concerns and having more number of rotating parts makes the powertrain complex due to effective management of dual power sources is essential optimum performance.

Practically, environmental impact due to fuel should be considered from well to tailpipe or from the source of raw material to conversion into power for vehicle propulsion. Considering this criterion battery vehicles are not completely emission-free vehicles. In a true sense, fuel cell vehicles (refer **Figure 7**) are practically green vehicles as they are not emitting any emission to the environment. Fuel cell powertrain uses hydrogen as prime energy source and utilizes chemical reactions process to charge the battery. Post electric energy conversion hydrogen atoms react with oxygen and forms water (H_2O) which gets emitted from the tailpipe. Battery electric vehicles and fuel cell vehicles are having similar configurations except in addition to battery storage the fuel cell vehicles also require hydrogen fuel storage.
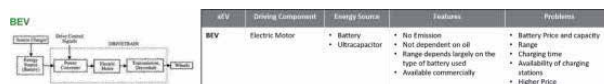
Figure 5.
Battery electric vehicle powertrain.

Figure 6.
Hybrid electric powertrains (HEV).

Figure 7.
Fuel cell vehicle powertrain.

All the modern powertrains are available commercially, however, its penetration is driven by multiple commercial factors including acquisition cost, operation cost, and ease of re-charging (refueling). All these modern powertrain configurations uses multiple types of bearings in the powertrain including deep groove ball bearings, needle roller bearings, special ceramic rolling element bearings with many other features to provide intended functions in the vehicles which are discussed in the following sections.

2. Role of bearings in modern powertrains

In modern powertrain, bearings are utilized not only for primary functions i.e. supporting the load and reducing the friction but also bearings are used with multiple other integrated functions like signal transmitting device on the motor, rotor positioning sensing bearings, etc.

In conventional powertrain bearings, functions are limited to its primary functions to support operating load on the shaft and facilitate the torque transfer smoothly.

Additional functions like lower the noise, the vibration of the system, and providing stiffness to the shaft system are few of the expected functions of bearing in the powertrain.

However, modern powertrains are having different requirements from the bearing considering constrains like lower weight, space as well as demanding operating conditions includes higher temperatures, speeds, inability to lubrication as well as longer service intervals, or no service for the design life of the system. The role of bearing is changing in modern automobiles. This demanding operating requirements putting immense pressure on bearing performance and achieving the desired specifications of the bearings. The role of bearing is moving from shaft support component to system solution to achieve multiple performance parameters in the intended aggregates. Bearing plays the role of catapult for the system health monitoring utilizing the vibration signature on bearing for identifying, predicting, and proactively preventing the potential breakdown of the system. The modern electronics hardware and miniaturization of the sensors facilitate integration pf the same with bearing to achieve many other intended functionalities.

Battery electric powertrains run at higher rotational speed and having a higher operating temperature. Being an electric system ensuring the lubrication to rotating parts is one of the major challenges. Hence, maintenance-free silent operation is one of the critical technical requirements for the bearings. The bearing design must fulfill the criteria of high-speed operation, lower NVH characteristics, high-performance lubrication, and robust sealing to retain the lubrication inside the bearing as well as protecting the bearing raceways from foreign contaminations.

Modern powertrains, particularly motors operates at a higher rate of acceleration as well as decelerations and to facilitate the same bearing design should be capable to handle the acceleration requirements. Inappropriately design of bearings can experience the functional as well as reliability issues in the system which may leads to system breakdown or reduced life the powertrain or also invite unwanted services of the system.

Bearing load carrying capacity is required to be higher considering the higher power of the prime movers and availability of less space due to lower weight expected from the system. The design of bearing from geometry, material selection, and manufacturing process plays a critical role to achieve higher load carrying

Figure 8.
Conventional ICE automatic transmission [6].

Figure 9.
Traction motor EV powertrain.

capacities in smaller envelope dimensions. The reduced the size of bearings facilitate lower overall system weight.

Bearings are playing a mission-critical functions in modern automotive powertrains. A deeper understanding of applications and expected functionalities play a crucial role to design of appropriate bearing for the modern automobile systems.

Figure 8 illustrates the internal combustion engine vehicles' conventional transmission. It can be observed that bearings in this transmission are having comparatively different technical requirements. The bearings are well lubricated, having comparatively lower speeds of operation.

Figure 9 is one of the EV power train configuration of modern electric vehicle transmission. Compare to conventional IC Engine vehicles the transmission layout is simpler in modern electric automotive vehicles. However, technical specifications and performance requirements of bearings are demanding.

3. Aggregates bearings and its requirements

Application and intended function in the aggregate is having an influence on the selection of bearings as well as on the performance of bearing. It is important to understand the bearing working environment, technical requirements, and application details for optimizing the performance [7]. Different aggregate applications are having different technical requirements that need to be fulfilled by bearing for optimum performance of the system. In this section, different aggregate and technical requirements of bearing in these aggregates are discussed,

3.1 Transmission system bearings

Automobile transmission facilitates speed and torque variation as per vehicle requirements and support engine to run in optimum performance range. The transmission system is having gears, shafts, shift system, and bearings arranged in the housing which perform speed and torque variation function together in coordination with the control system.

Transmission bearings are having multiple requirements to achieve the desired functions, some of them are mentioned below,

3.1.1 Axial and radial load carrying capacity

Transmission bearings experience combined axial and radial loads during the operation based on types of gears as well as shaft arrangement. The magnitude of the load depending upon the bearing position, gear arrangement, and torque transmission. The transmission bearings must be capable of handling these varying speeds and loads.

3.1.2 Lower space and weight

Vehicle powertrains are becoming compact due to the availability of space and emphasize on the reduction of the overall weight of vehicles. Power dense bearings that are capable to carry higher loads in a smaller size are the key selection criteria of bearings for modern transmission. Power density for the bearing is achieved with the usage of better material cleanliness from commonly used bearing materials like 100Cr6, 52100 with stringent specification of nonmetallic inclusions, oxygen content etc., optimized geometry, and precise manufacturing of bearings. It is worth mentioning here that each bearing manufacturer are having its own material specifications customized based on common bearing material chemistry. Most common bearing materials are SAE 52100, DIN 100Cr6, SUJ1, SUJ2 and many more.

3.1.3 Optimized friction

System efficiency is largely influenced by friction. Bearing contributes to the transmission system largely. Generally, Sealed bearings are having more friction compared to open bearings. Transmission bearings selection must have consideration of the friction.

3.1.4 Lower NVH

Modern automobiles particularly battery electric vehicles operate quietly. In the case of ICE, the engine noise suppresses some of the bearing noise, however, in modern automobiles bearings, noise is one of the major concerns. It is expected bearings with lower noise are implemented in the transmission system. In addition to noise, vibration and harshness are also to be given due consideration for the transmission bearings.

Automobile manufacturers specify the system level NVH requirements and typically bearing noise requirements are derived from system level requirements. However, very few manufacturers are having clearly defined NVH specifications for bearing. It is common practice in bearing industry to specify the bearing vibration level and measure at the end of the bearing assembly line. Each bearing manufacturer is having its specification for noise quality level of bearing. Low dB, Gen C, Q44 and other bearing manufacturer internal nomenclature of bearings quality

classes have been developed and specified accordingly [8]. Low-frequency noise is barely audible while high-frequency vibration does not audible to human ear. Hence noise problems at low frequency are categorized as "vibration problems" and at high frequency vibration are as "noise problems". As a rule of thumb, the arbitrary border separating vibration problems from noise problems is 1000 Hz. In other words, below 1000 Hz is vibration and above 1000 Hz is considered as sound or noise [8].

3.1.5 Assembly and disassembly friendliness: easy to mount and adjust (preload/pressing, etc.)

Modern automobile transmissions are expected to be assembly and disassembly friendly considering the automation of the manufacturing process. Complex adjustment during bearing assemblies also calls for a complex assembly process, higher assembly time which increases the overall manufacturing process complexity as well as capacities.

It is expected the bearings implemented in the transmission systems are assembly as well as disassembly friendly. Most suitable bearings need to have a minimum or no adjustment during the assembly.

3.1.6 Compatibility with lubricants

Lower viscosity lubricants with multiple other additives and chemicals are used as lubricants of the transmission for the reasons like reducing the churning losses in the system etc. However, lubricants in the system having influence on the bearing selection and bearing must be suitable to operate and compatible with lubricants in the transmission. Additionally, the sealed bearing application is also common in modern transmissions, so compatible seal material should be selected to avoid damage or performance issues.

3.1.7 Higher tolerance to demanding operating conditions (varying load and speed, temperatures, contaminations)

Bearing field issues analysis over the years suggests that external contamination, poor lubrication, and abusive operating conditions are major reasons for premature bearing failure. However, in modern powertrains, it is expected that bearing manufacturers should consider these conditions and develop bearing suitable to operate or having better capabilities to handle these operating conditions.

3.2 Engine system bearings

A hybrid powertrain utilizes dual power sources and one of the prominent power sources is the internal combustion engine. The importance of engine is prominent even though electric battery-powered vehicles are penetrating its presence. Engine is one of the great innovations of our time and will be around for many reasons. It is expected that more than half of the vehicles will be transformed into electric, but still majority will be hybrid vehicles. Engine bearings are having some typical requirements and some of them are mentioned below,

3.2.1 High-temperature operation

The engine converts chemical energy into thermal/mechanical energy via the fuel-burning process. The engine operates at elevated temperatures due

to fuel burning. Engine bearings must have dimensional stability at elevated temperature in addition to other performance parameters. Bearing mounting and operating clearances are largely affected due to different materials and their expansion rates.

3.2.2 Varying loads and speeds

Engine loads and speeds are varying during the operation. Bearing kinetic should be considered for varying speeds and loads. Rolling bearings use on crankshaft and camshaft is increased in recent time. However, at the connecting rod end, needle bearings or journal bearing are commonly used in an engine for multiple reasons including varying load and speeds.

3.2.3 Demanding operating conditions like contamination

Crankshaft bearings are positioned bottom of the crankcase in the engine. The engine piston is reciprocating (sliding motion), so the wear of the engine part is not uncommon. However, wear particles are mixed in the oil contaminate the oil. Engine oil is the primary source of lubrication to bearings. The contaminated oil is having a negative influence on bearing operation and due consideration should be given to have good performance of bearing in this condition. Special heat treatment can be considered on the bearings rolling elements and raceways in such demanding operating conditions. Optimum ball pass frequencies selection is also important to ensure the hunting of rolling elements is not affecting the raceways or rolling element.

3.2.4 Mounting and dismounting of bearings

Engine bearing mounting and dismounting is one of the important considerations, not only from a service, assembly perspective but also from the operational performance perspective. Appropriate fits must be applied to the bearing to ensure bearing is loaded and operates in favorable clearance zone. Wrong selection of fits can lead to catastrophic damages to bearing with prolonged use.

3.3 eMotors bearings

Battery electric vehicles are using motors as prime mover of the vehicle. Hybrid powertrain vehicles are also uses motors to propel the vehicle. Traction motors used in vehicles are having many special technical requirements that are different from conventional motors.

Some typical requirements are discussed in the following session,

3.3.1 Bearing arrangement

Traction motors bearing arrangement plays an important role in bearing selection. In most of the traction motors application two bearing arrangement (drive and non-drive end) is preferred. However, integration of transmission and motors is also common practice in electric powertrain due to which three inline bearings arrangement is also implemented.

The bearing arrangement adds complexity to the overall bearing system and the need for the appropriate distribution of bearing loads. Comparatively, two bearing arrangement is simple compare to three bearings arrangements.

3.3.2 Handling higher and varying speed/load

The traction motors that drive vehicles are required to run at very high speeds – up to 30,000 rpm, or almost three times the speed of the typical industrial motor. This high-speed operation places enormous strain on the bearings in the system. High-speed operation of bearing calls for special raceway geometry as well as separator designs to handle the additional centrifugal forces.

3.3.3 The higher temperature in operation

In the conventional system, lubrication oil dissipates the heat from the system and ensure the specific operating temperature. However, in electric motors heat dissipation is done via a cooling fan. Additionally, bearings are running at high speed, so the heat generation rate is higher hence the operating temperature. Motor bearing with seals and grease must have the ability to retain the lubricant inside the bearing at elevated temperature.

3.3.4 NVH and lower friction

Motor bearings are expected to operate at lower noise and lower vibrations. This is one of the key requirements for the motor bearings considering the high speed of operation, varying loads, and acceleration.

3.3.5 Maintenance free and sealing performance

Motor bearings are expected to be maintenance free so the grease selection, seal selection plays a major role in bearings performance and life.

3.3.6 Handling acceleration and deceleration during operation

Electric motors are very responsive to vehicle operating conditions. Motors accelerate as well as decelerate faster compare to ICE. The bearings must be designed to handling this rapid acceleration as well as deceleration. Rolling element separators, raceways geometry should be designed appropriately. Rapid acceleration and deceleration generate sliding motion in the bearing which can lead to damage to bearing raceways or other surfaces. In extreme acceleration and deceleration conditions, may result in catastrophic bearing damage or malfunction of bearing.

3.3.7 Tolerance to electric current leakage

Present bearings are made up of bearing steel material which is good conductor of electric current. In electric motor current passed though the bearing for any reason is detrimental to bearing function. However, motor feature that can affect conventional steel bearings is the high-frequency voltage switching of the inverter that produces current leakage, particularly at high motor speeds. This current leakage can pass through the bearing and causes, surface damage like surface pitting also called fluting. The initial stage of surface damage generates bearing noise, but the advance stage of surface damage can be catastrophic.

3.4 FEAD bearings

Front End Accessories Drive (FEAD) system is a combination of multiple subsystem drives in the vehicle for the purpose like air condition compressor drive

or alternator drive etc. The system requires basic requirements like axial and radial loads, static load carrying capacity, dynamic load-carrying capacity, speed, or rpm. However, the FEAD system requirement range beyond basic load-carrying capacities. Modern automobiles are expected to provide more comfort, steering pumps and air conditioner compressors have been added to the FEAD system in addition to alternator or BSG system. Modern automobiles are using comparatively more electronics parts/system operates using electricity which are rising the battery charging capacity. The charging capacity of alternators has increased its size, accordingly, leading to a rise in the amount of torque to be transferred to alternators. The increased torque transfer demands from higher load capacities for the FEAD system bearings.

Below are few technical requirements of FEAD system bearings.

3.4.1 Higher speed capabilities

FEAD systems are running at higher speeds like alternators are running in excess of 20000 rpm, the bearing must-have capability to handle the system increased speed. Additionally, the tendency of the engine running at a slower idle speed is also implying bearing selection due to extended time slower speed operations.

3.4.2 Handling acceleration and deceleration during operation

Acceleration and deceleration handling requirements coming from higher system speed, variation in loads.

3.4.3 Lower friction

Lower friction is a common requirement for all the modern automobile system bearings that are also applicable for FEAD system bearings.

3.4.4 Lower space and weight

Higher emphasis on the compact and lower weight of the system demands for lower size of the bearing with a higher load-carrying capacity.

3.4.5 Higher temperature operation

Higher operating temperature due to proximity to the engine as well as higher operating speed requires bearings seals, lubrication as well as dimensional stability at the higher operating temperature. The alternator bearings are expected to work at 180 to 200 Deg C temperature.

3.4.6 Maintenance-free operations (better sealing performance)

Maintenance-free operation is predominantly driven from no lubrication to bearing for life and sealing performance. The seals should be capable of running for the life of the vehicle and retain the lubricant inside the bearing.

3.5 Wheel bearings

The wheel bearings enable low-resistance rotations of the wheels by transferring axial and radial forces and support for wheel hub, wheel, and brake disc or brake drum. In modern automobiles, the wheel bearings are equipped with sensors that

send rotational speed signals to driver assistance systems like ABS, ESP, etc. [9]. The wheel bearings perform multiple functions, some of them are listed below.

3.5.1 Precise wheel guidance

Wheel bearing provides support to wheels, so rotation accuracy of bearing facilitates the guidance to the wheel. It is an important function for vehicle stability and control during operation.

3.5.2 Low weight, high bearing stiffness/rigidity (stability)

Wheel bearings are expected to have a lower weight. However, higher stiffness or rigidity requirement is an important consideration for wheel guidance and vehicle stability. As modern automobiles are having higher road speeds achieving safety of vehicle wheel bearings plays an important role.

3.5.3 Reduction in unsprung masses, which contributes to better driving dynamics

Unbalanced wheel bearing adds the unsprung mass to the system which affects the vehicle driving dynamics. As the speed of the vehicle increases the unsprung mass becomes more detrimental from the driving dynamics perspectives.

3.5.4 Absorption of external forces

Wheel bearings are subjected to many unknown forces due to constant changing road conditions and speeds, corners, and other conditions. The wheel bearings must be capable of absorbing the external loads without affecting the performance.

3.5.5 Long service life, lower maintenance and sustainability (environment and disposal), corrosion resistance

In operation, the wheel bearing is subjected to many unusual conditions like contact with mud, dirt, undulations, etc. However, in modern automobiles wheel bearing is expected to sustain all the working conditions without or with minimal need for maintenance. In addition to bearing design, lubricant and seal performance is an important parameter for long service life.

3.5.6 Thermal stability

Bearing should be stable in all aspects with all operating temperature ranges and perform as per the intended level. Temperatures can affect the preload of the bearing which can be detrimental for bearing performance.

3.5.7 Simple assembly/disassembly

As mentioned in the transmission system section, modern manufacturing considerations like automatic assembly, less complex mounting to reduce the complexity in the assembly process as well as at service time (**Figures 10** and **11**).

3.6 Steering system bearing

The steering system controls the direction of the vehicle, so the steering system bearings are having typical requirements to receive the feedback as well as facilitate

the execution the operators' intended command to operate the vehicle with minimum lag in the system.

3.6.1 Low frictional torque

Steering system bearing must have lower frictional torque for the system to be responsive.

Higher frictional torque adds operator fatigue as well as a slow response from the steering system which can influence the effective functioning of the vehicle control system.

3.6.2 Relatively high rigidity

Steering system bearing must have higher rigidity to enhance the system integrity as well as to achieve the system responsiveness and removing any sluggishness in the system.

3.6.3 Lower wear rate

All the bearings should have a lower wear rate, however, the steering system bearing it is critical requirements. The higher wear rate of bearings calls for frequent system adjustments or malfunctioning of the system operation.

Figure 10.
Electric vehicle transmission.

Figure 11.
Electric vehicle transmission.

3.7 Suspensions system bearings

Suspension system bearing relates to comfort and vehicle stability. Suspension system bearing have some unique requirements are mentioned below considering other requirements are common with other bearings as well.

3.7.1 Low-friction and distortion-free movement of the shock absorber spring during steering and deflection, enabling the spring

Suspension system bearings are connecting vehicle chassis with suspension/shock absorbers, so movement in response to road conditions should smooth.

3.7.2 Operate without self-aligning torque

Suspension bearing requires a self-aligning function considering the movement. It is expected that bearing should self-align without requirements of any additional external force for smooth operation.

3.7.3 Locate the shock-absorber spring and form a support surface for full deflection of the shock absorber

Suspension bearings support and locate to shock absorbers so it should function to provide the full deflection of the shock absorber.

3.7.4 Help isolate the body from road noise

Suspension bearing connects the suspension system with the vehicle body so any noise or undulation coming from the system results in noise. The bearing should be capable to isolate such noise from the vehicle body. A non-metallic bearing body is one of the ways to achieve this function.

In general, bearings play a significant role in vital aggregates to achieve the intended objective of modern automobiles. A deeper understanding of technical requirements and intended functions help bearing engineering to provide the most appropriate solutions which optimizes vehicle performance.

Figure 12 summarizes the requirements of bearings in modern automobiles and available options to achieve the same.

Refer to the discussions of the last section it can be observed that bearings requirements are driving trouble-free operations, longer service life, the lower

Figure 12.
Bearing requirements and means to achieve in bearings.

total cost of ownership, compact construction, lower friction, noise, better sealing performance as well as integrated functions.

Bearing engineers achieve these requirements in the right proportionately blending and integrating engineering know-how of different bearing materials, manufacturing processes like heat treatment, surface finishes, and geometries. Long service life functions are achieved with lubricants, better sealing in addition to optimized geometries and design parameters. Integrated functions and application-specific solutions make bearing versatile with few additional features to be used for multiple applications.

4. Bearing technology development focus areas

4.1 Identification of bearing technology focus areas

Modern automobiles are improved by challenging the status quo as well as by adopting the technology changes to current level of performance. The modern automobiles are also empowering and enforcing bearings innovations and technological limits to further enhance the performance of the vehicles.

Patent filing data provide great insights about the innovation areas in the industry. In order to understand the bearing technology development focus areas patent analysis is performed on last 10 years of global patents filing in bearing area, modern automobiles. **Figure 13** is a word cloud plot of 11,300 patents titles in bearing, modern automobiles areas filed in different global patent offices. The word cloud analysis provides quick insights into the analysis areas based on the frequency of keywords in the analysis data. It does not provide in-depth analysis; however, it is a good way of understanding the focus areas in technology development and the direction industry's research is leading.

Rolling bearing and bearing assembly is an obvious appearing word in the patent title hence not considered for further analysis discussion (**Figure 13**).

Figure 13.
Bearing technology focus word cloud plot of patent analysis.

Word cloud analysis pointing more research is being focused on electric motor bearings, bearing cage, sealing, anti-friction, fluid dynamics, lubrication (areas generally connected with the higher speed of operation), bearing steel, sintered bearing (areas indicating the material related research), motor control, sensors, active hub, load detection, level adjustment, abnormality detection (areas indicates the focus on bearing plus integrated functions like sensorization), camshaft, crankshaft, magnetic bearing, sealing devices, axial bearings (indicates areas of special bearing development, application-specific solutions development), special bearings in the current family of bearings also is the areas of technological research. Patent filing analysis is good indicator of the technology areas and direction.

Interactions with the automobile industry players are also summarized for connecting the technology focus areas with customer mandate or request for solutions. These areas can also be considered customer challenges, pain areas, or directions for the modern automobile development.

Modern automobile powertrain and system customer's voice is captured in two fundamental buckets i.e. must-have requirements (highly desirable) and good to have (differentiating) requirements.

High-speed bearings, high operating temperature, current insulations or conduction, lower friction bearings, power-dense solutions, and lower noise, vibration, and harshness (NVH) solutions are highly desired by automotive customers. However, long life, maintenance-free, better reliability, integrated functions, condition monitoring, sensor bearings, lower weight bearings are considered as differentiating features.

Patent analysis and modern automobile customer's voices are having a high level of similitude to interpret that bearing technology development customer requirements are indicating future development trends for the bearing. The above analysis also indicates that bearings are playing a vital role in automobiles and will also play a vital role in modern automobiles in the future.

4.2 Bearing technology development focus areas and ways of achievements

In the previous section, it is mentioned that haptic requirements from bearings are fulfilled with blending the bearing constituents in different proportions. In this section, some of the key influencers are discussed which facilitate the bearing technology development as well as achieving the modern automobiles bearing requirements.

Figure 15 is a summary of different constituents of bearings is its influence on bearing requirement achievement.

Typically, bearing materials are the backbones to achieve the bearings' fundamental functions. Different grades of materials can be implemented based on the intended requirements of the application. Bearing materials also facilitate next processes like heat treatment, machining, and many other parameters.

Heat treatment of bearing is very important to achieve the next level requirements of bearing. Standard heat treatment also called through hardening is commonly used to all-purpose bearings. However, if the bearings are required to operate in the demanding operating conditions, appropriate special heat treatment can be considered to enhance the bearing utility to application.

Bearing geometry plays a role in bearing friction, NVH, and different load handing areas. Bearings geometries need to be applied based on expected application requirements. Accuracy and functional requirement need to be well balanced to achieve economics.

Large number lubricants are available based on application requirements. The right selection of lubricants and seals increases the bearing utility in the application.

Many times, multiple application requirements can be achieved by applying suitable sealing/lubricant on the fundamentally same bearings (**Figures 14** and **15**).

The left side of **Figure 15**, summarizes the special or application-specific functional requirement fulfilling means of bearings. Customization of bearings is addressing the exact application needs however, customized solutions make bearing special and expensive.

4.3 Major bearing technology development areas for modern automobiles

4.3.1 Reliability improvement solutions

Reliability improvement of bearing relates to bearing performance and service life in the actual application. Reliability improvement of bearing means increasing the mean time between failure of bearing.

Bearing reliability can be improved by implementing special consideration to demanding operating conditions with special heat treatment, better materials, lesser intervention from the operator by unitized bearings, increasing wear resistance, implementing the better lubricants, tighter manufacturing tolerances.

Bearing life can be increased by multifold by right selection of heat treatment like compare to through hardening heat treatment, case hardening heat treatment (CN) can give 2 to 5 times more life to bearing in contaminated working environment. In addition to base material bearings can be coated to increase resistance of
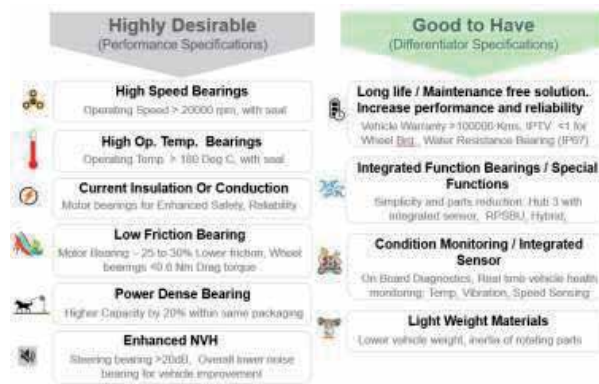
Figure 14.
Modern automobile "Voice of Customers" for bearings requirements.
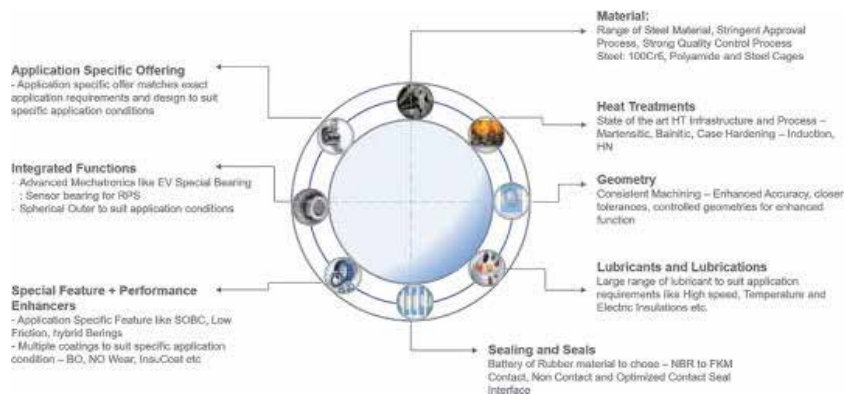
Figure 15.
Means of achieving intended bearing functions for modern automobiles.

bearing in specific working condition. Carbide based coatings are popular in some application, alumina material coatings are used for electrical insulations.

4.3.2 Power dense solutions

Power dense solutions related to more load carrying capacity per unit bearing size. As mentioned in the last sections, the bearings are catalysts to achieve a lower weight of the aggregate. Weight is the enemy for vehicle performance particularly in electric vehicles as it directly influences range as well as battery capacity. Lower size of bearings accumulates lesser space as well is makes the aggregate system compact. An additional advantage of power-dense bearing it utilizes lesser material, so it is also another means of achieving environmentally friendly solutions.

Current bearing material development and steel cleanliness is increase material mechanical properties. Additionally, manufacturing technologies increased control over the tolerances are enabling the power dense solution. Typically, 20 to 30% higher load carrying capacity can be improved within same envelope of bearings with right selection of material, geometries and manufacturing process including heat treatment.

4.3.3 Integrated functions

In recent times, frugal engineering is typically connected with terms like "more for less". In this text, integrated functions can relate to frugal engineering and can be termed as "more functions per bearing". Bearings can be attached with sensors and utilize for the position, speed as well as direction signals. Bearings are integrated with multiple functions like in new generation wheel bearings brake and wheel mountings are combined with bearings. Integrated bearing functions support compactness, reliability improvement, however, in some cases also adds complexity.

4.3.4 Friction optimization

Friction optimization solutions are intended to achieve better efficiency, lower losses in the bearing. Type of bearing and depending upon the application requirements bearing friction level can be achieved with the manufacturing process and tighter specification controls. Generally, bearing friction is a function of multiple factors like internal geometry, type of seals, material, lubricant, and the rolling element grade. Kinetics of bearing also plays a role in achieving the optimum friction of bearing. Adjustment in assembly, preload requirements, and assembly process influence final friction behavior of bearing in the application.

Lower friction of bearings directly contributes to wear performance as well as the efficiency of the system.

Figure 16 depicts the typical wheel bearing friction rate. Conventionally, vehicle manufacturers were assembling different parts together including bearings into wheel hubs. However, this arrangement is not effective considering the performance parameters. Hub 1 bearing is integration of two bearing into one, so it provides 10 to 15% better friction rate, Hub 2 is further improvement having integration of out race of bearing into housing and it provided 10 to 15% friction reduction compare Hub 1. Currently most of the modern automobiles are using Hub3 which are complete integration of bearing and wheel mounting.

This arrangement provides 50 to 60% friction reduction compare to conventional arrangements and additional 10 to 12% improvement compare to hub 2 arrangement.
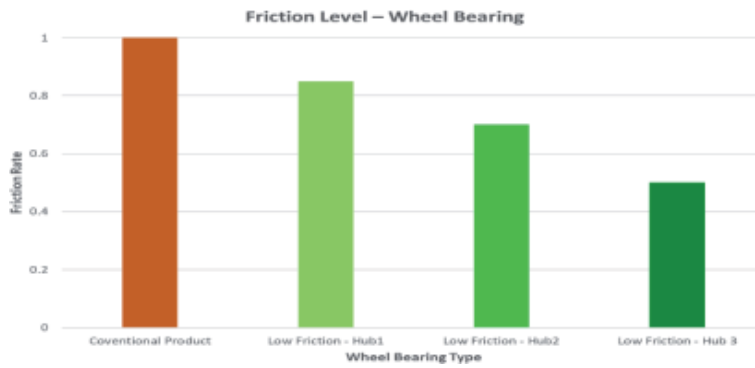
Figure 16.
Typical wheel bearing friction rate.

4.3.5 Sealing and lubrication solutions

Modern automobiles are targeting maintenance-free or maintenance less and fit for life reliable systems. Bearing sealing and lubrication solutions play a vital role in the achieving maintenance and reliability target of the system. Type of sealing (seal material, geometry, type of contacts, etc.) and lubrication selection for the bearing directly affect the bearing performance in operating conditions like temperature, speed, and friction. Good sealing on the bearings also increases bearing resistance to operating condition likes keeping the contaminations out of bearing raceways. Sealed bearings are not only maintenance-friendly but also environmentally friendly too.

Figure 17 depict the importance of capping (sealing) type in the bearing. Non-contact type of capping is good when bearing need to contain the lubricant like grease into the bearing with fair protection against exclusions, however, contact types of seals gives excellent protection against exclusions as well as retention of lubricants. Low contact capping compromise based on application requirements. However, all these capping is having impact on power loss or additional friction in the system. Non-contact type of capping gives lowest power lost among the all the capping types. Contact type capping is having highest power loss compare to both the non-contact and contact type capping. Typically, low contact type seals are having 30 to 40% higher power lost compare to non-contact type. Contact type capping is having 35 to 45% higher power lost compare to low contact type capping and about 70 to 80% higher power loss compare to non-contact type capping.
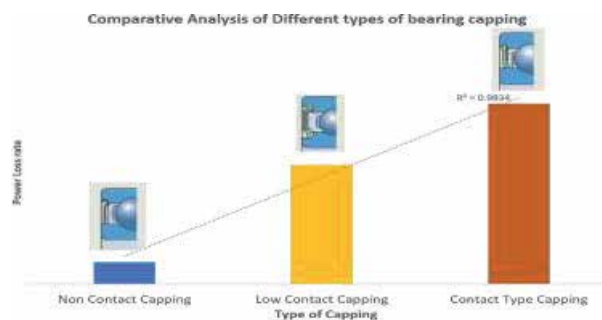
Figure 17.
Comparison of different type of capping and power loss.

Figure 18.
Modern automotive eMotor challenges.

4.3.6 "Sensorization" solutions

Modern automotive uses of electronics are increasing for vehicle control as well as operator comfort purposes. Vehicle control systems primarily need feedback from various systems which required sensor. Sensors are typically mounted on or around the critical rotating parts, hence sensors integrated bearings are a natural good choice for reliable signals. It is already proven that in rotating system's generate unique vibration signatures on the support bearing. These unique vibration signals can be processed electronically for multiple vehicle systems health monitoring via sensors. Sensor bearings provides better location as well as the accuracy of the signal for different feedbacks like speed, load, temperatures, etc. for effective vehicle monitoring. The miniaturization of sensor technology is an opportunity for the integration of bearings and sensors for modern automobile sensing needs.

4.3.7 Special electric motor bearings

Above bearing technology focus areas are covering major areas of eMotor bearings as well. However, some special requirements like current leakage and performance of bearing need special mention in this section (**Figure 18**).

High-frequency current passing through the bearing is detrimental for the bearing performance and there is a high probability of current leakage in eMotor bearings. If the current passed through the bearing generally results in "fluting" or micro pitting on the bearing races and start generating noise. The continued running of the bearing in this condition may encounter catastrophic damage. Bearing with special electric insulation coating, special materials for the rolling element (e.g. Ceramic) are developed and also under development for mass vehicle adoption by lowering cost. In addition to electric current insulations, technology development is also focused on electrical conduction solutions so the leakage current can be bypassed from the rolling area.

5. Conclusion

Modern Automobiles technology is transforming to enable "connected, autmonomous, shared and electric (CASE). Modern automobile powertrain development is focused on higher efficiency, maintenance free (higher reliability), compactness, light weight and autonomous control using mechatronics capabilities. New generation powertrains utilize lighter materials, lesser number of components and

integrated fuctions to achieve these objectives. Battery electric powertrains, hybrid power trains and hydrogen fueled fuel cell technologies are becoming popular in modern automobiles. Bearings are one of critical component (sub-system) to achieve modern powertrain's demanding technical requirements. It is imperative to bearing engineers to understand critical technical requirements of modern automobiles aggregates functions and bearing performance expection. Understanding aggregate performance and expected bearing technical requirements facilitate optimized solution development. Bearing plays crucial role in enhancing efficiency, integrating the functions, facilitate the compactness to achieve the lightweight powertrain. Bearing technology development focus area concentrating to addressing the modern powertrain's requirements. Bearing technology research and development areas focused on reliability improvement, power dense solutions, integrated functions, friction optimization, sealing/lubrication solutions, adoption of sensors and special application specific eMotors bearings. In addition to primary functions of bearing with the help of modern electronic technologies bearings are performing critical role of overall system health monitoring in the vehicle.

Bearing research is typically aligned to applications requirements and trends of the machine's technology. Modern automobiles are focusing more of passenger comfort with focus on autonomous driving, connected vehicles and electrification of vehicle. These technological requirements pushing bearing research more on sensorization, lower noise, vibration and harshness in addition to reliability improvement, maintenance free operation and application specific solutions. Bearing noise is one of the key concerns in modern powertrain specifically in electric drive trains. Bearing technologist are focusing on this aspect more than ever before. The bearing noise is directly connected to passenger comfort as well as overall system health. Bearing noise is also indication of system health as the issues with any part in the chain directly reflect to bearing vibrations. Leading bearing manufacturers are focusing on the sensor bearing technology as this feedback from vehicle critical parts is key to autonomation of modern automobile vehicles. Chronologically bearing research focus is more on application specific solutions, sensorization, maintenance operations. At system level bearings research is also focused on the "connected vehicle technologies" using on-board diagnostic using vibration signature identification capabilities at the bearing.

However, bearings are having furthermore potential to contribute and enhance role in modern automobiles in future. Future bearing technologies will focus more on the "bearing as a service" than typical product. Bearing as a service includes ability to collect the data, process the data and transfer the data for better understanding of vehicle dynamic behaviors. In modern automobiles bearing role will be second to electronics. The miniaturization of electronics complements to bearings utility exploitations and expansion to bearing space for additional functionalities. In modern automobiles the role bearings are as important and vital as the electronics considering potentials bearings provide for further integration and research.

Author details

Maruti Khaire
Electric Vehicles and Special Project, Pune, MH, India

*Address all correspondence to: officialmaruti@gmail.com

References

[1] Ehsani Mehrdad, Gao Yimin, Gay Sebastien E., Emadi Ali, Modern Electric, Hybrid Electric, And Fuel Cell Vehicles: Fundamentals, Theory, And Design. CRC Press LLC. USA.

[2] Khaire, Maruti, Electrical vehicles' bearings: Technological impact, applications and requirements. International Journal of Electric and Hybrid Vehicles. 2018: 10. 310. 10.1504/IJEHV.2018.098093.

[3] Hybird Vehicle Layout [Internet]. Available from: https://auto.economictimes.indiatimes.com/news/auto-components/global-powertrain-market-to-grow-to-524-6-bn-by-2020-report/71564971 [Accessed on 2020-08-17]

[4] Full Hyrbid Vehicle Powertrain layout [Internet]: Available from: https://electrek.co/2020/05/04/tesla-hybrid-battery-electric-car-range-extender/ 71564971 [Accessed on 2020-08-17]

[5] Battery pack of electric vehicles [Internet] Available from: https://www.whichcar.com.au/features/jaguar-i-pace-vs-tesla-model-x-on-paper [Accessed on: 2020-08-17]

[6] Typical Transmission crosssection [Internet]. Available from : https://www.zf.com/products/en/cars/products_46338.html

[7] SKF Group, Rolling Bearing Catalogue (2018)

[8] Bearing noise related specifications [Internet]. 2020. Available from https://www.consulting-trading.com/noise-measurement-in-ball-and-roller-bearings/#:~:text=In%20other%20words%2C%20below%201000,used%20to%20assess%20bearing%20quality [Accessd: 2020-09-20]

[9] Schaeller Website Wheel bearing catalogue [Internet]. 2020. Available at: https://www.schaeffler.com/remotemedien/media/_shared_media/08_media_library/01_publications/automotiveaftermarket/brochure_1/download_4/saam_3/schaeffler-aftermarket-brochure-fag-radlager-en-7640. [Accessed:2020-09-15]

Generation and Relaxation of Residual Stresses in Automotive Cylinder Blocks

Serageldin Salem Mohamed, Agnes M. Samuel,
Herbert W. Doty, Salvador Valtierra and Fawzy H. Samuel

Abstract

There is direct proportionality between ultimate tensile stress (UTS) and residual stresses (RS). Residual stresses gradually decrease with decreasing cooling/quenching rates. Quenching in cold water develops highest, whereas air cooling produces lowest, residual stresses. Significant increase in RS is observed in specimens with low dendrite arm spacing (high solidification rate), while lower residual stresses are measured in specimens with high dendrite arm spacing (low solidification rate). For I-4 and V-6 engine blocks, there is refinement in microstructure due to the increase in solidification rate along the cylinder length. The developed residual stresses are normally tensile in both engine types. Air cooling following solution heat treatment produces higher RS compared to warm water and cold water quenching. Solution heat treatment and freezing lead to maximum RS relaxation where 50% of the stresses are reduced after the solution heat treatment step. Aging time and temperature are directly proportional to the residual stresses relaxation. Relaxation of RS also depends on the geometry and size of the workpiece. It should be mentioned here that the I-4 and V-6 cylinder blocks were provided by Nemak-Canada (Windsor-Ontario-Canada). Residual stress measurements technique and procedure are typical of those used by the automotive industry in order to provide reliable data for industrial applications supported by intensive experiments.

Keywords: residual stresses, Al cylinder blocks, stress relaxation, effect of microstructure, heat treatment, quenching conditions

1. Introduction

Residual stress is generally referred as an internal stress, which exists in equilibrium inside a component in the absence of any external forces or constraints, temperature gradients, or any other external influences [1]. Any existing residual stresses are considered as elastic stresses that are kept under static equilibrium. Elastic limit is the maximum value that can be reached by any residual stresses. Any stresses higher than the value of elastic limit with no opposing forces will be relieved by plastic deformation until it reaches the value of the yield stress [2].

Excessive residual stresses may be generated due to the large difference in thermal expansion coefficient between the aluminum alloy ($2.4 \times 10^{-5}\,\mathrm{K}^{-1}$) and cast iron ($1.5 \times 10^{-5}\,\mathrm{K}^{-1}$) [3]. The presence of these residual stresses renders engine

blocks prone to either distortion or failure. Distortion of the cylinder bores results in a loss in compression of the air-fuel mixture due to improper sealing between the cylinder wall and the piston. This loss of sealing causes a portion of the compressed air-fuel mixture to leak out of the combustion chamber by a process known as "blow-by" [4] which reduces the engine efficiency. In conclusion, aluminum engine blocks with gray iron cylinder liners are prone to tensile residual stresses along the cylinder bores, which results in distortion, cracks, and a reduction in engine efficiency. Several ideas have been introduced in order to change the cast iron liners with another suitable replacement but due to technical and economic problems cast in liners are considered the most effective option in engine block manufacturing [5].

Many automobile parts are made of aluminum alloys such as engine blocks, cylinder heads, and suspension parts, and to perform efficiently and eliminate premature failure, residual stresses must be minimized. During service, these parts undergo heating and cooling cycles which promote residual stresses. Presence of residual stresses in the casting deteriorates fatigue life and dimensional stability of the part [6]. Tensile residual stresses can result in distortion and cracking of the component during quenching or machining and if this occurs during service, it can cause a reduction in efficiency or failure of the part [7]. The presence of residual stresses and/or distortion in a structural component, such as an aluminum casting, has a negative influence on the component's dimensional tolerance, performance and fatigue life [6].

Dynamic simulation was conducted on two crankshafts, cast iron and forged steel, from similar single cylinder four stroke engines [8]. Finite element analysis was done for different engine speeds and as a result, critical engine speed and critical region on the crankshafts were obtained. Stress variation over the engine cycle and the effect of torsional load in the analysis were investigated. Results from FE analysis were verified by strain gages attached to several locations on the forged steel crankshaft. Modeling of residual stresses in quenched cast aluminum components was carried out by Wang et al. [9]. To simulate residual stress and distortion induced during quenching, a finite element based approach was developed by coupling an iterative zone-based transient heat transfer algorithm with material thermo-viscoplastic constitutive model. With the integrated models, the numeric predictions of residual stresses and distortion in the quenched aluminum castings are in a good agreement with experimental measurements.

The automotive industry is the largest consumer of Al-Si cast alloys, where these alloys have replaced steel for the sake of greater fuel efficiency and higher performance, attributed to their much lighter weight and high thermal conductivity. Thus, Al-Si castings have gradually replaced automobile parts such as transmission cases, intake manifolds, engine blocks and cylinder heads that were formerly manufactured using steel and cast iron. The most common aluminum casting alloys that are used in the automotive industry are 319.0 (Al-6Si-3.5Cu), 332.0 (Al-9.5Si-3Cu-l.0Mg), 355.0 (Al-5Si-l.3Cu-0.5Mg), A356.0 (Al-7Si-0.3Mg), A357.0 (Al-7Si-0.5Mg), 380.0 (Al-8.5Si-3.5Cu), 390.0 (Al-17.0Si-4.5Cu-0.6Mg), 413.0 (Al-12Si) and 443.0 (Al-5.2Si) alloys. Amounts of alloying elements differ between different series, leading to changes in the final properties [5, 8].

Residual stresses can be classified into two groups according to their origin: the first one is macroscopic residual stresses which correspond to the residual stresses originating from heat treatment, machining, and mechanical processing, while the second group is microscopic residual stresses which often originate from lattice defects such as vacancies, dislocation pile-ups and thermal expansion/contraction mismatch between phases and constituents, or from phase transformations [6, 9].

The magnitude of residual stress depends on the stress-strain behavior and the degree of the temperature gradient attained during the quenching operation, which produces strain mismatch. It is found that the magnitude of the residual stresses is

directly proportional to the yield stress and Young's modulus (E). Furthermore, the stress-strain behavior at elevated temperature is an important factor in determining the amount of residual stresses [2]. Certain physical properties also increase the amount of strain mismatch (residual stresses) such as low thermal conductivity (k), high specific heat (c), high coefficient of thermal expansion (α) and high density (ρ) [2].

Residual stresses are often regarded as undesirable and harmful. Prolonging service life of any product can be achieved if such harmful residual stresses are eliminated or reduced. Several methods have been introduced in order to reduce these residual stresses. Annealing is one of these methods which involves exposing the material to very slow rates of cooling and heating with the aim of relieving stresses without altering the microstructure. If the temperature is too high then recrystallization might happen, leading to change in properties such as the yield stress which may not be desirable. The residual stresses relaxation by annealing occurs by one of two main mechanisms. The first is plasticity caused by reduced yield strength at an elevated temperature where instantaneous relief of stress occurs as the temperature is increased. The second mechanism is a creep based mechanism, which allows stress relief to occur over time [1].

Residual stresses can be quantified by many techniques. There are mechanical techniques such as sectioning, hole-drilling, curvature measurements, and crack compliance methods. These techniques correlate the measured residual stresses in components to the distortion. Diffraction techniques cover electron diffraction, X-ray diffraction, and neutron diffraction, which quantify the residual stresses by measuring the elastic strains in components. Other techniques, including magnetic and ultrasonic techniques, and piezo spectroscopy are also used to measure the residual stresses developed [6]. The mechanical techniques are considered destructive tests while the others are non-destructive tests but their accuracy is dependent on the microstructural variation and geometric complexity of the component structure.

An engine block as shown in **Figure 1** is the largest metal component in a car and is the most intricate. It holds and supports all other engine components such as cylinders and pistons and contains passages for coolant. The engine block is where combustion converts into mechanical energy that drives transmission propelling the car. Engine blocks used to be made of iron but today most of them are made of
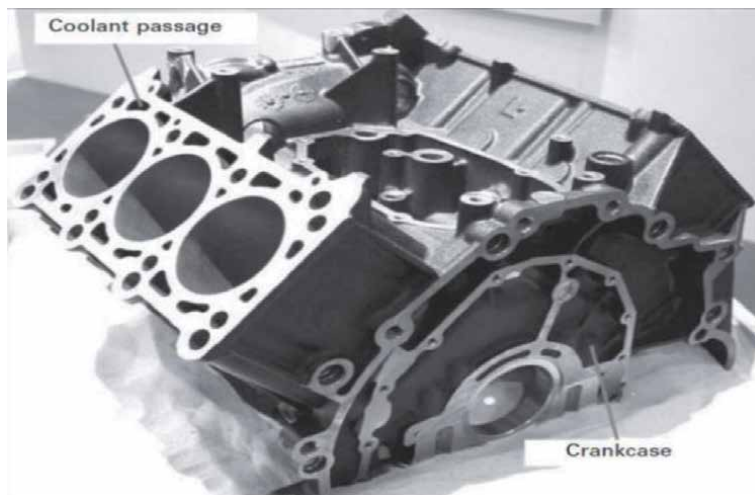
Figure 1.
Cast iron V-cylinder block (closed deck type) including a crankcase [10].

aluminum alloy for fuel efficiency. It is the largest and most complex single piece component in the car to which all other parts are attached. It represents from 3 to 4% of the total weight of the car. The block is typically arranged in a "V," inline, or I-4 horizontally-opposed (also referred to as flat) configuration and the number of cylinders may range from 3 to as much as 16 [10].

Carrera et al. [11] conducted a series of experimental tests to measure the residual stresses using strain gauges attached to different automotive engine blocks **Figure 2**. They discovered the development of tensile stresses higher than 150 MPa when the engine block contained the cast iron liners, while the engine blocks without cast iron liners exhibited 20 MPa compressive stresses in the cylinder bridge (**Table 1**). Furthermore, it has been observed that the residual stresses are affected by the dimension of the block and the wall thickness of the cylinder bridge where residual stresses decrease as the thickness increases. It was also found that V-8 engine blocks develop higher residual stresses than I-4 blocks with equivalent walls thickness [11]. These observations match the results for residual stresses obtained from the finite element model made by Su et al. [12].

Carrera et al. [13] and Colas et al. [14] analyzed residual stresses in complex aluminum castings. Measurements of residual stresses were carried out by extensometric means in automotive engine blocks. The results indicate that tensile stresses are caused during cooling of the aluminum alloy restricted by iron liners. Such observation is confirmed by measurements carried out in engine blocks cast without liners that develop compressive stresses in their cylinder bridges. The residual stresses are affected by the dimension of the block and the wall thickness of the interliner bridge, implying that a bigger block, such as a V-8 will develop higher
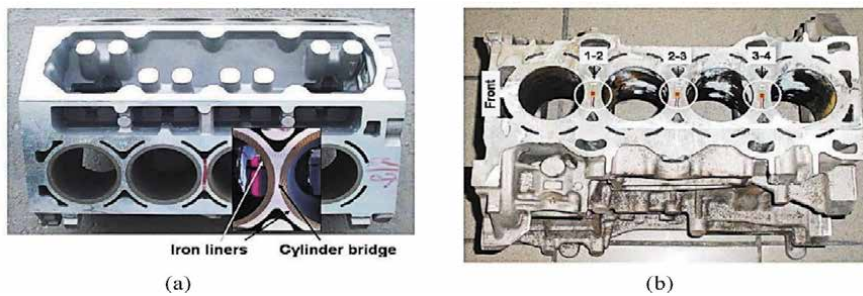
Figure 2.
Identification of the cylinder bridges in an I-4 block. Glued strain gauges are indicated: (a) eight cylinders and (b) four cylinder blocks.

Trial	Block	Weight (kg)	Wall thickness (mm)	Condition	Liners	Stress (MPa)	
						Average	Standard deviation
A	I-4	30.6	3.5	As-cast	Cast-in	113.8	3.5
B	I-4	30.6	3.5	T7	Cast-in	94.5	3.2
C	V-8	54.7	4.8	T7	Cast-in	121.8	9.9
D	V-8	56.2	3.0	T7	Cast-in	148.9	17.4
E	V-8	55.4	3.4	T7	Cast-in	158.7	14.6
F	V-8	43.5	8.5	T7	Inserted	–18.7	3.8

Table 1.
Characteristics of the studied blocks.

residual stresses than an I-4 that has walls of equivalent dimensions. Heat treating contribute to reduce the residual stresses.

A practice of shaking the blocks at an early stage contributes in reducing the residual stresses. Measurements of residual stresses in automotive blocks can be used as an early warning of changes taking place during processing of the material, and can be an aid when changes in design have to be made. According to Elmquist et al. [15], the feeders, which act as extra heat sources, affect residual stresses locally and helps to differences in stresses beneath the feeders, compared to corresponding areas between the feeders. **Table 2** lists the most frequently used alloys in the production of automotive components. Residual stresses as shown in **Figure 3** can be classified into two groups according to their origin: the first one is macroscopic residual stresses originating from heat treatment, machining, and mechanical processing. The second group is microscopic residual stresses which often originate from lattice defects.

2. Experimental procedure

The present work was divided into two parts: stage I aiming at evaluating the effect of metallurgical parameters on the residual stress in B319-based alloys and stage II measuring the residual stresses in I-4 and V-6 engine blocks using the information gathered from stage I.

2.1 Stage I

The chemical composition of the B319.1 base alloy coded E is shown in **Table 3**. The as-received ingots were melted in a 120-kg capacity SiC crucible, using an electrical resistance furnace. The melting temperature was maintained at $750 \pm 5°C$. Both alloy melts were grain refined and modified using Al-5% Ti-1%B and Al-10% Sr master alloys, respectively, to obtain levels of 0.25% Ti and 200 ppm Sr in the melt. Finally, the melts were degassed for ~15–20 min with a rotary graphite impeller rotating at ~130 rpm, using pure dry argon. Following this, the melt was carefully skimmed to remove oxide layers from the surface.

The melt was poured into different molds for various purposes, namely (a) ASTM B-108 permanent mold, for preparing the tensile test bars; (b) an L-shaped rectangular graphite-coated metallic mold; and (c) a block shaped graphite-coated metallic mold. All molds were preheated to 450°C to drive out moisture and avoid cold shut of the blocks. Regarding ASTM B-108 mold, each casting provides two test bars, with a gauge length of 70 mm and a cross-sectional diameter of 12.7 mm. Three samplings for chemical analysis were also taken simultaneously at the time of the casting; this was done at the beginning, in the middle, and at the end of the casting process to ascertain the exact chemical composition of each alloy.

The L-shaped mold and block castings were mainly used for residual stress measurements and microstructure samples and for preparing samples for micro-structural examination. The molds were preheated to 250°C. Samples were prepared for the measurement of secondary dendrite arm spacing (SDAS) and grain size in both alloys. Bars were cut from both molds with the dimensions of $200 \times 40 \times 40$ mm³ for measuring of residual stresses using the sectioning method. All the samples, tensile test bars for residual stress measurements treated. Tensile test bars were to the point of fracture using a servohydraulic mechanical testing machine (model 801 produced by MTS), at a strain rate of $4 \times 10^{-4} \, s^{-1}$.

Samples for microstructural characterization were used for secondary dendrite arm spacing (SDAS) and grain size measurements. For grain size measurements,

Aluminum foundry and die cast alloys

A.A. No.	Former commercial designation	Cu	Zn	Fe	Si	Mn	Mg	Cr	Nl	Sn	Tl	Others Ea.	Total	Al
2081	108	3.5 4.5	1.0	0.9	2.5 3.50	0.50	0.10		0.35		0.25		0.50	Bal.
296.1	B295.0/B195	4.0 5.0	0.50	0.9	2.0 3.0	0.35	0.05		0.35		0.25		0.35	Bal.
319.1	319	3.0 40	1.0	0.8	5.5 6.5	0.50	0.10		0.35		0.25		0.50	Bal.
319.1sr		3.0 4.0	1.0	0.9	5.5 6.5	0.50	0.25 40		0.35		0.25	(1)	0.50	Bal.
355.1	355	1.0 1.5	0.35	0.50	4.5 5.5	0.50	0.45 0.6	0.25			0.25	0.05	0.15	Bal.
356.1	356	0.25	0.35	0.50	6.5 7.5	0.35	0.25 0.40				0.25	0.05	0.15	Bal.
A360.1	A360	0.6	0.40	1.0	9.0–10.0	0.35	0.45–0.6		0.50	0.15			0.25	Remainder
A380.1	A380	3.0–4.0	2.9	1.0	7.5–9.5	0.50	0.10		0.50	0.35			0.50	Remainder
B380.1		3.0–4.0	0.9	1.0	7.5–9.5	0.50	0.10		050	0.35			0.50	Remainder
383.1	383	2.0–3.0	2.9	1.0	9.5–11.5	0.50	0.10		0.30	0.15			0.50	Remainder
383-1		2.0–3.0	0.90	1.0	9.5–11.5	0.50	0.10		0.30	0.15			0.50	Remainder
384.1	384	3.0–4.5	2.9	1.0	10.5–120	0.50	0.10		0.50	0.35			0.50	Remainder
A384.1		3.0–4.5	0.9	1.0	10.5–12.0	0.50	0.10		0.50	0.35			0.50	Remainder
B390.1		4.0–5.0	1.4	1.0	16.0–18.0	0.50	0.50–0.65		0.10		0.20	0.10	0.20	Remainder
A413.1	13	1.0	0.40	1.0	11.0–13.0	0.35	0.10		0.50	0.15			0.25	Remainder
C443.1	43	0.6	0.40	1.1	4.5–6.0	0.35	0.10		0.50	0.15			0.25	Remainder

		Aluminum foundry and die cast alloys										Others		Al
A.A. No.	Former commercial designation	Cu	Zn	Fe	Sl	Mn	Mg	Cr	Nl	Sn	Tl	Ea.	Total	
705.1	603, Ternalloy 5	0.20	2.7 3.3	0.6	0.20	0.40 0.6	1.5 1.8	0.20 0.40			0.25	0.05	0.15	Bal.
712.2	D712.2, D612, 40E	0.25	6.0 6.5	0.4	0.15	0.10	0.50 0.65	0.40 0.60			0.16 0.25	0.05	0.20	Bal.
713.1	613, Tenzaloy	0.40 1.0	7.0 8.0	0.8	0.25	0.6	0.25 0.50	0.36	0.15		0.25	0.10	0.25	Bal.

Table 2.
Aluminum foundry and die casting alloys (standard and custom specification aluminum ingots).
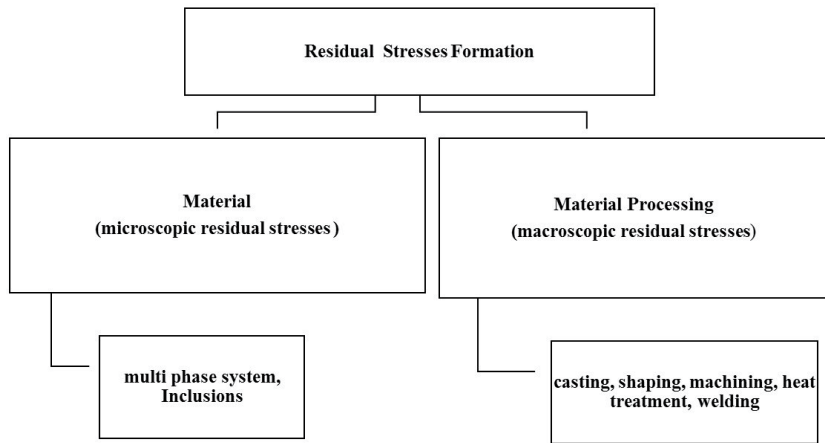
Figure 3.
Origin of residual stress formation.

Element wt.%	%Si	%Cu	%Fe	%Mn	%Mg	%Sr	%Ti	%Al
B319.1	7.4	3	0.4	0.2	0.26	0.05	0.26	Bal.

Table 3.
Chemical composition of the B319.1 alloy.

the polished samples were etched for 15 seconds, using a solution containing 2 ml HF (48%) + 3 ml HCl (conc.) + 5 ml HNO_3 (conc.) and 190 ml distilled water.

Residual stress measurements using the sectioning technique require block surface preparation and strain gauge installation prior to strain measurement and calculation of residual stress.

1. The block surface of the alloy is machined, and then abraded manually successively using SiC papers of grit size 120, 320 and 600.

2. Strain gage installation: place strain gauge (bonding side down) on a chemically clean and neutral plastic plate surface. It is important to mention that all strain measurements are performed at/under the same ambient temperature (23°C) and dry condition (humidity was less than 13%) (**Figure 4**).

2.2 Stage II

In this stage, the investigation will focus on the analysis of residual stresses evolved in I-4 and V-6 engine blocks following different types of heat treatments
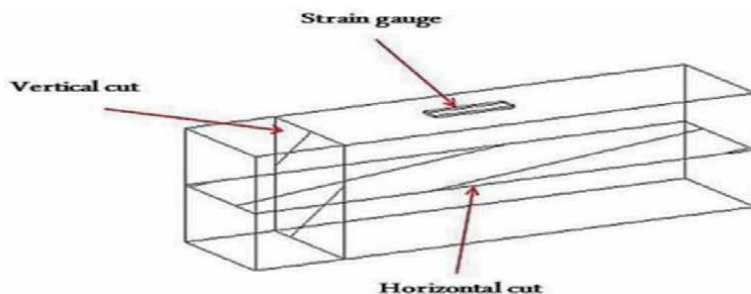
Figure 4.
Sketch illustrating cutting directions.
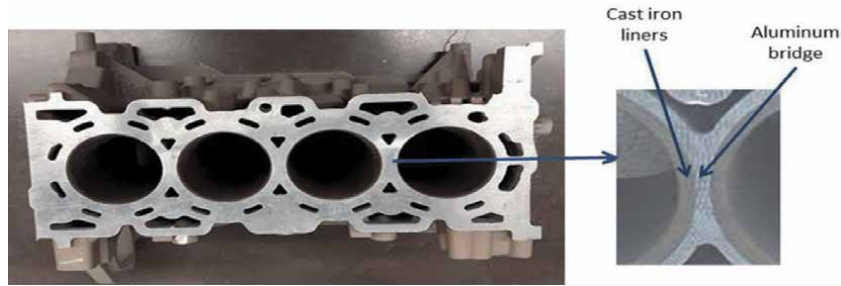
Figure 5.
I-4 engine block.

(solutionizing as well as artificial aging). The liners used in these blocks were preheated to 400°C using induction coils, prior to being inserted into the mold to promote a more uniform microstructure (**Figure 5**) [16].

The engine blocks followed solution heat treatment (SHT) at 500°C for 8 hours, then quenching/cooling in different media, prior to T6 and T7 aging treatment for various aging times. Two quenching media were applied: cold water, warm water. Artificial aging, T6 aging is carried out at for 10, 50 and 100 hours 170°C (T6 aging). As for T7 treatment, samples were aged at 250°C for 10, 50, and 100 hours aging times. The T7 treatment is used industrially. To facilitate the handling of the engine block in the foundry, the I4 engine blocks were cut in half. This procedure was carried out after validating that there would be no change in results between the whole block (four cylinders) and half the block (two cylinders).

The sectioning method is a complete destructive test and can be considered as the first proposed method for measuring residual stresses. It involves cutting of the component with an electric strain gauge attached, and relies on the measurement of local strain (using strain gages) induced due to the release of residual stress upon removal of material from the specimen [14–16].

3. Results and discussion

3.1 Stage I

Results of secondary dendrite arm spacing (SDAS—**Figure 6**) measurements show that the average SDAS for the block casting is 60 μm which is reflected by the large grain size observed in **Figure 7(a)**. Due to the high solidification rate obtained

(a)   (b)
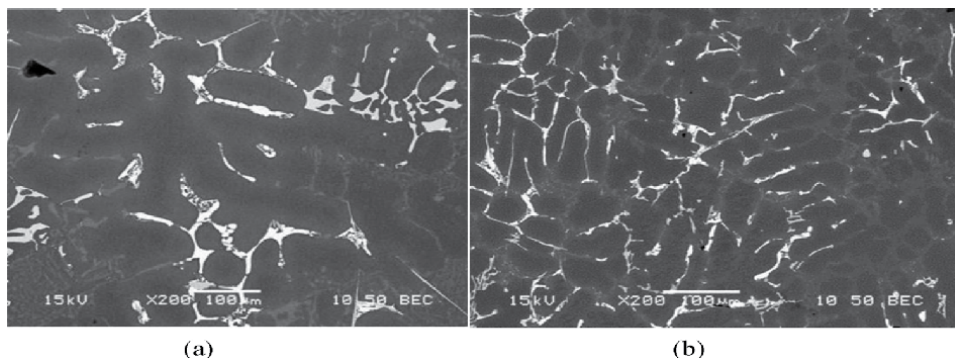
Figure 6.
Backscattered electron images of as cast B319.1 (a) block mold casting. (b) L-shaped mold casting.
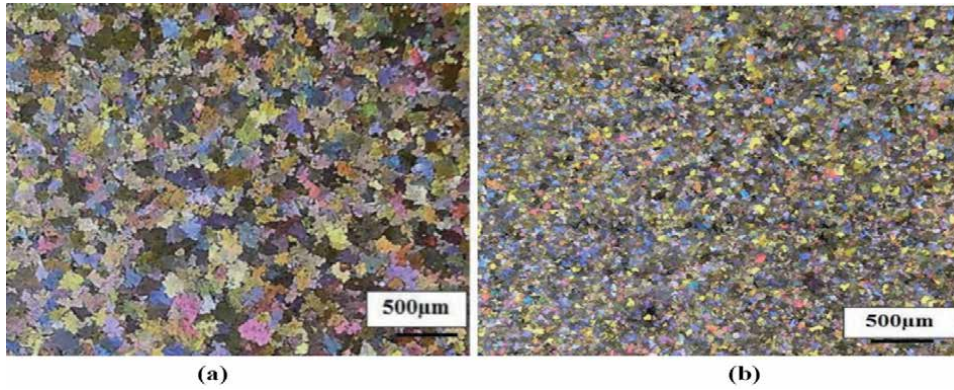
Figure 7.
Macrographs of B319.1 alloy for (a) block casting and (b) L-shaped casting.

with the L-shaped casting, the average SDAS was found to be 25 μm, as is also confirmed by the small grain size noted in **Figure 7(b)**.

From **Figure 8**, it will be observed that the strength values for the as-cast alloy samples of B319.1 exhibit UTS values of about 319 MPa. The B319.1 alloy contains Al, Si and Cu, and Mg and Fe as strengthening elements. The primary strengthening phases for B319.1 are the θ Al_2Cu phase and eutectic silicon. The alloying elements added to B319.1 enhanced both yield and tensile strength. The T6 temper allows for increased strength where it develops more stable mechanical properties with a corresponding loss of ductility. Aging at 170°C for 10 hours hardens the alloy, due to the formation of Guinier-Preston zones and coherent θ' Al2Cu phase particles [17–20]. Overaging can be done either at high temperatures or prolonged exposure at an intermediate temperature, and results in the simultaneous formation of relatively large, non-coherent θ' Al2Cu plates which act as hard non-shearable obstacles to dislocations. Such non-shearable particles lead to lower UTS but with high strain-hardening rate, due to the accumulation of Orowan loops around the strengthening particles. As the strain is increased, the buildup of primary shear loops generates intense stress fields around the strengthening precipitates. [21–23].

As coarsening occurs, the inter-particle spacing is widened which will have a direct effect on the dislocation motion. According to the Orowan relationship (**Figure 9**), larger inter-particle spacing results in a decrease in the resistance to
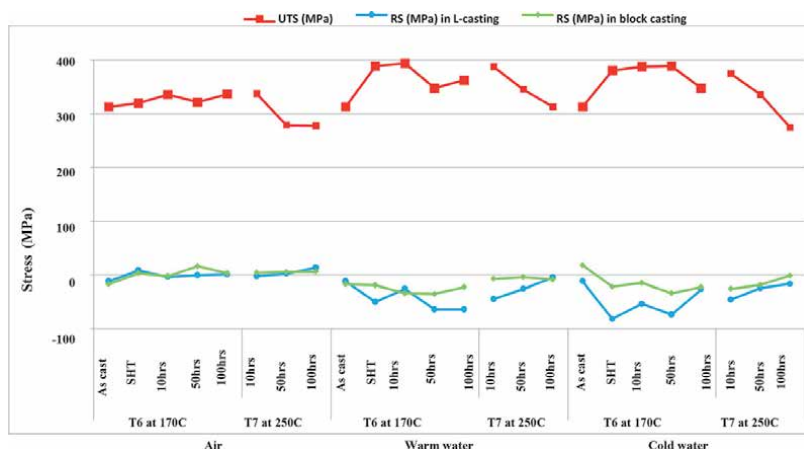
Figure 8.
Variation in YS, UTS and %El at different quenching rates and different aging parameters for B319.1 alloy.
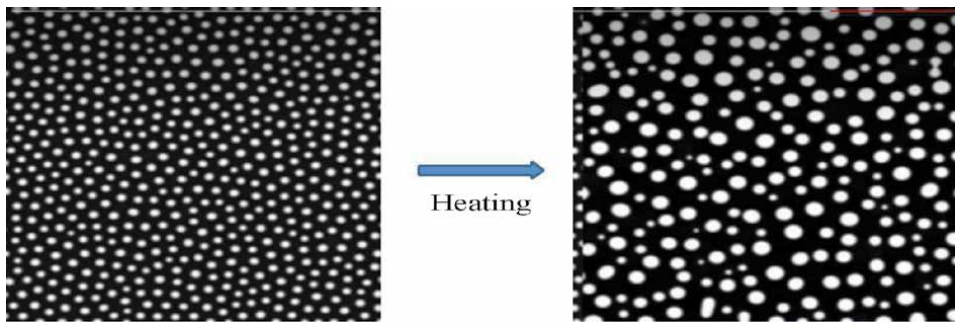
Figure 9.
Ostwald ripening mechanism: larger particles grow at the expense of the smaller particles [28].

dislocation motion thereby facilitating the occurrence of Orowan looping. The increased deformability of the matrix via the easy dislocation motions leads to reduced strength and subsequently diminished quality index values in the castings [24–30]. Aging at lower temperature results in formation of precipitates; with fine sizes, high density and lower inter-particle spacing. In this case, the precipitates provide strong resistance to dislocation motion and the occurrence of Orowan looping becomes difficult leading to a hardening of the materials and an increase in the overall strength, as shown in **Figure 8** [28].

Residual stresses (RS) are elastic accommodation of non-uniform plastic strains generated either thermally or by phase transformation. Generally, the hardness is inversely proportional to the square root of grain size (Hall-Petch equation). Greater the hardness, greater will be the residual stresses. Thus, it could be concluded that grain size has an inverse effect on residual stresses. In general, it is observed that the residual stresses measured are compressive in nature, and are generated due to the steep thermal gradient between core and outer layer at the start of the quenching/cooling process [10] as well the precipitation of complex phases such as α Al15(Mn,Fe)3Si2, β-Al5FeSi and CuAl2 in the B319.1 alloy [16, 31–33].

Generally, stress relief involves uniform heating of a part to a suitable temperature, holding at this temperature for a period of time, followed by slow cooling to prevent the reintroduction of thermal stresses, as stress relieving is highly dependent on the temperature. At high temperatures, such as those used in solution heat treatment, the material yield strength is remarkably reduced, causing plasticity mechanisms to relieve the elastic strain through rapid thermal activation of dislocations. It should be noted that at high temperature, major reduction in residual stresses can be encountered with major decrease in the properties of the material as the precipitates get coarser and lose their hardening capabilities during annealing at high temperatures [34–36]. In other words, heat-treatable aluminum alloys cannot be stress relieved by annealing as the temperature required to encourage stress relief will coincide with that which promotes the precipitation of the second phase constituents, so that stress relieving must be attained at a lower temperature (i.e. during aging).

The amount of residual stresses relieved through T6 treatment provides only modest reduction in residual stresses; while aging at 250°C causes at least 75% residual stress relaxation and can annihilate most locked-in residual stresses with increasing time. This behavior could be attributed to the fact that dislocation glide or climb occurs more readily at higher temperatures. Specimens with large SDAS (60 μm) were also found to be more prone to residual stress relief. In general, the increase in SDAS is found to reduce the amount of residual stresses that originate and facilitate residual stress relaxation which is related to the reduction of
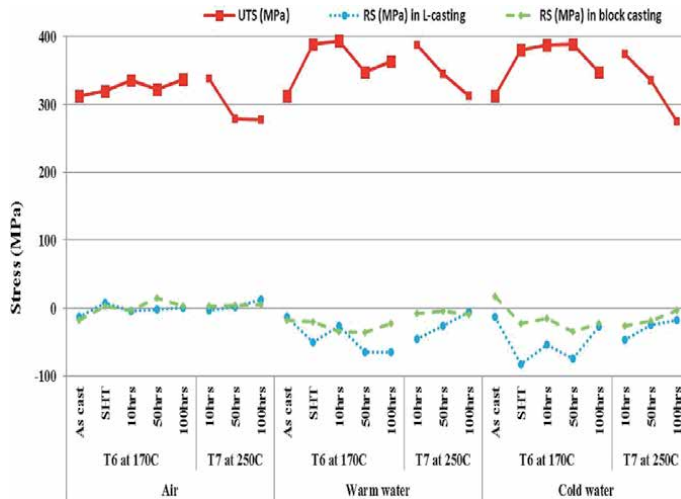
Figure 10.
Variation of tensile stresses and residual stresses in B319.1, as a function of different working parameters.

mechanical strength at lower solidification rates. Finally, the levels of residual stress are markedly reduced because of stress dissipation through the dislocation glide mechanism.

Figure 10 summarizes the ultimate tensile stress (UTS) and residual stress (RS) values obtained for the B319.1 alloy, as a function of different working parameters and quenching media. The figure demonstrates that material with higher strength, as in the case of B319.1 alloy, produces higher residual stresses (compared to 356 alloy under same heat treatment conditions [24]). It also shows that there is direct proportionality between UTS and RS with quenching rate. The relaxation of residual stresses is significantly dependent on aging temperature and proceeds smoothly with the increase in aging time. A significant increase in the residual stresses is observed in specimens with low SDAS, as in the L-shaped casting, while lower residual stresses are measured in specimens obtained from the block casting, with high SDAS.

3.2 Stage II: influence of working parameters on the development of stresses in I4 and V-6 engine blocks

Microstructural analysis was carried out using optical microscopy to observe the dendrite structure in both I4 and V6 engine blocks at different locations. Optical microscopy revealed a variation in the dendritic structure along the length of the cylinder bridge region of both I-4 and V-6 engine blocks. It was observed that the top of the cylinder bridge contained relatively coarse dendrites, while the bottom of the cylinder contained finer dendrites, **Figure 11**.

The secondary dendrite arm spacing (SDAS) was measured at the top and bottom regions of the cylinder bridges. The average SDAS was found to decrease from 57 to 40 μm for the I-4 engine block, and from 41 to 21 μm in the case of the V6 engine block. For both types of engine blocks, the SDAS results for the bottom region of the cylinder bridge indicate a shorter solidification time, i.e. a higher cooling rate compared to the top region of the cylinder bridge [37].

Figure 12(a) and **(b)** illustrate partial spheroidization of Si eutectic phase after the application of solution heat treatment. However, full modification of the Al-Si eutectic was not observed since the modified B319.1 alloy used in engine block
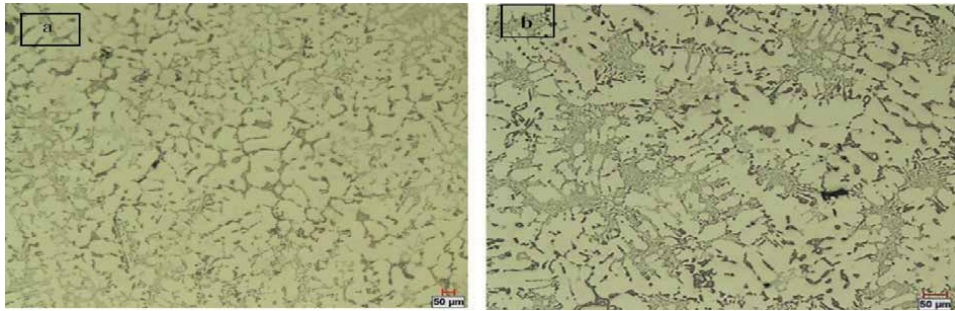
Figure 11.
Optical micrographs showing the dendrite structure of (a) top region of I-4 engine and (b) top region of V-6 engine.
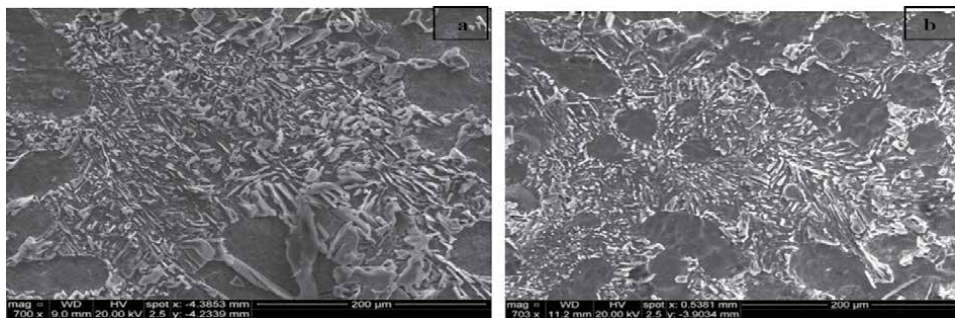
Figure 12.
Optical micrographs showing Si morphology in I4-engine blocks: (a) as received and (b) 8 h solution treatment at 500°C condition.

production, contained a larger amount of Si than the standard 319 alloy [38]. To reach full modification of the Al-Si eutectic, larger additions of Sr., longer heat treatment times, and higher cooling rates would be required. **Figure 13** demonstrated the actual size and density of the precipitates obtained after T6 and T7 aging treatments, for aging times of 10 and 100 hours. As may be seen, at the T7 aging temperature of 250°C, the precipitates are coarser, rod-like in shape, and spread further apart after 100 hours aging time, compared to what is observed at the T6 aging temperature of 170°C.

3.3 Distortion of an engine block is inevitable with time due to the presence of residual stresses

The distortion may either be a product of thermal growth or the product of tensile residual stresses that exceed the yield stress of the block material or alloy. Thermal growth means changes in volume related to phase transformation during heat treatment of the alloy. In case of thermal growth, it is found that the T7 treatment offers the best dimensional stability over T4 and T6 treatments as it produces the stable θ (Al$_2$Cu), phase which has a lower specific volume when compared to θ' (Al$_2$Cu) neglecting the effect of thermal growth distortion [39]. Such distortion may occur through the introduction of excessive residual stresses. When theses residual stresses exceed the yield stress of the material, distortion occurs [40].

The residual stresses in the I-4 engine blocks in the as-cast, air cooled, and air cooled + freezing conditions (−30°C) were 100, 70, and 50 MPa, respectively. These results indicate that the SHT process partially relieved some of the tensile
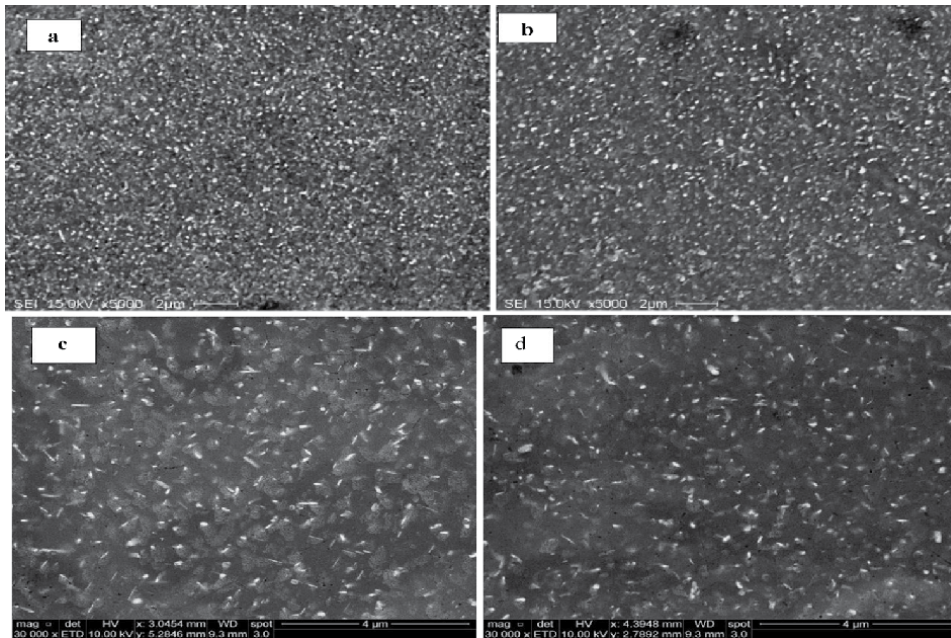
Figure 13.
Backscattered electron images of the size and density of the precipitates in I-4 engine block: (a) after aging at 170°C for 10 hours; (b) after aging at 170°C for 100 hours (c) after aging at 250°C for 10 hours; (d) after aging at 250°C for 100 hours.

residual stresses which evolved in the Al-cylinder bridge region, with a subsequent reduction when freezing was performed through the operation. **Figure 14** reveals that there is significant relieving of residual stresses ongoing from the as-cast and to the SHT condition where these residual stresses are relieved by 25, 75, and 65%, respectively, when subjected to air cooling, warm water quenching and cold-water quenching. This trend indicates that SHT plays an important role in the relieving of residual stresses. Previous research studies [10, 41] concluded that residual stresses can be relieved thermally either instantaneously, when locked-in stresses exceed the yield strength or gradually through creep mechanisms.

At slow cooling rates, there is no significant difference in cooling rates between aluminum (Al) and cast iron (CI) liners and since the aluminum contracts to a greater extent with decreasing temperature, large residual stresses are developed due to the thermo-mechanical mismatch between the two materials resulting from the hindrance of free contraction of the aluminum. On the other hand, at high cooling rates such as when the blocks are quenched in water, the CI liners cool at very high rates similar to the surrounding aluminum. This leads to the contraction
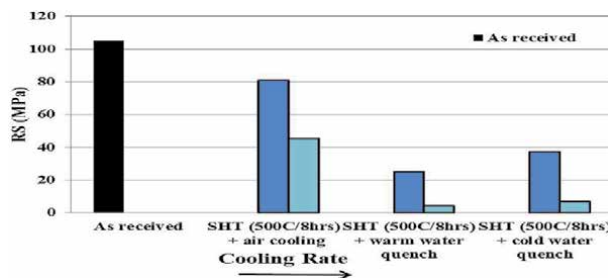
Figure 14.
Residual stress development at different quenching/cooling rates.
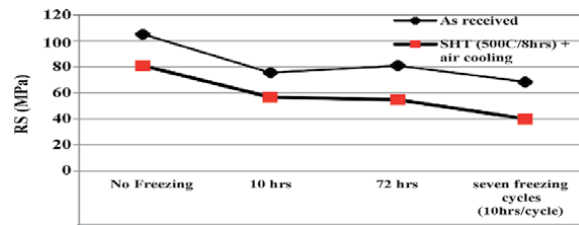
Figure 15.
Effect of stable vs. cyclic freezing on the development of residual stresses.

of both Al and CI liners at similar rates, reducing the thermo-mechanical mismatch between them, resulting in much lower stresses inside the engine blocks.

Freezing after quenching is considered one of the techniques which can be used to further reduce the amount of residual stresses by reversing the pattern of thermal gradient imposed during solution heat treatment. Despite the benefits of cryogenic treatment on both mechanical properties and the residual stresses developed in ferrous alloys, there are few reports in the literature related to the freezing treatment of nonferrous materials and the consequent effect on residual stress and mechanical properties [32, 34].

Figure 15 illustrates the effect of freezing on the development of residual stresses. At least 20% reduction in residual stresses after the implementation of the freezing process is noted, which supports the effectiveness of the freezing
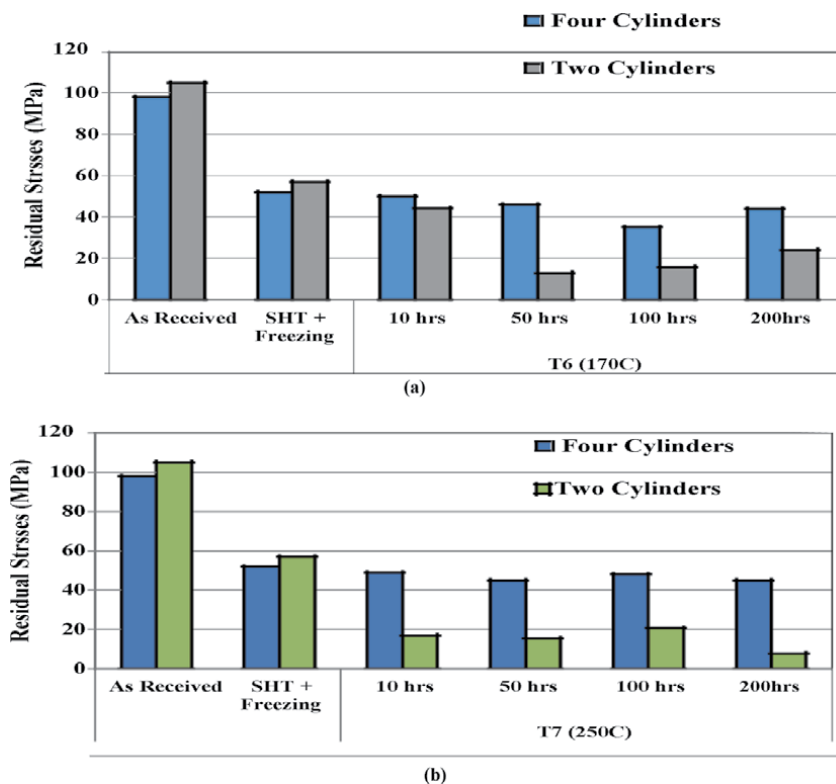
Figure 16.
Effect of freezing and aging on the development of residual stresses in two- and four-cylinder engine blocks: (a) T6 at 170°C and (b) T7 at 250°C.

treatment. Increasing the freezing time has no significant effect on controlling the residual stresses, as may be seen from **Figure 15**, around 30% reduction in residual stresses is observed after stable freezing despite prolonged exposure to freezing. Reduction in residual stresses reaches 45% after cyclic freezing. However, for most of the current study, stable freezing rather than cyclic freezing was used, where the samples were exposed to −30°C for 24 hours, for reasons of cost efficiency and easy handling associated with the process. This method may be considered as a "shallow" cryogenic treatment, as the freezing was extended to only −30°C (compared to temperatures of – 100°C used in industrial cryogenic treatments) (**Figure 16**).

4. Conclusions

Based on the obtained data, the present conclusions may be drawn.

4.1 Stage I

1. Results obtained for B319.1 alloy indicate that highest residual stresses are obtained after quenching in cold water whereas in all condition,

2. Air quenching produces no significant residual stresses.

3. Stress relieving treatments (T6 and T7) lead to the relaxation of residual stresses.

4. Also, the rate of relaxation increases with increasing temperature and time.

5. Significant increase in the residual stresses is observed in specimens with lower SDAS.

6. Thus, SDAS has a significant effect on the evolution of residual stresses.

4.2 Stage II

1. After quenching, the residual stresses evolved in engine blocks are the same either for the whole block (four cylinders) or for the sectioned half-block (two cylinders).

2. Solution heat treatment and freezing (cryogenic treatment) maximizes the amount of residual stress relaxation where 50% of the residual stresses were reduced after the solution heat treatment step.

3. With freezing, around 30% of residual stress relaxation may be obtained. Increasing the freezing time or the use of cyclic freezing has no significant effect on relieving the residual stress.

4. In spite of the effect of quenching rate, residual stresses are gradually relaxed till they reach the limit at 20 MPa. Two-cylinder engine blocks undergo greater residual stress relaxation after aging compared to that observed in four-cylinder engine blocks.

Author details

Serageldin Salem Mohamed[1], Agnes M. Samuel[1], Herbert W. Doty[2],
Salvador Valtierra[3] and Fawzy H. Samuel[1]*

1 Université du Québec à Chicoutimi, Chicoutimi, Québec, Canada

2 General Motors Materials Engineering, Pontiac, MI, USA

3 Corporativo Nemak, Garza Garcia, NL, Mexico

*Address all correspondence to: fhsamuel@uqac.ca

IntechOpen

References

[1] Withers PJ. Residual stress and its role in failure. Reports on Progress in Physics. 2007;**70**(12):2211-2264

[2] Dieter GE, Bacon D. Mechanical Metallurgy. Vol. 3. New York: McGraw-Hill; 1986

[3] Lombardi A et al. Determining the mechanism of in-service cylinder distortion in aluminum engine blocks with cast-in gray iron liners. Metallurgical and Materials Transactions A: Physical Metallurgy and Materials Science. 2014;**45A**(13): 6291-6303

[4] Prasad P. Characterization of New, Cast, High Temperature Aluminum Alloys for Diesel Engine Applications. Cincinnati, OH: University of Cincinnati; 2006

[5] Lenny J. Jr. Replacing the cast iron liners for aluminum engine cylinder blocks: A comparative assessment of potential candidates [engineering thesis submitted to graduate]. Hartford, Connecticut: Faculty of Rensselaer Polytechnic Institute; 2011

[6] Wang Q et al. Methods of predicting residual stresses and distortion in quenched aluminum castings. Google Patents; 2012

[7] Wang Q et al. Modeling of residual stresses in aluminum castings. In: 117th Metalcasting Congress. Schaumberg, IL: AFS Inc.; 2013

[8] Montazersadgh FH, Fatemi A. Stress Analysis and Optimization of Crankshafts Subject to Dynamic Loading. Toledo, OH: The University of Toledo; 2007

[9] Wang Q, Chang C, Zhang G, Paluch D. Modeling of residual stresses in quenched cast aluminum components.

SAE International Journal of Materials and Manufacturing. 2011;**4**(1):844-852. DOI: 10.4271/2011-01-0539

[10] Lados DA, Apelian D, Wang L. Minimization of residual stress in heat-treated Al–Si–Mg cast alloys using uphill quenching: Mechanisms and effects on static and dynamic properties. Materials Science and Engineering A. 2010;**527** (13–14):3159-3165

[11] Carrera E et al. Measurement of residual stresses in cast aluminium engine blocks. Journal of Materials Processing Technology. 2007;**189**(1): 206-210

[12] Lombardi A. A study of cylinder bore distortion in V6 aluminum alloy engine block. In: Mechanical Engineering. Toronto, ON: Ryerson University; 2011

[13] Carrera E et al. Study of residual stresses in complex aluminium castings. International Journal of Cast Metals Research. 2012;**25**(5):264-269

[14] Colas R, Rodríguez A, Talamantes J, Valtierra S. Solidification analysis of aluminium engine block. International Journal of Cast Metals Research. 2004; **17**:332-338

[15] Elmquist L, Brehmer A, Schmidt P, Israelsson B. Residual stresses in cast iron components – Simulated results verified by experimental, measurements. Materials Science Forum Submitted. 2017;**925**:326-333

[16] Rossini N et al. Methods of measuring residual stresses in components. Materials and Design. 2012;**35**:572-588

[17] Tavitas-Medrano FJ et al. Effect of Mg and Sr-modification on the mechanical properties of 319-type aluminum cast alloys subjected to

artificial aging. Materials Science and Engineering A. 2008;**480**(1–2):356-364

[18] Elsebaie O et al. The role of alloying additives and aging treatment on the impact behavior of 319 cast alloy. Materials & Design. 2011;**32**(6): 3205-3220

[19] Han Y et al. Optimizing the tensile properties of Al–Si–Cu–Mg 319-type alloys: Role of solution heat treatment. Materials & Design. 2014;**58**(0):426-438

[20] García-García G, Espinoza-Cuadra J, Mancha-Molinar H. Copper content and cooling rate effects over second phase particles behavior in industrial aluminum–silicon alloy 319. Materials & Design. 2007;**28**(2):428-433

[21] Torsten EM, Staab D, Folegati P, Wolfertz I, Puska MJ. Stability of Cu-precipitates in Al-Cu alloys. Applied Sciences. 2018;**8**:1003. DOI: 10.3390/app8061003

[22] Guinier A. La diffraction de rayon X aux tres petis angles: Application a l'etude de phenomenes ultramicroscopiques. Ann. Phys. 1938; **12**:161-237

[23] Preston G. The diffraction of X-rays by an age-hardening aluminum and copper alloys. Proceedings of the Royal Society of London. Series A, Mathematical and Physical Sciences. 1938;**167**:526-538

[24] Ibrahim MF, Samuel AM, Doty HW, Samuel FH. Effect of aging conditions on precipitation hardening in Al–Si–Mg and Al–Si–Cu–Mg alloys. International Journal of Metalcasting. 2017;**11**(2):274-286

[25] Ratke L, Voorhees PW. Growth and Coarsening: Ostwald Ripening in Material Processing. Berlin, Germany: Springer Science & Business Media; 2013

[26] Voorhees PW. The theory of Ostwald ripening. Journal of Statistical Physics. 1985;**38**(1):231-252

[27] Gladman T. Precipitation hardening in metals. Materials Science and Technology. 1999;**15**(1):30-36

[28] Ogris E. Development of Al-Si-Mg Alloys for Semi-Solid Processing and Silicon Spheroidization Treatment (SST) for Al-Si-Cast Alloys. Zurich, Switzerland: ETH; 2002

[29] Santos-Güemes R, Bellón B, Esteban-Manzanares G, Segurado J, Capolungo L, LLorca J. Multiscale modelling of precipitation hardening in Al–Cu alloys: Dislocation dynamics simulations and experimental validation. Acta Materialia. 2020;**188**:475-485

[30] Kleiven D, Akola J. Precipitate formation in aluminium alloys: Multi-scale modelling approach. Acta Materialia. 2020;**195**:123-131

[31] Furukawa M, Horita Z, Nemoto M, Valiev RZ. Microhardness measurements and the Hall-Petch relationship in an Al-Mg alloy with submicrometer grain size. Acta Materialia. 1996;**44**:4619-4629

[32] Withers PJ, Bhadeshia H. Residual stress. Part 2–Nature and origins. Materials Science and Technology. 2001;**17**(4):366-375

[33] Withers PJ, Bhadeshia H. Residual stress. Part 1–Measurement techniques. Materials Science and Technology. 2001;**17**(4):355-365

[34] Robinson J, Tanner D, Truman C. 50th anniversary article: The origin and management of residual stress in heat-treatable aluminium alloys. Strain. 2014; **50**(3):185-207

[35] Hunsicker HY. Dimensional changes in heat treating aluminum alloys.

Metallurgical Transactions A. 1980;
11(5):759-773

[36] James M. Relaxation of residual
stresses an overview. In: Advances in
Surface Treatments. Technology–
Applications–Effects. Vol. 4. Oxford,
UK: Pergamon Press; 1987. pp. 349-365

[37] Wang Q. Microstructural effects on
the tensile and fracture behavior of
aluminum casting alloys A356/357.
Metallurgical and Materials
Transactions A. 2003;**34**:2887-2899

[38] Bäckerud L, Chai G, Tamminen J.
Solidification Characteristics of
Aluminum Alloys. Vol. 2: Foundry
Alloys. Des Plaines, IL: AFS/
SKANALUMINIUM; 1990

[39] Godlewski LA et al. The effect of
aging on the relaxation of residual stress
in cast aluminum. Metallurgical and
Materials Transactions A. 2013;**44**(10):
4809-4818

[40] Wiesner D et al. Residual stress
measurements of cast aluminum engine
blocks using diffraction. Advances in
X-Ray Analysis. 2005;**48**:136-142

[41] Araghchi M, Mansori H, Vafaei R,
Gou Y. A novel cryogenic treatment for
reduction of residual stresses in 2024
aluminum alloy. Materials Science and
Engineering A. 2017;**689**:48-52

Quality and Trends of Automotive Fuels

David Andrew Gauci and Panagiotis Arkoudeas

Abstract

Automotive engines are designed to convert chemical energy to mechanical energy. The efficiency of this conversion is governed by thermodynamics. The two most common engines utilize gas oil and gasoline fuels for this purpose. However, the combustion processes are radically different. The combustion sequence and relative characteristics for both engine types will be discussed. Due to different combustion requirements, the fundamental properties of both fuels will also be examined as these are significantly different for the two fuel types. The main fuel properties discussed are energy density, stability, fluidity, corrosion, contaminants, safety, wear and environmental aspects. Also, with the advent of various renewable components in both fuels, new trends are emerging for both fuel quality assessments as these are molecularly distinct from their crude oil counterparts.

Keywords: combustion process, fuel properties, emerging trends

1. Introduction

Automotive engines are designed to convert chemical energy stored in the fuel to mechanical energy through combustion. Thus, the working fluids in the engine are the fuel and air with which it is mixed. The combustion process can be viewed to convert chemical energy of the reactants to thermal energy of the products. The thermal energy translates into higher temperature and pressure in the combustion chamber which in turn is converted to work by the engine.

There are two main types of automotive engines which are classified according to how the ignition in the combustion chamber is induced. These are the spark ignition (SI) engine and the compression ignition (CI) engine which determine which fuel is fit for purpose.

It is worth noticing that the combustion of both types of engines are governed by the laws of thermodynamics. The first law states that internal chemical energy in the reactants is converted in heat added to the system and work done by the system. The second law precludes the possibility of a perfect engine where all the internal chemical energy is converted to work as some heat must be exhausted to the environment. Thus, engines are designed to extract the maximum amount of work and minimizes the heat release which improves efficiency.

In this chapter the two types of engines will be discussed which leads to the desired combustion characteristics of the fuels. However, combustion is not the only aspect to be tested for automotive fuels. In fact, the quality assessment performed on the fuels to ensure that, in addition to combustion, other aspects

of the fuel are properly measured such as energy density, stability, fluidity, corrosion, contaminants, handling, wear, composition and environmental aspects will be illustrated. Impact of additives and renewable components will also be discussed.

2. Gasoline automotive engines

The gasoline automotive engine works by injecting a mixture of gasoline and air in the combustion chamber and after compressing them the timing of the combustion is just as the piston arrives at the top dead centre (highest point in the combustion chamber). The combustion timing is induced by a spark which causes a rapid rise in temperature and pressure which in turn push the piston down again turning the camshaft which translates this rotational motion into linear motion used by the vehicle. Thus in an ideal engine the reactants would all ignite with the spark instantaneously and thus it is called the spark ignition engine.

This cycle is called the Otto-cycle which is shown as follows together with the relative P-V diagrams:

Intake stroke is performed by an isobaric (same pressure) expansion of fuel/air mixture represented by point 1 to point 2 (**Figure 1**).

Followed by an adiabatic (no heat exchange) compression stroke represented by point 2 to point 3 (**Figure 2**).

Ignition starts power stroke isochoric (same volume) process shown by point 3 to point 4 (**Figure 3**).

Adiabatic expansion process follows, characterizing the power stroke as per point 4 to point 5 (**Figure 4**).

The exhaust stroke is characterized by isochoric (constant volume) cooling compression processes as per point 5 to point 6 (**Figure 5**).

And the cycle is completed by an isobaric compression as represented from point 6 to point 1 (**Figure 6**).
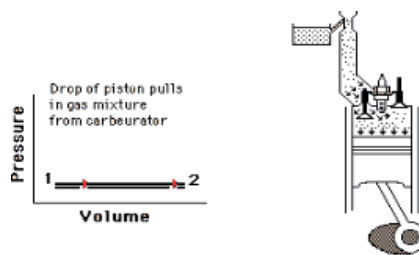
Figure 1.
Drop of piston pulls in gas mixture from carburettor.
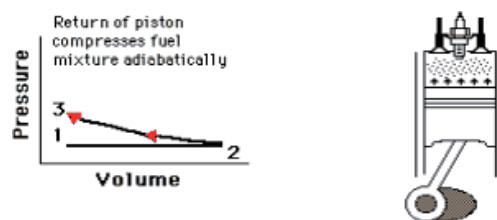
Figure 2.
Return of piston compresses fuel mixture adiabatically.
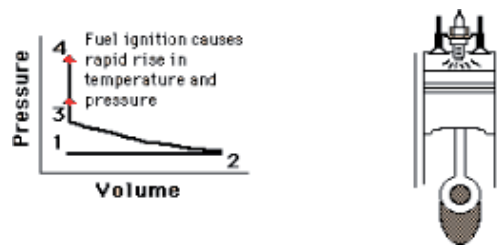
Figure 3.
Fuel ignition causes rapid rise in temperature and pressure.
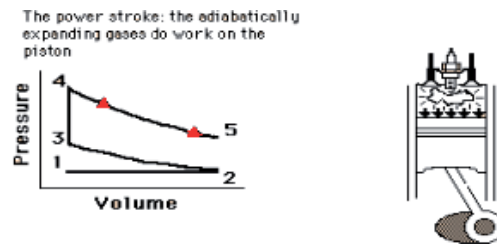
Figure 4.
The power stroke: the adiabatically expanding gases do work on piston.
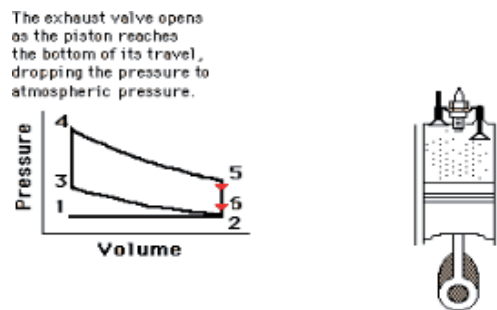
Figure 5.
The exhaust valve opens as the piston reaches the bottom of its travel dropping the pressure to atmospheric pressure.
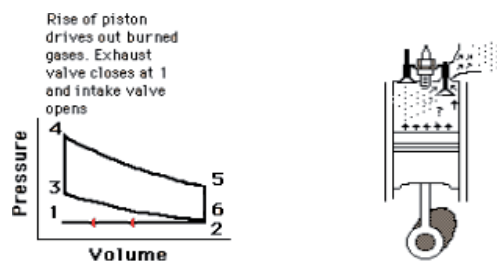
Figure 6.
Rise of piston drives out burned gases. Exhaust valve closes at 1 and intake valve opens.

3. Gas oil automotive engine

The gas oil automotive engine injects only air at the start of the cycle. This is compressed and consequently the temperature also rises. Ignition is induced by timing of the fuel injection in the hot air already in the combustion chamber. The

fuel can be heated by a glow plug before injection to enhance efficient combustion. As the air temperature and pressure inside the combustion chamber are designed to be above the fuel's ignition point, spontaneous ignition of the most combustible components commences. This in turn induces combustion in the balance of the components. This is called compression ignition engine and relies on the spontaneous combustion as given temperatures and pressures.

Note that while spontaneous ignition is not desirable in spark ignition engine, it is the basis of compression ignition engines. The ideal diesel cycle is shown as follows together with the relative P-V diagrams:

Intake stroke is performed by an isobaric (same pressure) expansion of air represented by point 1 to point 2 (**Figure 7**).

The air is compressed adiabatically (no heat loss) causing a rise in pressure and temperature from point 2 to point 3 (**Figure 8**).

The fuel is injected and point 3 to point 4 represents a constant pressure heating following injection. This is caused by the initial combustion of the fuel which is a slow process compared to gasoline in the Otto cycle. Thus, an isobaric process is observed as opposed to isochoric in Otto cycle (**Figure 9**).

When the remainder of the fuel ignites the products force the volume in the combustion chamber to increase leading to the power stroke. This is shown in point 4 to point 5 (**Figure 10**).

The exhaust stroke is characterized by isochoric (constant volume) cooling compression processes as per point 5 to point 6 (**Figure 11**).
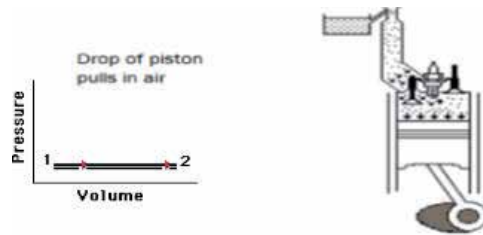
Figure 7.
Drop of piston pulls in air.
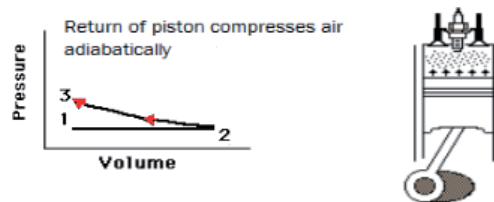
Figure 8.
Return of piston compresses air adiabatically.
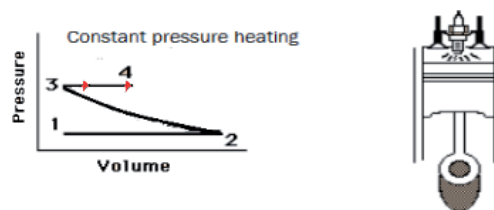
Figure 9.
Constant pressure heating.
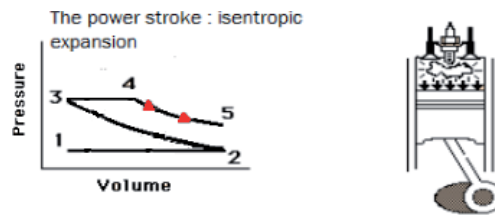
Figure 10.
The power stroke: isentropic expansion.
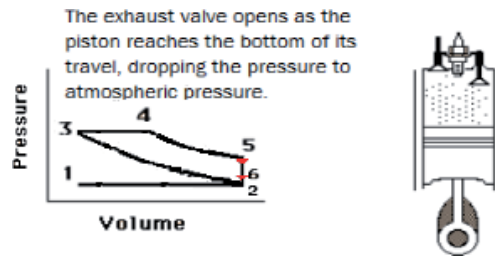
Figure 11.
The exhaust valve opens as the piston reaches the bottom of its travel, dropping the pressure to atmospheric pressure.
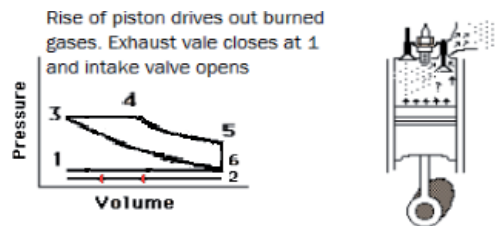
Figure 12.
Rise of piston drives out burned gases. Exhaust valve closes at 1 and intake valve opens.

And the cycle is completed by an isobaric compression as represented from point 6 to point 1 (**Figure 12**).

4. Combustion characteristics

As seen in the previous section, the main fuel characteristic which dominates both spark ignition engines and compression ignition engines is auto-ignition. Note that other engine design factors also come into play for auto-ignition such as combustion chamber pressure, temperature and compression ratio but we will focus on the fuel factors.

Auto-ignition is responsible for knocking in spark ignition engines. Two types of auto-ignition are known. Knocking is defined when the fuel spontaneously starts to combust in another area of the combustion chamber and the flame front clashes with the spark plug induced advancing flame front while pre-ignition is caused by hot surfaces in the combustion chamber rather than the spark plug. While knocking is the more common of the two auto-ignition types they both lead to uncontrolled combustion which, if severe, can cause major engine damage in a spark ignition engine utilizing gasoline fuel.

On the other hand, auto-ignition is a desired quality for compression engine using gas oil fuels. As the fuel is injected the faster the fuel starts combustion the more time it will have to completely burn. The time needed from when the fuel is injected in the combustion chamber to when it starts burning is called the ignition delay. The shorter the ignition delay the easier it is to start the engine, the lower the combustion generated noise and the lower the exhaust emissions of a compression ignition engine using gas oil fuel.

As fuels are composed of a mixture of hydrocarbons, the auto-ignition characteristics of each class will determine if they are more adequate to be used in a spark ignition engine or a compression ignition engine. The classes of hydrocarbons which mostly make up gasoline and gas oil fuels are paraffins (including n-paraffins, iso-paraffins and cycloparaffins), olefins and aromatics.

Based on the reaction mechanisms presented by Curran, Gaffuri, Pitz and Westbrook [1], the main reaction pathways for long chained paraffins can be drawn schematically as shown below (**Figure 13**):

The main pathways are as follows (**Figure 14**):

1. Alkyl radicals R˙ are initially formed via hydrogen abstraction due to low activation energy.

2. This is followed by oxygen addition to produce alkylperoxyl radicals RO_2˙

3. Next is the rate determining step where an internal hydrogen migrates to produce peroxyalkyl radicals Q˙OOH isomers via a transition state composed of five to seven membered ring structures as shown below:

4. Peroxyalkyl radicals Q˙OOH radicals subsequently react further with oxygen to form peroxyalkylhydroperoxide radicals (O_2Q˙OOH) at temperatures below 850 K or decomposes at higher temperatures up to 1200 K.

5. Decomposition reactions from 850 k to 1200 K lead to stable products such as hydrogen peroxide H_2O_2 which slow down the reaction. At temperatures approach 1200 K H_2O_2 decomposes into two reactive hydroxyl OH radicals. This
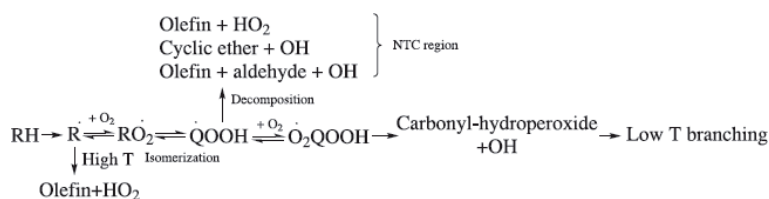
Figure 13.
Reaction mechanisms presented by Gurran, Gaffuri, Pitz and Westbrook.
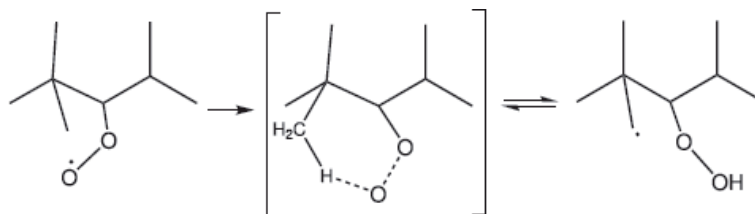
Figure 14.
Main paths of reaction mechanisms.

is called the negative temperature coefficient where the rate of reaction slowly increases in this temperature range.

6. $O_2Q \cdot OOH$ radicals, in turn, tend to abstract H atoms from the C atom which attached to the OOH group, producing $Q \cdot (OOH)_2$ radicals.

7. $Q \cdot (OOH)_2$ radicals yield OH radicals and carbonyl hydroperoxide species via isomerization and decomposition reactions as shown below.

8. OH and carbonyl radicals, accelerate the overall reaction rate leading to rapid low temperature chemistry.

Note that point 3. of this pathway requires a transition state of 5 to 7 membered structure. Thus iso-paraffins and cycloparaffins are less likely to form these transition states leading to longer ignition delays compared to n-paraffins (**Figure 15**).

Olefins tend to have a slower combustion reaction rates than corresponding paraffins. In fact at low temperatures the double bond induces an addition reaction first which slows down the overall rate. At higher temperatures hydrogen abstraction tends to occur in an allyl site which leads to stable allyl radicals which also slows down the reaction. The rate decrease with respect to n-paraffins depends on the chain length and position of the double bond.

Aromatics' combustion rates are even slower than olefins. This is due to the delocalization stability of the π bond ring which makes addition, substitution and extraction of a hydrogen (as per point 1) tough. Thus low temperature combustion reactions are not observed for aromatics. At sufficiently high temperatures, electrophilic substitution and H abstraction reactions create a phenyl radical. This reacts with HO_2 radical, O_2 or O atom, to produce phenoxy radicals. This is a stable radical due to resonance but it is an intermediate for ring opening reactions at high temperatures. Note that low temperature combustion reactions increases for aromatics with side chains as paraffinic reactions occur in the side chain.

Thus the auto-ignition characteristics for the most common classes of corresponding hydrocarbons can be summarized as follows starting from the most prone to least prone:

$$Paraffins > iso-paraffins > cycloparaffins > Olefins > Aromatics.$$

Thus paraffins are the most adequate for combustion ignition engines due to their propensity for auto-ignition. In fact gas oil fuel tend to have a significant proportion of this class of hydrocarbons. Aromatics are the most adequate for spark
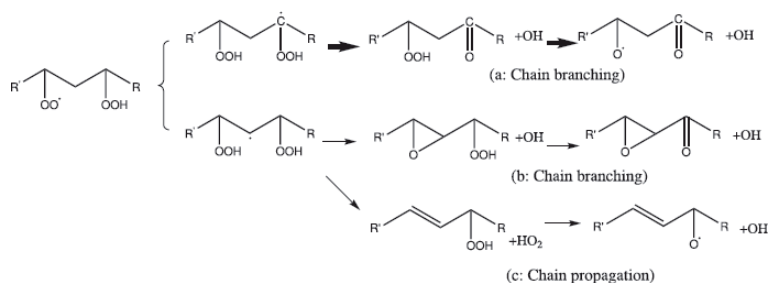
Figure 15.
Main paths or reaction mechanisms – Carbonyl and -OH radicals.

ignition due to the lack of susceptibility of auto-ignition which make it ideal for gasoline fuel.

The cetane number test as per ASTM D613 is used for gas oils to measure the auto-ignition tendency. In fact a high cetane number indicates a short ignition delay from the start if injection to start of combustion. The higher the cetane number the longer the time available for complete combustion. Thus particulate matter and carbon monoxide emissions decrease.

Various derived cetane number equipments are available today (ASTM D6890, D7170, D7668 ad D8183) which mostly exhibit improved precision limits. The cetane index is an estimation of the cetane number by calculation from distillation and density. Note that cetane number additives are not detected by cetane index calculations as the distillation and density are not altered.

Cetane number additives are thus promoting auto-ignition. They are organic nitrates (mostly 2-ethylhexyl nitrate and alkyl nitrate) or peroxides which start to auto-ignite early and thus induces the hydrocarbons to follow suit [2]. This reduces the overall ignition delay and thus increases the cetane number.

On the other hand, the RON by ASTM D2699 and MON by ASTM D2700 are used for gasolines in order to measure the resistance for auto-ignition. RON is the anti-knock performance at lower engine speed and typical acceleration conditions while MON reflects the anti-knock performance of a fuel under high engine speed and higher load conditions.

RON and MON additives are intended to inhibit auto-ignition which cause knocking. These additives decompose in the combustion chamber into a metal, metal oxides and hydrocarbon radicals which have a very limited lifetime. The metal and metal oxides role are to scavenge any radical intermediates which stops the auto-ignition in its tracks. Most common additives are based on lead, manganese and iron. Nowadays however the use of these additives is being limited on health grounds and are replaced by higher octane oxygenated components in the gasoline pool.

5. Energy density

Energy density is the amount of energy stored per unit volume when the fuel is burned. The most influential factor for the determination of net calorific value for both gas oil and gasoline fuels is the density as this determines how much mass it available per unit volume. In fact, the fuel's density has a direct effect on engine maximum power output and volumetric fuel consumption. If density is reduced, heating value per volume decreases and engines need higher fuel volume in order to provide the same energy output.

Densities of different classes of hydrocarbons are influenced by:

- Intermolecular attractions (including polarizability)

- The three dimensional structure

Intermolecular attractions in n-paraffins are the relatively weak Van der Walls forces. These increase with chain length as there is more surface area per molecule and thus the density increases with carbon number.

Isoparaffins also have Van der Walls forces. These tend to be weaker than in n-paraffins as for an equivalent carbon number they have less surface area. Thus the densities of iso-paraffins are lower than for n-paraffins due to their three dimensional structure.

Hydrocarbon density at 20°C for comparison

Carbon number	5	6	7	8	9	10	11	12	13	14	15	16
N-paraffin	0.630	0.664	0.683	0.702	0.719	0.730	0.740	0.750	0.756	0.760	0.769	0.773
Iso-paraffin: 2,2-dimetylalkane	0.590	0.648	0.674	0.691	0.711	0.724						
Cycloparaffins (no side chains)	0.746	0.777	0.810	0.831	0.849	0.857						
Alkylcyclohexane			0.770	0.788	0.794	0.800	0.804	0.808	0.811	0.814	0.816	0.819
Olefins: 1-alkene	0.641	0.673	0.697	0.715	0.733	0.741	0.751	0.758	0.766	0.779	0.776	0.781
Aromatics: n- alkylbenzene		0.880	0.866	0.866	0.863	0.860	0.859	0.858	0.857	0.856	0.858	0.855

Table 1.
Densities for comparison for the hydrocarbon classes discussed.

Cycloparaffins also have similar forces to n-paraffins but they exhibit higher densities. This is due to stronger Van der Waals forces caused by their ring structure which allows for a larger area of contact. Their locked conformations also give an increased plane of intermolecular contact.

Olefins are characterized by the double bond. Since the relative π bond is more polarizable than the δ bonds, the Van der Walls attractions in olefins are augmented by polarizability. Thus, olefin densities are higher than n-paraffins but still lower than cycloparaffins which are enhanced by their structure.

Aromatics have a delocalized π bond system which further increases the polarizability and thus intermolecular attractions. Also, benzene rings must be flat in order to allow the p orbital overlap for all six carbons. This is a more compact structure than other hydrocarbons and contributes to increased density (**Table 1**).

Even though gasoline has got more aromatics (the highest density hydrocarbon) than gas oil the densities are lower due to the shorter chains. In fact, gasoline cuts typically range between C5 and C12 while gas oils range from C10 to C25. The requirement to narrow the density range of automotive fuels is driven largely by engine manufacturers to improve fuel economy and combustion through fuel management systems by regulating the fuel to air mixture to values at least 20% lean of stoichiometric. Lower density would imply a lower energy density and thus poor fuel economy and rough engine idle. A higher density would result in increased emissions due to incomplete combustion. Reductions in the upper limit have generally been for the purposes of limiting heavier aromatic components, thereby reducing emissions, principally particulates. This effect is also achieved to some extent by control of the high end of the distillation curve. The higher content in aromatics in gasolines lead to higher octane numbers (better combustion) and in contrast the higher content in paraffins leads to higher cetane numbers (better combustion and less harmful emissions in general).

6. Stability

All petroleum products will degrade when exposed to certain environmental conditions such as high temperatures, oxygen, mechanical shear, and UV exposure. This degradation will often cause plugging of filters and engine deposits. Instability involves the chemical conversion of precursors to species of higher molecular weight with limited fuel solubility and tend to be nitrogen- and sulfur containing compounds, organic acids, and reactive olefins. The number and rate of these deleterious reactions depends on the concentration of reaction precursors, the concentration of oxygen, catalytic species presence (such as metals), the light intensity and storage temperature.

Oxidation stability is a measure of the fuel's resistance to degradation by oxidation. In the oxidation stability test, the automotive fuel is subjected to conditions which promote oxidation (by subjecting the fuel to oxygen and an elevated temperature for a fixed time). The pressure is monitored for gasoline by ASTM D525 (or equivalent ISO7536 [3] and IP40 [4]) as pressure drops when smaller gasoline molecules oxidize to form larger and less volatile ones. As gas oils are not so volatile, the product after oxidation is cooled and the total insolubles are measured by ASTM D2274, D4625, D5304 and UOP413. These methods differ in oxygen administration technique (continuous bubbling or by pressure vessel), oxidation time and testing temperature. ASTM D2274, D5304 and UOP413 are rapid screening tests used for comparative purposes for evaluation of the tendency to form sediment in storage. In order to accelerate the oxidation process the testing temperatures used are 95°C, 90°C and 100°C respectively. ASTM D2274 tends to be mostly used in current

specifications even though screening tests may not be fully representative of the aging process. ASTM D4625 is a much slower technique which takes up to 24 weeks at a temperature of 43°C. The degradation observed is much closer to real life conditions but is not adequate to be used in specifications due to the length of time required.

A myriad of chemical reaction pathways could be derived from various functional groups in the following mechanisms (**Figure 16**):

- In gasoline fuel, hydroperoxide initiated polymerization oxidation reactions with olefins to produce gums are the most common oxidation mechanism. Chain radical reactions generate oxygenated products such as hydroperoxides, polyperoxides, and carbonyls that have the potential to deposit gums. These reactions can be stopped with antioxidants which are essentially are radical scavengers that react with peroxyl radicals and hydroperoxides.

- In gas oil fuel soluble macromolecular oxidatively reactive species (SMORS) may cause two fuels that, individually have good stability, to form a less stable blend when they are combined [5] (**Figure 16**). In this case, each fuel contains some of the precursors needed for the formation of higher molecular weight species. Only when the fuels are mixed are all the precursors available, enabling the conversion to proceed.

- The hydroperoxide oxidization of organo-sulfur compounds such as mercaptans to sulphonic acids. Sulphonic acids then subsequently catalyze reactions such as condensations between organo-sulfur and nitrogen compounds and esterification reaction leading both to incorporation of heteroatoms and a simultaneous increase in polarity and molecular weight and thus precipitation from the fuel. This is the slowest of the oxidation reactions because of the hydroperoxide induction period and the subsequent oxidation of the organo-sulfur compounds. Also, since sulfur is heavily restricted due to environmental concerns, this marginally contributes to instability in automotive fuels.
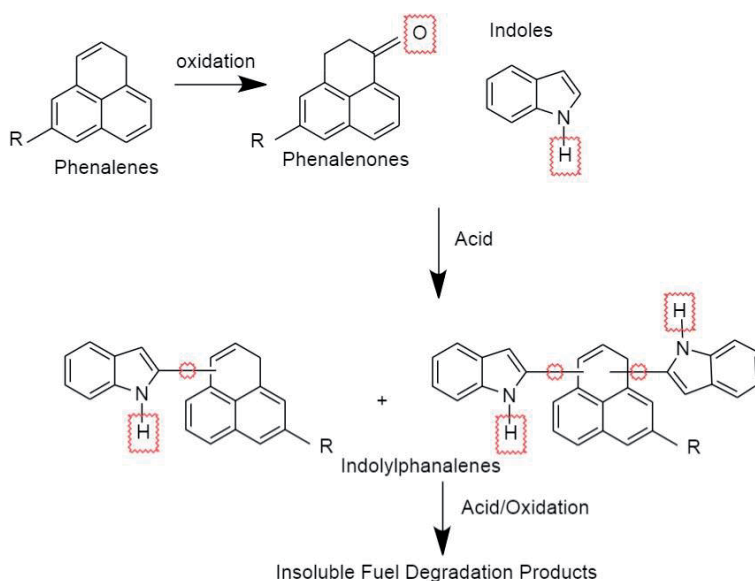
Figure 16.
Path mechanisms for insoluble fuel degradation products.

- A well-known oxidation mechanism in gas oil fuels is the acid-catalyzed conversion of phenalenones and indoles to complex indolylphenalene salts. Phenalenones are formed by oxidation of certain reactive olefins; indoles occur naturally in certain blend components of diesel fuel. The required organic acid is either present in a blend component or is generated by the oxidation of mercaptans to sulfonic acids as shown below.

ASTM D 6748 test method can be used for gas oil fuels to determine potential instability caused by phenalenes and phenalenones to determine the potential for storage instability.

7. Fluidity

Fluidity encompasses all aspects of the ability of the automotive fuel to flow. This encompasses the fuel's characteristics when it is moved when in liquid state and what happens when it is cooled. These properties are measured by viscosity (ASTM D445) and cold flow properties where viscosity is a measure of the fuel's resistance to flow and cold flow properties (cloud point, CFPP and pour point) describe the fuel's reaction on cooling.

Viscosity is determined by the intermolecular structure. Thus, the same considerations for density apply where viscosity is dependent on composition and temperature at which it is measured. N-paraffins have the lowest viscosity (as intermolecular interactions are the weakest Van der Walls forces) while the aromatics have the highest viscosity (as they are polarizable). Also, the longer the chains the greater the intermolecular forces, and thus the higher the viscosity. As gas oil fuel typically is in the C10 to C25 range compared to gasoline fuel, which is C5 to C12, gas oil fuels have a higher viscosity. In fact, gasolines viscosity is so low that it is not normally requested in specifications.

Both a minimum and maximum are normally specified for viscosity at 40˙C for gas oil fuel. This is done as the pump which carries the fuel from the fuel tank to the combustion chamber are either mechanical pumps (such as a diaphragm pump) or electrical pumps which deliver a constant pressure on the fuel. Thus is the viscosity is too low excessive fuel may be delivered resulting in incomplete combustion. This would increase the fuel consumption and result in harmful exhaust emissions. On the other hand, if the viscosity is too high flow rates can reduce to an extent where insufficient fuel is being delivered to the engine resulting in difficulty in start-up.

Cold flow properties measure the characteristics when the sample is cooled. In addition to intermolecular forces, these are also greatly determined by molecular symmetry. Since molecules in the liquid state are crystallizing into a solid, ability to pack well into a crystalline lattice is of fundamental importance. In fact, n-paraffins tend to be the main contributors to cold flow properties as they are symmetrical when compared to iso-paraffins or cycloparaffins and aromatics with side chains.

Once again the short molecular structures of gasoline fuel precludes cold flow issues while there are three cold flow properties which can be performed for gas oil fuel. These are:

- Cloud point by ASTM D2500, D5771, D5772, D5773 and D7689 where the wax crystals first appear out of the fuel.

- CFPP by IP309 [4], EN116 or ASTM D6371 where the wax crystals continue to increase in size on progressive cooling and block a 45 µm filter up to specified conditions. This is intended to mimic clogging of fuel lines.

• Pour point by ASTM D97, D5949, D6749 or D7346 where the wax crystals forms an interlocked 3D network lattice big enough to trap the remaining liquid. This prevents the fuel from moving and thus no fuel can be transported.

Cold flow improvers can be added to improve low temperature performance of the gas oil fuels. These consist of different types of polymeric materials of hydrocarbon chains and polar segments. The polymers' hydrocarbon chains provide interactions with the gas oil's paraffin segment while the polymers' polar groups are responsible for modifying the wax crystals. This results in a sort of scaffolding where wax crystals are not allowed to agglomerate resulting in crystal morphological changes. There is no universal additive for all gas oils and the choice of additive would depend on the interaction of the additive with the particular fuel.

8. Corrosion

Corrosion in automotive fuels is normally caused by acids. An important distinction is that weak organic acids can be present in the crude oil itself and thus carried over to automotive fuels. However strong inorganic acids are not found in crude oils. These are used by various refinery processes and should be removed thereafter. Thus, detection of string acids is a clear sign of contamination while weak acids could originate from the crude oil.

Total acid number (TAN) by ASTM D974 is defined as the amount of milligrams potassium hydroxide (KOH) required to neutralize all acid compounds in 1 g of oil sample. This test determines the amount of soluble or nearly soluble acids in a sample dissolved in a toluene and 2-propanol mixture. The higher the TAN, the more corrosive the fuel possibly is. However, TAN does not distinguish between different acid strengths and further investigation related to the proportion of acids molecules which have dissociated into cations and anions could be required if a fuel is found to have high TAN.

Normally corrosiveness is both automotive fuels is measured by copper strip corrosion measured by ASTM D130. Corrosion can affect metallic components in vehicle fuel systems, dispenser pumps and fuel storage systems and is related to the fuels' acidity. The test procedure uses a strip of polished copper which is immersed in a sample of the fuel and heated to a stated temperature for a prescribed time. The degree of corrosion is measured by comparing the staining with a reference sample.

9. Contaminants

The most common contaminants for automotive fuels are water and particulate matter which can be picked up in the distribution system.

Water can accumulate in the fuel due to leaks or condensation in pipelines. Since liquids are held together by intermolecular forces the hydrocarbon solvent molecules would have to overcome these forces in the water solute in order to find their way between the solute molecules. This process is most efficient when the intermolecular forces of solvent and solute are similar. As water is a polar molecule (while hydrocarbons are not polar) its solubility in hydrocarbons is limited. In fact, oil and automotive fuels do not mix well because the water molecules are strongly attracted to each other and will not allow the weakly attracted oil molecules between them.

Although the degree of water solubility depends on composition, the bigger the density variance the lower the solubility is expected. For example, water solubility in unoxygenated gasoline fuel is expected to be lower than gas oil fuel with

ROH + SO2 + R'N   -> [R'NH]SO3R + H2O + I2 + 2R'N   -> 2[R'NH]I   + [R'NH]SO4R
[alcohol]   [base]   [alkylsulfite salt]   [water] [iodine]   [hydroiodic acid salt]   [alkylsulfate salt]
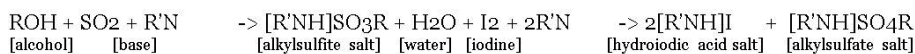
Figure 17.
Main paths of reactions for water detection in fuels.

no biofuel as the hydrocarbon molecules are smaller and thus have less intermolecular forces when compared to the polar water. Water is thus not a contaminant which greatly effects gasoline, but it must be monitored for gas oil fuels as it may cause injector and piston groove deposits and corrode engine components. This is achieved by Karl Fisher technique where the reaction below is used to measure water. As water and iodine are consumed in a 1:1 ratio in the below reaction, when all of the water present is consumed, the presence of excess iodine is detected voltametrically by the titrator's indicator electrode. That signals the end-point of the titration (**Figure 17**).

Another source of contamination is particulate matter. This encompasses any solid material which finds its way to the automotive fuel during transportation. The most common would be rust particles which could plug filters and injectors and thus starves the engine of the required combustion energy for optimal operation. This parameter is tested in gas oil fuels gravimetrically by EN12662 or IP440 [4] where the fuel is filtered through a glass fiber filter of 0.7 μm porosity. Thus, particles larger than 0.7 μm are trapped and weighed in percentage of the fuel filtered.

Appearance by ASTM D4176 is quick indicator of water and particulate matter. A rough indication is that 200 ppm of water at 20°C is expected to be the threshold for water retention in gas oil fuel not containing biofuels. The test method also specifies to observe and report any particulates in the sample.

It is worth noticing that when oxygenates are added to hydrocarbon based mineral fuels the water retention is greatly increased. This is due to the increased polarity of the oxygenates such as esters (biodiesel) in gas oil which are better suited to interact with the water molecules. This increased interaction leads to a much higher water retention threshold for biodiesel to about 1500 ppm at 20°C. When the biodiesel is then mixed with mineral gas oil the overall blend could become hazy as the water retained in the biodiesel is not soluble in the mixture.

10. Safety

During storage and transportation one of the main concerns is the volatility of the fuels. This is directly linked with the intermolecular forces acting on the various classes of hydrocarbons. As discussed in the Energy density section, aromatics have the strongest forces. However, gasolines are very volatile when compared to gas oil fuels due to their shorter chains.

At ambient temperature gasoline fuels are considered as volatile products. Thus, gasoline fuels are stored and transported in an inert atmosphere by removing oxygen and preventing combustion. The test which controls the volatility of gasoline fuels is the RVP which is normally tested by ASTM D5191. ASTM D5191 determines the total vapor pressure exerted in a vacuum by air-containing chilled, air-saturated, volatile, liquid petroleum products. This test method is performed at 37.8°C (100°F) at a 4:1 vapor-to-liquid ratio (internal volume that is five times that of the total test specimen introduced into the chamber). The sum of the partial pressure of the sample and the partial pressure of the dissolved air is obtained. The dry vapor pressure equivalent (DVPE) is calculated by removing the partial pressure exerted by the water vapor in the air.

Alternative methods are available such as ASTM D323, D4953, D5190, D5482 and D6378. D323 is a manual procedure where a chamber is filled with air saturated sample and immersed in a bath at 37.8°C (100°F) until a constant pressure is observed. D4953 is a modification of D323 where the interior surfaces of the liquid and vapor chambers be free of water. Hence, this method is often referred to as the Dry Reid method. D5190 and D5482 are very similar to D5191, with the exception that the test chamber is not evacuated at the start of the test. D5482 employs a small volume test chamber. D6378 is also similar to D5191 with the exception is the fact that air-saturation and chilling of the sample is not required. The relative bias correlating D6378 to D5191 is also known.

RVP also affects starting gasoline fuels performance, warm-up, and tendency to vapor lock with high temperature or high altitudes. The RVP results can be converted to the true vapor pressure at ambient conditions by API MPMS Ch 19.4 or AP-42 by EPA formulae which is a prerequisite to determine if a storage tank or vessel tank are adequate for storing a volatile product.

As gas oil fuels are less volatile, the temperature at which they can ignite when exposed to a flame is tested. This is the definition of the flash point which is normally tested by closed cup Penske Martens by ASTM D93. Note that flash point has no relationship with the combustion characteristics and is used only as a safety measure. In general the temperature of the product is kept at least 10˙C below the flash point during storage and transportation in order to ensure that the product cannot combust.

Other concerns are also addressed by limiting the total aromatics in gasoline. Benzene is the simplest aromatic compound but others common in gasoline include toluene and xylene. As aromatics, particularly benzene, are known to be carcinogenic. They are limited in gasoline fuel and not in gas oil since aromatics are resistant to auto-ignition and cetane number specifications would not be met for highly aromatic gas oils. For the same reason they are desirable for gasoline fuels and thus they are limited as this is the most practical way of limiting human exposure to these substances from evaporative losses and in exhaust emissions.

Alternative high octane products are used in substitution of aromatics such as oxygenates and olefins. Both come with limitations though as olefins induce instability and thus adversely affect oxidation stability test while oxygenates can impact RVP. In fact mixing ethanol and mineral gasoline may increase evaporative emissions. The relationship between vapor pressure and ethanol content of a blend is non-linear as the hydrogen bonding previously holding the ethanol molecules together are greatly reduced when the ethanol is blended as mineral oil gasoline is devoid of oxygen. Thus, the mixture may have a higher vapor pressure than either product alone.

11. Wear

Automotive fuels protect some moving parts such as fuel pumps and injectors from wear. This is achieved by forming a layer between the moving parts thus not allowing the metal to metal contact which would otherwise result, and it is measured by the lubricity test. As gasoline fuel is composed of shorter chains this ability to form a layer between moving surfaces is less efficient. However, spark ignition engines inject the gasoline fuel and air mixture upstream of the combustion chamber and thus operates at low pressures. However, gas oil fuel is injected directly in the combustion chamber containing compressed air. Thus, compression ignition engines require a much higher degree of lubricating property. In fact lubricity is only tested for gas oil fuels with ASTM D6079 using a high frequency reciprocating

rig (HFRR) technique. This uses a laboratory rig to measure the effective wear than can be expected by determining a wear scar diameter in microns (μm). The specification is a maximum wear scar diameter of 460 μm (microns) at 60°C.

The ability of automotive fuels to form a protective layer is given by their propensity to stick to the metal surfaces. Therefor it is only natural to expect polar compounds to have this property as non-polar hydrocarbons would not have any means to interact with the metal surface. In gas oils the most polar compounds are oxygen and nitrogen containing compounds. Lubricity does not tend to be an issue for high sulfur gas oil fuels derived from atmospheric crude oil distillation as these compounds were providing adequate protection.

However lubricity issues were first noted when ULSD was first used in 1991 by sulfur removal via hydrodesulphurization (HDS) in Sweden. It was discovered that while HDS removed sulfur (to the benefit of the environment) it also attacked these oxygen and nitrogen containing compounds which imparted lubrication resulting in pump and injector failures. This required suitable additives to be added to the gas oil to restore the lubrication. It is to be noted that these polar additives must be injected at moderate doses to reach the specification limit as if their concentration is too high they can have adverse effects such as fuel injector deposits, water separation problems, or premature filter plugging.

Gasoline fuel is a blended product from a variety of sources such as isomerate, reformate, alkylate, dimate or polygasoline and catalytic naphtha which do not contain polar molecules. Thus, such blends are bound to have a lubricity higher than the gas oil specification mentioned. Even though lubrication is less important for spark ignition engines it could still cause long term wear. However, antiknock properties is conveyed by metal containing additives or by oxygenates. Both of these also impart the minimum lubricity needed. This parameter was tested in gasoline fuel and found that anti-knock additives like the ones used in LRP gasolines in 2000 enhanced the lubricating ability of these gasoline fuels (lower wear characteristics that bulk gasoline samples). Also, MTBE and ETBE lower the wear with optimum percentage in commercial gasolines around 8 to 9% per volume. Gasoline lubricity is a complex phenomenon, involving many complicated and interrelated factors, such as the presence of water, oxygenates diolefins, diaromatics, the effect of viscosity and the synergistic effect of different wear mechanisms. The lubricity mechanism of gasoline is quite different from that of diesel fuels that leads to severe adhesive wear. With low-sulfur fuels, adhesive wear is observed instead of corrosive and mild oxidative wear, and deposits build up on top land.

Metallurgy and mechanical properties of test specimens have important effects on the lubricating mechanisms of fuels. When the hardness of the lower specimen in an HFRR test is not enough to support the generated oxide films formed by the reaction between surfaces and dissolved oxygen and the adsorption films formed on top of the oxide films by gasoline polar impurities, severe adhesion and metal transfer occur.

Lubricating properties are also influenced by the relationship of viscosity to applied pressure termed as 'α'. The α-values of toluene and normal alkanes in gasoline boiling range are significantly lower than those of corresponding diesel fuel components. The α-values of these gasoline components are almost temperature independent in moderate temperature. In contrast, the α-values of long chain hydrocarbons (diesel fuel components) decreases significantly with increasing temperature. In general, the α-values of gasoline and diesel fuel obtained using film thickness results are about 20 percent lower than corresponding average α-values of their main components.

Although the variation of film does not seem to be related to the value of the corrected wear scar diameter in the case of the mixtures of gasoline refinery streams, some of the categories of the refinery streams separately present the value of the corrected wear scar diameter (CWSD1.4) to decrease exponentially with increasing

of the lubricating film, such as the refinery streams from the isomerisation, reformation and dimerization unit. Generally there are two areas of film variation with the corrected wear scar diameter, where in the first region is observed a relative reduction in film increasing the corrected wear scar diameter to 900 μm, while for higher values of the corrected wear scar diameter is observed a relative increase of film, but there is not a sufficiently high correlation observed. It was carried out numerical analysis for finding the optimum rate of addition for the 7 different refinery streams according to the maximum and minimum addition, as it was obtained from the data of 36 gasoline blends. The optimum addition rate is following the mixing rules that prevail in modern refineries and specifically an optimum rate of 35% for the stream of catalytic cracking FCC unit and 26% for the stream of catalytic reformer unit were observed. The methodology used to measure gasoline lubricity is the ASTM G133 standard test method for linearly reciprocating ball-on-flat sliding wear [6] (**Figure 18**).

The lambda ratio (λ) is the ratio of minimum lubricant film thickness (h) to composite surface roughness (σ) which correlates with surface contact fatigue. The interface between mixed and boundary lubrication is far more questionable. In 1990, Schipper demonstrated that some micro-EHD (elastohydrodynamic) occurs in lubricated concentrated contacts even down to a lambda ratio value of 0.03. More recently ultra-thin film interferometry in conjunction with friction measurements have demonstrated that the transition from mixed to boundary lubrication can occur at even lower lambda ratio value, probable approaching to 0.01.

For the diesel fuels, friction/film thickness shows the classical Stribeck behavior and illustrates that full, speed-independent friction is reached with in the film thickness range studied. (The further drop in friction at high speed is generally considered to result from heating of the EHD film in the contact). For gasolines, the friction/film thickness plots show no sign of leveling at high film thickness.

The composite surface roughness in the MTM test was approximately 30 nm, so the maximum film thickness reached of 20 nm corresponding to lambda ratio of about 0.7. This indicates that the gasolines are probably not reaching full boundary lubrication even at the highest speed -they are still in the mixed regime [6, 7].

From 1990's fuel quality improvement has become the most important subject for automobile industry, because it is the key factor for the energy saving and the reduction of CO_2, one of the most harmful greenhouse effect gas. In order to meet this requirement, energetic research activities started to establish the direct injection gasoline engine technologies that can be applied to the practical engines in the real world. It has been a common target of research activities to develop a direct
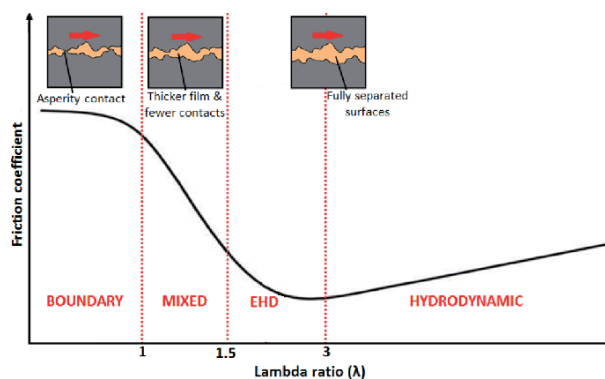
Figure 18.
Variation of friction coefficient with film parameter (λ).

injection gasoline engine realizing greater fuel economy compared with a diesel engine at partial loads and to realize better performance than the conventional MPI (Multi Point Injection) engines at high loads. In order to realize its fuel economy potential, the direct injection gasoline engine should be operated unthrottled in an extremely lean condition by distinctively stratifying the charge. In order to achieve its higher performance potential at high loads, the direct injection gasoline engine should be operated under stoichiometric or slightly rich conditions. When the charge is stratified, soot is generated in the rich zone. Sufficient excess air should be provided around the combustion zone containing soot, in order to burn-up the generated soot. Therefore, when the average mixture strength is stoichiometric or slightly rich, that is when the equivalence ratio is larger than unity, the mixture should be homogenous to suppress the soot formation. Additional pressure through pump and injection might generate issues on gasoline lubricity in the future [8].

12. Composition

In a refinery process the atmospheric and vacuum distillation are the first steps for separation of crude oil into various fractions or "cuts" which are composed of large numbers of hydrocarbons. These cuts have specific boiling-point ranges and can be classified in order of decreasing volatility into gases, light distillates, middle distillates, gas oils, and residuum. Modern refineries are much more complex and are able to extract a variety of streams from cracking processes. These are carefully distilled to fit into the required cut boiling points making this parameter as a primary selection criteria for automotive fuels.

Both the volatile and heavy components in automotive fuels are needed and thus a distillation curve is tested by ASTM D86 to ensure that all the requirements are met. The distillation curve is the temperature vs. percentage volume recovered. It is related with the volatility and flash point of the fuel initially and with density at the back end as the high boiling point components tend to be long chain and/or aromatic which increases the density.

The distillation curve can be split in three for a better understanding [9]. The front end is typically the first 25% recovered, the next 60% is the mid-range while the final 15% is the back end which are all regulated (**Figure 19**).

If the front end is too volatile it would incur is evaporative losses and flash point issues for gas oil fuel and high RVP for gasoline fuel. If gasoline fuels are too volatile they could also vaporize in the fuel lines when the engine is hot impeding fuel flow (known as vapor lock). If less volatile combustion on a cold day would be problematic as the fuel would not vaporize easily.

The bulk of the curve is the mid-range. If this section is too volatile the majority of the chains would be composed of shorter chain molecules and thus would tend to have a poorer cold properties for gas oil fuels and increased icing tendency for gasoline fuels. If it is not volatile enough it would release less chemical energy and it would incur in poor warm-up time, rough acceleration and poor short trip economy.

The last section deals with the heaviest components. If these are too volatile poor long trip economy would result as these give the highest combustion chemical energy release. If this is not volatile enough these heavy components would result in increased incomplete combustion that would give soot or smoke in the exhaust emissions. These heavier components have more potential for incomplete vaporization and combustion and limiting the high-end temperatures reduces their proportion giving cleaner burning. The products left after incomplete combustion can cause oil dilution and increased cylinder wear and may lead to combustion chamber and inlet system deposits and spark plug fouling in spark ignition engines and injector deposits in compression
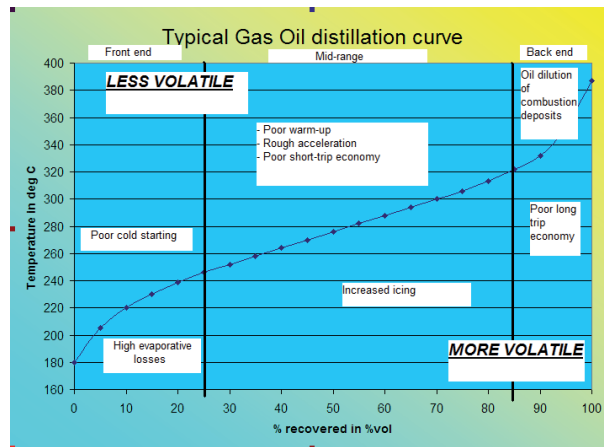
Figure 19.
Chart illustrating the effects of having more or less volatile components in the gas oil pool.

ignition engines. Note that the end point in a gas oil fuel is related to the polyaromatic hydrocarbon content which typically have the highest boiling points.

13. Environmental aspects

Environmental specifications include RVP in gasoline to control evaporative emissions. The specifications recognize that the ambient temperatures varies in different regions and thus allows for various ranges.

Another environmental aspect which has been regulated is the sulfur content. Sulfur in automotive fuels is converted to sulfur dioxide and small amount of sulfur trioxide. If released to the atmosphere, they will form acid rain. Sulfur trioxide and dissolve in water to form sulfuric acid that will cause engine corrosion. However, the main contributor to sulfur reduction in automotive fuels is environmental as only 1 to 3% of sulfur dioxide is oxidized to sulfur trioxide in the combustion chamber. Sulfur occurs naturally in crude oils and must be removed to an acceptable level during the refining process by hydrodesulphurization (HDS) as previously discussed for effects on lubricity. The current specification for both automotive fuels is set at 10 ppm.

Sulfur in automotive fuel reduces the efficiency of catalytic converters as sulfur dioxide inhibits most gaseous heterogeneous catalytic reactions by strongly competing with the exhaust pollutants for space on the active catalyst surface [10].

Developing gasoline engine technologies such as gasoline direct injection (GDI) and lean burn will require advanced catalyst technology in order to control of hydrocarbons (HC), carbon monoxide (CO) and oxides of nitrogen (NOx) exhaust emissions [11]. Sulfur inhibition varies in degree according to the gasoline sulfur level, the catalyst formulation, catalytic function, combustion products from various air/fuel mixtures, and exhaust temperature range.

In compression ignition engines the diesel oxidation catalyst (DOC) is a fundamental device of exhaust after-treatment. Reduction of the NOx emission is achieved mainly by a significant delay of the fuel injection and using the high rates of the exhaust gas recirculation. However, these cause a significant increase in the emission of products of the non-complete combustion process i.e. carbon monoxide, hydrocarbons and particulate matter. In order to keep the emissions low it is necessary to eliminate such compounds by using the catalyst DOC which is able to oxidize CO and HC and the soluble organic fraction (SOF) of the particulate matter.

Thus, apart from its direct environmental detrimental effects, sulfur also contributes to formation of particulate matter (PM) in engine exhaust and affects the performance of vehicle emissions control equipment. It therefore has an indirect effect on emissions of carbon monoxide, hydrocarbons and NOx.

In gas oil fuels another environmentally regulated parameter is the polyaromatic hydrocarbons. These aromatics contain multiple benzene rings and their boiling points are in the gas oil range. PAHs contribute to particulate emissions while some PAHs such as benzo(a)pyrene are known to be carcinogenic. These tend to be the heaviest components in gas oil and are the slowest to burn due to their extended delocalization over several benzene ring systems. Thus, they contribute the most to incomplete combustion and thus to hydrocarbon and particulate matter emissions. The current specification has reduced the limit for PAH from 11mass% to 8mass% maximum which are tested using an HPLC technique. An additional indirect way to control PAH in gas oils is to limit the end point of the distillation curve. In fact, as PAH are the heaviest components in gas oil fuel, limiting the end point will also reduce the PAH content.

14. Renewable components

Mineral oil gas oil and gasoline fuels are derived from crude oil. This is a fossil fuel because it was formed from the remains of tiny sea plants and animals that died millions of years ago and thus cannot be regenerated. On the other hand, renewable components are any type of fuel with can be replenished and thus will not be depleted within the foreseeable future. They are part of a closed cycle and do not create a net surplus of carbon dioxide greenhouse gases when used. The most common are biodiesel and ethanol. Biodiesel is blended with gas oil fuel while ethanol and MTBE (as well as other oxygenates) are blended with gasoline fuel.

All renewable fuels contain oxygen. Thus, their combustion characteristics are significantly different from mineral oil derived fuels.

Ethanol

Ethanol is one of the main octane boosters used due to its high knock resistance. The presence of a hydroxyl group on the chain affects otherwise paraffinic chemistry scheme. The main combustion pathways are (**Figure 20**):

Hydroperoxyalkyl (RO2) radicals can now, besides isomerization to QOOH and subsequent low temperature branching reactions as for paraffins, also react via three other routes that compete with the chain branching reactions (**Figures 21–23**).
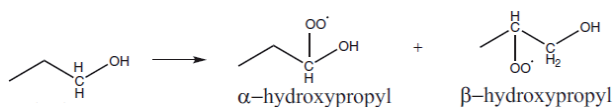
Figure 20.
H atom abstraction favors Cα-H, forming α-hydroxypropyl sites radicals.
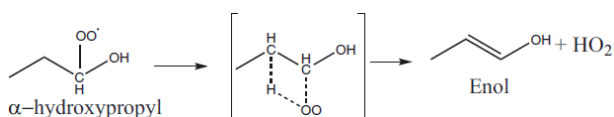
Figure 21.
The first involves HO2 concerted elimination of α-hydroperoxyalkyl radicals, including one via a 5-membered transition ring, forming enol and HO2.
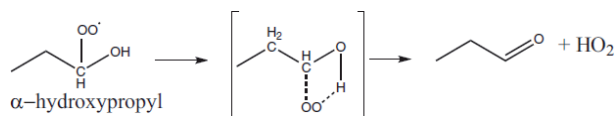
Figure 22.
The second reaction concerns the formation of α-hydroperoxyalkyl directly form carbonyl and HO2.
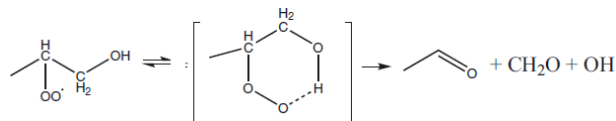
Figure 23.
The third and final route occurs via Waddington type chemistry for β-hydroperoxyalkyl and involves H atom transfers from C-OH to Cβ-OO radical sites, thereby producing two aldehydes and an OH radical.

Thus, low temperature reactivity of alcohols is greatly reduced by the presence of the hydroxyl group as radicals first have to form the enol or aldehyde/ketone intermediates. As for olefins this slows down the overall reaction rate. Branched alcohols with less paraffinic chain will have longer ignition delays and thus be the preferred octane booster.

When blending ethanol in gasoline particular attention must be given to RVP. Ethanol has a relatively low RMM but it is a liquid at ambient temperature due to a type of intermolecular force that is possible due to the hydroxyl radical. This is the hydrogen bonding where a hydrogen on one molecule is attracted to the lone pairs of an oxygen on another molecule. This is clearly seen when comparing the RVP of ethanol (having a molar mass of 46.07 and an RVP of about 2 psi) to a paraffin such as butane (having a molar mass of 58.12 and RVP of 51.7 psi). However, when blending ethanol in gasoline below 10%vol, the ethanol molecules are now separated by hydrocarbons and are thus unable to interact via the hydrogen bonding. Thus, ethanol molecules become very volatile and the RVP of the blend is higher than the highest component. When the ethanol percentage increases above 10%vol the ethanol molecules start encountering each other more often and hydrogen bonding starts to be restored thus lower the RVP again.

In order to accommodate increased ethanol use as an octane component both EPA and EN228 introduced ethanol waivers. These give RVP allowances on the upper limit in view of this occurrence. As RVP is related to the distillation, ethanol will also decrease the distillation points mostly up to the back-end section. Because of its effect on distillation it affects the driveability index (intended to control cold start and warm-up driveability) and the vapor lock index (intended to protect against excessive volatility in the lines, pumps and carburettors impeding flow).

Also, ethanol has an affinity for water as both molecules interact with hydrogen bonding. Thus care must be taken not have excessive water in the distribution system and storage [12]. If a gasoline/ethanol blend encounters excessive water, it can pull the ethanol out of the blend resulting in tank bottoms comprised of water, ethanol, and some hydrocarbon content. When the water is drained out this will result in a volume loss as well as an octane loss.

Finally ethanol in gasoline blends may cause the elastomers (namely Neoprenerubber, Nitrilerubber, hydrogenatedNitrilebutadienerubber (HNBR), and Polyvinylchloride/Nitrilebutadienerubber blend (PVC/NBR)) and two types of plastic materials (namely Nylon-66 and Polyoxymethylene) in vehicle fuel systems to swell and lose strength [13]. This would lead to failures of critical components such as fuel pumps, engine seals, gaskets, fuel system seals and hoses and promote risk of fire.

Biodiesel

Biodiesel refers to the esters obtained by transesterification of triglycerides found in oils and fats. Biodiesel can be produced from different triglyceride sources such as vegetable oils (that can be edible, non-edible or waste oils [14]), animal fats (mostly edible fats or waste fats) and microalgae oil. The crops identified for biodiesel production are corn, sunflower, palm, olive, canola, soybean, rape and peanut oils. The main transesterification reaction for biofuel production is as follows (**Figure 24**):

This conversion goes in three steps where triglycerides react with methanol to give diglylcerides. These react with another methanol to monoglycerides. Finally monoglycerides react with a third methanol to five long chain esters (also called fatty acid methyl esters - FAME) and glycerol. European EN 590 specifications require gas oil fuel to contain a maximum of 7%vol biodiesel which must be compliant with the standard EN 14214 while US specifications ASTM D975 allows mixing commercial diesel oil with 5%vol biodiesel that meets the requirements of ASTM D6751.

Long chain esters (where the triglyceride R chain is from C8 to C20) are used as a blending component for gas oil fuels since the combustion ignition delay is generally long enough to be used for this application. In fact, esters display a paraffin-like reaction chemistry as their functional group provides an attractive site for H atom abstraction. These radicals are stabilized by resonance which slows down the reaction to yield an unsaturated ester which is resonance stabilized and thus has poor low temperature reactivity as follows:

Another reaction path is an elimination reaction involving a six-membered transition state producing olefins, small esters or acids. However, this is the preferred route only when the O-alkyl side is long. This clearly not the case for FAME as the O-alkyl side is the shortest possible (a methyl) (**Figures 25** and **26**).

Thus, the slow H atom abstraction is the predominant route for FAME which increase their ignition delay and consequently increase the cetane number. Note that branching effect reduces the activation energy needed for the six-membered transition state and thus straight chain and saturated R chains promote higher cetane numbers.

The main quality concerns for biodiesel are cetane number, cold properties and stability. As discussed, unbranched and saturated alkyl chains promote
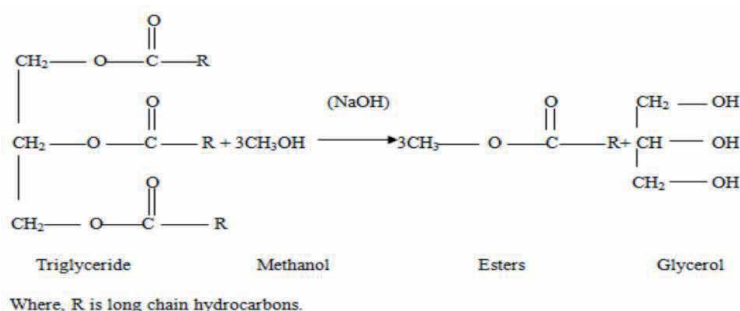
Figure 24.
Transesterification reaction.
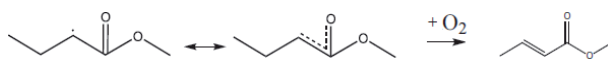
Figure 25.
Stabilized resonance and poor low temperature reactivity.
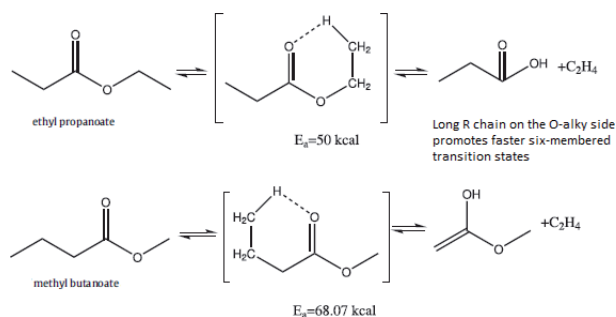
Figure 26.
Reaction paths for producing olefins, small esters or acids.
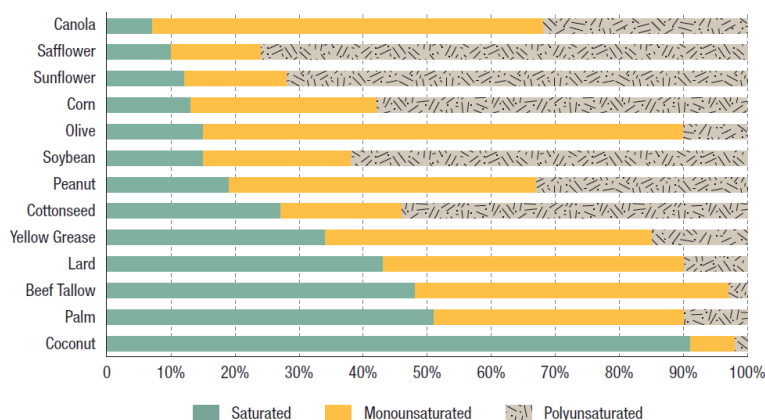
Figure 27.
Each feedstock is set apart from the others because it is made of different proportions of saturated, monounsaturated, and polyunsaturated fatty acids.

cetane number. Saturation also promotes stability as olefinic sites promote oxidation reactions. However, saturation also promotes high melting points and thus leads to high cold properties. The middle ground is to have a monounsaturated FAME such as rape seed oil methyl ester which is composed of 63.9mass% C18:1 (alkyl group is 18 carbon atoms long having one double bond). However, as shown below (**Figure 27**):

Advantages of biodiesel are cleaner burning of engines, lower emissions, better lubrication of fuel injection pumps, safe due to high flash points, non-toxic and low volatility, spills are biodegradable, mixes well with mineral diesel and needs little engine adaptations [15]. However, disadvantages are cost, restricted shelf life, season sensitive, hygroscopic, housekeeping critical, filterability issues and could be foodstuff competitive.

Hydrotreating of oils and fats is a novel process for producing renewable paraffinic diesel, abbreviated HVO. In production, hydrogen is used to remove oxygen from the triglyceride vegetable oil or animal fat molecules. Hydrogen needed for the HVO process is today made from natural gas, but it could also be made from biogas or other renewable sources. When comparing HVO and biodiesel (FAME) production processes it can be concluded that both need about the same amount fossil feed i.e. hydrogen for HVO and methanol for FAME. However, HVO production is even more expensive than biodiesel.

According to research the latest twenty years the maximum allowable limit of biodiesel in gasoil fuels is 20% v/v named B20 without engine or other issues.

15. Conclusion

Internal combustion engines are still the most common means of imparting vehicular power even though lately electric and hybrid systems have emerged. Thus legislation is progressively becoming more stringent on various aspects regulating polluting exhaust and environmental impact which incentivize manufacturers to produce ever more clean and fuel efficient vehicles. As discussed direct injection gasoline technology has already been successfully employed to reduce fuel consumption and carbon dioxide emissions for the same power output. Further research on both fuels and combustion technology is currently underway to continue improving the environmental impact. Future work in LNG powered vehicles and homogeneous charge compression ignition (HCCI) are two areas where vehicles' power units can continue reducing environmental impact.

Conflict of interest

The authors declare no conflict of interest on the information delivered in this chapter.

Author details

David Andrew Gauci[1]* and Panagiotis Arkoudeas[2]

1 BSc Chemistry, University of Malta, Zurrieq, Malta

2 PhD Chemical Engineer, NTUA, Petroleum Engineer, Texas A&M University (TAMU), Greece

*Address all correspondence to: dagauci@yahoo.co.uk

References

[1] Impact of fuel molecular structure on auto ignition behaviour Design rules for future high performance gasolines by Michael D. Boot, Miao Tian, Emiel J.M. Hensen, ManiSarathy

[2] Effect of cetane improver additives on emissions by K. Velmurugan and S. Gowthamn

[3] ISO methods, www.iso.org

[4] IP Methods, www.energyinst.org

[5] Diesel fuels technical review by Chevron corporation

[6] Lubricity assessment of gasoline fuels by Panagiotis Arkoudeas

[7] Analysis of the Premature Failure of Wind Turbine Gearbox Bearings by Tom Bruce

[8] Direct Fuel Injection for Gasoline Engines, Society of Automotive Engineers SAE, Edited by Arun Solomon, Richard Anderson, Paul Najt, Fuquan Zhao

[9] Distillation and vapour pressure measurement in petroleum products by Rey G. Montemayor

[10] The Impact of Gasoline Fuel Sulphur on Catalytic Emission Control Systems by Manufacturers of Emission Controls Association

[11] The mechanics of fuel sulphur influence on exhaust emissions from diesel engines by Miloslaw Kozak and Jerzy Merisz

[12] Ethanol Motor Fuel Storage Overview by Wisconsin department of commerce

[13] Compatibility Studies on Elastomers and Polymers with Ethanol Blended Gasoline by J.S.Dhaliwal, M.S.Negi, G.S.Kapur and Shashi Kant

[14] Biodiesel production from waste cooking oil by Mohammed Abdul Raqeeb and Bhargavi R.

[15] Biodiesel Handling and Use Guide by U.S. Department of Energy

Section 2

Hydrogen in the Future Transportation System

Chapter 6

Light Weight Complex Metal Hydrides for Reversible Hydrogen Storage

Sesha Srinivasan, Luis Rivera, Diego Escobar and Elias Stefanakos

Abstract

We have investigated the complex metal hydrides involving light weight elements or compounds for the reversible hydrogen storage. The complex hydrides are prepared via an inexpensive solid state mechanochemical process under reactive atmosphere at ambient temperatures. The complex metal hydride, $LiBH_4$ with different mole concentrations of $ZnCl_2$ were characterized for the new phase formation and hydrogen decomposition characteristics of $Zn(BH_4)_2$. Furthermore, the complex metal hydride is destabilized using the addition of nano MgH_2 for the reversible hydrogen storage characteristics. The structural, microstructural, surface, and other physicochemical behaviors of these lightweight complex metal hydrides have been studied via various metrological tools such as x-ray diffraction, Fourier transform infrared spectroscopy, thermal programed desorption, and PCT hydrogen absorption methods.

Keywords: hydrogen storage, mechanochemistry, complex metal hydrides, hydrogen sorption, thermal decomposition

1. Introduction

Complex metal hydrides are basically composed of various light weight elements and compounds that bonded with the hydrogen atom in binary, ternary, or quaternary structures [1–3]. The binary hydrides are made of light-weight elements and compounds, for example, LiH and MgH_2 often releases the absorbed hydrogen at very high temperatures (>400°C) and are irreversible in nature [4, 5]. The reversibility of hydrogen absorption and desorption can be improved by bringing either the cationic or anionic substitution to form a ternary compound for example, $LiBH_4$, Mg_2FeH_6, or $Zn(BH_4)_2$ [6, 7]. Further to decrease the temperature of hydrogen sorption can be facilitated by destabilizing via introducing alkaline metal hydrides, to form a quaternary structure, for example, $LaMg_2NiH_7$ [8] or $LiMg_2RuH_7$ [9]. There are consistent efforts underway towards the development of a *holy-grail* light weight reversible hydrogen storage materials to meet the 2025 DOE technical targets [10].

Lithium and Magnesium are considered to be lightest and highly reactive elements due to their placement next to hydrogen in the periodic table. The ternary hydride of Lithium, namely, $LiBH_4$ possesses very high storage density of hydrogen

up to ~20 wt.% and ~ 125 kgH$_2$/m^3 in terms of gravimetric and volumetric measurements [11–14]. However, the significant hydrogen decomposition occurs at temperatures >400°C [15]. The dehydriding and reversible hydriding of LiBH$_4$ follows the typical metal-hydrogen bonding reactions per the equations below.

$$LiBH_4 \leftrightarrow LiH + B + \frac{3}{2}H_2 \qquad (1)$$
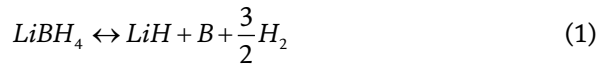
The reversibility enhancements and destabilization of LiBH$_4$ at lower temperature was demonstrated by admixing of SiO$_2$ [14], and MgH$_2$ [16]. Particularly, the addition of half a mole of MgH$_2$ destabilizes the LiBH$_4$ structure and enables the formation of intermediate meta-stable MgB$_2$ alloy phase during the hydrogen release and absorption phases per the equation below [16].

$$LiBH_4 + \frac{1}{2}MgH_2 \leftrightarrow LiH + \frac{1}{2}MgB_2 + H_2 \qquad (2)$$
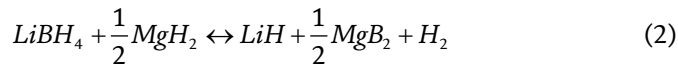
MgH$_2$ on the other hand, has a comparative hydrogen storage capacity of ~7.6 wt.%, at temperatures >325°C, however, the slow kinetics of reaction makes this metal hydride not usable for potential applications [5]. The role of different 3d transition metal catalysts for example, Ti, V, Mn, Fe, Co, Ni [17–21] and transition metal oxide, namely, Nb$_2$O$_5$ [22, 23], has demonstrated greater reversibility of hydrogen from the magnesium lattice with faster kinetics hydrogen enabled applications.

A new ternary complex metal hydride Zn(BH$_4$)$_2$, was formulated for the low temperature hydrogen decomposition by reacting either NaBH$_4$ or LiBH$_4$ with ZnCl$_2$ salt in a mechanochemical process at room temperature according to the Equation [24, 25].

$$2LiBH_4 + ZnCl_2 \rightarrow Zn(BH_4)_2 + 2LiCl \qquad (3)$$
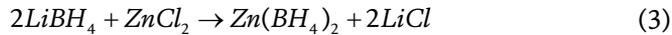
Keeping the aforementioned metal hydrides and its salient characteristics, we have successfully synthesized new complex hydrides with combinations of LiBH$_4$ and MgH$_2$ for the formation of Zn substituted systems and catalysts assisted complex metal hydrides for reversible hydrogen storage and for vehicular on-board applications.

2. Experimental details

The various chemical compounds with purities (in parentheses) such as, ZnCl$_2$ (99.999%), TiF$_3$ (99.999%), nano-Ni (99.9%), nano-Zn (99 + %) are procured from Sigma-Aldrich. The binary and ternary metal hydrides such as LiBH$_4$ (95%), MgH$_2$ (98%) are purchased from Alfa Aesar. The high purity nano-Ni (99.999%) was purchased from QuantumSphere Inc. All the chemicals have been stored in a nitrogen filled glove box, used readily without further purification. A mechanochemical milling of the mixtures have been carried out in a Fritsch Pulversitte planetary mono mill P6 using 80 ml stainless steel bowl sealed with a specially designed lid with two scharder valves for inert or reactive gas purging. Various experimental parameters such as ball to powder weight ratio (20:1), milling speed (300 rpm), milling time (20 min. to 2 h) and milling medium (hydrogen purging, 1 atm for every 30 minutes of milling) were optimized. All the sample manufacturing and manipulation for both synthesis and characterization were done in a nitrogen filled glove box (Innovation Technology).

The thermogravimetric and the differential scanning calorimetric analyses were performed using the TA Instrument's SDT-600 with alumina crucibles heated at 5°C/min in flow of nitrogen or argon ambient. The Universal Analysis software V4.0C was deployed to analyze the results obtained from the SDT. The reversible hydrogen absorption and desorption measurements have been carried out using Setaram's PCTPro Sievert's type instrument with pre-calibrated volumes with an accuracy of $\mp$1°C. A Lab View software program was used for data monitoring and recording, and the measurement analysis was executed using Hy-Analysis macros in the Igor program.

X-ray diffraction characterization was carried out using a Philips X'pert diffractometer with CuKα radiation of λ = 5.4060 Å. The x-ray beam from the cathode ray tube was incident on the sample, via incident slit of 1°, a 10 mm beam mask and soller slit of 0.04 rad. The diffracted x-ray beam was received by the detector via the receiving slit, a 2° anti scatter slit and a monochromator. The collected XRD patterns were analyzed using the PANalytical X'pert Highscore software version 1.0e for phase identification and crystallite size distribution. A polyethylene clear plastic wrap (thin foil) was used to protect the samples from air and moisture by wrapping the sample holder completely with the thin foil which shows diffraction peaks in the 2θ range of 21–28°. The chemical environment of the complex metal hydrides, such as B-H stretches and BH_2 deformation bands were explored using a Perkin Elmer's FTIR spectrometer and the samples were specially prepared with KBr in nitrogen filled glove box.

3. Results and discussion

Two different sets of complex metal hydrides have been studied in this work, one is with the mixture, $2LiBH_4 + ZnCl_2$ with different catalysts and the other set related to destabilized materials $LiBH_4 + \frac{1}{2}MgH_2 + Xmol\% ZnCl_2$ with different catalysts. The results of various physicochemical characterizations such TGA, DSC, XRD, FTIR and PCT are discussed for these two sets of complex metal hydrides in the following sub sections.

3.1 Complex metal hydride - $2LiBH_4 + ZnCl_2$ without and with different catalysts

The complex metal hydride mixture, $2LiBH_4 + ZnCl_2$ was prepared by hand mixing in ceramic mortar and via ball milling for different time duration under inert or reactive ambient. The obtained $Zn(BH_4)_2$ per the Eq. (3) was further treated with different catalysts doping. All these as-synthesized materials are then subjected to thermogravimetric and differential scanning calorimetric measurements (TGA-DSC or SDT). **Table 1** represents the onset, and peak temperature of hydrogen decomposition from the complex metal hydride with total weight loss. From the **Table 1**, it is discernible that the pristine mixture $2LiBH_4 + ZnCl_2$ milled shows lower hydrogen decomposition temperature by at least 25°C when compared to hand mix counterparts. Additionally, the nano-Ni doping concentration of at least 1–4 mol% on the complex metal hydride mixture shows temperature reduction of at least 15–20°C for the hydrogen release. Overall, the total gravimetric weight loss due to hydrogen decomposition at the peak temperature, ranges from 12 to 15 wt% of hydrogen was obtained for both undoped and doped complex metal hydride mixtures. The hand mix sample show the weight loss of 9.4 wt.% due to partial formation of $Zn(BH_4)_2$. The TGA and DSC profiles as shown in **Figures 1** and **2** supports the **Table 1** results.

Complex Hydride	On-set Temp. °C	Peak Temp. °C	Weight Loss. Wt%
$2LiBH_4 + ZnCl_2$	114.07	125.06	14.80
$2LiBH_4 + ZnCl_2 + 1$ mol% TiF_3	114.13	129.21	14.92
$2LiBH_4 + ZnCl_2 + 2$ mol% TiF_3	112.57	128.00	14.18
$2LiBH_4 + ZnCl_2 + 2$ mol% MgH_2	113.96	128.11	13.70
$2LiBH_4 + ZnCl_2$ Hand mix	138.69	150.50	9.435
$2LiBH_4 + ZnCl_2 + 1$ mol% nanoNi	114.38	116.90	13.54
$2LiBH_4 + ZnCl_2 + 2$ mol% nanoNi	110.38	113.00	14.73
$2LiBH_4 + ZnCl_2 + 3$ mol% nanoNi	106.05	107.30	14.82

Table 1.
TGA-DSC measurements data of pristine and catalyst doped complex metal hydride mixture, $2LiBH_4 + ZnCl_2$.
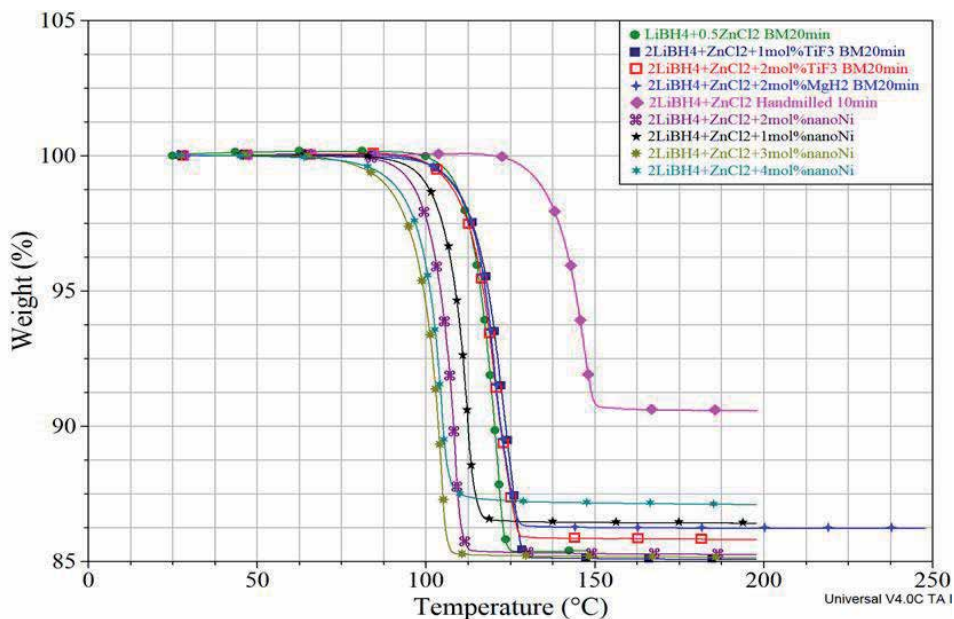
Figure 1.
Thermogravimetric profiles of $2LiBH_4 + ZnCl_2$ mixture with different catalysts (up to 4 mol%), such as TiF_3, MgH_2, nano-Ni.

A closer look of the TGA profiles (**Figure 1**), one can find a detailed observation as follows. Comparison between the metal hydride mixtures, $LiBH_4 + ½ ZnCl_2$ ball milled for 20 minutes shows greater hydrogen release at lower temperatures than the sample, $2LiBH_4 + ZnCl_2$ hand mixed for 10 minutes, which emphasize the need of mechanical milling to complete the reaction stated in Eq. (3). Regarding the different concentrations of TiF_3, 2 mol% reveals at least 0.5% more of hydrogen release and at temperatures at least 1°C lesser than the concentration 1 mol% TiF_3. For the 2 mol% MgH_2 doping, which showed similar performance like TiF_3 dopant in terms of both thermal decomposition temperature and weight loss characteristics and are inferior to the pristine $LiBH_4 + ½ ZnCl_2$ mixture milled for 20 minutes. Nano-nickel on the other hand, doping with different concentrations, 1–4 mol%, demonstrated

superior thermal decomposition behavior with 3 mol% as an optimum concentration as shown in **Figure 1**.

The DSC profiles as exhibited in **Figure 2**; the endothermic peaks are due to thermal hydrogen decomposition where the weight loss was observed in **Figure 1**. As it is mentioned that the partial reaction of the hand mixed compounds as noted earlier is supported well with the DSC studies in which there were two endo- peaks obtained, one may be due to the $LiBH_4$ phase and other may be due to the partial $Zn(BH_4)_2$ phase. However, the ball milled samples show only one endo sharp peak, the area under this curve enhanced at lower temperatures, by nano-Ni catalyst doping as shown in **Figure 2**.

The x-ray diffraction patterns of all the samples listed in **Table 1** are carried out with the similar experimental conditions and background parameters and are depicted in **Figure 3**. It is very well confirmed from the XRD profiles that the hand mix metal hydride samples show the existence of unreacted $LiBH_4$ and $ZnCl_2$. Whereas, the ball milled counterparts reveals the appearance of by-product, LiCl, thus the consumption or reaction of $2LiBH_4$ and $ZnCl_2$ to produce a new $Zn(BH_4)_2$ compound, with unknown peak appeared at around 20.5^o. For the catalysts, doped $2LiBH_4 + ZnCl_2$, the peaks correspond to TiF_3, or nano-Ni are not visible due to the low concentration (<4 mol%), and the XRD patterns were very similar to the pristine complex metal hydride ball milled for 20 minutes. The presence of LiCl phase affects the total hydrogen storage capacity reported in **Table 1**, because of the dead weight contribution from the LiCl. Overall, the XRD profiles of the complex metal hydrides supports the reaction (3) and the thermal characteristics as discussed above.

3.2 Complex Metal Hydride - $LiBH_4 + \frac{1}{2}MgH_2 + Xmol\% ZnCl_2$

Based on the by-product LiCl appearance in the reaction discussed in Section 3.1 and to enhance the hydrogen storage capacity, the concentration of $ZnCl_2$ was
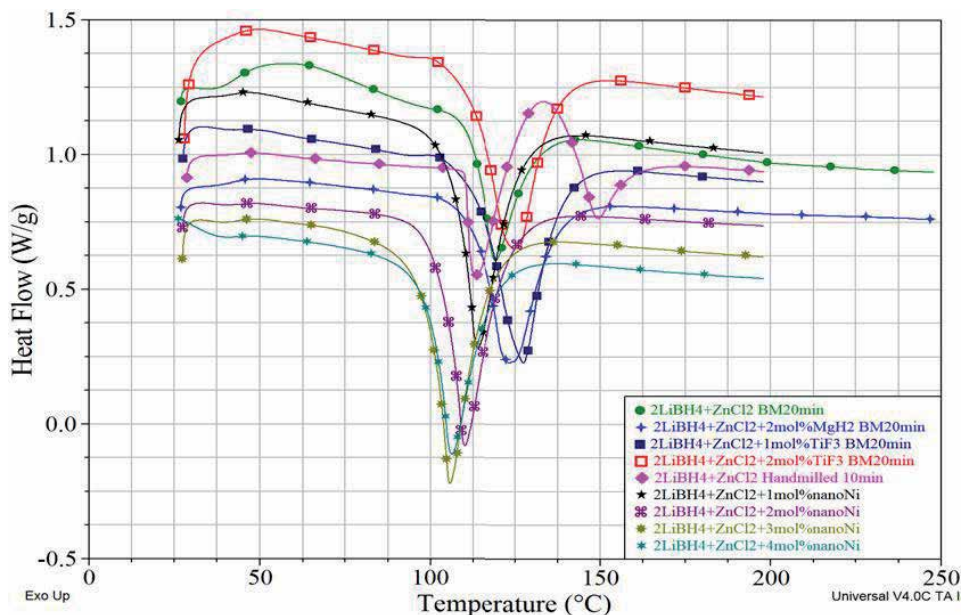
Figure 2.
Differential Scanning Calorimetric profiles of $2LiBH_4 + ZnCl_2$ mixture with different catalysts (up to 3 mol%), such as TiF_3, MgH_2, nano-Ni.

reduced in steps of few mol% on the $LiBH_4$ + $\frac{1}{2}MgH_2$ complex metal hydride system. $LiBH_4$ and MgH_2 were ball milled (2 hours) together with 1:0.5 ratio and $ZnCl_2$ have been admixed with different mol% concentrations to form complex composite hydride, $LiBH$ + $\frac{1}{2}MgH_2$ + Xmol% $ZnCl_2$ (X = 0, 2, 4, 6, 8 and 10). **Figure 4** represents the XRD patterns of the complex metal hydride with different value of X. When X = 0, with no $ZnCl_2$, the structure is more or less the mixture of $LiBH_4$ and MgH_2. However, if the value of X increases to 2 mol%, the appearance Zn peak and the reduction of $LiBH_4$ relative intensity are observed. For X = 4, an unknown peak appears around 20.5° because of the reaction of
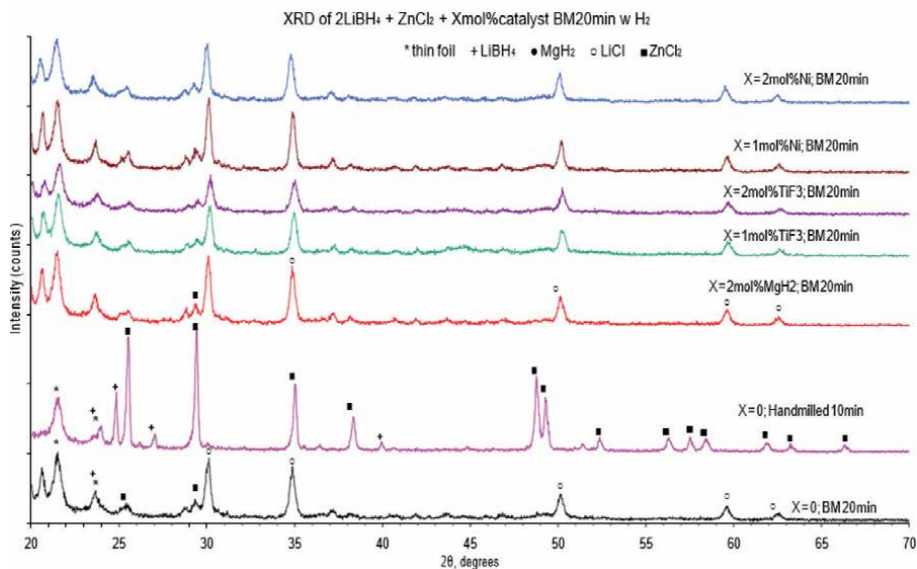
Figure 3.
X-ray diffraction patters of $2LiBH_4$ + $ZnCl_2$ mixture without and with different catalysts (1–4 mol% concentrations).
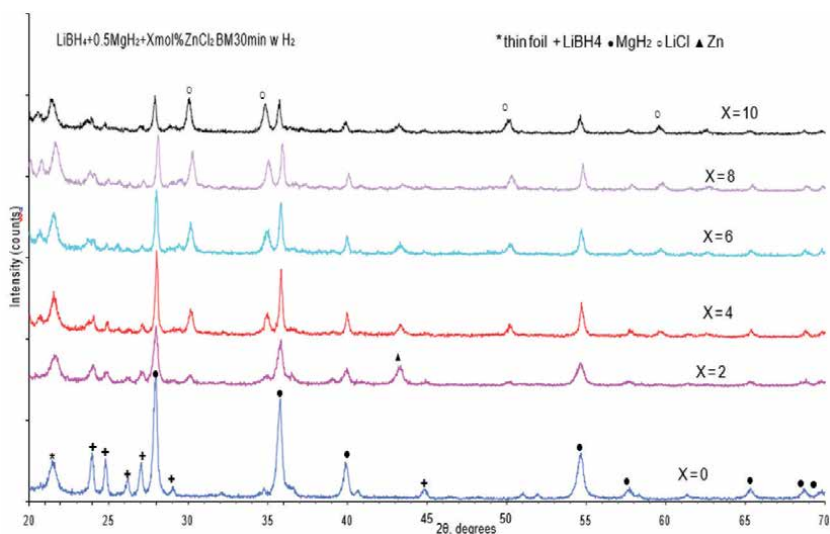
Figure 4.
XRD profiles of $LiBH_4$ + $\frac{1}{2}MgH_2$ + Xmol% $ZnCl_2$ ball milled for 30 min in reactive (H_2) atmosphere.

LiBH$_4$ and available Zn to form Zn(BH$_4$)$_2$ as per the Eq. (3) and hence the by-product formation of LiCl was inevitable. For the X value of 10 mol%, the LiBH$_4$ phase and the pure Zn phase drastically reduced, however there was no changes in the MgH$_2$ structural phase. Therefore, the XRD profiles confirm the Eq. (3) with concentration optimization of ZnCl$_2$ which could further control the by-product LiCl formation. The Fourier Transform Infrared (FTIR) Spectroscopic profiles of LiBH$_4$ + ½MgH$_2$ + Xmol% ZnCl$_2$ (X = 0, 2, 4, 6, 8 and 10) shows the presence of B-H stretch, at wavenumbers, 2276 cm^{-1} and 2213 cm^{-1} and another peak
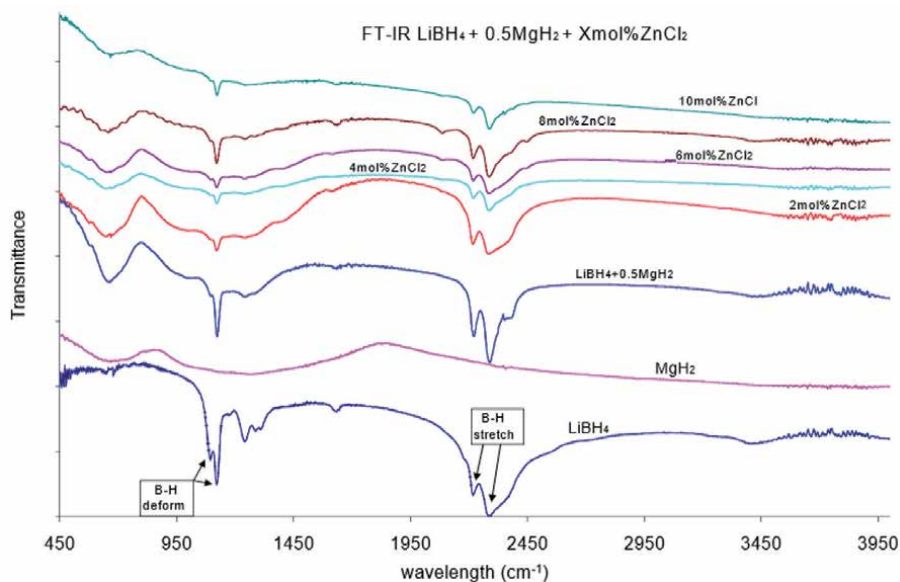
Figure 5.
FTIR of LiBH$_4$ + ½MgH$_2$ + Xmol% ZnCl$_2$ (X = 0, 2, 4, 6, 8 and 10) ball milled for 30 min in reactive (H$_2$) atmosphere.
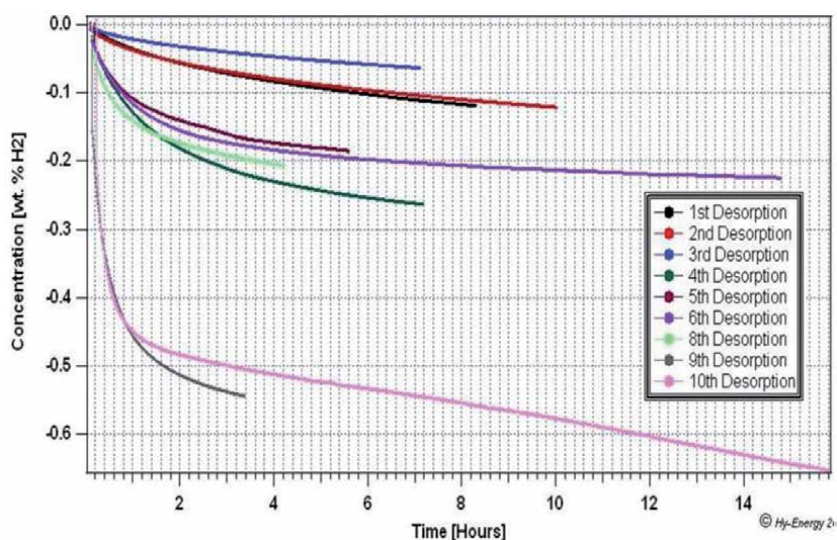
Figure 6.
Desorption Data Collected on a PCT for LiBH$_4$ + ½MgH$_2$ + 2 mol% ZnCl$_2$ Ball Milled 2 Hours Under H$_2$ Ambient.
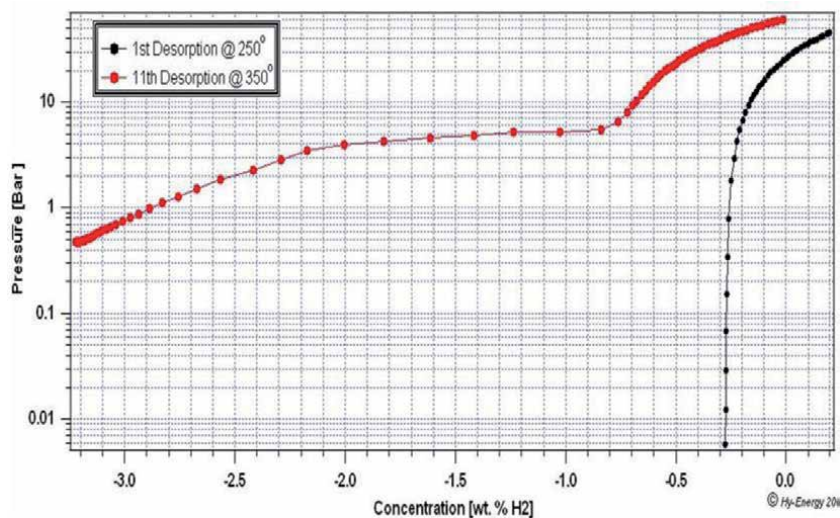
Figure 7.
PCT Desorption at 250°C and 350°C for the mixture, LiBH$_4$ + ½MgH$_2$ + 2 mol% ZnCl$_2$ Ball Milled 2 Hours Under H$_2$ Ambient.

correspond to BH$_2$ deformation band was observed at 1118 cm^{-1} and 1091 cm^{-1} due to LiBH$_4$ (see **Figure 5**). These stretches were decreased in transmittance values when X increases from 2 to 10 mol%. No additional impurity peaks were observed.

The hydrogen absorption and desorption characteristics of LiBH$_4$ + ½MgH$_2$ + 2 mol% ZnCl$_2$ was demonstrated using the PCT Sievert's type apparatus. The hydrogen desorption experiments were performed at various temperatures, for example from 1 to 3 cycles at 250°C, 4–6 cycles at 300°C and 8–10 cycles at 350°C. As the temperatures increased from 250–350°C, the hydrogen storage capacity increases five-fold as shown in **Figure 6**. At the end of each desorption run, the sample was hydrogenated at high pressure, up to 40 atmosphere and at temperature of 200°C for several hours. The PCT isotherm of 11th desorption run at 350°C demonstrates the plateau pressure of hydrogen desorption, at around 4–5 bars and the storage capacity of ~3.0 wt.% (see **Figure 7**). Based on the aforementioned characteristics, these complex metal hydrides bearing light weight elements or compounds, for example LiBH$_4$ and MgH$_2$ with catalysts dopants may be considered as potential applications for clean energy or fuel (hydrogen) storage.

4. Conclusion

Two sets of complex metal hydrides comprising light weight elements and compounds have been prepared via solid state mechanochemical process. The transition metal chloride, for example, ZnCl$_2$ addition to LiBH$_4$ in the ratio of 1;2, ends up forming a new complex hydride, Zn(BH$_4$)$_2$ with thermal decomposition of hydrogen release at lower temperatures, <130°C and high hydrogen capacity >10 wt.%. The 1:0.5 ratio of LiBH$_4$:MgH$_2$ (and 2 mol% ZnCl$_2$) in this complex structure thus destabilizes and maintain the plateau pressure, 4–5 atmospheres for the hydrogen desorption with total reversible hydrogen storage capacity ~3.0 wt.% at around 350°C. The structural and chemical characteristics of LiBH$_4$ + ½MgH$_2$ + 2 mol% ZnCl$_2$ and other concentration variations, including catalytic doping via nano-Ni shows reversible hydrogen storage behavior.

Acknowledgements

Conflict of interest

The authors declare no conflict of interest.

Author details

Sesha Srinivasan[1]*, Luis Rivera[2], Diego Escobar[3] and Elias Stefanakos[4]

1 Department of Natural Sciences, Florida Polytechnic University, Lakeland, Florida, USA

2 Environmental/Mechanical Engineering, Fleet Standards Branch, Military Sealift Command, Norfolk, USA

3 Department of Field Services, Tigo Colombia, Medellin, Colombia

4 Clean Energy Research Center, College of Engineering, University of South Florida, Tampa, Florida, USA

*Address all correspondence to: ssrinivasan@floridapoly.edu

IntechOpen

References

[1] Guzik MN, Mohtadi R, Sartori S. Lightweight complex metal hydrides for Li-, Na- and Mg- based batteries. J. Materials Research. 2019:34:6:877-904. DOI: 10.1557/jmr.2019.82

[2] Schuth F, Bogdanovic B, Felderhoff M. Light metal hydrides and complex hydrides for hydrogen storage. Chem. Comm. 2004:2249-2258. DOI: 10.1039/B406522K

[3] Moller KT, Sheppard D, Ravisbaek DB, Buckley CE, Akiba E, Hi H-W, Jensen TR. Complex metal hydrides for hydrogen, thermal and electrochemical energy storage. Energies. 2017:10:1645:1-30. DOI: 10.3390/en10101645

[4] Bourgeois N, Crivello J-C, Cenedese P, Joubert J-M. Systematic first-principles study of binary metal hydrides. ACS Comb. Sci. 2017:19:8″513-523. DOI: 10.1021/acscombsci.7b00050

[5] Grochala W, Edwards P. Thermal decomposition of non-interstitial hydrides for the storage and production of hydrogen. Chem. Rev. 2004:104: 1283-1315. DOI: 10.1021/cr030691s

[6] Yamaguchi M, Akiba E. Ternary hydrides. In: Materials Science and Technology. Wiley-VCH Verlag GmbH & Co KGaA; 2006. DOI: 10.1002/9783527603978.mst0043

[7] Bronger W. Complex transition metal hydrides. Angewandte Chemie International Edition. 1991:L30:7: 759-768. DOI: 10.1002/anie.199107591

[8] Renaudin G, Guenee L, Yvon K. LaMg$_2$NiH$_7$, a novel quaternary metal hydride containing tetrahedral [NiH$_4$]$^{4-}$ complexes and hydride anions. J. Alloys and Compounds. 2003:350:145-150. DOI: 10.1016/S0925-8388(02)00963-5

[9] Huang B, Yvon K, Fischer P. LiMg$_2$RuH$_7$, a new quaternary metal hydride containing octahedral [Ru(H) H$_6$]$^{4-}$ complex anions. J Alloys and Compounds. 1994:210:1-2:243-246. DOI: 10.1016/0925-8388(94)90144-9

[10] DOE Technical Targets for Onboard Hydrogen Storage for Ligh-Duty Vehicles [Internet]. 2020. Available from: https://www.energy.gov/eere/ fuelcells/doe-technical-targets-onboard-hydrogen-storage-light-duty-vehicles

[11] Zuttel A, Rentsch S, Fisher P, Wenger P, Sudan P, Mauron, Ph, Emmenegger Ch. Hydrogen storage properties of LiBH$_4$. J. Alloys and Compounds. 2003:356-357:515-520. DOI: 10.1016/S0925-8388(02)01253-7

[12] Schlesinger HI, Herbert CB. Metallo borohydrides. III. Lithium borohydride. J. Am. Chem. Soc. 1940:62:12:3429-3435. DOI: 10.1021/ja01869a039

[13] Kong VCY, Foulkes FR, Kirk DW, Hinatsu JT. Development of hydrogen storage for fuel cell generators, i. hydrogen generation using hydrolysis hydrides. Int. J. Hydrogen Energy. 1999:24:7:665-675. DOI: 10.1016/ S0360-3199(98)00113-X

[14] Kojima Y, Kawai Y, Kimbara M, Nakanishi H, Matsumoto S. Hydrogen generation by hydrolysis reaction of lithium borohydride. Int. J. Hydrogen Energy. 2004:29:12:1213-1217. DOI: 10.1016/j.ijhydene.2003.12.009

[15] Orimo S, Nakamori Y, Gitahara G, Miwa K, Ohba N, Towata S, Zuttel A. Dehydriding and rehydriding reactions of LiBH$_4$. J. Alloys and Compounds. 2005:404-406:427-430. DOE: 10.1016/j. jalcom.2004.10.091

[16] Vajo JJ, Skeith SL, Mertens F. Reversible storage of hydrogen in destabilized LiBH$_4$. J. Phys. Chem. B. 2005:109:9:3719-3722. DOI: 10.1021/ jp040769o

[17] Huot J, Liang G, Boily S, Van Neste A, Schulz R. Structural study and hydrogen storption kinetics of ball-milled magnesium hydride. J. Alloys and Compounds. 1999:293-295:495-500. DOI: 10.1016/S0925-8388(99)00474-0

[18] Liang G, Huot J, Boily S, Van Neste A, Schulz R. Hydrogens storage properties of the mechanically milled MgH$_2$-V nanocomposite. J. Alloys and Compounds. 1999:291:1-2:295-299. DOI: 10.1016/S0925-8388(99)00268-6

[19] Liang G, Huot J, Boily S, Schulz R. Hydrogen desorption kinetics of a mechanically milled MgH$_2$+5at.%V nanocomposite. J. Alloys and Compounds. 2000:305:1-2:239-245. DOI: 10.1016/S0925-8388(00)00708-8

[20] Dehouche Z, Djaozandry R, Huot J, Boily S, Goyette J, Bost TK, Schulz R. Influence of cycling on the thermodynamic and structure properties of nanocrystalline magnesium-based hydride. J. Alloys and Compounds. 2000:305:1-2:264-271. DOI: 10.1016/S0925-8388(00)00718-0

[21] Huot J, Pelletier JF, Liang G, Scutton M, Schulz R. Structure of nanocomposite metal hydrides. J. Alloys and Compounds. 2002:330-332:727-731. DOI: 10.1016/S0925-8388(01)01662-0

[22] Barkhordarian G, Klassen T, Bormann R. Fast hydrogen storption kinetics of nanocrystalline Mg using Nb$_2$O$_5$ as catalyst. Scripta Materialia. 2003:49:3:213-217. DOI: 10.1016/S1359-6462(03)00259-8

[23] Barkhordarian G, Klassen T, Bormann R. Effect of Nb$_2$O$_5$ content on hydrogen reaction kinetics of Mg. J. Alloys and Compounds. 2004:304:1-2:242-246. DOI: 10.1016/S0925-8388(03)00530-9

[24] Jeon E, Cho YW. Mechanochemical synthesis and thermal decomposition of zinc borohydride. J. Alloys and Compounds. 2006:422:1-2:273-275. DOI: 10.1016/j.jalclcom.2005.11.045

[25] Srinivasan S, Escobar D, Jurczyk M, Goswami Y, Stefanakos E. Nanocatalyst doping of Zn(BH$_4$)$_2$ for on-board hydrogen storage. J. Alloys and Compounds, 2008:462:1-2:294-302. DOI: 10.1016/j.jallcom.2007.08.028

Hydrogen Storage: Materials, Kinetics and Thermodynamics

Athule Ngqalakwezi and Diakanua Bevon Nkazi

Abstract

The need for cleaner sources of energy has become a serious need now more than ever due to the rising effects of fossil fuels on the environment. Technological advancement in society today has necessitated the need for fast and robust materials that will match the speed at which society is moving forward. Hydrogen as an alternative source, has garnered a lot of attention due to its zero emission characteristic. In this chapter, a background on hydrogen storage and its impact on the 'envisaged green environment' is discussed. Graphene and borohydrides hydrogen storage materials are reviewed extensively and the kinetic models thereof. Furthermore, the reaction mechanism of graphene nanocomposites is also discussed.

Keywords: hydrogen storage, hydrides, kinetics, graphene, nanocomposites

1. Introduction

The generation of the 21st century has had to deal with the effects of centuries of environmental mismanagement due to industrialization and modernization. To put things into perspective, approximately 6587 billion metric tons of carbon dioxide, a main contributor to climate change, were emitted into the atmosphere in 2015 through the use of fossil fuels [1]. In 2017, these numbers increased and they are continually increasing every year (**Figure 1**).

As such, the implementation of green systems and processes has become a priority in order to try and mitigate the damages to the environment. The remedial actions implemented to reduce the effects on the environment include the institution of legislations that fine high carbon emitters, green technologies and green alternatives to support energy and electricity demands. Hydrogen is amongst the green alternative researched as a substitute for fossil fuels. However, it is acknowledged that the transition from fossil fuels or carbon based sources is not going to be an easy one because of the demand and the complexity of introducing a different system. The United States of America has already started introducing the hydrogen fuelled cars and currently, there is about 6558 hydrogen fuelled cars. This number is expected to surge in the coming years, in 2027 it is expected that there demand would increase to 70,000 units [2].

The implementation of the hydrogen economy is driven by the Department of Energy in the United States. The DoE set the standards and requirements for hydrogen storage materials for practical application in hybrid cars (**Figure 2**).

Various hydrogen storage materials have been synthesized and tested for hydrogen storage applications. However most of these materials have not met the
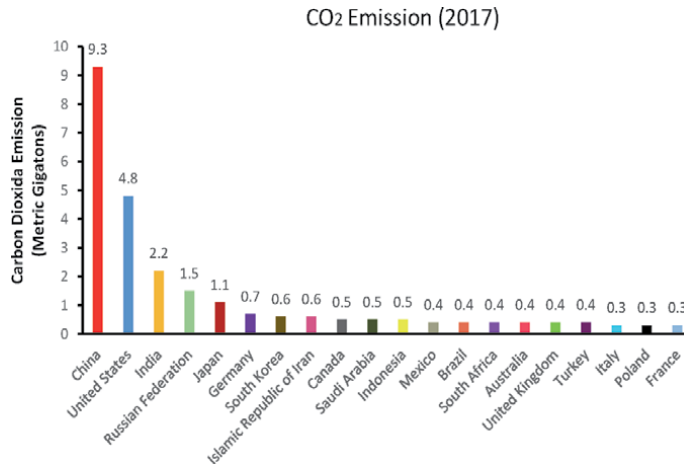
Figure 1.
World's biggest carbon dioxide emitters (Economics help, 2017 [2]).
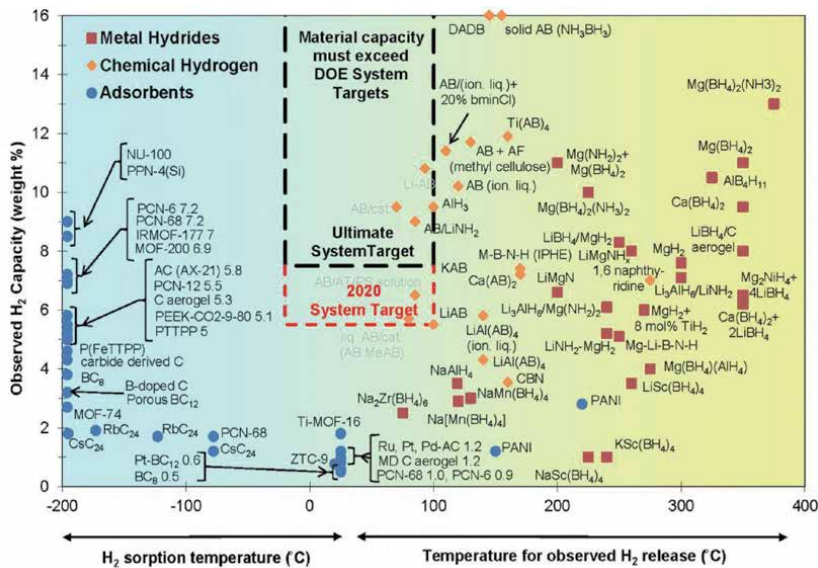
Figure 2.
2020 hydrogen storage requirements for hybrid cars (Department of Energy, United States).

requirements for applicable hydrogen storage. In this book chapter, the synthesis and first principles studies thereof of new classes of materials will be reviewed, their kinetics will also be reviewed in great details.

An immense effort has been put towards finding novel material for hydrogen storage that will have optimum conditions as indicated by the D.o.E. A great number of light-weight nanostructures consisting of nitrogen, carbon and boron have received favorable attention due to their large volume-to- surface ratio and light-weight characteristic [3]. These materials have been studied intensely and recent works, depicts an improvement and a ray of light in terms of practical applicable hydrogen storage in them.

The interest in these materials was instigated by their unique characteristics. Boron based nanostructures have similar porous structural characteristics with carbon based materials however, boron based materials are much more lighter [3]

making them an interesting candidate for practical hydrogen storage. Boron based materials are synthesized using various methods such as hydrolysis and pyrolysis of chemical hydrides.

Hydrolysis:

Hydrolysis is the liberation of hydrogen gas through the reaction of water with a hydride. The overall reaction is summed up as follows:

$$MHx + xH_2O \rightarrow M(OH)_x + xH_2 \qquad (1)$$

$$MXH_4 + 4H_2O \rightarrow 4H_2 + MOH + H_3XO_3 \qquad (2)$$
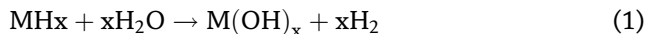
Where x is the valence number of the metal, M is the metal and X is a trivalent group III element.

Pyrolysis:

Pyrolysis is the breakdown of a substance due to heating. The overall pyrolysis reaction is summed up as follows:

$$2M + xH_2 \rightarrow 2MHx + HEAT \qquad (3)$$

Where M is an alloy or a metal.

Boron hydrides are interesting chemical H2 storage materials that have high hydrogen capacity however the kinetics and thermodynamics of these materials have limited their practical use for hydrogen storage. Different approaches have been employed to decrease the kinetics and thermodynamics of these materials. Popular boron hydrides include LiBH4 (Lithium borohydride) and NH3BH3 (ammonia borane) [1]. The reaction mechanism with boron hydrides can be summed up into four main steps: 1. the decomposition or breakdown of the material through heating to generate hydrogen (Pyrolysis), 2. The interaction of the material with water to release hydrogen (pyrolysis), 3. Improvement of the kinetics through the addition of boron to the electrodes on the metal hydride battery, 4. The storage of hydrogen via the boron nitride nanotubes which can also release the hydrogen when heating [4]. A lot of remedial actions have been employed to improve the kinetics of these materials however the research still continue.

2. Graphene based materials

Graphene, a 2D carbon allotrope that is positioned in a sp^2-bonded aromatic structure, has attracted a lot of attention for hydrogen storage application due to its low weight, cost and ability to be synthesized in large quantities [5]. This two dimensional material configuration is formed by covalent bonds that are distributed on the hexagonal honeycomb lattice [6]. Apart from this, graphene has intriguing properties which have made them applicable in these fields: energy storage, sensors, electrodes, field effect devices, nanocomposites and solar cells [6].

The large surface area of graphene ($2630 \, g^2m^{-1}$) is tremendously beneficial for hydrogen storage. The interaction of graphene systems is based on instantaneous dipole–dipole induced forces because hydrogen is a non-polar molar [7]. A number of theoretical studies have been undertaken to explain the adsorption of hydrogen on the surface of graphene material and give more information on the pathway experimentalist need to take [7]. These studies have shown that the spatial distribution of adsorbed hydrogen on the surface of graphene is delocalized and that molecular hydrogen exhibits unrestricted lateral movement [7].

3. Graphene nanocomposites

Nanocomposites, where nanocatalysis and nanostructure are combined, are the next research advancement of high performance of hydrogen storage materials. These materials have distinct functionalities due to the shorten diffusion distance, increased surface area and the multiplied grain boundaries [6]. Graphene, graphene nanocomposites and its derivatives depict a promising potential for different applications such as automotive industry, aerospace, electronics and green energy. This is because graphene has intriguing thermal, mechanical and electrical properties [6, 8, 9].

A lot of studies have been done with graphene and nanocomposites thereof for the practical application in on-board application [7–10]. Graphene nanocomposites can be synthesized using various techniques. These include the self-assembly technique, solution mixing, sol–gel method, hydrothermal or the solvothermal method and other methods [11]. Graphene nanocomposites have been preferred for hydrogen storage application mainly because of their light weight characteristic. Weight of the material is an important factor when considering the practical applications for hybrid cars according to the DoE standards. Graphene alone is a physisorbent material and does not take up a lot of hydrogen however its kinetics are interesting [11–15]. The incorporation of metals on the graphene matrix enhances the functions of the system and improves the hydrogenation of this material to make it more appealing for practical use in hybrid cars [16, 17]. Various metals have been used in this regard to improve the hydrogen uptake of the graphene nanocomposite. Zhou et al., synthesized a Ni/graphene nanocomposite and a Pd/graphene nanocomposite [18]. Ngqalakwezi et al. synthesized a novel Ca/graphene nanocomposite [10]. The graphene nanocomposites can be used and applied in different industries for hydrogen generation in the electrolysis process, in the photo degradation of pollutants, energy storage and other applications.

Furthermore, nanomaterials permit favorable charge, mass and heat transfer, these are added advantages when considering practical application of these materials for on board applications [13, 17, 19]. In addition, nanomaterials assist in dimensional alteration of particular phase transitions and chemical reactions [6]. Nanomaterials not only help and aid in the kinetics of hydrogen storage materials, but they also help to destabilize the thermodynamics of chemisorption materials.

4. Synthesis methods for graphene nanocomposites

4.1 Self-assembly technique

The self-assembly process is one of the primary techniques for synthesizing complex materials from molecules in macro, micro and nano scales [20]. In the bottom up techniques in nanotechnology, this method has been considered as one of the most effective methods [21]. In this technique, molecules are utilized as precursor material for synthesizing graphene nanocomposites under environmentally conducive parameters. As such, graphene sheets prepared using the top down approach (mechanical and chemical exfoliation of graphite), can be utilizing as precursor material for the self-assembly technique [20]. The mechanism of self-assembly of graphene can be quite complex and understanding it necessitates the full understanding of the non-covalent and interlayer covalent interactions between graphene derivatives [22]. These interactions include the dipole–dipole interactions, p–p interactions, van Der Waals forces and electrostatic forces. Non- covalent interactions in the self-assembly technique, aid the graphene in producing composites with novel functions and structures [22, 23].

These non-covalent interactions are active in various organic solvents and they permit homogenous dispersion for the anticipated self-assembly. Furthermore, graphene molecules allow for functionalization which is double sided and thus creates novel structural architecture with double-sized decoration of functional groups on the graphene sheet. These functional groups in principle, permit layer-by-layer coordinated assembly in a supramolecular manner [23].

To take advantage of the characteristics of graphene at nanoscale in macro-sized devices, it is crucial to incorporate the graphene sheets into 3D micro-sized structures with better maneuver of the geometry and dimensionality of the material [24]. Various methods have been reported for the fabrication of 3D porous structures, 2D thin films and 1 dimensional fiber-like molecules [24]. For 3D porous structures these methods have been used; freeze casting self-assembly, breath figure 3D assembly, diffusion driven 3D self-assembly, 3D self-assembly through the hydrothermal process, pickering emulsions for 3D molecules and 3D assembly through chemical reduction [25–28]. For 2D structures these methods have been used; vacuum assisted assembly, Rayleigh and Taylor instability and Marangoni effect self-assembly method, liquid–liquid interfacial 2D assembly method, evaporation induced 2D self-assembly method, electrophoretic method and the Langmuire-Blodgett method [27, 29, 30]. For 1D fibers these methods have employed; 1D self-assembly self-intertwining method, direct drawing self-assembly method, electrophoretic 1D self-assembly and flow directed wet-spinning 1D self-assembly. All of these methods have been successfully employed to synthesize these different structures under various parameters [31–33].

4.2 Solution mixing method

The solution mixing method is one of the easiest method for the synthesis of polymer based graphene nanocomposites. The method comprises of three simple steps which are; the scattering of the filler, the polymer incorporation and the solvent removal through the distillation process or evaporation [34]. This method is also relatively cheap because it does not need the use of expensive equipment or expensive operative protocols, although it has a many steps [35]. Other advantages about this technique are; the method allows for good dispersion of thin particles because of the efficient fragmentation of organoclay agglomerates [35, 36]. This in effect, generates greatly filled key batches that can later be mixed with pristine polymer through the melt compounding process. Furthermore this process allows for the production of highly exfoliated graphene nanocomposites that can be attained through mixing the physical coupling process with chemical reaction.

The synthesis step of this method typically involves dissipating a polymer in a solvent and suspending the filler in a different compatible solvent. Different solvents such as acetone, tetrahydrofuran (THF), toluene, chloroform, dimethylformamide and cyclohexane are utilized in this method [35]. As mentioned above, the solution blending generates ensures excellent exfoliation and dispersion of the filler within the elastomeric matrix [37].

Ultrasonication or high speed shear mixing are employed during the solution blending process to ensure the polymer solution and filler suspension are mixed thoroughly [36]. This technique has been efficient in dispersing nanofillers regardless of the polarity of the polymer. As much as this method has a lot of advantages, it does however have disadvantages as well. The main disadvantage of this technique is the thorough and efficient removal of solvents utilized during the process. Another major disadvantage is the scale up; the solvents utilized are very expensive and scaling up this process would pose financial difficulties and strains [35, 36].

Lastly, the entire process involves a lot of steps and this can influence the subsequent outcome of the process.

A couple of researcher have used this method to synthesize graphene nanocomposites. Wang et al. utilized Cu (OH)$_2$ composite sheets and reduced graphene oxide to synthesize thin micro layered structure of rGo-Cu powder [38]. Tang et al. synthesized graphene nanosheets decorated with Ni nanoparticles utilizing the in situ chemical reduction method [39]. The resulting nanocomposite after wet mixing electrolytic Cu to obtain Ni-graphene nanosheets/Cu nanocomposite, depicted interesting mechanical properties with a yield strength of 268 MPa and a high Young Modulus of 132 GPa [39]. Furthermore, Zeng et al. incorporated Al powder in the GO suspension solution and ultrasonicated the mixture [40]. Al-graphene nanocomposite was obtained with a tensile strength of 255 MPa [40]. Li et. al, on the other hand used precursor organic graphite to synthesize graphene oxide using the Hummers method and decorated the graphene with Ni nanoparticles [41]. Ngqalakwezi et al. also synthesized Ca/graphene using the Improved Tours Method and chemical reduction the Ca ions on the surface of the GO [10].

The solution mixing method has been successfully employed to synthesis graphene nanocomposites.

4.3 Sol-gel method

The sol–gel method is also a simple method that allows the synthesis of a homogenous material that has great compositional controls [42]. This method utilizes metal chlorides or metal alkoxides as the precursor material [11]. The chlorides or alkoxides are treated through a series of condensation and hydrolysis reactions and later the cured composites are dried and calcined [11]. A number of researchers have prepared graphene nanocomposites through the sol–gel method. A SiO$_2$/graphene nanocomposite was synthesized with good cyclic stability and spectacular specific capacitance of Fg^{-1} with a current density of 1 Ag^{-1} by Rezaei et al. [43]. Patil et al. fabricated functional nanographene sheets using cobalt sulphide which had a good rate of cyclic ability and high reversible capacity ranging at about 466 mAhg^{-1} [44]. Wang et al. fabricated TiC/graphene nanocomposite using the sol gel method [45]. In this work, furfuryl alcohol was utilized as a carbon and this nanocomposite was synthesized for impact or shock absorptions [45]. Furthermore, Sun et al. synthesized various nanoparticles of platinum on sulfonated graphene and used them as anode electrocatalysts in direct ethanol fuel cell using the sol gel method [46]. The particles sized of the nanoparticles on the graphene surface ranged 1.7 nm to 13.9 nm. The sulfonic acid on the graphene improved the adsorption energy of platinum, this was observed through theoretical calculations [46].

The synthesis work done using the sol gel method has proved to be effective in synthesis graphene nanocomposites and thin-film coating materials. This method required decreased reaction temperatures and it is also not complex to follow and conduct although the still challenges in the formation of the sol.

4.4 Hydrothermal method

The hydrothermal technique has been utilized to fabricate graphene nanocomposites using autoclaves under high pressures and temperatures. The first hydrothermal reaction was reported in 1845 by Schafhautl when he noticed the synthesis of quartz microcrystals from silicic acid [47]. Since then, his method has been developed over the years by many other scientists and other novel synthesis methods have also been reported. The hydrothermal technique is not restricted to the fabrication of common and advanced materials but it also covers a wide range of

interdisciplinary subdivisions in the sector of energy storage, simulating biohydrothermal and geothermal process and waste treatment [48]. In principle, the word hydrothermal, was initiated from geological sciences where it refers to a regime of water pressures and high temperatures [49]. Hydrothermal reaction traditionally involves water as catalyst and seldom, as a component of the solid phase during the synthesis at high pressures and temperatures. This technique has many advantages to it such as, excellent dispersion in water, the synthesis using this method is inexpensive due to instrumentation, environmentally friendly, one pot synthesis method, mild operation conditions and the material precursor are also inexpensive [50].

Lee et al. discovered a novel hydrothermal fabrication route to synthesize graphene nanocomposites to improve the photocatalytic activity of TiO_2 under visible light. In the method, graphene was decorated or wrapped with TiO_2 particles [51]. A high catalytic CeO_2/graphene was synthesized by Srivastava using the hydrothermal method [52]. A Ag/graphene nanocomposite with exceptional electroconductivity was synthesized by Yang et al. using the hydrothermal method. In this work, Yang et al. used a hydrazine reductant as a reducing agent and had control over the morphology and the size of Ag nanoparticle on the surface of graphene [53]. Zhang et al. prepared a one pot method for the synthesis of Fe_2O_3–Ni $(OH)_2$/graphene nanocomposite. The nanocomposite had a good rate capability (at 100% retention), impressive cyclic stability (5000 cycles) and elevated specific capacitance at approximately 857 F/g [54]. A ZnO/graphene nanocomposite was synthesized using the hydrothermal at lower temperature 90 and 80°C [55]. The nanocomposites both displayed good catalytic activity during photocatalytic degradation against rhodamine-B dye [55].

5. Graphene nanocomposites reaction mechanism for hydrogen storage

Various authors have synthesized the graphene nanocomposites and discussed the kinetics thereof. Ngqalakwezi et al. synthesized a Ca/graphene nanocomposite using the solution mixing method for hydrogen storage purposes [10]. The calcium clusters in the nanocomposite bind hydrogen molecules without dissociation through the Kubas interaction and through the unidirectional polarization. Furthermore, they realized the Ca atoms on the graphene matrix increased the binding energy and therefore catalyzed the adsorption of the hydrogen molecule because of the polarization of the molecule [10]. The diagram below depicts the kinetic of the hydrogen storage into the graphene matrix (**Figure 3**).

Zhou et al. synthesized Pd/graphene nanocomposite for hydrogen storage [9]. In this work, four hydrogen storage performances were hypothesized for the uptake of hydrogen in the Pd/graphene nanocomposite: hydrogen molecules bind to the Pd atoms on the graphene matrix, hydrogen dissociates and forms a palladium hydride (PdHx), atomic hydrogen binds at the unsaturated sites of graphene or the hydrogen molecule is trapped within the graphene matrix [9]. The presence of the Pd atoms on the graphene matrix also elevate the binding energy and thus speeding up the adsorption of the hydrogen molecule due to the polarization of the hydrogen molecule orbitals with the Pd orbitals. The sluggish kinetics of Pd result in the dissociation of the hydrogen molecule on the surface of the Pd atom. Some of the dissociated hydrogen atoms are ejected into the gas phase and some diffuse into the Pd lattice and form the palladium hydride (PdHx) [9]. The diagram below is a conceptual figure of the reaction mechanism for the Pd/graphene nanocomposite. Zhou et al. further synthesized a Ni/Graphene nanocomposite and hypothesized the same reaction mechanism as the Pd/graphene nanocomposite [18] (**Figure 4**).
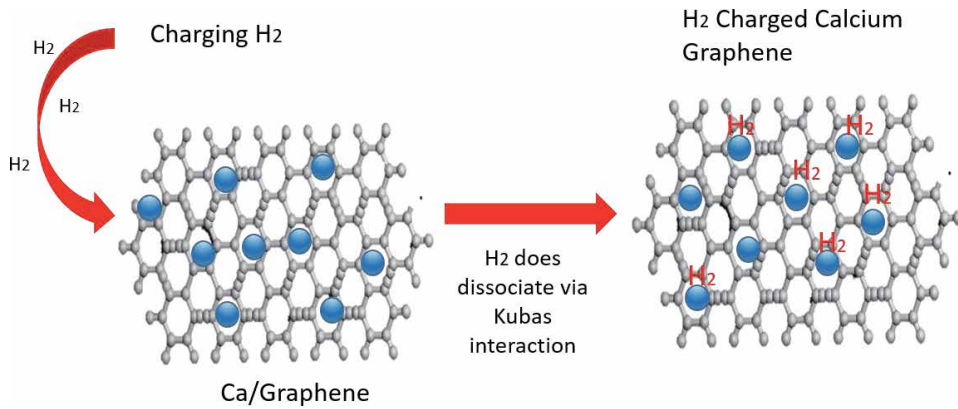
Figure 3.
Reaction mechanism of Ca/Graphene nanocomposite.
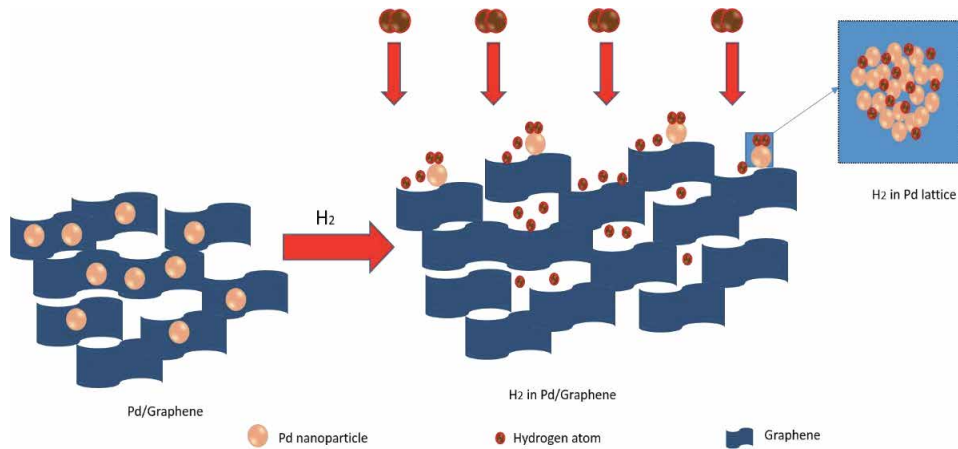
Figure 4.
Reaction mechanism of Pd/Graphene nanocomposite (adapted from [18]).

6. Kinetics of energy storage materials

The issues of kinetics in energy storage has been tackled through many scientific interventions including ball milling, alloying, thin films and catalysis. However, to date, no material has satisfied the requirement for practical energy storage. The development of hybrid material such as graphene nanocomposites has been researched to fill in the gap. In energy storage, kinetics of the materials considered for practical energy storage are complex and not easily understand and thus in this section, hydrogen storage kinetic models are reviewed.

6.1 Kinetic models

The uptake of hydrogen and release of hydrogen in hydrogen storage systems is made of adsorption, penetration through the surface, internal diffusion and chemical reaction [56]. **Figure 5** below show the detailed steps of these processes:

The two possible reaction modes for hydrogenation and dehydrogenation reactions are geometrical contraction and nucleation growth. These reaction routes are supported by theoretical and experimental research [57]. Hydrogen storage
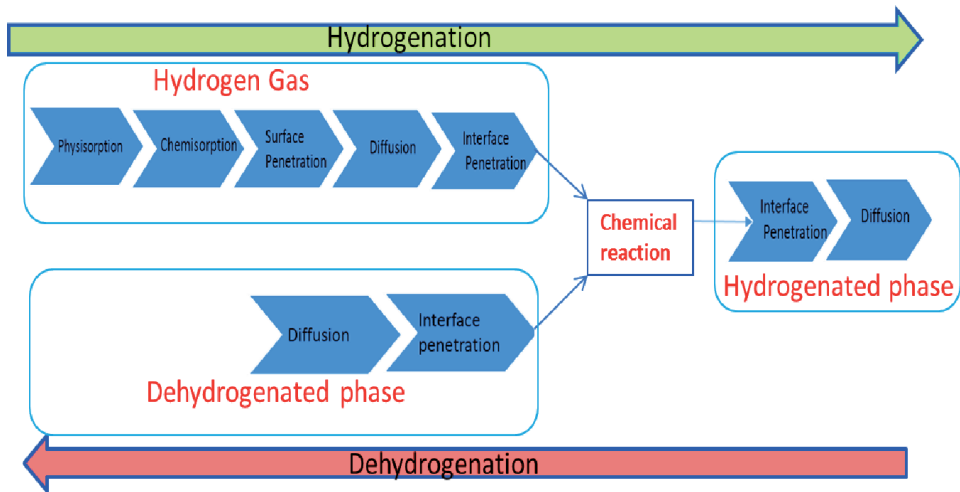
Figure 5.
Hydrogenation and dehydrogenation steps (Adapted from [58]).

kinetic models are thereby segregated according to these reaction routes. These models are founded on isothermal fitting and non-isothermal calculation analysis methods [58]. These methods help determine kinetic parameters and reaction modes this subsequently leads to a better understanding of the kinetic mechanism.

6.2 Geometrical contraction models

The basis of this model is that hydrogenation and dehydrogenation reactions transpire uniformly from the surface into the bulk of particle and the particles are uniform in size and shape [58]. The reaction fraction relationship between distances in particles of various shapes (sphere, plate and cylinder) is given by:

$$\varepsilon = 1 - \left(\frac{r}{r_0}\right)^d \tag{4}$$

Where d = dimensionality, r = lengths of the unreacted part, r_0 = length of the whole particles, ε = reaction fraction.

The geometrical contraction models are derived from this relationship equation and assumptions of isothermal conditions ([59–62]; N [63]; Nobuyoshi [64]). These are the geometrical contraction models:

6.3 Contracting volume model

$$\frac{d_r}{d_t} = -k_{int} \tag{5}$$

$$1 - (1 - \varepsilon)^{\frac{1}{d}} = \frac{k_{int}}{r_0} t = kt \tag{6}$$

Where k_{int} = rate constant (interface controlled reaction), k = generalized rate constant.

6.4 Jander model

$$\frac{\rho d_r}{d_t} = \frac{D \Delta C}{r_0 - r} \tag{7}$$

$$\left[1 - (1 - \varepsilon)^{\frac{1}{d}}\right]^2 = \frac{2 D \Delta C}{r_0^2 \rho} t = kt \tag{8}$$

Where ΔC = concentration difference, D = diffusion constant, ρ = density.

6.5 Ginstling-Brounshtein model

$$\frac{\rho d_r}{d_t} = \frac{D \Delta C}{r \ln\left(\frac{r_0}{r}\right)} \tag{9}$$

$$(1 - \varepsilon) \ln(1 - \varepsilon) + \varepsilon = \frac{4 D \Delta C}{r_0^2 \rho} t = kt \tag{10}$$

For two dimensional cylinder:

$$\frac{\rho d_r}{d_t} = \frac{D \Delta C r_0}{(r_0 - r) r} \tag{11}$$

$$1 - \frac{2}{3}\varepsilon - (1 - \epsilon)^{\frac{2}{3}} = \frac{2 D \Delta C}{r_0^2 \rho} t = kt \tag{12}$$

For three dimensional cylinder:

6.6 Valensi-Carter model

$$\frac{\rho d_r}{d_t} = \frac{D \Delta C}{r - \frac{r^2}{\left(Zr_0^3 + r^3(1-z)\right)^{\frac{1}{3}}}} \tag{13}$$

$$\frac{z - (1 + (z - 1)\varepsilon)^{\frac{2}{3}} - (z - 1)(1 - \varepsilon)^{\frac{2}{3}}}{z - 1} = \frac{2 D \Delta C}{r_0^2 \rho} t = kt \tag{14}$$

Where z = volume ratio of product to reactant.

The *contracting volume model* assumes that rate of hydrogenation is regulated by the interface process. This model is deemed as the simplest method in geometrical contraction volume models because no other assumptions are made. Through this method the dimensionality and a generalized constant can be obtained through fitting a simplified isothermal curve [58, 60]. Bösenberg et al. proved that LiH-MgB$_2$ with transition metal deposits such as Titanium and Vanadium follow the CV model very well because it is interface control [65].

The *Jander Model* however is readily used for diffusion regulated reactions. The two important assumptions made in this model are: 1. the volume of hydrogen storage materials remains constant before and after absorption and desorption reactions 2. Two and three dimensional diffusion are deemed as one meaning the interface area remains constant for diffusion [59, 66]. However these assumptions are not always applicable for hydrogen storage materials because the volume of some materials increases during the uptake of hydrogen and decrease with the

release of it. In contrast Shao et al. found that nanocrystalline Mg doped with Ti under 1Mpa of H_2 follow this model very well [67].

According to Ginstling and Crank the Ginstling-Brounshtein model develops the Jander Model using Fick's Law for radial diffusion for 2D and 3D spheres [61, 68]. Although intricate; this method is regarded as a more accurate model due to its consideration of the variance in interface area due to diffusion. Chaudhary et al. reported that MgH_2-Si synthesized by ball milling, cryomilling and ultrasonicating produces desorption curves which follow this model well [69]. The Valensi-Carter model is an extension of the G-B model which regards the change in volume in hydrogen storage materials during adsorption and desorption. This model is reportedly the most accurate in geometrical contraction model however it has not yet been applied to hydrogen storage materials [70–72].

6.7 Nucleation-growth impingement models

The Nucleation growth impingement models are generally described as the Johnson-Mehl-Avrami-Kolomogorov (JMAK) models. The JMAK models define hydrogenation and dehydrogenation reactions as three synchronized processes: nucleation, growth and impingement ([73]; Melvin [72, 74–78]). **Figure 6** is a diagram showing the three processes:

This model is founded on the basis of; 1. Enhancing nucleation, growth and impingement 2. Solving analytical problems [78]. This model is given as:

$$\varepsilon = F\left[\int_0^t I(r)V(r)d_r\right] \tag{15}$$

Where I = nucleation module, r = nucleation rate, F = impingement module defining the relationship between real reaction fraction and extended reaction fraction, V = Growth module [79].

A variation of this equation, classical JMAK (C-JMAK), which takes into consideration interface controlled growth and diffusion controlled is given by:

$$V_{(r)} = \left[G_0\int_r^t exp\left(\frac{-\Delta E_g}{RT}\right)d\eta\right]^{\frac{d}{m}} \tag{16}$$

Where ΔE_g = activation energy for growth, G_0 = intrinsic growth rate, m = growth mode parameter, $\frac{d}{m}$ = growth inde.

Nucleation   **Growth**   **Impingement**
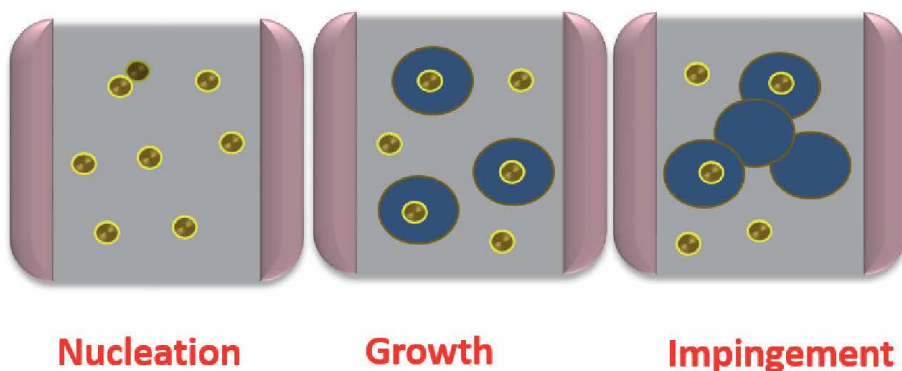
Figure 6.
Nucleation, growth and impingement (Adapted from [58]).

The C-JMAK model defines absorption and desorption of nucleation, growth and impingement very well. Nucleation in this regard refers to site saturation, growth mode to interface and diffusion controlled sites and impingement to randomly scattered nuclei isotropic growth [80]. The Avrami exponent of the desorption reaction of $NaAlH_4$ doped with Titanium was determined using this model and was found to be 3. This proved that the three dimensional interface process is the rate controlling step. Pang et al. however discovered that the actual nucleation modes propagate continuous nucleation and are not restricted to linear continuous nucleation and site saturation an assumption which this model is founded on [78, 81]. This inhibits the practical application of this model for progressive hydrogen storage applications.

Analysis methods are used to obtain kinetic mechanism by determining and comparing the best fit models and kinetic parameters that go along with it. The two most used analysis methods is isothermal fitting and non-isothermal fitting [82]. However based on literature reviewed understanding the kinetic mechanisms for hydrogen storage materials can be difficult because the analysis have downfalls which may result in misunderstanding of the kinetic mechanisms entirely [58].

7. Conclusion

Nanocomposites have proven to be materials of the 21st century with their flexibility and wide range application. These materials bridge the gap between heterogenous and homogenous catalysis through the combination of different nanomaterials. In this chapter, graphene based nanocomposites were reviewed and discussed intensely for hydrogen storage applications. The kinetic models of hydrogen storage materials was also reviewed. More work needs to be done in terms of the practical application of these material for energy storage, because to date, no material meets the standards for practical application in energy storage.

Author details

Athule Ngqalakwezi[1,2]* and Diakanua Bevon Nkazi[2]

1 Advanced Materials Division, Mintek, Randburg, Gauteng, South Africa

2 School of Chemical and Metallurgical Engineering, University of the Witwatersrand, Johannesburg, South Africa

*Address all correspondence to: 1321059@students.wits.ac.za

IntechOpen

References

[1] Wu, R., Zhang, X., Liu, Y., Zhang, L., Hu, J., Gao, M., & Pan, H. (2020). A Unique Double-Layered Carbon Nanobowl-Confined Lithium Borohydride for Highly Reversible Hydrogen Storage. Small, 16(32), 2001963. https://doi.org/10.1002/smll.202001963

[2] Department of Energy. May 2018, Hydrogen Storage. Accessed from: https://www.energy.gov/eere/fuelcells/hydrogen-storage

[3] Wen TZ, Xie AZ, Li JL, Yang YH. Novel Ti-decorated borophene χ3 as potential high-performance for hydrogen storage medium. International Journal of Hydrogen Energy. 2020 https://doi.org/10.1016/j.ijhydene.2020.07.278

[4] Ding Z, Li S, Zhou Y, Chen Z, Yang W, Ma W, et al. LiBH4 for hydrogen storage - new perspectives. Nano Materials Science. 2020;**2**(2):109-119 https://doi.org/10.1016/j.nanoms.2019.09.003

[5] A. Venkatesan, R. N. Patel, and E. S. Kannan, "Reduced Graphene Oxide for Room Temperature Hydrogen Storage Application," Adv. Mater. Res., vol. 1086, pp. 91–95, 2015, doi: 10.4028/www.scientific.net/AMR.1086.9

[6] Wang, M. (2012). Graphene Nanocomposites (C. Yan (ed.); p. Ch. 2). IntechOpen. https://doi.org/10.5772/50840

[7] Pumera M. Graphene-based nanomaterials for energy storage. Energy & Environmental Science. 2011;**4**(3):668-674 https://doi.org/10.1039/C0EE00295J

[8] Bindumadhavan K, Srivastava S, Srivastava I. Green synthesis of Graphene. Journal of Nanoscience and Nanotechnology. 2013;**13**:4320-4324 https://doi.org/10.1166/jnn.2013.7461

[9] Zhou C, Szpunar JA. Hydrogen storage performance in Pd/Graphene Nanocomposites. ACS Applied Materials & Interfaces. 2016;**8**(39):25933-25940 https://doi.org/10.1021/acsami.6b07122

[10] Ngqalakwezi A, Nkazi D, Seifert G, Ntho T. Effects of reduction of graphene oxide on the hydrogen storage capacities of metal graphene nanocomposite. Catalysis Today. 2019 https://doi.org/10.1016/j.cattod.2019.06.029

[11] Hu C, Lu T, Chen F, Zhang R. A brief review of graphene–metal oxide composites synthesis and applications in photocatalysis. Journal of the Chinese Advanced Materials Society. 2013;**1**(1):21-39 https://doi.org/10.1080/22243682.2013.771917

[12] Abe JO, Popoola API, Ajenifuja E, Popoola OM. Hydrogen energy, economy and storage: Review and recommendation. International Journal of Hydrogen Energy. 2019;**44**(29):15072-15086 https://doi.org/10.1016/J.IJHYDENE.2019.04.068

[13] Heine T, Zhechkov L, Seifert G. Hydrogen storage by physisorption on nanostructured graphite platelets. Physical Chemistry Chemical Physics. 2004;**6**(5):980-984 https://doi.org/10.1039/B316209E

[14] Kartick B, Srivastava SK, Srivastava I. Green synthesis of graphene. Journal of Nanoscience and Nanotechnology. 2013;**13**(6):4320-4324 https://doi.org/10.1166/jnn.2013.7461

[15] Ruse E, Buzaglo M, Pri-Bar I, Shunak L, Nadiv R, Pevzner S, et al. Hydrogen storage kinetics: The graphene nanoplatelet size effect. Carbon. 2018;**130**:369-376 https://doi.org/10.1016/J.CARBON.2018.01.012

[16] Nagar R, Vinayan BP, Samantaray SS, Ramaprabhu S. Recent advances in

hydrogen storage using catalytically and chemically modified graphene nanocomposites. Journal of Materials Chemistry A. 2017;**5**(44):22897-22912 https://doi.org/10.1039/C7TA05068B

[17] Schniepp HC, Li JL, McAllister MJ, Sai H, Herrera-Alonso M, Adamson DH, et al. Functionalized single Graphene sheets derived from splitting graphite oxide. The Journal of Physical Chemistry. B. 2006;**110**:8535

[18] Zhou C, Szpunar JA, Cui X. Synthesis of Ni/Graphene Nanocomposite for hydrogen storage. ACS Applied Materials & Interfaces. 2016;**8**(24):15232-15241 https://doi.org/10.1021/acsami.6b02607

[19] Hummers WS, Offeman RE. Preparation of graphitic oxide. Journal of the American Chemical Society. 1958;**80**:1339

[20] Li B, Cao X, Ong HG, Cheah JW, Zhou X, Yin Z, et al. All-carbon electronic devices fabricated by directly grown single-walled carbon nanotubes on reduced graphene oxide electrodes. Advanced Materials (Deerfield Beach, Fla.). 2010;**22**(28):3058-3061 https://doi.org/10.1002/adma.201000736

[21] Thiruvengadathan R, Korampally V, Ghosh A, Chanda N, Gangopadhyay K, Gangopadhyay S. Nanomaterial processing using self-assembly-bottom-up chemical and biological approaches. Reports on Progress in Physics. Physical Society (Great Britain). 2013;**76**:66501 https://doi.org/10.1088/0034-4885/76/6/066501

[22] Xu Y, Shi G. Assembly of chemically modified graphene: Methods and applications. Journal of Materials Chemistry. 2011;**21**(10):3311-3323 https://doi.org/10.1039/C0JM02319A

[23] Yuan, Z., Xiao, X., Li, J., Zhao, Z., Yu, D., & Li, Q. (2018). Self-Assembled Graphene-Based Architectures and

Their Applications. Advanced Science, 5 (2), 1700626. https://doi.org/10.1002/advs.201700626

[24] Nine, M. J., Tung, T., & Losic, D. (2017). Self-Assembly of Graphene Derivatives: Methods, Structures, and Applications. In Comprehensive Supramolecular Chemistry II (pp. 47–74). https://doi.org/10.1016/B978-0-12-409547-2.12634-4

[25] Chen W, Yan L. In situ self-assembly of mild chemical reduction graphene for three-dimensional architectures. Nanoscale. 2011;**3**(8): 3132-3137 https://doi.org/10.1039/C1NR10355E

[26] Deville S. Freeze-casting of porous ceramics: A review of current achievements and issues. Advanced Engineering Materials. 2008;**10**(3):155-169 https://doi.org/10.1002/adem.200700270

[27] Putz KW, Compton OC, Palmeri MJ, Nguyen ST, Brinson LC. High-Nanofiller-content Graphene oxide–polymer Nanocomposites via vacuum-assisted self-assembly. Advanced Functional Materials. 2010;**20**(19):3322-3329 https://doi.org/10.1002/adfm.201000723

[28] Xu Y, Sheng K, Li C, Shi G. Self-assembled Graphene hydrogel via a one-step hydrothermal process. ACS Nano. 2010;**4**(7):4324-4330 https://doi.org/10.1021/nn101187z

[29] Chavez-Valdez A, Shaffer MSP, Boccaccini AR. Applications of Graphene electrophoretic deposition. A review. The Journal of Physical Chemistry B. 2013;**117**(6):1502-1515 https://doi.org/10.1021/jp3064917

[30] Kim F, Cote LJ, Huang J. Graphene oxide: Surface activity and two-dimensional assembly. Advanced Materials. 2010;**22**(17):1954-1958 https://doi.org/10.1002/adma.200903932

[31] Jalili R, Aboutalebi SH, Esrafilzadeh D, Shepherd RL, Chen J, Aminorroaya-Yamini S, et al. Scalable one-step wet-spinning of Graphene fibers and yarns from liquid crystalline dispersions of Graphene oxide: Towards multifunctional textiles. Advanced Functional Materials. 2013;**23**(43):5345-5354 https://doi.org/10.1002/adf m.201300765

[32] Li X, Zhao T, Wang K, Yang Y, Wei J, Kang F, et al. Directly drawing self-assembled, porous, and monolithic Graphene fiber from chemical vapor deposition grown Graphene film and its electrochemical properties. Langmuir. 2011;**27**(19):12164-12171 https://doi.org/10.1021/la202380g

[33] Yun YJ, Hong WG, Kim W-J, Jun Y, Kim BH. A novel method for applying reduced Graphene oxide directly to electronic textiles from yarns to fabrics. Advanced Materials. 2013;**25**(40):5701-5705 https://doi.org/10.1002/adma .201303225

[34] Deshmukh, K., Basheer Ahamed, M., Deshmukh, R. R., Khadheer Pasha, S. K., Bhagat, P. R., & Chidambaram, K. (2017). 3 - Biopolymer Composites With High Dielectric Performance: Interface Engineering (K. K. Sadasivuni, D. Ponnamma, J. Kim, J.-J. Cabibihan, & M. A. B. T.-B. C. in E. AlMaadeed (eds.); pp. 27–128). Elsevier. https://doi.org/10.1016/B978-0-12-809261-3.00003-6

[35] Tang, L.-C., Zhao, L., Qiang, F., Wu, Q., Gong, L.-X., & Peng, J.-P. (2019). Chapter Twelve - Mechanical Properties of Rubber Nanocomposites Containing Carbon Nanofillers (S. Yaragalla, R. K. Mishra, S. Thomas, N. Kalarikkal, & H. J. B. T.-C.-B. N. and T. R. N. Maria (eds.); pp. 367–423). Elsevier. https://doi.org/10.1016/B978-0-12-817342-8.00012-3

[36] Vasudeo Rane, A., Kanny, K., Abitha, V. K., Patil, S. S., & Thomas, S. (2017). Chapter 4 - Clay–Polymer Composites: Design of Clay Polymer Nanocomposite by Mixing (K. Jlassi, M. M. Chehimi, & S. B. T.-C.-P. N. Thomas (eds.); pp. 113–144). Elsevier. https://doi.org/https://doi.org/10.1016/B978-0-323-46153-5.00004-5

[37] Chee WK, Lim HN, Huang NM, Harrison I. Nanocomposites of graphene/polymers: A review. RSC Advances. 2015;**5**(83):68014-68051 https://doi.org/10.1039/C5RA07989F

[38] Wang L, Yang Z, Cui Y, Wei B, Xu S, Sheng J, et al. Graphene-copper composite with micro-layered grains and ultrahigh strength. Scientific Reports. 2017;**7**(1):41896 https://doi.org/10.1038/srep41896

[39] Tang X-Z, Li X, Cao Z, Yang J, Wang H, Pu X, et al. Synthesis of graphene decorated with silver nanoparticles by simultaneous reduction of graphene oxide and silver ions with glucose. Carbon. 2013;**59**:93-99 https://doi.org/10.1016/j.carbon.2013.02.058

[40] Zeng X, Teng J, Tan A, Fu D, Zhang H. Fabrication of homogeneously dispersed graphene/Al composites by solution mixing and powder metallurgy. International Journal of Minerals, Metallurgy, and Materials. 2018;**25**:102-109 https://doi.org/10.1007/s12613-018-1552-4

[41] Li N, Cao M, Wu Q, Hu C. A facile one-step method to produce Ni/graphene nanocomposites and their application to the thermal decomposition of ammonium perchlorate. CrystEngComm. 2012;**14**(2):428-434 https://doi.org/10.1039/C1CE05858D

[42] Lu, Y., Dong, W., Ding, J., Wang, W., & Wang, A. (2019). 10 - Hydroxyapatite Nanomaterials: Synthesis, Properties, and Functional Applications. In A. Wang & W. B. T.-N. from C. M. Wang (Eds.), Micro and Nano Technologies (pp. 485–536).

Elsevier. https://doi.org/10.1016/B978-0-12-814533-3.00010-7

[43] Rezaei R, Deng C, Tavakoli-Anbaran H, Shariati M. Deformation twinning-mediated pseudoelasticity in metal–graphene nanolayered membrane. Philosophical Magazine Letters. 2016;**96**(8):322-329 https://doi.org/10.1080/09500839.2016.1216195

[44] Patil SJ, Kim JH, Lee DW. Graphene-nanosheet wrapped cobalt sulphide as a binder free hybrid electrode for asymmetric solid-state supercapacitor. Journal of Power Sources. 2017;**342**:652-665 https://doi.org/10.1016/j.jpowsour.2016.12.096

[45] Wang X, Lu M, Qiu L, Huang H, Li D, Wang H, et al. Graphene/titanium carbide composites prepared by sol–gel infiltration and spark plasma sintering. Ceramics International. 2016;**42**(1, Part A):122-131 https://doi.org/10.1016/j.ceramint.2015.08.017

[46] Sun C-L, Tang J-S, Brazeau N, Wu J-J, Ntais S, Yin C-W, et al. Particle size effects of sulfonated graphene supported Pt nanoparticles on ethanol electrooxidation. Electrochimica Acta. 2015;**162**:282-289 https://doi.org/10.1016/j.electacta.2014.12.099

[47] O'Hare, D. (2001). Hydrothermal Synthesis (K. H. J. Buschow, R. W. Cahn, M. C. Flemings, B. Ilschner, E. J. Kramer, S. Mahajan, & P. B. T.-E. of M. S. and T. Veyssière (eds.); pp. 3989–3992). Elsevier. https://doi.org/10.1016/B0-08-043152-6/00701-4

[48] Feng, S.-H., & Li, G.-H. (2017). Chapter 4 - Hydrothermal and Solvothermal Syntheses (R. Xu & Y. B. T.-M. I. S. C. (Second E. Xu (eds.); pp. 73–104). Elsevier. https://doi.org/10.1016/B978-0-444-63591-4.00004-5

[49] Byrappa, K., & Yoshimura, M. (2001). 2 - History of Hydrothermal Technology (K. Byrappa & M. B. T.-H.

of H. T. Yoshimura (eds.); pp. 53–81). William Andrew Publishing. https://doi.org/10.1016/B978-081551445-9.50003-9

[50] Li, A. D., & Liu, W. C. (2010). 4 - Optical properties of ferroelectric nanocrystal/polymer composites. In S. C. Tjong & Y.-W. B. T.-P. P. and A. of P. N. Mai (Eds.), Woodhead Publishing Series in Composites Science and Engineering (pp. 108–158). Woodhead Publishing. https://doi.org/10.1533/9780857090249.1.108

[51] Lee JS, You KH, Park CB. Highly photoactive, low bandgap TiO2 nanoparticles wrapped by graphene. Advanced Materials (Deerfield Beach, Fla.). 2012;**24**(8):1084-1088 https://doi.org/10.1002/adma.201104110

[52] Srivastava M, Das AK, Khanra P, Kim NH, Lee JH. A facile one-step hydrothermal synthesis of Graphene/CeO2 Nanocomposite and its catalytic properties. Advanced Materials Research. 2013;**747**:242-245 https://doi.org/10.4028/www.scientific.net/AMR.747.242

[53] Yang J, Zang C, Sun L, Zhao N, Cheng X. Synthesis of graphene/Ag nanocomposite with good dispersibility and electroconductibility via solvothermal method. Materials Chemistry and Physics. 2011;**129**(1):270-274 https://doi.org/10.1016/j.matchemphys.2011.04.002

[54] Zhang H, Ye Y, Li Z, Chen Y, Deng P, Li Y. Synthesis of Fe2O3–Ni(OH)2/graphene nanocomposite by one-step hydrothermal method for high-performance supercapacitor. Journal of Materials Science. 2016;**51**(6):2877-2885 https://doi.org/10.1007/s10853-015-9596-6

[55] Saravanakumar B, Mohan R, Kim S-J. Facile synthesis of graphene/ZnO nanocomposites by low temperature hydrothermal method. Materials Research Bulletin. 2013;**48**(2):878-883

https://doi.org/10.1016/j.materresb
ull.2012.11.048

[56] Abd.Khalim Khafidz, N. Z., Yaakob, Z., Lim, K. L., & Timmiati, S. N. (2016). The kinetics of lightweight solid-state hydrogen storage materials: A review. International Journal of Hydrogen Energy, 41(30), 13131–13151. https:// doi.org/10.1016/j.ijhydene.2016.05.169

[57] Chou K-C, Xu K. A new model for hydriding and dehydriding reactions in intermetallics. Intermetallics. 2007;**15** (5):767-777 https://doi.org/10.1016/j. intermet.2006.10.004

[58] Pang Y, Li Q. A review on kinetic models and corresponding analysis methods for hydrogen storage materials. International Journal of Hydrogen Energy. 2016;**41**(40):18072-18087 https://doi.org/10.1016/j.ijhydene .2016.08.018

[59] Booth F. A note on the theory of surface diffusion reactions. Transactions of the Faraday Society. 1948;**44**(0):796-801 https://doi.org/10.1039/ TF9484400796

[60] Carstensen JT. Stability of solids and solid dosage forms. Journal of Pharmaceutical Sciences. 1974;**63**(1):1-14 https://doi.org/10.1002/ jps.2600630103

[61] Crank 1916-, J. (John). (1975). The mathematics of diffusion/by J. Crank. Clarendon Press.

[62] Khawam A, Flanagan DR. Solid-state kinetic models: Basics and mathematical fundamentals. The Journal of Physical Chemistry B. 2006; **110**(35):17315-17328 https://doi.org/ 10.1021/jp062746a

[63] Koga N, Criado JM. Influence of the particle size distribution on the CRTA curves for the solid-state reactions of interface shrinkage type. Journal of Thermal Analysis. 1997;**49**(3):1477-

1484 https://doi.org/10.1007/ BF01983706

[64] Koga N, Criado JM. Kinetic analyses of solid-state reactions with a particle-size distribution. Journal of the American Ceramic Society. 1998;**81**(11): 2901-2909 https://doi.org/10.1111/ j.1151-2916.1998.tb02712.x

[65] Bösenberg U, Kim JW, Gosslar D, Eigen N, Jensen TR, Von Colbe JMB, et al. Role of additives in LiBH 4–MgH 2 reactive hydride composites for sorption kinetics. Acta Materialia. 2010;**58**(9): 3381-3389

[66] Jander W. Reaktionen im festen Zustande bei höheren Temperaturen. Reaktionsgeschwindigkeiten endotherm verlaufender Umsetzungen. Zeitschrift für Anorganische und Allgemeine Chemie. 1927;**163**(1):1-30 https://doi. org/10.1002/zaac.19271630102

[67] Shao H, Xin G, Zheng J, Li X, Akiba E. Nanotechnology in Mg-based materials for hydrogen storage. Nano Energy. 2012;**1**(4):590-601 https://doi. org/10.1016/j.nanoen.2012.05.005

[68] Ginstling A, B. B. (1950). Concerning the diffusion kinetics of reactions in spherical particles. Journal of Applied Chemistry, 23, 1327–1338.

[69] Chaudhary A-L, Sheppard DA, Paskevicius M, Pistidda C, Dornheim M, Buckley CE. Reaction kinetic behaviour with relation to crystallite/grain size dependency in the Mg–Si–H system. Acta Materialia. 2015;**95**:244-253 https:// doi.org/10.1016/j.actamat.2015.05.046

[70] Carter RE. Kinetic model for solid-state reactions. The Journal of Chemical Physics. 1967;**34**:2010-2015

[71] Shimada E, Yamashita H, Matsumoto S, Ikuma Y, Ichimura H. The oxidation kinetics of spherically shaped palladium powder. Journal of

Materials Science. 1999;**34**(16):4011-4015 https://doi.org/10.1023/A:1004655713727

[72] Valensi G. Kinetics of the oxidation of metallic spherules and powdersNo title. Compt Rend. 1936;**202**:309-312

[73] Avrami M. Kinetics of phase change III: Granulation, phase change, and microstructure. The Journal of Chemical Physics. 1941;**9**:177-184

[74] Avrami M. Kinetics of phase change. I general theory. The Journal of Chemical Physics. 1939;**7**(12):1103-1112 https://doi.org/10.1063/1.1750380

[75] Avrami M. Kinetics of phase change. II transformation-time relations for random distribution of nuclei. The Journal of Chemical Physics. 1940;**8**(2):212-224 https://doi.org/10.1063/1.1750631

[76] Johnson W.A., M. R. F. (1939). Reaction kinetics in processes of nucleation and growth. Transactions of AIME, 135, 396–415.

[77] Kolmogorov AN. On the statistical theory of the crystallization of metals. Bull Acad Sci USSR Math Ser. 1937;**1**:355-359

[78] Pang Y, Sun D, Gu Q, Chou K-C, Wang X, Li Q. Comprehensive determination of kinetic parameters in solid-state phase transitions: An extended Jonhson–Mehl–Avrami–Kolomogorov model with analytical solutions. Crystal Growth & Design. 2016;**16**(4):2404-2415 https://doi.org/10.1021/acs.cgd.6b00187

[79] Kempen ATW, Sommer F, Mittemeijer EJ. Determination and interpretation of isothermal and non-isothermal transformation kinetics; the effective activation energies in terms of nucleation and growth. Journal of Materials Science. 2002;**37**(7):1321-1332 https://doi.org/10.1023/A:1014556109351

[80] Christian, J. W. (2002). CHAPTER 10 - The Classical Theory of Nucleation (J. W. B. T.-T. T. of T. in M. and A. CHRISTIAN (ed.); pp. 422–479). Pergamon. https://doi.org/10.1016/B978-008044019-4/50014-3

[81] Liu F, Sommer F, Bos C, Mittemeijer EJ. Analysis of solid state phase transformation kinetics: Models and recipes. International Materials Reviews. 2007;**52**(4):193-212 https://doi.org/10.1179/174328007X160308

[82] Gross K.J., C. K. R. (2012). Recommended best practices for the characterization of storage properties of hydrogen storage materials.

Hydrogen Fuel Cell Implementation for the Transportation Sector

Rungsima Yeetsorn and Yaowaret Maiket

Abstract

Global transportation possesses have compelling rationales for reducing the consumption of oil, emissions of carbon dioxide, and noise pollution. Transitions to alternative transportation technologies such as electric vehicles (EVs) have gained increased attention from the automotive industries. A fuel cell electric vehicle (FCEV) occupying a hydrogen engine is one of the most stupendous technologies, since it is suitable for a large-scale transportation. However, its performance limitations are in question due to voltage degradation in long term operations through steady conditions under constant load and dynamic working conditions. Other drawbacks of using fuel cells in EVs are energy balances and management issues necessary for vehicle power and energy requirements. An efficient solution to accommodate driving behavior like dynamic loads comprises of hybridizing PEMFCs with energy storage devices like supercapacitors and batteries. This opening chapter reviews the projected gist of FCEV status; considers the factors that are going to affect how FCEVs could enter commercialization, including the importance of fuel cells for EV technologies; the degradation diagnoses using accelerated stress test (AST) procedures; FCEV hybridization; and the contribution of an energy storage device for charging EVs. The article also addresses case studies relating to material degradation occurring from driving behavior. Information about material degradation can be compiled into a database for the improvement of cell component performance and durability, leading to the creation of new materials and new fuel cell hybridization designs. To support the growth of EV technologies, an energy storage is required for the integrated alternative electricity generations. A redox flow battery is considered as a promising candidate in terms of attractive charging station for EVs or HEVs.

Keywords: electric vehicle, fuel cell technology, energy storage, fuel cell hybridization, accelerated stress test, flow battery technology

1. Introduction

1.1 New transportation interface

Leading automotive and energy executives from industries all around the world are looking at implementing strategies for promoting the use of electric vehicles and helping reduce oil consumption and climate-related emissions by trying to become

an industrial leadership position in advanced electric-drive and hybrid vehicle technologies. The environmental advantages of electric vehicles (EVs) compared to conventional internal combustion engine vehicle (ICEV) are overwhelming for the environment. The life cycle of a combustion engine relies heavily upon fossil fuels to generate the electricity it runs on, therefore emitting dangerous and harmful emissions during manufacturing. In comparison to ICEV, EVs have two superior technical features: better upstream energy source flexibility and higher vehicle efficiency [1]. The lower efficiency of ICEVs is due to friction losses, fuel pumping losses, transmission losses, and thermodynamic energy losses in the vehicle configuration. EVs should obtain highly efficient electric powertrains to evade these losses. In the scenario of utilizing alternative fuels, such as biofuels to reduce environmental problems, many countries may face supply limitations. EV deployment has been steadily rising over the past ten years, with the global stock of electric passenger cars achieving 5 million in 2018, an increase of 63% from 2017 [2]. According to the Global EV Outlook 2020, sales of EVs reached 2.1 million globally in 2019. The significant barriers for expected EV commercialization comprise of vehicle price, range, charge time, battery life uncertainty, electric generator durability, vehicle model availability, charging infrastructure, and awareness and understanding of the technology. EVs typically use one or more electric motors or traction motors for propulsion. They may be powered via a collector system by electricity from off-vehicle sources, or may be self-contained with an electric generator or energy storage device. Thus, they can be mainly categorized into two basic types of EVs all-electric vehicles (AEVs) and plug-in hybrid electric vehicles (PHEVs). If considered in details, EVs can be classified into five groups: Hybrid Electric Vehicle (HEV), Plug-in Hybrid Electric Vehicle (PHEV), Battery Electric Vehicle (BEV), Fuel Cell Electric Vehicle (FCEV), and Solar Electric Vehicle (SEV) [3].

1.2 Fuel cell electric vehicle

Among the different technologies of interest, the FCEVs containing hydrogen engines have been developed (**Figure 1**), mainly due to their high-power density, quick start-up and low operating temperatures. FCEVs use a fuel cell such as a proton exchange membrane fuel cell (PEMFC) or solid oxide fuel cells (SOFC) to convert the chemical energy in hydrogen and oxygen directly into electrical energy. Hydrogen is currently produced through many technologies either from non-fossil fuels or from fossil fuels. Examples of non-fossil fuel technologies are water electrolysis, thermolysis, thermochemical water splitting, and photonic process.
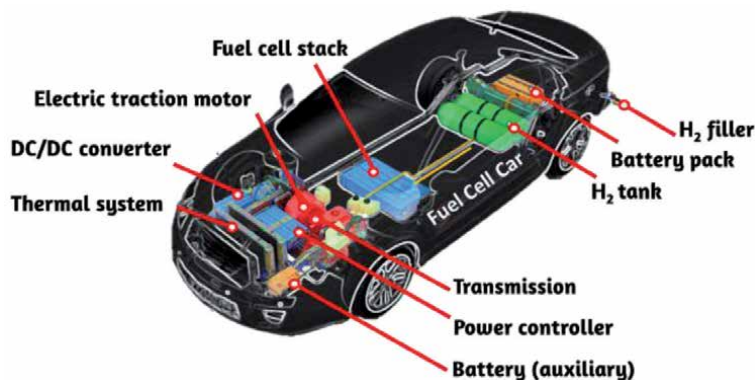
Figure 1.
Fuel cell electric vehicle configuration.

Fossil fuel technologies involve hydrocarbons reforming, these processes are carried out by methods such as steam reforming, auto-thermal, and partial oxidation [4]. FCEVs emphasized in this chapter are FCEVs that are using PEMFC as an electric generator. The dynamic response from driving behavior is one of the limitations for using PEMFC, especially if the system achieves a high load demand to acquire the desired speed ability. According to this situation the FC system would be unable to feed the fuel and oxidant in time, so "fuel and oxidant starvation" phenomenon would occur leading to materials degrading over time [5]. The auxiliary electrical source is one of solutions used to stabilize the electrical potential of the PEMFC system. Therefore, one part of this chapter discusses practical solutions to accommodate driving behavior via "Hybridization System". The missions of the hybridization system are relevant to the supply of traction power during PEMFC start-up, power assistance during driving cycles, regenerative braking energy recovery, the supply of electrical accessory loads, and PEMFC start-up and shutdown [6, 7]. An energy storage system such as a battery or a supercapacitor should be the preferred choice for the PEMFC hybridization system. A supercapacitor (SC) has interesting and effective functions such as its fast charge–discharge rate that can potentially support PEMFCs when they are operated under dynamic load demands [8]. Its fast responsiveness fulfills the power demand, rises the system power density and has to generate or absorb the power which either the PEMFC is not capable of generating or absorbing [9]. **Figure 2** indicates an example of PEMFC-SC hybridization. A supercapacitor offers transient power to PEMFC for attaining load demands in a short period. Moreover, the supercapacitor contributes advantages to PEMFC via capturing regenerative braking energy, enhancing fuel economy, providing a flexible operating strategy, overcoming PEMFC cold-start and transient shortfalls, and significantly lowering the cost per unit power [6].

Regarding transportation applications, the hybridization concept is not only applied for cars, but also for buses, trains, and tramways. The PEMFC-battery-supercapacitor hybridization was applied for electric trams [9] which possessed PEMFC for governing a stable operation. The battery offers a portion of the positive low frequency components of power demands which in turn decreases the responsibility of the PEMFC, and absorbs the slow-variation negative segments. The supercapacitor supplies the transient power demand effectively during sudden acceleration and braking.

The PEMFC performance investigations corresponding to driving behaviors will bring about information sustained to durability and lifetime of PEMFCs. Transportation applications require more than 5000 hours of PEMFC lifetime in order to be used under different circumstances [10]. This requirement results in
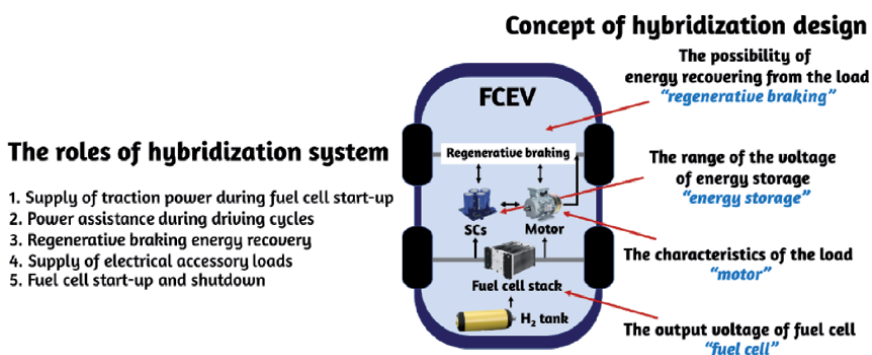
Figure 2.
Basic concept of PEMFC-SC hybridization.

time consuming and expensive methodology for experimental investigations. This chapter also provides information on the modification of Accelerated Stress Test (AST) created for exploring fuel cell degradation behavior and decreasing those restrictions [11].

Different driving behavior corresponds to various PEMFC operating conditions which can lead to numerous cases of PEMFC component degradation. For example, load cycling conditions such as voltage cycling, temperature cycling, and humidity cycling brings about membrane degradation; cracks, pinhole, and peroxide and hydrogen peroxide production [12]. These conditions also result in catalyst degradation such as Ostwald ripening of particles and sintering of particles [12]. If FCEV is driven at start-stop condition, PEMFCs will operate at high voltage, high temperature and low humidity [13, 14]. The detachment of catalyst particles from carbon support, Ostwald ripening of particles, sintering of particles, and dissolution of the catalyst can occur under start-stop circumstances [13, 14]. Evaluating and understanding material degradation and failure mechanisms through physical, chemical, and electrochemical analyses are important for material selection and fuel cell design. In terms of electrochemical analyses, electrochemical impedance spectroscopy (EIS) and cyclic voltammetry (CV) are preferable. EIS is applied for diagnosing behavior of PEMFC such as metal corrosion, electrode-electrolyte interface behavior, double-layer capacity, electrical properties of material and interfaces, and electrodeposition [15]. Morphological studies using Scanning Electron Microscopy (SEM) technique, Transmission Electron Microscopy (TEM), X-ray Diffraction (XRD) technique, and X-ray Photoelectron Spectroscopy (XPS) technique are proposed by scientists and engineers. This chapter presents case studies of material degradation occurring from driving behavior, since the information about the material degradation can be compiled into a database for the improvements of the cell component performance and durability, leading to the creation of new materials and new fuel cell hybridization designs.

1.3 EV charging station concept

Charging infrastructure and energy management are transforming in parallel with the growth in EV demand. The commercial success of the EV requires the development of an accessible charging infrastructure. Even though EVs do not produce the usual exhaust pipe emissions, main electricity utilized for EV charging systems is extensively generated from coal and natural gas that emits substantial CO_2 emissions. Even though electricity delivered for a charging system can be generated from renewable energy generators such as photovoltaic cells and wind turbines, these generators have weather-dependent issues. Weather and location play significant roles in how efficient a solution can be in regards to suppling generators. Integration of renewable energy sources, energy storage systems, and electrical vehicles with smart power distribution networks could be solution to this problem.

The type of battery mentioned in this article is a vanadium redox flow battery that captures energy generated from photovoltaic cells or wind turbines, this energy can be collect at one time and stored for use at a later time (**Figure 3**). Research works of literature focused on the abovementioned integrations include wind-PEM electrolyzer-hydrogen systems and solar-PEM electrolyzer-hydrogen systems [16]. In terms of FCEVs, hydrogen infrastructures are the most costly for many countries. Filling fuel of FCEV can be manipulated via charging stations and on-board PEMFC systems. This article would like to provide information of the stationary scenario. Hydrogen production using an integrated system between a redox flow battery and an electrolyzer is a remarkable new technology for FCEV fueling.
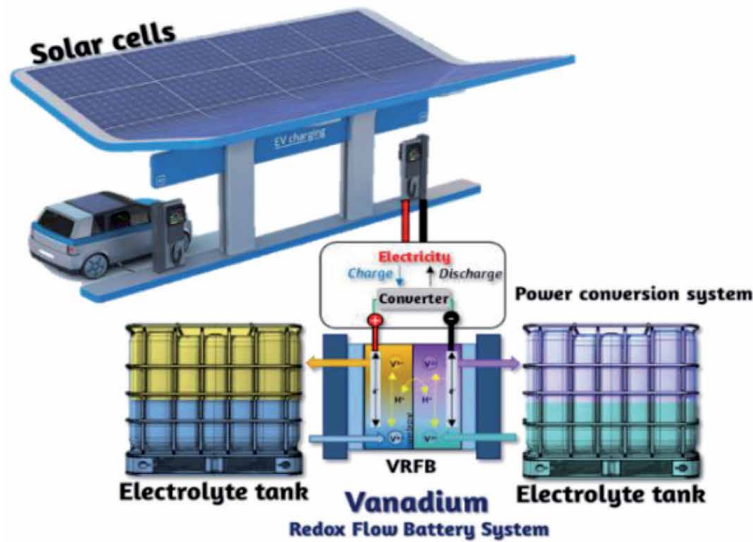
Figure 3.
Conceptual idea of using a redox flow battery for EV charging station.

It is possible to provide charging stations and hydrogen fueling stations in the same location. Prior to discussion about the contribution of an energy storage device for charging EVs, basic information of the redox flow battery is provided in the following statements. A redox flow battery technology is quite similar to PEMFC technology. The battery produces reduction and oxidation reactions between two active materials to capture and release energy. The redox flow battery system includes two external reservoirs for collecting soluble electroactive electrolytes, two electrodes, a membrane separator and a flow circulation system [17]. Flow batteries can be divided into three categories according to state of reactants such as all liquid phase, all solid phase, and hybrid redox flow batteries [17]. In a polymer electrolyte membrane electrolyzer is an electrolytic cell where water reacts at the anode to form oxygen and positively charge hydrogen ions. The applied electrons transfer through an external circuit, while the hydrogen ions selectively move across the PEM to the cathode. At the cathode side, hydrogen ions combine with electrons from the external circuit to form hydrogen gas [18]. Different types of electrolyzes consist of proton exchange membrane electrolyzer, alkaline electrolyzer, and solid oxide electrolyzer [18].

This chapter comprises of the following topics; the importance of fuel cells for EV technologies, the degradation diagnoses using accelerated stress test procedures, energy storage units integrated with fuel cells for the FCEV applications, and the contribution of an energy storage device for charging EVs. The authors expect to provide information related to hydrogen fuel cells for transportation prior to this technology becoming more frequent in daily life.

2. The importance of fuel cell for EV technologies

The EV market has witnessed rapid evolution with the ongoing developments in the transportation sector. The EVs market is projected to reach 35% of all globally vehicles by 2040 [19]. The factors impacting the market shares of this alternative advanced technology are retail price equivalent (RPE), energy cost per kilometer, range (kilometers between refuel/recharge events), maintenance cost (annual), fuel

availability, range limitation for battery electric vehicles (BEVs), public recharging availability, risk aversion, and diversity of make and model options available [20]. The principal factors affecting EV technology development relate to reliability, durability, efficiency, voltage losses, the current generation, power generation, and energy generation [21]. Reliability is defined as the ability of a product to perform the required function under stated conditions for a certain period of time [22]. Durability is the lifetime within the repair rate and cost of planned repairs, overhaul and maintenance [22]. Efficiency refers to the ratio between the useful energy output, which is the electrical energy produced, and the variation and energy input, which is the enthalpy of hydrogen [23]. Voltage losses are described as the voltage drop between standard voltage and real voltage [24].

2.1 Types of electric vehicles

In this sector five sorts of electric vehicles; HEV, PHEV, BEV, FCEV, and SEV, are discussed as follows:

- hybrid electric vehicle (HEV) which combines an internal combustion engine system with a hybrid vehicle drivetrain.

- plug-in hybrid electric vehicle (PHEV) is an HEV whose battery is recharged by plugging it into an external electricity source, as well as by its on-board engine and generator.

- battery electric vehicles completely consume chemical energy stored in rechargeable battery packs, without a secondary source of drivetrain.

- solar electric vehicle (SEV) powered exclusively by direct solar energy.

- fuel cell electric vehicle (FCEV) uses a fuel cell, sometimes in combination with a small battery or supercapacitor, to power its on-board electric motor.

Powertrain configurations of EVs are illustrated in **Figure 4**, and it indicates that an energy storage device is necessary for specific functions, for instance, demand response, transmission, flexible generation, improve operational practices and providing high energy density [25, 26].

Even if electric vehicles have more than their share of advantages, it is worth noting that they still have their drawbacks. It is imperative to recognize that EVs are usually changing and their technologies are evolving if considering EVs' pros and cons. HEV has an advantage in component availability, but it takes higher initial
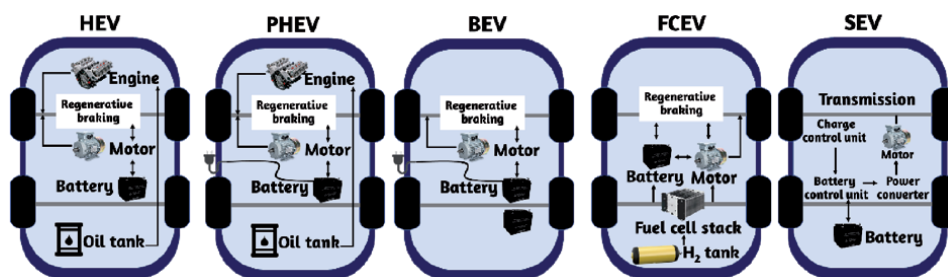
Figure 4.
The powertrain configurations of EVs.

cost. Furthermore, its two power trains build complexity of configurations and significant transmission energy loss. The characters of PHEV are similar to HEV, however, high cost of its batteries and battery replacement and added weight are taken into consideration. SEV does not have speed or power that regular cars have, and its operation is relevant to weather dependency. It seems likely that BEV is in the spotlight, nevertheless, there are some cons. It gives short distance range, while battery technology and public recharging infrastructure are needed to be improved these are the reasons that Toyota has long maintained that hydrogen fuel cell technology could be a zero-emission solution across a broad spectrum of vehicle types? Do FCEVs have a future?

Despite the development of hydrogen fuel cell cars started in 1966 with GM's Electrovan, they remain low in volume, expensive to produce, and restricted to sales in the few regions that have built hydrogen fueling stations. A big BEV manufacturer disagrees with this idea, and the CEO of the company described the fuel cell technology as a mind-bogglingly stupid technology. Why is Toyota still trying to make the fuel cell happen? Some scientists predicted that people would be able to drive FCEVs without any problems and to refuel 800 km of range in 2–3 minutes without any local emissions. BEVs maybe therefore only a temporary transitional technology.

Authors would like to provide readers with concise information that may help answer these questions. During PEMFC operations, hydrogen permeates through the anode via a bipolar plate and interacts with the catalyst for producing electrons and protons. The electrons are conducted via electrically conductive materials (catalyst, gas diffusion layers, bipolar plates, and current collectors) through an external circuit to the cathode, while the protons are simultaneously transferred via an ionic route through a polymer electrolyte membrane (Nafion membrane) to the cathode. At the cathode, oxygen permeates to the catalyst surface where it reacts with the protons and electrons with properly hydrated situations. Subsequently, the products of the fuel cell reactions are water, electricity and heat [27].

2.2 Filling fuel of FCEVs

FCEVs are charged using compressed hydrogen gas, and the hydrogen is drawn from an onboard tank and fuses it chemically with oxygen to create water. The BEV battery is recharged by connecting it to the electrical grid through a connector system. With 5 minutes for one tank filling, refuelling hydrogen is significantly faster than charging a BEV that is around 3 hours [28]. Additional 5 to 10 minutes are spent for a hydrogen pump to be ready for refuelling after a few refuelling operations until the fueling pressure is built up again. People have to drive FCEVs to a hydrogen gas station for refuelling, while BEV can be either charged at home or a station. As known. Hydrogen fuel stations are rare since construction costs of hydrogen stations are expensive. The costs are expected to be decreased via large-scale deployment and standardization. Moreover, a centralized control center for the hydrogen station is envisioned, accordingly dropping the operating costs.

Hydrogen production principally composes of 2 approaches; stream reforming and electrolysis [29]. Steam reforming is currently one of the most pervasive processes for hydrogen production. This technique gains advantages from high-efficiency production and low operational and production costs. Reactants used for the process are natural gas and lighter hydrocarbons, methanol, and other oxygenated hydrocarbons [30]. Electrolysis is a promising option for hydrogen production from a renewable resource such as water. The process uses electricity to split water into hydrogen and oxygen [30]. For charging the battery and fueling hydrogen via electrolytic cell, both come with energy and efficiency losses. In the case of BEV,

an electrical grid provides AC currents, while the batteries discharge DC currents. Quick charging efficiency is around 92%. If BEV runs with an AC motor, the inverter efficiency would be 90%. Also, a lithium-ion battery can lose energy due to current leakage, so a good estimate for charging a lithium-ion battery is about 90%. All these factors combined lead to 75–80% of total efficiency for charging BEV. In the case of FCEV, rectifier requires AC current from the electrical grid to drive the electrolysis, thus conversion efficiency would be about 92%. We also need to convert DC produced from fuel cell to power the AC motor with inverter efficiency 90%. Finally, the efficiency of the motor must be considered for both fuel cell and battery, currently around 90–95%. However, storage hydrogen into cylinder and transportation must be included for fuel cell efficiency losses. Once the hydrogen is produced and compressed into liquid or gas, available hydrogen infrastructure requires as hydrogen be able to be delivered from where it is produced to the point of end-use. Since hydrogen is exceedingly low density as a gas and liquid, to achieve satisfactory energy density, actual density must be increased. There are two choices, compressing and liquifying hydrogen, for increasing the density. Hydrogen can be compressed to 790 times atm pressure, but that takes energy nearby 13% of the total energy content of the hydrogen [29]. Hydrogen can be turned into liquid cryogenically. Hydrogen is liquified by decreasing its temperature to −253°C with 40% of an efficiency loss. The benefit of hydrogen liquefaction is that a cryogenic hydrogen cylinder is much lighter than a cylinder holding pressurized hydrogen. In conclude, pressurization is the better option for efficiency losses. Focusing on hydrogen transportation, hydrogen is being transported by truck or pipeline, where know energy loss from 10% up to 40%. In the worst case, the total efficiency of FCEV may be approximately 20%, while the BEV efficiency could be 56% [29]. Another weakness of FCEVs is the price per kg of hydrogen. The FCEV named Honda Clarity gets about 589 km with 5.5 kg of hydrogen, so that would cost about $0.14/km. In contrast, Tesla Model 3 (BEV) employs $0.03/km or $0.20/ kWh of energy. Noted, the information relates to the US hydrogen price in 2018 that was $15/kg.

2.3 The interesting things about FCEVs

The above data imply that FCEV is inferior to BEV, but FCEV might have its place. FCEV has key benefits; charging duration, electric range, energy density, and vehicle weight. In terms of electric range, FCEV seems to come out on top of BEV as same as charging duration. The electric range is the driving range of a vehicle using only power from its electric electricity supply to traverse a given driving cycle. In the case of an EVs, it means the total range per charge [31]. Current FCEVs have the electric range from 312 to 380 miles, whereas most of BEVs possess the range under 259 miles. From this benefit, 78% of automotive executive believe that FCEVs will be breakthrough for electric mobility. Increasing electric range requires a lot of batteries that will add the weight of the vehicles. At a certain point (350 miles of range) the additional battery weight no longer yields the additional range. For FCEVs, this battery weight compounding is not an issue, because they can be refueled less than 5 minutes. This case will occur when hydrogen fueling has good availability. Energy density is another important benefit of FCEVs. Hydrogen gives the energy density 39 kWh/kg, in contrast with batteries of 75 kWh extended range Tesla Model 3 providing the energy density around 0.2 kWh/kg [32]. Gasoline stocks up 13 kWh/kg. Adding an electric range of FCEVs can be done by simply increasing size if the hydrogen tank. For BEVs, that would mean an additional 100 kg of weight and $1000 in cost. In terms of specific energy of the FCEVs using compressed hydrogen, the specific energy is near 40,000 Wh/kg that differs from lithium-ion batteries having just 278 Wh/kg of specific energy. BEVs are suitable for

personal transportation, but current batteries can never replace gasoline applications as trucks, boats, airplanes, and trains. Considering energy density and specific energy, hydrogen very well could. In other words, FCEV is a potential solution for large scale transportation, and there are currently some interesting innovations and fuel cell products on the market worth taking [33]. For examples: Toshiba Energy Systems & Solutions Corporation announced that it has signed an agreement with New Energy and the Industrial Technology Development Organization (NEDO) for a multi-utility pure hydrogen fuel cell module for large modes of transport; the hydrogen train arrives in the Netherlands; hydrogen food retailer running in Norway; hydrogen truck in Japan [34]; Alstom (French manufacturer) plans to deliver 27 hydrogen fuel cell trains to subsidiary Fahma of regional public transport provider RMV in the central German state of Hesse by 2022, creating the world's largest fuel cell train fleet in passenger transport. Hydrogen fuel providers have invested in the expansion of hydrogen fuel production and distribution facilities to serve developing FCEV market, for instance, Germany aims to open hydrogen refueling stations by 2020, France is planning on opening renewable hydrogen station by 2020, and the UK wants to establish 100 hydrogen station by 2025 [34]. Is there adequate lithium to support the growth of BEV commercialization? BEVs and stationary storage revolutions are existing demand shooting up. If these revolutions occur, a hundred Gigafactory scenario may come true. The 13.5 million tons of reserves may be less than a 17-year supply.

As aforementioned, FCEVs should be developed for supporting an interface between the transport and the energy system. Therefore, basic knowledge and basic information of materials and applications of FCEVs should be comprehended. The U.S. Geological Survey produced a reserve estimate of lithium in early 2015, concluding that the world has enough known reserves for about 365 years of current global production of about 37,000 tons per year.

3. Degradation Diagnoses using Accelerated Stress Test (AST) Procedures

To analyze degradation data of the PEMFC components and system, the traditional observation of durability information involves the degradation data as a function of time. PEMFC typically show a continuing degradation in power output during their operations, and the cumulative influence of the gradual degradation is still acceptable. The degradation will be improper if the cumulative impacts of continuing degradation become too high. Regarding the characterizations, the modifications of accelerated stress test (AST) protocols have been created for diagnosing the PEMFC degradation behaviour to decrease those restrictions. ASTs are regularly created depending on a specific application, since the performed PEMFC degradations associate to the different cell components, the origins of the stresses, and their influences. Elevated temperature, reduced humidity, open-circuit voltage, and cycling conditions are the foremost accelerated factors ordinarily used for accelerated life diagnosing. The dynamic conditions consist of relative humidity (RH), temperature, potential, freeze/thaw, or start/stop [35]. The crucial conditions for transportation requirements are dynamic load cycling, startup-shutdown, and freeze–thaw [36].

The protocols were created to represent working behaviour in each application. The protocol can be divided into 2 sub-protocols such as static driving cycle and dynamic driving cycle. The Department of Energy (DOE) created the first protocol for the 2000-hour test. After that, the New European Drive Cycle (NEDC) was created, and it was created under the assumption of the European driving behaviour at

the maximum speed as 50 km/h (20 A) [37, 38]. In our previous work [39] driving protocol which is the combination of load cycling and start-stop behaviors was designed as presented in **Figure 5**. The proposed load cycling approach intended to accelerate the influences caused by the real operating conditions correlated to a generic dynamic load. The primitive concept was to design the AST protocol right on the real working conditions, assuming the load profile as the major degradation source. Thus, working conditions were accelerated stressing the real load cycles magnitude and frequency. To assure the similar degradation mechanisms the progress of the real load value was evaluated and kept during the accelerated cycle. The methodology allowed accomplishing the AST profile steady with the actual load dynamics, but amplified in magnitude and scaled in the time domain. Finally, the scaled cycles were repeated in a loop [39]. The profile of start-stop cyclic represented starting and shutting down a vehicle in a short time. At the starting situation, electrochemical reactions were speedily fed into the fuel cell to generate the desired power. On the other hand, the reactions were terminated by stopping the reactant supply.

This dynamic behaviour severely involved the operating condition changing that would cause material degradation. This created protocol presented an overview of ordinary approaches adopted in hybrid FCEV for power management, being the starting point for the load profile set-up for PEMFC operations [39].

The results of voltage degradation indicated that the voltage drop produced by load cycling gradually increased that corresponded to slowly operating condition differentiation. In contrast, the voltage degradation rate was significantly increased. This occurrence corresponded to the voltage lost in driving the chemical reaction at both on anode and cathode. The reduction of oxygen is a much slower reaction than the oxidation of hydrogen, therefore the system requires higher activation polarization, anode side losses can be neglected. This ageing regarded to damaging electrochemical surface areas of catalysts. The resistance to an electron flow through the electrically conductive PEMFC components and to an ion flow through the membrane caused a voltage drop as well. This loss generally happens in main components; bipolar plates, gas diffusion layers, catalyst, and membrane. The consumption of reactant gases at the catalyst layers leads to concentration
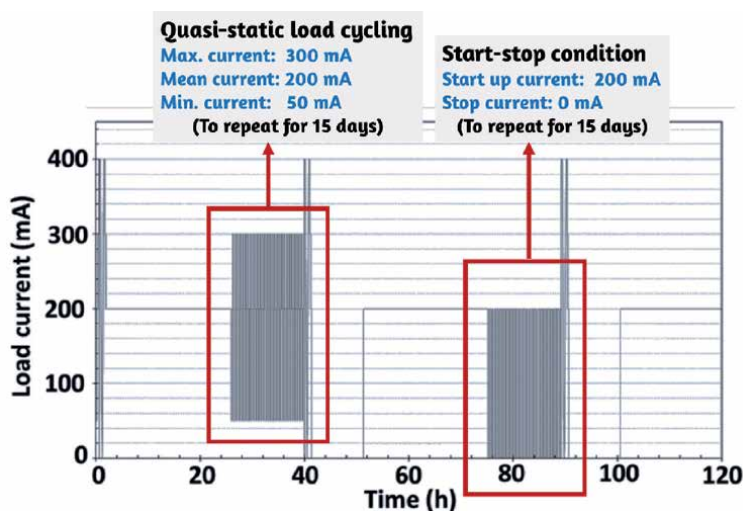
Figure 5.
The driving behaviors protocol [39].

gradients and the partial pressure of the reactants changing, affecting a decrease in fuel cell voltage [40]. **Figure 6** illustrates the case study of sudden load variation behaviour when the car speed varies from a low speed like driving to suddenly adding acceleration and overtaking cars in front. At high load demand, the system requires high power and voltage leading to high energy to drive electrochemical reactions thermodynamically. Under this situation system temperature increases significantly, while relative humidity decreases. This operating condition may result in membrane degradation; chemical and/or mechanical degradation [41]. In terms of chemical degradation, radicals such as peroxide or/and hydrogen peroxide radically react with the backbone of the membrane (Nafion: polytetrafluoroethylene). On the other hand, this reaction cannot occur if the backbone is not fluorinated [42–44].

The following mechanism, presented as Eqs. 1–3 [45], illustrates membrane damage where hydrofluoric acid was produced. **Figure 7** shows the morphological feature of a membrane electrode assembly (MEA) observed by scanning electron microscope and energy-dispersive X-ray (SEM–EDX) after 888 hours of operation duration. The investigated results found that the gas diffusion layer was dissolved by fluorine leaching, and the gas diffusion layer lost weight around 30.95%wt [46]. Small spots in **Figure 8** shows the catalyst removal from catalyst supports.
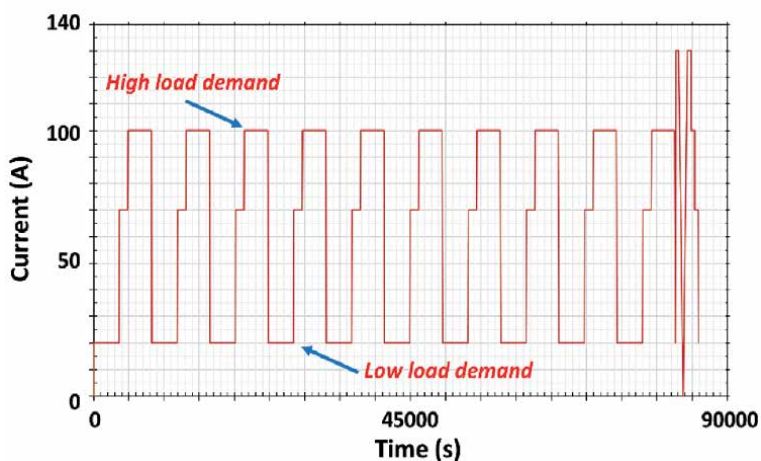
Figure 6.
The cyclic profile represents sudden load variation.
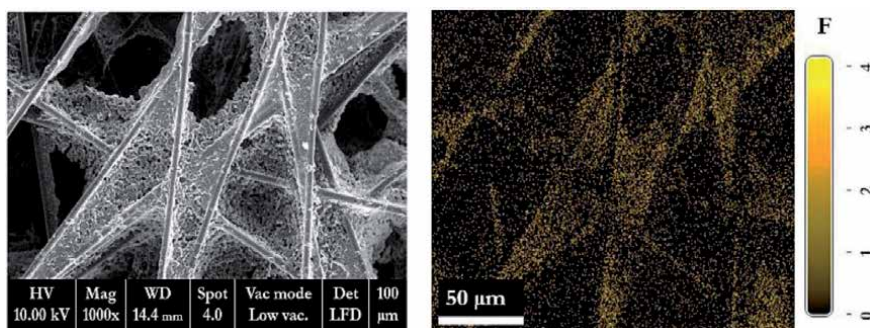
Figure 7.
SEM–EDX micrographs of gas diffusion layer damaged by hydrofluoric acid leaching.

Figure 8.
SEM–EDX micrograph of the catalyst layer on the PEMFC membrane.

Chemical degradation of the membrane [45]

$$R - CF_2COOH_2 + HO^* \rightarrow R - CF_2 + CO_2 + H_2O \tag{1}$$

$$R - CF_2^* + HO^* \rightarrow R - CF_2OH \rightarrow R - COF + HF \tag{2}$$

$$R - COFH + H_2O \rightarrow R - COOH + HF \tag{3}$$
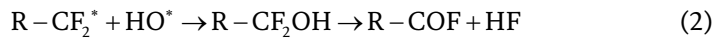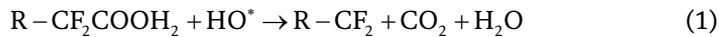
The relative humidity cycling related to load cyclic profile generated membrane swelling and shrinking. This phenomenon is associated with hydration state and operating temperature called mechanical degradation [27]. The postmortem analyses from the humidity cycling tests suggest that in-plane tensile membrane stresses result in cracks to initiate and propagate within the membranes in a subcritical fashion. Cyclic mechanical stresses cause if hydrophilic membranes are exposed to fluctuating hygrothermal conditions during the PEMFC operation [47]. Moreover, these phenomena may affect to catalyst degradation such as Ostwald ripening or sintering of catalyst particles. The Ostwald ripening appears from the thermodynamic driving force, while the sintering is caused by the reduction in surface energy with particle growth. The phenomenon leads to the dissolution of smaller particles and the growth of larger particles related to Eq. 4–6. In PEMFC, the platinum (Pt) transformation via a coupled process involving the transport of ions (Pt^{2+} and/or Pt^{4+}) through an ionomer/aqueous medium and a parallel (coupled) transport of electrons through the carbon support [48].

Pt dissolution reactions [49]

$$Pt \rightarrow Pt^{2+} + 2e - \quad (1.188\,V \text{ vs. RHE}) \tag{4}$$

$$Pt + H_2O \rightarrow PtO + 2H^+ + 2e^- \quad (0.980\,V \text{ vs. RHE}) \tag{5}$$

$$PtO + 2H^+ \rightarrow Pt^{2+} + H_2O + 2e^- \quad (0.208\,V \text{ vs. RHE}) \tag{6}$$
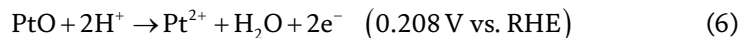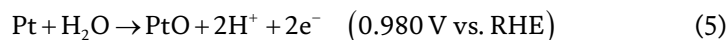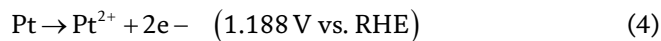
The catalyst degradation can be diagnosed via several techniques; electrochemical impedance spectroscopy (EIS) technique, cyclic voltammetry (CV) technique, SEM–EDX technique, and X-ray photoelectron spectroscopy (XPS). The investigated results from EIS explain the impact of ionic resistance, activation loss (relate to the loss of the electrochemical surface area), and mass transport losses [50]. The CV can be used to diagnose the evaluation of catalyst activity. With is analyzing, the counter and reference electrodes generally act as an anode side because the kinetics of the oxidation reaction is relatively fast. Working electrode acts as a cathode side

because the reduction reaction is a rate-determining step [51]. X-ray photoelectron spectroscopy (XPS) is a quantitative spectroscopic technique applied to characterize the surface chemistry of materials or to measure the elemental composition, empirical formula, chemical state, and electronic state of the elements existing in materials [51].

At low load demand in the sudden load variation, the system requires low voltage impacting slow reaction, so the system temperature decreases related to an increase in relative humidity. This operating condition causes a flooding phenomenon that can be studied via a hysteresis loop. The different voltage values from upward current testing and downward current testing in the hysteresis loop indicate accumulated water inside the PEMFC. The water flooding effects catalyst oxidation, reactant starvation, electro-osmosis, and back diffusion [52].

4. Why should energy storage unit be integrated with fuel cell for the FCEV application?

Although there are a lot of merits, PEMFCs are still not close to perfect. The major concern is relevant to performance and lifetime of the fuel cell. The performance of PEMFC is influenced by many internal and external factors, for instance fuel cell design and assembly, degradation of materials, operational conditions, and impurities [53]. Hybridization is one of solutions to reduce the problems. The hybridization in the energy sector can be categorized into four systems as follows:

- Hybridization between alternative energy and backup power unit, which is usually integrated with a high level to provide local energy security, is created to provide the intermittent availability of alternative energy sources.

- Hybridization between alternative primary sources, two or more alternative primary sources, is used to deliver complementary advantages.

- Hybridization between alternative energy and energy storage systems is the combination of energy storage with alternative energy. It is applied to ensure reliability and security of the distributed power generation system, while maximizing its benefit using alternative energy.

- Hybridization constructed with various types of energy storage devices is utilized for fast-dynamic storage devices and long-term storage devices [54].

In terms of transportation applications, PEMFC material suffers from closely random power load cycling such as the frequent start-up and shut-down [55]. An interesting approach to improve the efficiency and increase the lifetime of the PEMFC is to incorporate the new emerged energy storage, named Supercapacitor, in the system. A system that include several sources and/or energy storage devices is also known as hybrid system.

The concept of fuel cell-supercapacitor hybridization is quite new compared to the fuel cell-battery hybridization. The advantages of supercapacitors over the batteries are the higher number of charge/discharge cycles and the higher current rating. Once the supercapacitor is connected to the system, the stress due to the transient current were handled by the supercapacitor. There are many topologies of fuel cell-supercapacitor hybridization but most of them are connected together via various types of DC/DC converter. The very new concept of fuel cell/supercapacitor hybridization is to connect them directly together, this method is call

direct-hybridization [56–59]. This concept is very interesting because it is able to increase efficiency, lifetime and reduce the system cost due to the absence of the DC/DC converter, which has significant impact on system design. **Table 1** presents the crucial characteristics of a supercapacitor applied to the energy storage hybridization. The supercapacitor generates higher power than a battery does, and either charging or discharging time is faster than the ability of a battery. The fast charging and discharging characters can diminish materials degradation and PEMFC lifespan. Also, a supercapacitor can offer transient power to meet load demand in a short time. According to this advantage feature chemical kinetic energy can be recovered during regenerative braking occurring while the automobile is slowing down or stopping. The supercapacitor can also save energy and protect materials components inside PEMFCs from deterioration [60].

Supercapacitors in a FCEV operate with two features; charging electricity by PEMFC and discharging electricity to PEMFC. Once electrical current is charged into a supercapacitor, the positive charges of electrolyte move to a negative electrode using electrostatic force, and the negative charges of electrolyte transfers to the positive electrode. Supercapacitors are normally composed of three main structures; electrolytes, electrodes, and separators. Typically, the electrode of the supercapacitor is made from carbon particles due to they have high surface areas and high porosity required for collecting the charge. During charging duration [61], the charges transfer through the pores, and then they are stacked layer by layer as shown in **Figure 9**. On the other hand, a discharging process is an inversion operation of the charging step. Supercapacitors discharge electricity to load based on charge volume and voltage change over time leading to speedy response to load.

The powertrain configuration of the FCEV is usually comprised of supercapacitors connected with PEMFC. The supercapacitor and convertor can be directly connected with PEMFC. The supercapacitor can also be connected in parallel with PEMFC through energy converters. A converter is an electromechanical device

Characteristics	Supercapacitors	Batteries
Specific energy (Wh/kg)	1–10	100–265
Specific energy is defined as energy per unit mass. It is used to quantify.		
Specific power (W/kg)	500–10,000	300–1500
Specific power is a measure of performance for the system. It is defined as the power output by it divided by its mass.		
Cell voltage (V)	1.2–3.3	2.5–4.2
A voltage or electromotive force, is a quantitative expression of the potential difference in charge between two points in an electrical field.		
Capacitance (F)	0.1–12,000	—
Capacitance is the ability to store electrical energy.		
Discharge time	s-min	min-h
Discharge time is time to release electrical energy from device by a discharge.		
Charge time	s-min	min-h
Charging time is time to accumulate electrical energy from device by a charge.		
Charge/discharge efficiency (%)	85–98	90
Charge/discharge efficiency is indications of how much energy is put into or drained from a cell relative to the amount of energy that is dissipated within the cell as a result of its internal impedance.		

Table 1.
Characteristics of battery and supercapacitor for hybridization.

transforming a source of direct current (DC) from one voltage level to another. The energy converter functions as an energy collector storing generated energy. If the system quickly requires energy, the generated energy will be supplied by the converter. This connection feature makes the system more complex and expensive. A directly connected structure that a supercapacitor directly connects in parallel with PEMFC plays a role in self-energy management, therefore, the system requires an energy management design. This scenario can directly protect against rapid power variations that can increase the dynamics of the hybridization system. It is worth noting that a directly connected structure between PEMFC and supercapacitor, a supercapacitor is a necessity to be pre-charged before utilization to limit inrush current [62]. A hybrid system requires PEMFC as the main power source and supercapacitors as an auxiliary energy source. The supercapacitors assist the system to reduce voltage fluctuations at an unstable demand. The supercapacitor also stores electrical energy from PEMFC when there is excess energy. In contrast to this, the supercapacitor will supply power to PEMFC once the load demand is high. This system acquires less equipment, less sophistication, and provides higher effectiveness [63].

The noticeable data from investigation of supercapacitor effect on PEMFC-supercapacitor direct hybridization performance related to a driving behavior
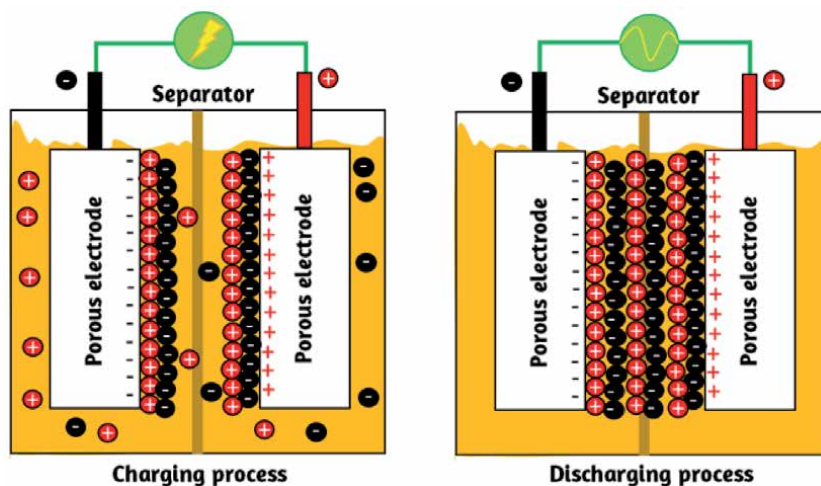
Figure 9.
The operations of a supercapacitor.
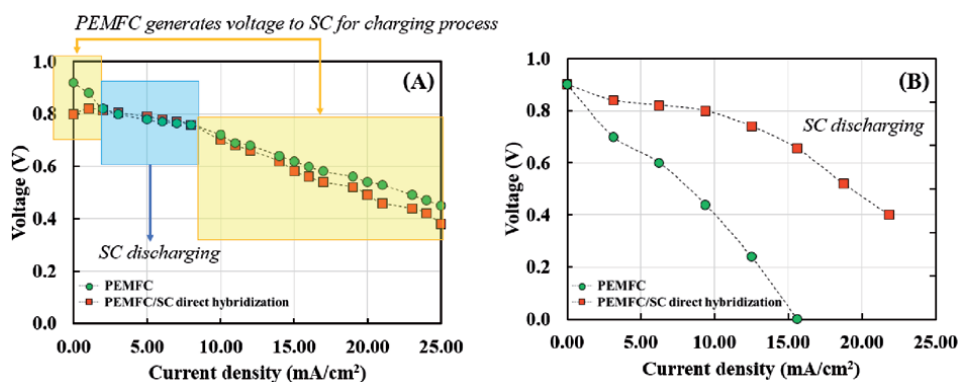
Figure 10.
The polarization curves of PEMFC and PEMFC-SC direct hybridization (A) non-charging supercapacitor (B) pre-charging supercapacitor at 0.90 V.

protocol are shown **Figure 10** [64]. Throughout the testing period, the PEMFC generates electricity to load demand and supercapacitor for charging process until the voltage level between PEMFC and supercapacitor are equivalent.

The curves in **Figure 10** can be separated into three transitions. In the first step of the test using a non-charging supercapacitor, the PEMFC charge electricity to load as indicated in low current density range (yellow area) until the electrical power of the PEMFC and supercapacitor is in the same level. Both of electrical providers supply electrical power to load demand in the second step. Due to supercapacitor properties, fast charging and discharging, the voltage of supercapacitor dramatically decreases observed in the third step. At this situation the voltage level of supercapacitor is lower than the one belongs to the PEMFC, thus, the PEMFC charges electricity to charge supercapacitor again. In pre-charging point of view, the voltage of PEMFC-SC direct hybridization is higher than PEMFC in all transition. It implies that the PEMFC and supercapacitor jointly supply electrical power to load demand. The supercapacitor assists the system to reduce voltage loss at high current density. The major voltage loss occurs from the mass transport [65].

5. The contribution of an energy storage device for charging EVs

It is estimated that over the next 15 years there will be more than a million electric vehicles in a small country as Thailand [66]. To reach this target both government and business sectors must provide infrastructure and technologies corresponding to technology for electric power supply within vehicles and electric vehicle charging station technology. Currently Thailand has 400 electric vehicle charging stations nationwide [67]. The acquisition of electric energy supplied for charging an electric vehicle is to connect a charging system through a meter to a transformer. If the EV demand grows significantly the share of electricity consumption from industrial and household sectors will be a serious issue. The EV driven 311 km requires approximately 40 kWh of energy which costs approximately 200 THB ($6.40) [68]. Thinking about 10,760,499 EVs in Bangkok, 430 million kWh, worth 2152 million baht per charge will be a requirement [69]. Using renewable energy sources to generate electricity for the charging system should give a positive effect on the country's energy security. Furthermore, an energy storage is needed for the integrated alternative electricity generation. The part aim to emphasize the information related to applying redox flow battery for the integrated charging system. Redox flow battery is considered as the most promising candidate in terms of its unlimited capacity, flexible security design and fast-response [70, 71]. In 2025, the forecast of rechargeable battery in the world expects to increase flow batteries using from 0.4% to 6.6%. Interesting properties of redox flow batteries are 85% of efficiency, 13,000 of cycle life, and 5–80 $/MWh•cycles of capital cost. The major costs of the redox flow battery are electrolyte solution at 37% and stack cell at 31% [72] (**Table 2**).

The priority performance of battery can be considered as following data.

Top power: Flow batteries > Lead acid > Li-ion > Electrolyzer.

The power of flow battery is defined by the size and number of cells.

Top energy: Flow batteries > Li-ion > Electrolyzer > Lead acid.

The energetic capacity is set by the amount of electrolyte stored in the reservoirs.

Discharge time: Flow battery > Electrolyzer > Lithium ion = Lead acid.

Round trip efficiency: Li-ion > Flow batteries > Lead acid > Electrolyzer.

Cycle life: Electrolyzer > Flow batteries > Li-ion > Lead acid.

Capital cost ($/MWh·cycles): Electrolyzer > Li-ion > Lead acid > Flow batteries.

Parameters	Technologies			
	Lead-acid	Li-ion	Electrolyzer/ Fuel cell	Redox flow battery
Top power (MW)	10–40	16	1	2–100
Top energy (MW h)	1–10	20	>10	6–120
Energy density (Wh/kg)	25–50	100–200	800–1300	10–50
Discharge time	1 h	1 h	> 1 h	1–10 h
Response time	ms	ms	ms	ms
Round-trip efficiency	75–85%	95%	35–45%	85%
Cycle life	3000	4000-8000	50,000	> > 13,000
Voltage	2	3.6	1.23	0.7–2.2
Energy cost (k$/kW)	200–400	500–2500	—	150–1000
Power cost ($/kWh)	300–600	175–400	—	600–1500
Capital cost ($/MWh·cycles)	150	150–200	200	<< 70

Table 2.
Performance of energy storage devices [72].

A conventionally single cell of the redox flow battery system consists of two external tanks storing electrolytes, electrodes both anode and cathode sides, a membrane separator, and pumps to generate circulation system. In a discharging process, the anolyte solution is fed in the anode side by the pump and electrolyte flow on bipolar. The electrolyte diffuses through the electrode and it occurs oxidation reaction creating electrons. The electrons move back from an electrode to a bipolar plate and take path around an electrical circuit from the anode side to cathode side. The charge-carrying species directly transfer from the anode to the cathode passing the ion-exchange membrane separating the anolyte and catholyte solution. The catholyte solution is fed in the cathode side, flows on the bipolar plate, and flows via a porous electrode occurring a reduction reaction where catholyte combines with the electron and proton. Once the flow battery is charged, a reduction takes place in the anolyte, while an oxidation is in the catholyte (**Figure 11**) [73, 74].

There are rational decisions for using redox flow battery as a generator in charging station as following examples. People mainly recharge vehicles between 7:00 to 9:00 am, and between 18:00 and 20:00 pm. Grid operators would not be capable to suppress peak power requirements without critically oversizing installed power. Supplement a battery to a fast charging station is a feasible approach to alleviate the oversizing installed power. This electric storage system acts as a buffer to decrease the peak power request on the network without increasing EV charging time [75]. In this situation, the redox flow battery charges installed power during low electricity demand periods to supply electricity for the fast charging. The redox flow battery possesses specific characteristics; ability to decouple rated power from rated capacity, good design flexibility, and nearly unrestricted life. Additionally, the liquid electrolyte contained in the redox flow battery system allowing their installation inside deactivated underground gas container located at gas stations. This installation method authorizes a transition of a conventional gas station to a commercial charging station [76, 77].
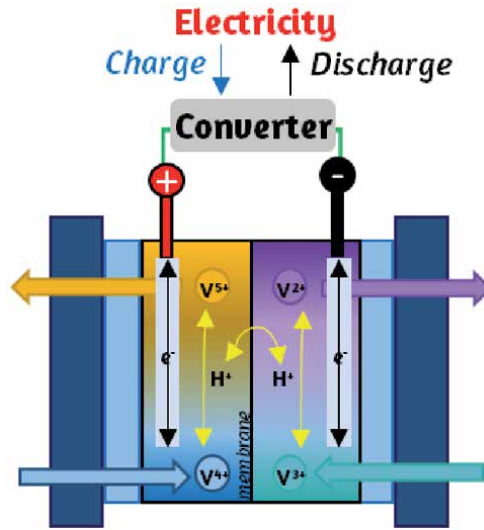
Figure 11.
The schematic diagram of a redox flow battery.
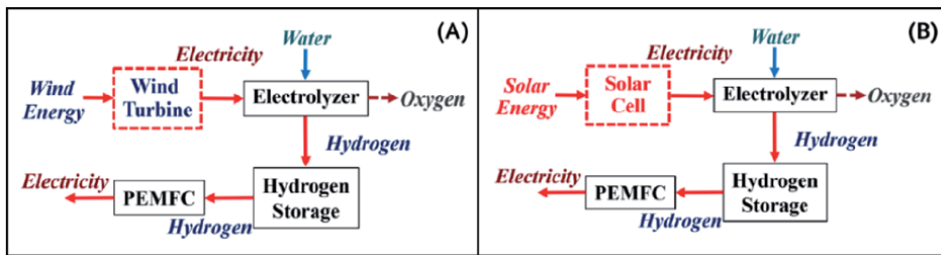
Figure 12.
(A) the overall process of electricity production initiated by a wind turbine. (B) the overall process of electricity generation initiated by a solar cell [79].

In terms of research related to a scaled-up vanadium redox flow battery for HEVs [78], it rapidly charged by electrolyte replacement making it attractive for charging EVs or HEVs. In the not so distant future, redox flow batteries will be useful for EVs, forklift truck, and golf-cart. EVs used for long journey distance may be conceivable if the infrastructure is in place. PEMFC can be another option for charging station when integrated system as primarily renewable source/electrolyzer/PEMFC is constructed. According to these two systems, the wind/PEM electrolyzer/ compressed hydrogen/PEMFC (**Figure 12 (A)**) generates 688.57 W of power. This generated power is significantly higher than the produced power of solar/PEM electrolyzer/ compressed hydrogen/PEMFC (262.37 W) (**Figure 12 (B)**).

Author details

Rungsima Yeetsorn[1]* and Yaowaret Maiket[2]

1 Department of Mechanical and Process Engineering, The Sirindhorn International Thai-German Graduate School of Engineering, King Mongkut's University of Technology North Bangkok, Bangkok, Thailand

2 Thai-French Innovation Institute, King Mongkut's University of Technology North Bangkok, Bangkok, Thailand

*Address all correspondence to: rungsima.y@tggs.kmutnb.ac.th

IntechOpen

References

[1] Lutsey, N. (2015). Transition to a global zero-emission vehicle fleet: A collaborative agenda for governments. 1

[2] IEA. (2019). Global EV Outlook 2019: Scaling up the transition to electric mobility.

[3] Mahmoudi, C., Flah, A., & Sbita, L. (2014, November). An overview of electric Vehicle concept and power management strategies. In 2014 International Conference on Electrical Sciences and Technologies in Maghreb (CISTEM) (pp. 1-8). IEEE.

[4] El-Shafie, M., Kambara, S., & Hayakawa, Y. (2019). Hydrogen production technologies overview. Journal of Power and Energy Engineering, 7(01), 107.

[5] Rodatz, P., Paganelli, G., Sciarretta, A., & Guzzella, L. (2005). Optimal power management of an experimental fuel cell/supercapacitor-powered hybrid vehicle. Control engineering practice, 13(1), 41-53.

[6] Sattler, G. (2000). Fuel cells going on-board. Journal of power sources, 86(1-2), 61-67.

[7] Feroldi, D., Serra, M., & Riera, J. (2009). Design and analysis of fuel-cell hybrid systems oriented to automotive applications. IEEE transactions on vehicular technology, 58(9), 4720-4729.

[8] Zhao, H., & Burke, A. F. (2010). Fuel cell powered vehicles using supercapacitors–device characteristics, control strategies, and simulation results. Fuel Cells, 10(5), 879-896.

[9] Li, Q., Yang, H., Han, Y., Li, M., & Chen, W. (2016). A state machine strategy based on droop control for an energy management system of PEMFC-battery-supercapacitor hybrid tramway.

International Journal of Hydrogen Energy, 41(36), 16148-16159.

[10] Fowler, M., Amphlett, J. C., Mann, R. F., Peppley, B. A., & Roberge, P. R. (2002). Issues associated with voltage degradation in a PEMFC. Journal of New Materials for Electrochemical Systems, 5(4), 255-262.

[11] Tian, T., Tang, J., Chen, Y., Tan, J., Li, S., & Pan, M. (2018). Study on accelerated stress test for fuel cell lifetime. Int. J. Electrochem. Sci, 13(2), 2022-2032.

[12] Madden, T., Perry, M., Protsailo, L., Gummalla, M., Burlatsky, S., Cipollini, N., ... & Jarvi, T. (2010). Proton exchange membrane fuel cell degradation: mechanisms and recent progress. Handbook of Fuel Cells.

[13] Borup, R., Meyers, J., Pivovar, B., Kim, Y. S., Mukundan, R., Garland, N., ... & Zelenay, P. (2007). Scientific aspects of polymer electrolyte fuel cell durability and degradation. Chemical reviews, 107(10), 3904-3951.

[14] Petrone, R., Yeetsorn, R., Harel, F., Hissel, D., Pera, M. C., Breaz, E., & Giurgea, S. (2017, December). Accelerated stress tests oriented load profile for PEM Fuel Cells durability in automotive applications. In 2017 IEEE Vehicle Power and Propulsion Conference (VPPC) (pp. 1-5). IEEE.

[15] Zhang, J., Wu, J., & Zhang, H. (2013). PEM fuel cell testing and diagnosis. Newnes.

[16] Yeetsorn, R., Prapainainar, C., & Maiket, Y. (2019). Energy Efficiency Evaluation Assessing Hydrogen Production, Energy Storage and Utilization in Integrated Alternative Energy Solutions. International Journal of Renewable Energy Research (IJRER), 9(4), 1957-1966.

[17] Leung, P., Li, X., De León, C. P., Berlouis, L., Low, C. J., & Walsh, F. C. (2012). Progress in redox flow batteries, remaining challenges and their applications in energy storage. Rsc Advances, 2(27), 10125-10156.

[18] Mohammadi, A., & Mehrpooya, M. (2018). A comprehensive review on coupling different types of electrolyzer to renewable energy sources. Energy, 158, 632-655.

[19] KPMG. (2020). Electric vehicles industry focus; Electric vehicles.

[20] National Research Council. (2013). Transitions to alternative vehicles and fuels. National Academies Press.

[21] Stevic, Z., & Radovanovic, I. (2012). Energy efficiency of electric vehicles. In New Generation of Electric Vehicles. InTech.

[22] Wang, J. (2017). System integration, durability and reliability of fuel cells: Challenges and solutions. Applied Energy, 189, 460-479.

[23] Alberto, Coralli, A., Sarruf, B., Miranda, P., Osmieri, L., Specchia, S., Minh, N. (2019). Fuel Cells. Science and Engineering of Hydrogen-Based Energy Technologies, 39-122.

[24] Arora, D., Gérardin, K., Raël, S., Bonnet, C., & Lapicque, F. (2018). Effect of supercapacitors directly hybridized with PEMFC on the component contribution and the performance of the system. Journal of Applied Electrochemistry, 48(6), 691-699.

[25] Mahmoudi, C., Flah, A., & Sbita, L. (2014, November). An overview of electric Vehicle concept and power management strategies. In 2014 International Conference on Electrical Sciences and Technologies in Maghreb (CISTEM) (pp. 1-8). IEEE.

[26] Paul, D., Ela, E., Kirby, B., & Milligan, M. (2010). The role of energy storage with renewable electricity generation. Technical report NREL/TP-6A2-47187. National Renewable Energy Laboratory, Golden, CO, USA.

[27] Voelcker, J. Why we still can't deliver on the promise of hydrogen cars [Internet]. 2020. Available from: https://www.thedrive.com/tech/33408/why-we-still-cant-deliver-on-the-promise-of-hydrogen-cars [Accessed: 2020-10-09]

[28] Two Bit da Vinci, Why Battery Electric Cars are Dominating Hydrogen Fuel Cell Cars [Internet]. 2018. Available from: https://www.youtube.com/watch?v=k7JRI UPhSJE&t=882s&ab_channel=TwoBitdaVinci [Accessed: 2020-10-09]

[29] Real Engineering, The truth about hydrogen [Internet]. 2018. Available from: https://www.youtube.com/watch?v=f7MzFfuNOtY&t=785s&ab_channel=RealEngineering [Accessed: 2020-10-09]

[30] Kalamaras, C. M., & Efstathiou, A. M. (2013). Hydrogen production technologies: current state and future developments. In Conference papers in energy (Vol. 2013). Hindawi.

[31] Thomas, C. E. (2009). Fuel cell and battery electric vehicles compared. international journal of hydrogen energy, 34(15), 6005-6020.

[32] Two Bit da Vinci, Why Battery Electric Cars are Dominating Hydrogen Fuel Cell Cars [Internet]. 2018. Available from: https://www.youtube.com/watch?v=k7JRI UPhSJE&t=882s&ab_channel=TwoBitdaVinci [Accessed: 2020-10-09]

[33] Undecided with Matt Ferrell, The truth about hydrogen fuel cell - a future beyond cars [Internet]. 2020. Available from: https://www.youtube.com/

watch?v=DTPt32 lZY30&t=394s&ab_
channel=UndecidedwithMattFerrell
[Accessed: 2020-10-09]

[34] FuelCellsWorks, Europe, News,
Research News [Internet]. 2020.
Available from: https://fuelcellsworks.
com/news/ [Accessed: 2020-03-06]

[35] Zatoń, M., Rozière, J., & Jones, D.
J. (2017). Current understanding of
chemical degradation mechanisms of
perfluorosulfonic acid membranes and
their mitigation strategies: a review.
Sustainable Energy & Fuels, 1(3),
409-438.

[36] Martins, L., Vasconcelos, G.,
Lourenço, P. B., & Palha, C. (2016).
Influence of the freeze-thaw cycles on
the physical and mechanical properties
of granites. Journal of Materials in Civil
Engineering, 28(5), 04015201.

[37] Borup, R., Meyers, J., Pivovar, B.,
Kim, Y. S., Mukundan, R., Garland,
N., ... & Zelenay, P. (2007). Scientific
aspects of polymer electrolyte fuel cell
durability and degradation. Chemical
reviews, 107(10), 3904-3951.

[38] Hwang, J. J., Hu, J. S., & Lin, C. H.
(2015). Design of a range extension
strategy for power decentralized
fuel cell/battery electric vehicles.
International Journal of Hydrogen
Energy, 40(35), 11704-11712.

[39] Petrone, R., Yeetsorn, R., Harel,
F., Hissel, D., Pera, M. C., Breaz, E.,
& Giurgea, S. (2017, December).
Accelerated stress tests oriented load
profile for PEM Fuel Cells durability
in automotive applications. In 2017
IEEE Vehicle Power and Propulsion
Conference (VPPC) (pp. 1-5). IEEE.

[40] Elia, G. (2015). Characterization
of voltage loss for proton exchange
membrane fuel cell (Bachelor's thesis,
Universitat Politècnica de Catalunya).

[41] Mbarek, S., El Kissi, N., Baccouch,
Z., & Iojoiu, C. (2019). Extrusion of
Nafion and Aquivion membranes:
environmentally friendly procedure and
good conductivities. Polymer Bulletin,
76(3), 1151-1166.

[42] Ishimoto, T., & Koyama, M.
(2012). A review of molecular-level
mechanism of membrane degradation
in the polymer electrolyte fuel cell.
Membranes, 2(3), 395-414.

[43] Collier, A., Wang, H., Yuan, X. Z.,
Zhang, J., & Wilkinson, D. P. (2006).
Degradation of polymer electrolyte
membranes. International Journal of
Hydrogen Energy, 31(13), 1838-1854.

[44] Madden, T., Perry, M., Protsailo,
L., Gummalla, M., Burlatsky, S.,
Cipollini, N., ... & Jarvi, T. (2010).
Proton exchange membrane fuel cell
degradation: mechanisms and recent
progress. Handbook of Fuel Cells.

[45] Kundu, S., Fowler, M., Simon, L. C.,
& Abouatallah, R. (2008). Reversible
and irreversible degradation in fuel cells
during open circuit voltage durability
testing. Journal of Power Sources,
182(1), 254-258.

[46] Yeetsorn, R., Maiket, Y., &
Kaewmanee, W. (2020). The
observation of supercapacitor
effects on PEMFC–supercapacitor
hybridization performance through
voltage degradation and electrochemical
processes. RSC Advances, 10(22),
13100-13111.

[47] Lai, Y. H., & Dillard, D. A. (2010).
Mechanical durability characterization
and modeling of ionomeric membranes.
Handbook of fuel cells.

[48] Parthasarathy, P., & Virkar, A.
V. (2013). Electrochemical Ostwald
ripening of Pt and Ag catalysts
supported on carbon. Journal of power
sources, 234, 82-90.

[49] Sasaki, K., Shao, M., & Adzic, R. (2009). Dissolution and stabilization of platinum in oxygen cathodes. In Polymer electrolyte fuel cell durability (pp. 7-27). Springer, New York, NY.

[50] Pivac, I., Bezmalinović, D., & Barbir, F. (2018). Catalyst degradation diagnostics of proton exchange membrane fuel cells using electrochemical impedance spectroscopy. International Journal of Hydrogen Energy, 43(29), 13512-13520.

[51] Zhang, J., Wu, J., & Zhang, H. (2013). PEM fuel cell testing and diagnosis. Newnes.

[52] Maiket, Y., Yeetsorn, R., Kaewmanee, W., & Hissel, D. (2018). Investigating performance and voltage degradation of PEMFC/supercapacitor direct hybridization system. In Grand Renewable Energy proceedings Japan council for Renewable Energy (2018) (p. 220). Japan Council for Renewable Energy.

[53] Bharath, K. V. S., Blaabjerg, F., Haque, A., & Khan, M. A. (2020). Model-Based Data Driven Approach for Fault Identification in Proton Exchange Membrane Fuel Cell. Energies, 13(12), 3144.

[54] Tabanjat, A. (2015). Modelling, control and supervision of multi-source system connected to the network with a buffer storage of electrical energy via hydrogen vector (Doctoral dissertation).

[55] Kocha, S. S. (2013). Polymer electrolyte membrane (PEM) fuel cells, automotive applications. In Fuel Cells (pp. 473-518). Springer, New York, NY.

[56] Zhan, Y., Guo, Y., Zhu, J., & Li, L. (2015). Power and energy management of grid/PEMFC/battery/supercapacitor hybrid power sources for UPS applications. International Journal of Electrical Power & Energy Systems, 67, 598-612.

[57] Benyahia, N., Denoun, H., Zaouia, M., Rekioua, T., & Benamrouche, N. (2015). Power system simulation of fuel cell and supercapacitor based electric vehicle using an interleaving technique. international journal of hydrogen energy, 40(45), 15806-15814.

[58] Kim, B. H., Kwon, O. J., Song, J. S., Cheon, S. H., & Oh, B. S. (2014). The characteristics of regenerative energy for PEMFC hybrid system with additional generator. International journal of hydrogen energy, 39(19), 10208-10215.

[59] Thounthong, P., Rael, S., & Davat, B. (2009). Energy management of fuel cell/battery/supercapacitor hybrid power source for vehicle applications. Journal of Power Sources, 193(1), 376-385.

[60] Rodat, S., Sailler, S., Druart, F., Thivel, P. X., Bultel, Y., & Ozil, P. (2010). EIS measurements in the diagnosis of the environment within a PEMFC stack. Journal of Applied Electrochemistry, 40(5), 911-920.

[61] Moussa, M., El-Kady, M. F., Zhao, Z., Majewski, P., & Ma, J. (2016). Recent progress and performance evaluation for polyaniline/graphene nanocomposites as supercapacitor electrodes. Nanotechnology, 27(44), 442001.

[62] Morin, B., Van Laethem, D., Turpin, C., Rallières, O., Astier, S., Jaafar, A., ... & Chaudron, V. (2014). Direct hybridization fuel cell–ultracapacitors. Fuel Cells, 14(3), 500-507.

[63] Zhao, H., & Burke, A. F. (2010). Fuel cell powered vehicles using supercapacitors–device characteristics, control strategies, and simulation results. Fuel Cells, 10(5), 879-896.

[64] Yeetsorn, R., Maiket, Y., & Kaewmanee, W. (2020). The observation of supercapacitor effects on PEMFC–supercapacitor hybridization performance through voltage degradation and electrochemical processes. RSC Advances, 10(22), 13100-13111.

[65] Elia, G. (2015). Characterization of voltage loss for proton exchange membrane fuel cell (Bachelor's thesis, Universitat Politècnica de Catalunya).

[66] KPMG. (2020). Electric vehicles industry focus; Electric vehicles.

[67] The nation Thailand, it's easy to find an EV charging station in Thailand [Internet]. 2019. Available from: https://www.nationthailand.com/auto/30372650 [Accessed: 2020-10-25]

[68] Doodenstudio, [Internet]. 2019. Available from: https://www.youtube.com/watch?v=TrPNREEE3XU [Accessed: 2020-04-04]

[69] Transport Statistics Sub, [Internet]. 2020. Available from: https://web.dlt.go.th/statistics/ [Accessed: 2020-04-04]

[70] Kim, K. H., & Kim, B. G. (2014). Development of carbon composite bipolar plate (BP) for vanadium redox flow battery (VRFB). Composite Structures, 109, 253-259.

[71] Moore, M., Counce, R., Watson, J., & Zawodzinski, T. (2015). A comparison of the capital costs of a vanadium redox-flow battery and a regenerative hydrogen-vanadium fuel cell. Journal of Advanced Chemical Engineering, 5(4).

[72] Alotto, P., Guarnieri, M., & Moro, F. (2014). Redox flow batteries for the storage of renewable energy: A review. Renewable and Sustainable Energy Reviews, 29, 325-335.

[73] Weber, A. Z., Mench, M. M., Meyers, J. P., Ross, P. N., Gostick,

J. T., & Liu, Q. (2011). Redox flow batteries: a review. Journal of applied electrochemistry, 41(10), 1137.

[74] Blanc, C., & Rufer, A. (2010). Understanding the vanadium redox flow batteries (No. BOOK_CHAP, pp. Chapter-18). Shanghai: InTech.

[75] De Simone, D., & Piegari, L. (2019). Integration of Stationary Batteries for Fast Charge EV Charging Stations. Energies, 12(24), 4638.

[76] Cunha, Á., Brito, F. P., Martins, J., Rodrigues, N., Monteiro, V., Afonso, J. L., & Ferreira, P. (2016). Assessment of the use of vanadium redox flow batteries for energy storage and fast charging of electric vehicles in gas stations. Energy, 115, 1478-1494.

[77] Cunha, Á., Martins, J., Brito, F. P., Rodrigues, N., Monteiro, V. D. F., & Afonso, J. L. (2015). Using vanadium redox flow batteries for the electricity storage towards the electric vehicles fast charging process.

[78] Mohamed, M. R., Sharkh, S. M., & Walsh, F. C. (2009, September). Redox flow batteries for hybrid electric vehicles: Progress and challenges. In 2009 IEEE Vehicle Power and Propulsion Conference (pp. 551-557). IEEE.

[79] Yeetsorn, R., Prapainainar, C., & Maiket, Y. (2019). Energy Efficiency Evaluation Assessing Hydrogen Production, Energy Storage and Utilization in Integrated Alternative Energy Solutions. International Journal of Renewable Energy Research (IJRER), 9(4), 1957-1966.

Quantum Calculations to Estimate the Heat of Hydrogenation Theoretically

Ali Amir Khairbek

Abstract

Standard enthalpies of hydrogenation of 29 unsaturated hydrocarbon compounds were calculated in the gas phase by CCSD(T) theory with complete basis set cc-pVXZ, where X = DZ, TZ, as well as by complete basis set limit extrapolation. Geometries of reactants and products were optimized at the M06-2X/6-31g(d) level. This M06-2X geometries were used in the CCSD(T)/cc-pVXZ//M06-2X/6-31g (d) and cc-pV(DT)Z extrapolation calculations. (MAD) the mean absolute deviations of the enthalpies of hydrogenation between the calculated and experimental results that range from 8.8 to 3.4 kJ mol^{-1} based on the Comparison between the calculation at CCSD(T) and experimental results. The MAD value has improved and decreased to 1.5 kJ mol^{-1} after using complete basis set limit extrapolation. The deviations of the experimental values are located inside the "chemical accuracy" (± 1 kcal mol$^{-1} \approx \pm 4.2$ kJ mol^{-1}) as some results showed. A very good linear correlations between experimental and calculated enthalpies of hydro-genation have been obtained at CCSD(T)/cc-pVTZ//M06-2X/6-31g(d) level and CCSD (T)/cc-pV(DT)Z extrapolation levels (SD =2.11 and 2.12 kJ mol^{-1}, respectively).

Keywords: complete basis set (CBS), density functional theory (DFT), CCSD (T), extrapolated method, molecules, energy, enthalpy, hydrocarbons

1. Introduction

The calculation of enthalpies of formation for the large unsaturated molecules, some of which are not included in the practical range of combustion thermochemistry, based on quantum mechanical first principles which have been possible basing on the recent important advances in computational chemistry. Necessary, Quantum mechanical calculations of molecular thermochemical properties are approximate. Approximations may be employed by the Composite quantum mechanical procedures at each of several computational steps and in the same time it may have an empirical factor to correct the cumulative error. When the error of the various approximations is known within narrow limits, but the question about the accuracy of the "known" value is noticed immediately because the uncertainty of the comparison between the approximate quantum mechanical result and the standard to which it is compared.

The most correct quantum mechanical procedure is been established after its ability to reproduce various accurate experimental results to calculate unknown

thermochemical values of explosive compounds or unstable, unsuited to classical thermochemical methods, or to calculate thermochemical properties of radicals, molecules, or ions of fleeting existence [1–15]. Here where a major advantage to create the accuracy of inherent hydrogen thermochemical results lies, and it works for encouraging and renewing interest in the diverse literature devoted to hydrogen thermochemistry.

The main part of the quantum chemistry is contended in the total electronic energy of a molecule. And this total electronic energy is a function of the nuclear geometric configuration after Born-Oppenheimer separation of electronic and nuclear motion, therefore generating hyper surfaces of potential energy–for electronically excited states as well as for the ground state.

At the end of this work a very important fact is clear now which clarify that wave function-based quantum-chemical methods can produce molecular electronic energies with an accuracy that surpasses that of experimental measurements of molecular energies (in terms of enthalpies of formation).

An important feature of the wavefunction-based quantum-chemical methodology is the ability to access the exact characterizing of the molecular electronic structure in a systematic manner. To achieve systematic approach two basic steps have been taken, the first step using advanced hierarchy of wavefunction models and the second step using systematic sequence of basis sets – or a nearly complete basis set – of atomic orbitals.

2. Basis-set convergence

It is noted that the type of wavefunction model used, or density functional, plays an important role in determining accuracy of computed molecular_electronic energies. In addition to the important role played by the flexibility of the one electron basis set of atomic orbitals (AOs) by which the molecular orbitals (MOs) are expanded. It is worth noting that Slater's determinants are constructed using MOs for use in Kohn - Sham theory or to expand the n-electron wavefunction.

Different ways can be chosen from basis sets of AOs (the literature [16–18]). As for the approach followed in study of molecular electronic-structure based on wavefunction methods, a well-defined procedure must have been used in order to generating sequences of the basis sets in order to increase flexibility. This way is very useful by generating hierarchies for basis sets, Each next higher level describes an improved systematically of the molecular electronic structure compared to the next lower level. Within the hierarchy the calculated results converge within a prescribed accuracy, and then the basis-set hierarchy ends up effectively complete basis [16]. Therein lies the problem where approaches of wavefunction that depend on the electron-correlation effects of the convergence to an effectively complete basis are very slow. When increasing the number N of AOs in the basis according to an optimal manner, it reduces the basis-set error as $\propto N^{-1}$, thus obtaining a good approximation. It is often noticed that the accuracy of the electronic correlation calculations is limited by computational technical constraints. This is due to computing times growing at least as N4 and the computational effort grows more quickly compared to gain in accuracy.

2.1 Correlation-consistent basis sets

The correlation-consistent basis sets from Dunning and his co-workers [19, 20] represent a popular hierarchy of basis sets. When the valence orbitals are

correlated in a calculations only then can the expansion mainly in the Limit extrapolation, until it ends to an effectively complete basis [21–26]. The term X-tuple zeta basis sets represents to correlation-consistent polarized valence, denoted by cc-pVXZ, and is used in the calculations of this work, where X = D, T, (double, triple zeta). It should be noted that when all the electrons are correlated (core as well as valence orbitals), the cc-pCVXZ basis sets must be used provided $2 \leq X \leq 5$.

Reactions	$\Delta_{hyd}H^0_{298}$ (exp .)
Ethyne +2 H$_2$ → ethane	−312.0 ± 0.63
Ethene + H$_2$ → ethane	−136.3 ± 0.3
Propadiene +2 H$_2$ → propane	−295.1 ± 0.1
Prop-1-yne + 2 H$_2$ → propane	−289.6 ± 0.63
Prop-1-ene + H$_2$ → propane	−125.0 ± 0.42
But-2-yne + 2 H$_2$ → butane	−272.4 ± 1.3
Isobutene + H$_2$ → isobutane	−117.8 ± 0.42
(2E)-but-2-ene + H$_2$ → butane	−118.5 ± 0.42
(2Z)-but-2-ene + H$_2$ → butane	−114.6 ± 0.42
(2E)-pent-2-ene + H$_2$ → pentane	−113.8 ± 0.8
(2Z)-pent-2-ene + H$_2$ → pentane	−117.7 ± 0.8
2-Methylbut-1-ene + H$_2$ → 2-methylbutane	−118.2 ± 0.42
2-Methylbut-2-ene + H$_2$ → 2-methylbutane	−111.6 ± 0.3
3-Methylbut-1-ene + H$_2$ → 2-methylbutane	−126.3 ± 0.3
Cyclopenta-1,3-diene +2 H$_2$ → cyclopentane	−210.8 ± 0.84
Hex-1,5-diene +2 H$_2$ → hexane	−251.2 ± 0.42
Hex-1-ene + H$_2$ → hexane	−126.0 ± 2.0
2,3-Dimethylbuta-1,3-diene +2 H$_2$ → 2,3-dimethylbutane	−223.4 ± 0.63
2,3-Dimethylbuta-1-ene + H$_2$ → 2,3-dimethylbutane	−116.1 ± 0.4
2,3-Dimethylbuta-2-ene + H$_2$ → 2,3-dimethylbutane	−110.4 ± 0.42
3,3-Dimethylbuta-1-ene + H$_2$ → 2,2-dimethylbutane	−125.9 ± 0.63
Benzene +3 H$_2$ → cyclohexane	−205.3 ± 0.6
Cyclohexa-1,3-diene +2 H$_2$ → cyclohexane	−229.6 ± 0.42
Cyclohexene + H$_2$ → cyclohexane	−118.6 ± 0.42
Hept-1-ene + H$_2$ → heptane	−125.1 ± 0.3
4,4-Dimethylpent-1-ene + H$_2$ → 2,2-dimethylpentane	−122.5 ± 0.42
Cyclohepta-1,3,5-triene +3 H$_2$ → cycloheptane	−301.7 ± 1.3
Cyclohepta-1,3-diene +2 H$_2$ → cycloheptane	−212.4 ± 0.63
Cycloheptene + H$_2$ → cycloheptane	−108.9 ± 0.63

NIST - JANAF thermochemical tables, Ref. [33]

Table 1.
Experimental values of hydrogenation enthalpy of some unsaturated hydrocarbons in the gas phase (in kJ Mol^{-1}).

2.2 Basis-set extrapolation

The correlation-consistent basis sets form a basis-set hierarchy well suited for complete basis-set limit extrapolations of the correlation-energy. Then the correlation energy can have been determined depending on X when $X \rightarrow \infty$.

In 1977, 27 formulas for two-point linear extrapolation were introduced by Helgaker et al. [27] via the basis sets cc-pCVXZ and cc-pCVYZ, the electron-correlation energies and are computed E_X and E_Y, and the $C_{XY} = X^3/(X^3 Y^3)$ coefficient is determined in Eq. (1),

$$E_{XY} = (E_X X^3 - E_Y Y^3)/(X^3 - Y^3) = C_{XY} E_X + (1 - C_{XY}) E_Y \qquad (1)$$

The EX correlation energy can be recovered in correlation-consistent basis of cc-pVXZ via the Eq. (2), When performing calculations according to the basis sets, cc-pVXZ and cc-pVYZ, two equations with two unknowns are obtained, *a* and *E*, whose Solving leads to Eq. (2), with that in mind $E = E_{XY}$

$$E_X = E_\infty + aX^3 \qquad (2)$$

Note that through experience [28–32] that the best estimate of complete basis set limit extrapolation is by using two consecutive basis set when X = Y - 1, for example the pair cc-pCVDZ/cc-pCVTZ, and so on).

The level at which the results were obtained by extrapolation is denoted by cc-pCV(XY)Z, where XY = DT, TQ, and so forth. It is only at this level that the correlation energy is extrapolated.

The CCSD(T)/cc-pV(XY)Z extrapolation will be applied to obtain estimates of the basis-set limit of corrections for M06-2X/6-31g(d) level of theory by calculations of hydrogenation enthalpies of some unsaturated hydrocarbon compounds (**Table 1**).

In Section 3, we shall describe the methods used, the molecular equilibrium geometries, and the basis sets. Results will be shown in Section 3.2, including molecular electronic energies, enthalpies of hydrogenation, and statistical analysis of the computational results.

3. Computational details

3.1 Computational methods

Electronic energies were computed by the density-functional (M06-2X) [34] approach with 6-31g(d) basis set. The M06-2X/6-31g(d) equilibrium geometries of the reactants and products was optimized with the Gaussian 09 program [35]. All CCSD(T)/cc-pV(DT)Z calculations were performed at fixed molecular equilibrium geometries that were optimized at the M06-2X/6-31g(d) level can be found in supporting information.

3.2 Results and discussion

3.2.1 Nonrelativistic electronic energies

The total electronic M06-2X/6-31g(d) energies, H_{corr}, G_{corr}, and the zero-point vibrational energies (ZPE) are reported in **Table 2**, while **Table 3** shows CCSD

Compounds	M06-2X/6-3g(d)			
	E_o	H_{corr}	G_{corr}	*ZPE*
H$_2$	−1.1635655	0.013609	−0.001167	0.010304
Ethane	−79.771814	0.080116	0.054255	0.075684
Ethyne	−77.287772	0.031118	0.008428	0.027383
Ethene	−78.536836	0.055732	0.030890	0.051757
Propane	−119.064602	0.110657	0.080306	0.105246
Propadiene	−116.591917	0.060782	0.033335	0.056103
Prop-1-yne	−116.591781	0.061355	0.033375	0.056509
Prop-1-ene	−117.834775	0.085736	0.055653	0.080695
Cis- butane	−158.357373	0.140439	0.106229	0.133684
But-2-yne	−155.894141	0.091157	0.060488	0.085379
Isobutene	−158.359492	0.139891	0.105558	0.133229
Isobutane	−157.133592	0.115796	0.083003	0.109592
Trans-butane	−158.356612	0.140562	0.106344	0.133858
(2E)-but-2-ene	−157.132136	0.116000	0.083013	0.109658
(2Z)-but-2-ene	−157.130271	0.115947	0.081911	0.109398
pentane	−197.650150	0.171137	0.133095	0.163224
(2E)-pent-2-ene	−196.424444	0.146203	0.108344	0.138462
(2Z)-pent-2-ene	−196.422473	0.146538	0.108366	0.138911
2-Methylbutane	−197.650616	0.170492	0.132540	0.162599
2-Methylbut-1-ene	−196.425399	0.145953	0.108348	0.138377
2-Methylbut-2-ene	−196.428427	0.145977	0.108516	0.138233
3-Methylbut-1-ene	−196.421594	0.146029	0.109827	0.138805
Cyclopentane	−196.447999	0.148834	0.115170	0.142836
Cyclopenta-1,3-diene	−194.004693	0.099092	0.067447	0.094033
Hexane	−236.942859	0.201129	0.159944	0.191831
Hex-1,2-diene	−234.482131	0.151996	0.111965	0.143762
Hex-1-ene	−235.712709	0.176575	0.135740	0.167804
2,3-Dimethylbutane	−236.944627	0.200377	0.160337	0.191276
2,3-Dimethylbuta-1,3-diene	−234.499027	0.152102	0.114663	0.144198
2,3-Dimethylbuta-1-ene	−235.719209	0.176092	0.136350	0.167500
2,3-Dimethylbuta-2-ene	−235.721700	0.175800	0.134436	0.166165
2,2-Dimethylbutane	−236.946825	0.199906	0.159467	0.190810
3,3-Dimethylbuta-1-ene	−235.717309	0.175580	0.136683	0.167108
Cyclohexane	−235.752287	0.179349	0.145101	0.172770
Benzene	−232.136474	0.107012	0.076593	0.101699
Cyclohexa-1,3-diene	−233.301453	0.130219	0.096574	0.124132
Cyclohexene	−234.525715	0.154825	0.119853	0.148434
Heptane	−276.235598	0.231328	0.186546	0.220693
Hept-1-ene	−275.005449	0.206749	0.162214	0.196621

Compounds	M06-2X/6-3g(d)			
	E_o	H_{corr}	G_{corr}	*ZPE*
2,2-Dimethylpentane	−276.239366	0.230120	0.186120	0.219693
4,4-Dimethylpent-1-ene	−275.010862	0.205633	0.163043	0.195795
Cycloheptane	−275.035841	0.209838	0.171462	0.201976
Cyclohepta-1,3,5-triene	−271.377165	0.136474	0.100791	0.129851
Cyclohepta-1,3-diene	−272.592107	0.161000	0.123047	0.153676
Cycloheptene	−273.812872	0.185183	0.147448	0.177646

Table 2.
Calculated total electronic energy (E_o), H_{corr}, G_{corr}, and the zero-point vibrational energies (ZPE) at the M06-2X/6-31g(d) level (in hartree).

Compounds	E_D[a]	E_T[b]	E_∞[c]
H_2	−1.1723118	−1.1737775	−1.17439464
Ethane	−79.582513	−79.674425	−79.713125
Ethyne	−77.109286	−77.187516	−77.220455
Ethene	−78.354614	−78.438673	−78.474067
Propane	−118.780810	−118.914036	−118.970132
Propadiene	−116.314867	−116.433424	−116.483343
Prop-1-yne	−116.315794	−116.435339	−116.485674
Prop-1-ene	−117.556774	−117.682351	−117.735225
Cis- butane	−157.978111	−158.152797	−158.226349
But-2-yne	−155.521138	−155.681776	−155.749412
Isobutene	−157.981505	−158.156035	−158.229521
Isobutane	−156.760003	−156.927219	−156.997626
Trans -butane	−157.979256	−158.153758	−158.227233
(2E)-but-2-ene	−156.758622	−156.925479	−156.995734
(2Z)-but-2-ene	−156.756385	−156.923701	−156.994150
Pentane	−197.176630	−197.392504	−197.483398
(2E)-pent-2-ene	−195.956786	−196.164955	−196.252605
(2Z)-pent-2-ene	−195.954467	−196.163063	−196.250893
2-Methylbutane	−197.177674	−197.393756	−197.484738
2-Methylbut-1-ene	−195.957367	−196.165990	−196.253832
2-Methylbut-2-ene	−195.959195	−196.167943	−196.255837
3-Methylbut-1-ene	−195.954457	−196.163021	−196.250837
Cyclopentane	−195.977809	−196.185015	−196.272260
Cyclopenta-1,3-diene	−193.544249	−193.735901	−193.816596
Hexane	−236.376059	−236.633206	−236.741478
1,5-Hexdiene	−233.926959	−234.168762	−234.270574
Hex-1-ene	−235.151737	−235.401337	−235.506432
2,3-Dimethylbutane	−236.377394	−236.635041	−236.743524

Compounds	$E_D{}^a$	$E_T{}^b$	$E_\infty{}^c$
2,3-Dimethylbuta-1,3-diene	−233.940431	−234.183237	−234.285471
2,3-Dimethylbuta-1-ene	−235.156478	−235.406736	−235.512108
2,3-Dimethylbuta-2-ene	−235.157255	−235.407711	−235.513167
2,2-Dimethylbutane	−236.380072	−236.637444	−236.745811
3,3-Dimethylbuta-1-ene	−235.156438	−235.406113	−235.511240
Cyclohexane	−235.187080	−235.434840	−235.539160
Benzene	−231.580490	−231.805751	−231.900598
Cyclohexa-1,3-diene	−232.746205	−232.978902	−233.076879
Cyclohexene	−233.965459	−234.205764	−234.306946
Heptane	−275.574466	−275.872952	−275.998630
Hept-1-ene	−274.350163	−274.641090	−274.763585
2,2-Dimethylpentane	−275.578608	−275.877182	−276.002897
4,4-Dimethylpent-1-ene	−274.355543	−274.646391	−274.768853
Cycloheptane	−274.375461	−274.664943	−274.786830
Cyclohepta-1,3,5-triene	−270.731145	−270.997511	−271.109665
Cyclohepta-1,3-diene	−271.941636	−272.215680	−272.331066
Cycloheptene	−273.157974	−273.439442	−273.557955

Limit energies were obtained using the web page http://sf.anu.edu.au/ ~vvv900/cbs/#ref_3 [36].
[a]M06-2X/cc-pVDZ//M06-2X/6-31g(d) level.
[b]M06-2X/cc-pVTZ//M06-2X/6-31g(d) level.
[c]cc-pV(TD)Z extrapolated level.

Table 3.
Computed CCSD(T)/ccpVXZ energies at the M06-2X/6-31g(d) geometries, where X = D, T, as well as extrapolated values by the Eq. (2) (in hartree).

(T)/cc-pVXZ energies computed at the M06-2X/6-31g(d) geometries, where X = D, T. **Table 3** also shows extrapolated values by the Eq. (2) (denoted E_∞).

It is noted from **Table 3** that the cc-pV(DT)Z extrapolated level yield electronic energies for all reactants and products less than CCSD(T)/cc-pVDZ and CCSD (T)/cc-pVTZ levels, and it is expected that the calculations of the hydrogenation enthalpies by cc-pV(DT)Z extrapolated level are compatible with the experimental values.

3.2.2 Enthalpies of hydrogenation at 298.15 K in gas phase

The usual way to calculate enthalpies of reaction is to calculate heats of formation, and take the appropriate sums and difference (Eq. (3)).

$$\Delta_{hyd}H^o(298) \sum_{products} \Delta_f H^o(298) - \sum_{reactans} \Delta_f H^o(298) \qquad (3)$$

However, since Gaussian program provides the sum of electronic and thermal enthalpies, there is a short cut: namely, to simply take the difference of the sums of these values for the reactants and the products. This works since the number of atoms of each element is the same on both sides of the reaction, therefore all the atomic information cancels out, and you need only the molecular data. For example,

using the information in **Table 2** (or **Table 3** for energies), the enthalpy of reaction can be calculated simply by Eq. (4):

$$\Delta_{hyd}H^0_{298} = \sum (E_0 + H_{corr})_{porducts} - \sum (E_0 + H_{corr})_{reactants} \tag{4}$$

E_0 can represent either E_{DZ}, E_{TZ}, E_{QZ} or E_∞ keeping the calculated H_{corr} value at M06-2X/6-31g(d) level is fixed. The calculated enthalpies of hydrogenation are

	CCSD(T)/cc-pVXZ//M06-2X/6–13(d)			
Reactions	**X = D[a]**	**X = T[b]**	**E_∞[c]**	**$\Delta_{hyd}H^o$(exp.)[d]**
Ethyne +2 H$_2$ → ethane	16.0	4.4	−0.5	−312.0 ± 0.63
Ethene + H$_2$ → ethane	5.1	2.0	0.7	−136.3 ± 0.3
Propadiene +2 H$_2$ → propane	11.4	4.1	−1.3	−295.1 ± 0.1
Prop-1-yne + 2 H$_2$ → propane	16.0	6.1	−0.5	−289.6 ± 0.63
Prop-1-ene + H$_2$ → propane	4.9	2.0	−0.4	−125.0 ± 0.42
But-2-yne + 2 H$_2$ → butane	15.2	4.1	−0.6	−272.4 ± 1.3
Isobutene + H$_2$ isobutane	7.6	3.0	1.1	−117.8 ± 0.42
(2E)-but-2-ene + H$_2$ → butane	6.1	1.7	−0.2	−118.5 ± 0.42
(2Z)-but-2-ene + H$_2$ → butane	7.6	3.9	2.4	−114.6 ± 0.42
(2E)-pent-2-ene + H$_2$ → pentane	5.8	2.3	0.8	−113.8 ± 0.8
(2Z)-pent-2-ene + H$_2$ → pentane	−1.7	−5.3	−6.7	−117.7 ± 0.8
2-Methylbut-1-ene + H$_2$ → 2-methylbutane	2.9	−1.3	−3.1	−118.2 ± 0.42
2-Methylbut-2-ene + H$_2$ → 2-methylbutane	4.7	0.2	−1.7	−111.6 ± 0.3
3-Methylbut-1-ene + H$_2$ → 2-methylbutane	2.6	−1.4	−3.1	−126.3 ± 0.3
Cyclopenta-1,3-diene +2 H$_2$ → cyclopentane	11.1	4.4	1.6	−210.8 ± 0.84
Hex-1,5-diene +2 H$_2$ → hexane	13.1	5.8	2.8	−251.2 ± 0.42
Hex-1-ene + H$_2$ → hexane	5.6	1.6	0.0	−126.0 ± 2.0
2,3-Dimethylbuta-1,3-diene +2 H$_2$ → 2,3-dimethylbutane	11.3	2.7	−0.9	−223.4 ± 0.63
2,3-Dimethylbuta-1-ene + H$_2$ → 2,3-dimethylbutane	7.2	2.9	1.0	−116.1 ± 0.4
2,3-Dimethylbuta-2-ene + H$_2$ → 2,3-dimethylbutane	10.1	2.7	−0.9	−110.4 ± 0.42
3,3-Dimethylbuta-1-ene + H$_2$ → 2,2-dimethylbutane	4.5	0.9	−0.6	−125.9 ± 0.63
Benzene +3 H$_2$ → cyclohexane	18.6	6.4	1.3	−205.3 ± 0.6
Cyclohexa-1,3-diene +2 H$_2$ → cyclohexane	13.1	5.1	1.8	−229.6 ± 0.42
Cyclohexene + H$_2$ → cyclohexane	6.0	1.8	0.0	−118.6 ± 0.42
Hept-1-ene + H$_2$ → heptane	6.4	2.4	0.8	−125.1 ± 0.3
4,4-Dimethylpent-1-ene + H$_2$ → 2,2-dimethylpentane	5.9	2.5	1.0	−122.5 ± 0.42
Cyclohepta-1,3,5-triene +3 H$_2$ → cycloheptane	18.6	8.0	3.5	−301.7 ± 1.3
Cyclohepta-1,3-diene +2 H$_2$ → cycloheptane	12.5	5.6	2.6	−212.4 ± 0.63
Cycloheptene + H$_2$ → cycloheptane	4.5	1.7	0.6	−108.9 ± 0.63

[a]*CCSD(T)/cc-pVDZ//M06-2X/6-31g(d) level.*
[b]*CCSD(T)/cc-pVTZ//M06-2X/6-31g(d) level.*
[c]*cc-pV(TD)Z extrapolated level.*
[d]*NIST-JANAF thermo-chemical tables.*

Table 4.
Difference between experimental and calculation values of standard enthalpies of hydrogenation of some unsaturated hydrocarbons in the gas phase at 298.15 K (in kJ Mol^{-1}).

Level	MAD	RMS	Error%	SD	R^2
CCSD(T)/cc-pVDZ//M06-2X/6-31g(d)	8.8	10.0	5.0%	2.78	0.9987
CCSD(T)//cc-pVTZ//M06-2X/6-31g(d)	3.4	3.9	2.0%	2.11	0.9992
cc-pV(DT)Z extrapolated level	1.5	2.1	1.0%	2.12	0.9992

Table 5.
Statistical parameters for all used methods to calculate hydrogenation enthalpies. (in kJ Mol^{-1}).
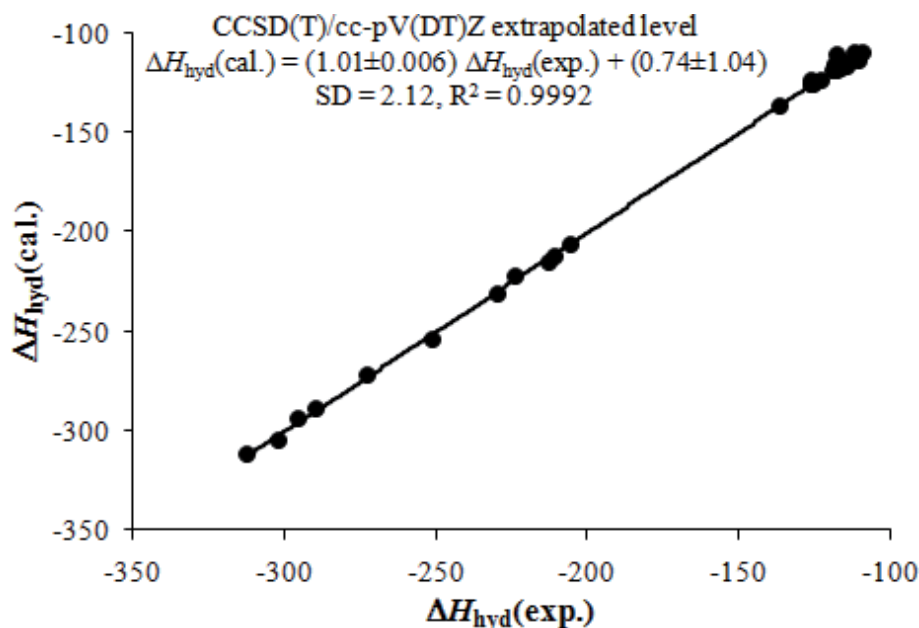
Figure 1.
Calculated versus experimental hydrogenation enthalpy $\left[\Delta H^{\circ}_{hyd}(298, 15\,K), kJ\,mol^{-1} \right]$ of 29 hydrocarbons.

reported in **Table 4**, along with the experimental values. **Table 5** shows statistical parameters for all used computational methods. **Figure 1** shows a linear analysis of the best calculated results in terms of experimental results.

Our best theoretical estimates of the enthalpies of hydrogenation are based on basis set limit extrapolation calculations, when the pair cc-pVDZ and cc-pVTZ are used, and the mean absolute deviation (MAD) between experimental and calculated values is 1.5 kJ mol^{-1} (**Table 5**). The enthalpies of hydrogenation of some alkenes (12 compounds) have been calculated at the HF, B3LYP, M06, MP2, G3, G4, CBS-QB3, CBS-APNO, and W1BD levels and, in the case of the first four methods, using a variety of basis sets up to aug-ccpVTZ [37], and it is found that the MAD decreases gradually from the first to the last method (18.4–4.2 kJ mol^{-1}). Moreover, Rogers et al. [38–40] calculated the hydrogenation enthalpy at 298.15 K for reactions involving cyclic and acyclic C4 (20 reactions), cyclic C5 (23 reactions) and C6 (24 reactions) hydrocarbons using the G2 and G2(MP2) ab initio methods, and it is found that the MAD is about 3.3, 3.7 and 5.0 kJ $^{-1}$, respectively.

4. Conclusion

Enthalpies of hydrogenation are relatively easy to calculate with CCSD(T)/cc-pVXZ/M06-31g(d)/6-31g(d) level, where X = D, T, giving fairly good agreement

with experiment, especially when cc-pVTZ basis set are used, and basis set extrapolation techniques by Eq. (2) seem to represent an easy-to-use alternative, especially when the pair cc-pVDZ and cc-pVTZ are used.

Appendix: supporting information (All computed molecule Cartesian coordinates (XYZ)) were optimized at the M06-2X/6-31g(d) level

1			
Hydrogen (H2)			
H	0.000000000	0.000000000	0.368263000
H	0.000000000	0.000000000	-0.368263000
2			
Ethane (C2H6)			
C	0.000000000	0.000000000	0.762978000
C	0.000000000	0.000000000	-0.762978000
H	0.000000000	1.019590000	1.159421000
H	-0.882991000	-0.509795000	1.159421000
H	0.882991000	-0.509795000	1.159421000
H	0.000000000	-1.019590000	-1.159421000
H	-0.882991000	0.509795000	-1.159421000
H	0.882991000	0.509795000	-1.159421000
3			
Ethene (C2H4)			
C	0.000000000	0.000000000	0.663573000
C	0.000000000	0.000000000	-0.663573000
H	0.000000000	0.923826000	1.234547000
H	0.000000000	-0.923826000	1.234547000
H	0.000000000	-0.923826000	-1.234547000
H	0.000000000	0.923826000	-1.234547000
4			
Ethyne (C2H2)			
C	0.000000000	0.000000000	0.600962000
H	0.000000000	0.000000000	1.668037000
C	0.000000000	0.000000000	-0.600962000
H	0.000000000	0.000000000	-1.668037000
5			
Propadiene			
C	0.000000000	0.000000000	0.000000000
C	0.000000000	0.000000000	1.304952000
C	0.000000000	0.000000000	-1.304952000
H	0.000000000	0.928749000	1.868109000
H	0.000000000	-0.928749000	1.868109000

H	0.928749000	0.000000000	−1.868109000
H	−0.928749000	0.000000000	−1.868109000
6			
Propane			
C	0.000000000	1.266248000	−0.260978000
C	0.000000000	0.000000000	0.591962000
H	0.000000000	2.169798000	0.355701000
H	0.883659000	1.299469000	−0.907461000
H	−0.883659000	1.299469000	−0.907461000
C	0.000000000	−1.266248000	−0.260978000
H	0.877466000	0.000000000	1.249203000
H	−0.877466000	0.000000000	1.249203000
H	0.000000000	−2.169798000	0.355701000
H	−0.883659000	−1.299469000	−0.907461000
H	0.883659000	−1.299469000	−0.907461000
7			
Propene			
C	−1.286905000	0.145875000	0.000000000
C	0.000000000	0.478432000	0.000000000
H	−1.601612000	−0.895181000	0.000000000
H	−2.072231000	0.895120000	0.000000000
H	0.274287000	1.533078000	0.000000000
C	1.134779000	−0.502407000	0.000000000
H	1.773172000	−0.366223000	0.880442000
H	0.765971000	−1.531971000	0.000000000
H	1.773172000	−0.366223000	−0.880442000
8			
Propyne			
C	0.000000000	0.000000000	1.423679000
C	0.000000000	0.000000000	0.219688000
H	0.000000000	0.000000000	2.490285000
C	0.000000000	0.000000000	−1.242799000
H	0.000000000	1.022382000	−1.631230000
H	0.885409000	−0.511191000	−1.631230000
H	−0.885409000	−0.511191000	−1.631230000
9			
But-2-yne			
C	0.000000000	0.000000000	2.066654000
H	0.000000000	1.021413000	2.458673000
H	0.884570000	−0.510706000	2.458673000
H	−0.884570000	−0.510706000	2.458673000

C	0.000000000	0.000000000	0.602950000
C	0.000000000	0.000000000	-2.066654000
H	0.000000000	1.021413000	-2.458673000
H	0.884570000	-0.510706000	-2.458673000
H	-0.884570000	-0.510706000	-2.458673000
C	0.000000000	0.000000000	-0.602950000
10			
(Z)-but-2-ane			
C	0.583174000	1.434814000	-0.567859000
C	0.583174000	0.495360000	0.636830000
C	-0.583174000	-0.495360000	0.636830000
C	-0.583174000	-1.434814000	-0.567859000
H	-0.372885000	1.964655000	-0.647990000
H	0.741015000	0.890494000	-1.503781000
H	1.375535000	2.184468000	-0.485094000
H	0.547339000	1.089204000	1.557738000
H	1.528690000	-0.062264000	0.665299000
H	-1.528690000	0.062264000	0.665299000
H	-0.547339000	-1.089204000	1.557738000
H	-1.375535000	-2.184468000	-0.485094000
H	0.372885000	-1.964655000	-0.647990000
H	-0.741015000	-0.890494000	-1.503781000
11			
(Z)-but-2-ene			
C	0.000000000	0.666919000	0.667097000
C	0.000000000	-0.666919000	0.667097000
H	0.000000000	1.168257000	1.634362000
H	0.000000000	-1.168257000	1.634362000
C	0.000000000	1.580592000	-0.524061000
C	0.000000000	-1.580592000	-0.524061000
H	-0.880001000	-2.233321000	-0.510523000
H	0.000000000	-1.037863000	-1.471533000
H	0.880001000	-2.233321000	-0.510523000
H	0.000000000	1.037863000	-1.471533000
H	-0.880001000	2.233321000	-0.510523000
H	0.880001000	2.233321000	-0.510523000
12			
Isobutene2-methylprop-1-ene			
C	0.000000000	0.000000000	0.124902000
C	0.000000000	0.000000000	1.456866000
C	0.000000000	1.272771000	-0.678500000

C	0.000000000	−1.272771000	−0.678500000
H	0.000000000	−0.925843000	2.025187000
H	0.000000000	0.925843000	2.025187000
H	−0.880053000	1.319051000	−1.331393000
H	0.880053000	1.319051000	−1.331393000
H	0.000000000	2.157033000	−0.036707000
H	−0.880053000	−1.319051000	−1.331393000
H	0.000000000	−2.157033000	−0.036707000
H	0.880053000	−1.319051000	−1.331393000
13			
Methylrpopane			
C	−0.878102000	1.160442000	0.000000000
C	0.318200000	0.209420000	0.000000000
C	0.318200000	−0.659704000	1.256954000
C	0.318200000	−0.659704000	−1.256954000
H	−1.816717000	0.592600000	0.000000000
H	−0.876505000	1.803417000	0.886375000
H	−0.876505000	1.803417000	−0.886375000
H	1.236570000	0.812776000	0.000000000
H	−0.585386000	−1.280771000	1.290810000
H	1.184708000	−1.328777000	1.278998000
H	0.337765000	−0.047918000	2.164877000
H	−0.585386000	−1.280771000	−1.290810000
H	0.337765000	−0.047918000	−2.164877000
H	1.184708000	−1.328777000	−1.278998000
14			
(E)-but-2-ane			
C	0.704814000	1.820298000	0.000000000
C	0.704814000	0.294113000	0.000000000
C	−0.704814000	−0.294113000	0.000000000
C	−0.704814000	−1.820298000	0.000000000
H	0.188158000	2.209779000	0.883837000
H	0.188158000	2.209779000	−0.883837000
H	1.721212000	2.224575000	0.000000000
H	1.249565000	−0.076964000	0.878126000
H	1.249565000	−0.076964000	−0.878126000
H	−1.249565000	0.076964000	−0.878126000
H	−1.249565000	0.076964000	0.878126000
H	−1.721212000	−2.224575000	0.000000000
H	−0.188158000	−2.209779000	0.883837000
H	−0.188158000	−2.209779000	−0.883837000

15			
(E)-but-2-ene			
C	−0.326383000	0.580069000	0.000000000
C	0.326383000	−0.580069000	0.000000000
H	−1.417413000	0.566444000	0.000000000
H	1.417413000	−0.566444000	0.000000000
C	0.326383000	1.930669000	0.000000000
C	−0.326383000	−1.930669000	0.000000000
H	−0.032478000	−2.513587000	0.880427000
H	−1.416586000	−1.840628000	0.000000000
H	−0.032478000	−2.513587000	−0.880427000
H	1.416586000	1.840628000	0.000000000
H	0.032478000	2.513587000	−0.880427000
H	0.032478000	2.513587000	0.880427000
16			
(2E)-pent-2-ene			
C	2.314095000	−0.475261000	0.268047000
C	1.301568000	0.569988000	−0.210535000
C	−0.062964000	−0.022508000	−0.417562000
C	−1.160170000	0.335620000	0.246048000
C	−2.517862000	−0.272036000	0.051547000
H	−0.132949000	−0.822240000	−1.158725000
H	−1.084442000	1.130940000	0.989387000
H	2.000934000	−0.903693000	1.224639000
H	2.397884000	−1.295127000	−0.453050000
H	3.308026000	−0.036515000	0.395398000
H	1.236711000	1.388220000	0.516039000
H	1.659489000	1.009665000	−1.150825000
H	−3.247227000	0.481088000	−0.268021000
H	−2.490794000	−1.061858000	−0.704665000
H	−2.895632000	−0.705300000	0.984558000
17			
(2E)-pentane			
C	−2.087737000	−0.686201000	0.167473000
C	−1.397858000	0.612858000	−0.246114000
H	−1.623234000	−1.556933000	−0.305129000
H	−2.032398000	−0.827405000	1.252942000
H	−3.144187000	−0.681110000	−0.116273000
H	−1.418421000	0.705421000	−1.339990000
H	−1.966593000	1.464569000	0.145544000
C	0.049630000	0.716811000	0.239083000

H	0.067617000	0.686754000	1.338032000
H	0.456416000	1.695525000	−0.048477000
C	0.968945000	−0.377016000	−0.304259000
H	0.891736000	−0.401137000	−1.399776000
H	0.629781000	−1.357571000	0.050730000
C	2.424147000	−0.166949000	0.106336000
H	2.802766000	0.788870000	−0.271303000
H	2.522458000	−0.153609000	1.197253000
H	3.071296000	−0.960391000	−0.278665000
18			
(2Z)-pent-2-ene			
C	−2.157668000	−0.306501000	−0.421749000
C	−1.015663000	−0.162833000	0.590132000
C	0.010326000	0.832747000	0.126525000
C	1.294369000	0.612662000	−0.160571000
C	2.043151000	−0.685516000	−0.070879000
H	−0.369285000	1.846982000	−0.004792000
H	1.886162000	1.462897000	−0.498228000
H	−1.779911000	−0.681064000	−1.377533000
H	−2.924349000	−0.997521000	−0.059313000
H	−2.635896000	0.660617000	−0.608730000
H	−1.429497000	0.172242000	1.550224000
H	−0.560025000	−1.140190000	0.773568000
H	2.868553000	−0.607338000	0.645958000
H	1.409139000	−1.519046000	0.237378000
H	2.488018000	−0.940929000	−1.039284000
19			
(2Z)-pentane			
C	−1.818548000	0.753538000	0.174327000
C	−1.147340000	−0.470732000	−0.450177000
H	−1.113210000	1.577154000	0.316941000
H	−2.639982000	1.118341000	−0.450018000
H	−2.232022000	0.501813000	1.156923000
H	−1.903976000	−1.254866000	−0.566214000
H	−0.805475000	−0.230539000	−1.466300000
C	0.036454000	−1.015801000	0.368373000
H	−0.115502000	−0.771139000	1.429186000
H	0.051833000	−2.110186000	0.308069000
C	1.407278000	−0.498829000	−0.079387000
H	2.180294000	−0.956901000	0.549432000
H	1.597958000	−0.846640000	−1.103214000

C	1.555115000	1.020482000	−0.032216000
H	2.574480000	1.324615000	−0.288218000
H	0.878078000	1.509222000	−0.740322000
H	1.329769000	1.407174000	0.968220000
20			
1,2 Di metgyl cyclo propane			
C	−0.983015000	0.923486000	0.000000000
C	0.245532000	0.490166000	0.753182000
C	0.245532000	0.490166000	−0.753182000
H	−1.826999000	0.237791000	0.000000000
H	−1.259771000	1.972523000	0.000000000
H	0.818353000	1.295146000	1.208149000
H	0.818353000	1.295146000	−1.208149000
C	0.245532000	−0.790236000	−1.556100000
C	0.245532000	−0.790236000	1.556100000
H	−0.406160000	−1.546084000	−1.108730000
H	−0.117937000	−0.607772000	−2.572546000
H	1.251787000	−1.216486000	−1.629081000
H	1.251787000	−1.216486000	1.629081000
H	−0.117937000	−0.607772000	2.572546000
H	−0.406160000	−1.546084000	1.108730000
21			
1,2 Di metgyl cyclo propene			
C	0.000000000	0.000000000	1.391105000
C	0.000000000	0.647537000	0.034858000
C	0.000000000	−0.647537000	0.034858000
C	0.000000000	−1.958662000	−0.652173000
C	0.000000000	1.958662000	−0.652173000
H	0.912511000	0.000000000	1.995747000
H	−0.912511000	0.000000000	1.995747000
H	−0.881068000	−2.541300000	−0.363244000
H	0.000000000	−1.840975000	−1.738686000
H	0.881068000	−2.541300000	−0.363244000
H	−0.881068000	2.541300000	−0.363244000
H	0.881068000	2.541300000	−0.363244000
H	0.000000000	1.840975000	−1.738686000
22			
1,3-Pentadiene(Z)			
C	2.386185000	0.144512000	0.000000000
C	1.101237000	−0.219798000	0.000000000
C	0.000000000	0.740650000	0.000000000

C	−1.309264000	0.457570000	0.000000000
C	−1.947457000	−0.899208000	0.000000000
H	2.674974000	1.192770000	0.000000000
H	3.188346000	−0.585678000	0.000000000
H	0.854201000	−1.278983000	0.000000000
H	0.299494000	1.788083000	0.000000000
H	−2.003506000	1.296454000	0.000000000
H	−1.218572000	−1.711476000	0.000000000
H	−2.589570000	−1.021763000	0.879756000
H	−2.589570000	−1.021763000	−0.879756000
23			
2-Methylbut-1-ene			
C	−1.897352000	0.069688000	−0.379011000
C	−0.803183000	−0.497117000	0.532182000
C	0.590454000	−0.115154000	0.094446000
C	0.898099000	1.358700000	0.048952000
C	1.496741000	−1.033911000	−0.237691000
H	−1.913284000	1.163502000	−0.353795000
H	−1.735338000	−0.242153000	−1.415566000
H	−2.884222000	−0.282783000	−0.066139000
H	−0.969559000	−0.131539000	1.555187000
H	−0.883921000	−1.588740000	0.568655000
H	0.309642000	1.863055000	−0.726222000
H	0.646334000	1.839248000	1.002285000
H	1.955247000	1.539160000	−0.160321000
H	2.500315000	−0.757627000	−0.549409000
H	1.266234000	−2.095358000	−0.207945000
24			
2-Methylbut-2-ene			
C	−1.739392000	−0.815690000	0.000068000
C	−0.445666000	−0.042781000	−0.000004000
C	0.731454000	−0.676023000	0.000031000
C	2.107037000	−0.076409000	−0.000012000
C	−0.622934000	1.452321000	−0.000085000
H	−2.344490000	−0.563945000	−0.879881000
H	−1.567257000	−1.895111000	0.000185000
H	−2.344512000	−0.563761000	0.879948000
H	0.707982000	−1.766396000	0.000117000
H	2.672750000	−0.405010000	−0.879551000
H	2.095891000	1.015122000	−0.000370000
H	2.672570000	−0.404435000	0.879859000

H	-1.198192000	1.767121000	-0.879475000
H	-1.197796000	1.767263000	0.879516000
H	0.320061000	2.000645000	-0.000338000
25			
2-Methylbutane			
C	1.780516000	-0.000029000	-0.519793000
C	0.912273000	-0.000063000	0.738834000
C	-0.603203000	0.000003000	0.481637000
C	-1.060235000	1.257557000	-0.259637000
H	2.841975000	0.000039000	-0.255438000
H	1.595066000	-0.884813000	-1.136689000
H	1.595016000	0.884859000	-1.136563000
H	1.163734000	-0.878612000	1.346829000
H	1.163751000	0.878509000	1.346795000
H	-0.724263000	2.166339000	0.251626000
H	-0.665606000	1.280184000	-1.281506000
H	-2.152272000	1.293270000	-0.330286000
H	-1.089018000	0.000004000	1.467320000
C	-1.060336000	-1.257501000	-0.259674000
H	-0.665592000	-1.280203000	-1.281495000
H	-0.724520000	-2.166308000	0.251651000
H	-2.152364000	-1.293073000	-0.330443000
26			
3-Methylbut-1-ene			
C	1.517055000	-0.862537000	0.318229000
C	0.477587000	-0.019857000	-0.432825000
C	-0.887587000	-0.639452000	-0.271180000
C	-1.965772000	-0.056795000	0.245400000
C	0.538897000	1.437769000	0.013736000
H	1.307767000	-0.848847000	1.393325000
H	1.502760000	-1.905424000	-0.014449000
H	2.526055000	-0.468418000	0.160305000
H	0.729278000	-0.062673000	-1.503161000
H	-0.960847000	-1.676811000	-0.601961000
H	-2.905847000	-0.591711000	0.336269000
H	-1.956820000	0.971942000	0.593763000
H	0.312097000	1.523918000	1.082556000
H	1.540556000	1.846234000	-0.150203000
H	-0.176082000	2.057026000	-0.536608000
27			
Cyclopenta			

C	0.000000000	1.237205000	0.367436000
C	0.340648000	0.685452000	-1.023943000
C	-0.340648000	-0.685452000	-1.023943000
C	0.000000000	-1.237205000	0.367436000
C	0.000000000	0.000000000	1.301698000
H	0.693538000	2.015338000	0.697761000
H	-0.999214000	1.686189000	0.341522000
H	1.425719000	0.553833000	-1.123100000
H	0.009942000	1.338647000	-1.836720000
H	-1.425719000	-0.553833000	-1.123100000
H	-0.009942000	-1.338647000	-1.836720000
H	-0.693538000	-2.015338000	0.697761000
H	0.999214000	-1.686189000	0.341522000
H	-0.877412000	0.005682000	1.954484000
H	0.877412000	-0.005682000	1.954484000
28			
Cyclopenta-1,3-diene			
C	-1.177268000	-0.280759000	-0.000082000
C	-0.735260000	0.988357000	0.000143000
C	0.735254000	0.988361000	-0.000114000
C	1.177270000	-0.280752000	0.000041000
H	-2.209216000	-0.610008000	-0.000131000
H	-1.348626000	1.882297000	0.000233000
H	1.348614000	1.882306000	-0.000183000
H	2.209219000	-0.609995000	0.000059000
C	0.000004000	-1.214780000	0.000009000
H	0.000033000	-1.873598000	-0.879427000
H	-0.000021000	-1.873571000	0.879466000
29			
Pentane			
C	1.275667000	-0.527113000	0.000000000
C	0.000000000	0.312488000	0.000000000
H	1.274183000	-1.185569000	0.878212000
H	1.274183000	-1.185569000	-0.878212000
C	-1.275794000	-0.527541000	0.000000000
H	-0.000235000	0.973329000	0.878523000
H	-0.000235000	0.973329000	-0.878523000
C	-2.540546000	0.327170000	0.000000000
H	-1.273566000	-1.186150000	-0.878131000
H	-1.273566000	-1.186150000	0.878131000
H	-3.444413000	-0.288920000	0.000000000

H	−2.573779000	0.973295000	0.883728000
H	−2.573779000	0.973295000	−0.883728000
C	2.540652000	0.328153000	0.000000000
H	3.444340000	−0.288153000	0.000000000
H	2.573497000	0.974161000	−0.883830000
H	2.573497000	0.974161000	0.883830000
30			
Hexane			
C	0.429918000	1.910882000	0.000000000
C	−0.416794000	0.639666000	0.000000000
H	1.088648000	1.905049000	0.878012000
H	1.088648000	1.905049000	−0.878012000
C	0.416794000	−0.639666000	0.000000000
H	−1.077316000	0.643829000	0.878621000
H	−1.077316000	0.643829000	−0.878621000
C	−0.429918000	−1.910882000	0.000000000
H	1.077316000	−0.643829000	−0.878621000
H	1.077316000	−0.643829000	0.878621000
H	−1.088648000	−1.905049000	0.878012000
H	−1.088648000	−1.905049000	−0.878012000
C	0.416794000	−3.181079000	0.000000000
C	−0.416794000	3.181079000	0.000000000
H	1.062641000	−3.219144000	0.883682000
H	−0.205277000	−4.080748000	0.000000000
H	1.062641000	−3.219144000	−0.883682000
H	−1.062641000	3.219144000	0.883682000
H	0.205277000	4.080748000	0.000000000
H	−1.062641000	3.219144000	−0.883682000
31			
Hex1−ene			
C	3.059992000	−0.191825000	0.443719000
C	2.031872000	−0.193363000	−0.399121000
C	0.770381000	0.599545000	−0.216038000
C	−0.469432000	−0.294413000	−0.100878000
C	−1.763936000	0.502583000	0.045414000
C	−2.993402000	−0.394630000	0.161583000
H	3.053025000	0.421594000	1.341658000
H	3.944231000	−0.796826000	0.270109000
H	2.072945000	−0.824722000	−1.287818000
H	0.634999000	1.279548000	−1.069067000
H	0.857556000	1.227717000	0.679261000

H	−0.348838000	−0.965753000	0.759219000
H	−0.537335000	−0.939318000	−0.988075000
H	−1.874101000	1.172797000	−0.816907000
H	−1.691686000	1.148473000	0.929906000
H	−2.913980000	−1.053717000	1.032463000
H	−3.098725000	−1.028497000	−0.725217000
H	−3.910937000	0.191320000	0.266394000
32			
1,5-Hexadiene			
C	0.758365000	1.082281000	0.132388000
C	−0.758365000	1.082282000	−0.132388000
C	1.443512000	−0.106603000	−0.476858000
C	−1.443512000	−0.106603000	0.476857000
C	2.164328000	−0.995960000	0.198166000
C	−2.164328000	−0.995960000	−0.198166000
H	1.184567000	2.006667000	−0.278514000
H	0.944888000	1.097748000	1.213365000
H	−0.944891000	1.097752000	−1.213365000
H	−1.184567000	2.006667000	0.278517000
H	1.309651000	−0.233049000	−1.552214000
H	−1.309647000	−0.233051000	1.552213000
H	2.634034000	−1.842946000	−0.291621000
H	2.310076000	−0.906735000	1.272141000
H	−2.634031000	−1.842948000	0.291621000
H	−2.310079000	−0.906734000	−1.272140000
33			
Cyclohexane			
C	1.262524000	0.728918000	0.234036000
C	0.000000000	1.457837000	−0.234036000
C	1.262524000	−0.728918000	−0.234036000
C	−1.262524000	0.728918000	0.234036000
C	0.000000000	−1.457837000	0.234036000
C	−1.262524000	−0.728918000	−0.234036000
H	2.158102000	1.246032000	−0.127892000
H	1.303908000	0.752778000	1.332235000
H	−0.000044000	2.491987000	0.127892000
H	0.000029000	1.505607000	−1.332235000
H	1.303879000	−0.752829000	−1.332235000
H	2.158146000	−1.245955000	0.127892000
H	−1.303879000	0.752829000	1.332235000
H	−2.158146000	1.245955000	−0.127892000

H	0.000044000	-2.491987000	-0.127892000
H	-0.000029000	-1.505607000	1.332235000
H	-2.158102000	-1.246032000	0.127892000
H	-1.303908000	-0.752778000	-1.332235000
34			
Cyclohexene			
C	1.493515000	0.041995000	0.112710000
C	0.663935000	1.299645000	0.060049000
C	0.689634000	-1.182733000	-0.330220000
C	-0.663940000	1.299643000	-0.060038000
C	-0.689633000	-1.182730000	0.330228000
C	-1.493513000	0.041991000	-0.112723000
H	2.383076000	0.161360000	-0.517404000
H	1.868656000	-0.105470000	1.135883000
H	1.195274000	2.247684000	0.118372000
H	0.563006000	-1.155757000	-1.420384000
H	1.236070000	-2.101254000	-0.092430000
H	-1.195279000	2.247680000	-0.118380000
H	-1.236069000	-2.101254000	0.092447000
H	-0.563007000	-1.155740000	1.420392000
H	-2.383086000	0.161354000	0.517372000
H	-1.868631000	-0.105478000	-1.135904000
35			
1,3-Cyclohexadiene			
C	0.053086000	1.420006000	0.110022000
C	-0.053086000	0.732806000	1.253379000
C	0.317632000	0.696571000	-1.188121000
C	0.053086000	-0.732806000	1.253379000
C	-0.317632000	-0.696571000	-1.188121000
C	-0.053086000	-1.420006000	0.110022000
H	0.009378000	2.505852000	0.107322000
H	-0.199118000	1.245544000	2.199955000
H	-0.048864000	1.277555000	-2.039930000
H	1.407129000	0.603229000	-1.319023000
H	0.199118000	-1.245544000	2.199955000
H	-1.407129000	-0.603229000	-1.319023000
H	0.048864000	-1.277555000	-2.039930000
H	-0.009378000	-2.505852000	0.107322000
36			
Benzene			
C	0.000000000	1.392899000	0.000000000

C	−1.206286000	0.696449000	0.000000000
C	−1.206286000	−0.696449000	0.000000000
C	0.000000000	−1.392899000	0.000000000
C	1.206286000	−0.696449000	0.000000000
C	1.206286000	0.696449000	0.000000000
H	0.000000000	2.478737000	0.000000000
H	−2.146649000	1.239368000	0.000000000
H	−2.146649000	−1.239368000	0.000000000
H	0.000000000	−2.478737000	0.000000000
H	2.146649000	−1.239368000	0.000000000
H	2.146649000	1.239368000	0.000000000
37			
2,2-Dimethylbutane			
C	−0.891138000	−0.493307000	1.251301000
C	−0.370919000	0.222873000	0.000000000
C	1.169743000	0.270629000	0.000000000
C	1.881540000	−1.081438000	0.000000000
C	−0.891138000	−0.493307000	−1.251301000
C	−0.891138000	1.664786000	0.000000000
H	−0.501945000	−0.023609000	2.162317000
H	−0.601978000	−1.549129000	1.262973000
H	−1.985360000	−0.450049000	1.291227000
H	1.493610000	0.845543000	0.878474000
H	1.493610000	0.845543000	−0.878474000
H	2.966509000	−0.941691000	0.000000000
H	1.627577000	−1.672866000	−0.884945000
H	1.627577000	−1.672866000	0.884945000
H	−0.501945000	−0.023609000	−2.162317000
H	−1.985360000	−0.450049000	−1.291227000
H	−0.601978000	−1.549129000	−1.262973000
H	−0.542658000	2.207179000	0.886401000
H	−1.986701000	1.686130000	0.000000000
H	−0.542658000	2.207179000	−0.886401000
38			
2,3-Dimethylbut-1-ene			
C	0.659232000	−0.195091000	−0.376320000
C	−0.758257000	0.238013000	−0.048663000
C	1.076755000	−1.393536000	0.489668000
C	−1.068744000	1.449914000	0.412114000
C	−1.827608000	−0.802948000	−0.270301000
C	1.691496000	0.922771000	−0.254484000

H	0.649873000	-0.535486000	-1.423394000
H	1.040697000	-1.122393000	1.550654000
H	2.099986000	-1.700065000	0.250914000
H	0.425460000	-2.258481000	0.336733000
H	-2.098779000	1.715751000	0.632887000
H	-0.322860000	2.217576000	0.588034000
H	-1.756161000	-1.611912000	0.465518000
H	-1.728065000	-1.263127000	-1.260728000
H	-2.826508000	-0.367173000	-0.192154000
H	1.774495000	1.264263000	0.783396000
H	1.428232000	1.782970000	-0.876827000
H	2.676389000	0.563342000	-0.567120000
39			
2,3-Dimethylbut-2-ene			
C	0.000000000	0.000000000	0.671173000
C	0.000000000	0.000000000	-0.671173000
C	-0.023373000	1.248611000	1.520147000
C	-0.023373000	-1.248611000	-1.520147000
C	0.023373000	1.248611000	-1.520147000
C	0.023373000	-1.248611000	1.520147000
H	0.927460000	1.370741000	2.054393000
H	-0.801416000	1.159365000	2.288220000
H	-0.218303000	2.163384000	0.961223000
H	0.927460000	-1.370741000	-2.054393000
H	-0.801416000	-1.159365000	-2.288220000
H	-0.218303000	-2.163384000	-0.961223000
H	0.218303000	2.163384000	-0.961223000
H	-0.927460000	1.370741000	-2.054393000
H	0.801416000	1.159365000	-2.288220000
H	0.218303000	-2.163384000	0.961223000
H	-0.927460000	-1.370741000	2.054393000
H	0.801416000	-1.159365000	2.288220000
40			
2,3-Dimethylbuta-1,3-diene			
C	-0.048431000	0.739804000	0.000000000
C	0.048431000	-0.739804000	0.000000000
C	1.232834000	-1.362556000	0.000000000
C	-1.232834000	1.362556000	0.000000000
C	-1.232834000	-1.534469000	0.000000000
C	1.232834000	1.534469000	0.000000000
H	1.292502000	-2.446623000	0.000000000

H	2.175776000	−0.826780000	0.000000000
H	−1.292502000	2.446623000	0.000000000
H	−2.175776000	0.826780000	0.000000000
H	−1.840021000	−1.303373000	0.881915000
H	−1.840021000	−1.303373000	−0.881915000
H	−1.023657000	−2.606232000	0.000000000
H	1.840021000	1.303373000	0.881915000
H	1.840021000	1.303373000	−0.881915000
H	1.023657000	2.606232000	0.000000000
41			
2,3-Dimethylbutane			
C	−0.234895000	0.734238000	0.000000000
C	0.234895000	−0.734238000	0.000000000
H	−1.336373000	0.723893000	0.000000000
H	1.336373000	−0.723893000	0.000000000
C	0.234895000	1.483701000	1.249947000
C	0.234895000	1.483701000	−1.249947000
C	−0.234895000	−1.483701000	1.249947000
C	−0.234895000	−1.483701000	−1.249947000
H	1.327318000	1.431574000	1.339772000
H	1.327318000	1.431574000	−1.339772000
H	−1.327318000	−1.431574000	1.339772000
H	−1.327318000	−1.431574000	−1.339772000
H	−0.043497000	2.540861000	1.194199000
H	−0.199022000	1.076299000	2.166612000
H	−0.043497000	2.540861000	−1.194199000
H	−0.199022000	1.076299000	−2.166612000
H	0.043497000	−2.540861000	1.194199000
H	0.199022000	−1.076299000	2.166612000
H	0.043497000	−2.540861000	−1.194199000
H	0.199022000	−1.076299000	−2.166612000
42			
3,3-Dimethylbut-1-ene			
C	0.353190000	0.000609000	−0.000026000
C	−0.999465000	−0.675214000	−0.000105000
C	−2.191693000	−0.086344000	−0.000016000
C	1.119964000	−0.454409000	−1.251863000
C	1.120240000	−0.455428000	1.251347000
C	0.236688000	1.524864000	0.000626000
H	−0.954618000	−1.766596000	−0.000166000
H	−3.106208000	−0.670982000	0.000021000

H	-2.305984000	0.993632000	-0.000028000
H	1.218068000	-1.545397000	-1.277328000
H	2.127783000	-0.024058000	-1.261702000
H	0.600398000	-0.138891000	-2.162255000
H	1.219797000	-1.546319000	1.275015000
H	0.600027000	-0.142057000	2.162145000
H	2.127460000	-0.023762000	1.262103000
H	-0.296827000	1.880611000	0.888408000
H	-0.297058000	1.881397000	-0.886724000
H	1.233616000	1.977959000	0.000725000
43			
Heptane			
C	0.000000000	3.816380000	-0.355934000
C	0.000000000	2.550538000	0.497249000
C	0.000000000	1.275049000	-0.343162000
C	0.000000000	0.000000000	0.497153000
C	0.000000000	-1.275049000	-0.343162000
C	0.000000000	-2.550538000	0.497249000
C	0.000000000	-3.816380000	-0.355934000
H	0.883668000	3.851044000	-1.001985000
H	-0.883668000	3.851044000	-1.001985000
H	0.000000000	4.719247000	0.261473000
H	0.877995000	2.547991000	1.156034000
H	-0.877995000	2.547991000	1.156034000
H	-0.878586000	1.275903000	-1.003697000
H	0.878586000	1.275903000	-1.003697000
H	0.878658000	0.000000000	1.157453000
H	-0.878658000	0.000000000	1.157453000
H	-0.878586000	-1.275903000	-1.003697000
H	0.878586000	-1.275903000	-1.003697000
H	0.877995000	-2.547991000	1.156034000
H	-0.877995000	-2.547991000	1.156034000
H	0.883668000	-3.851044000	-1.001985000
H	0.000000000	-4.719247000	0.261473000
H	-0.883668000	-3.851044000	-1.001985000
44			
Hept-1-ene			
C	3.692297000	0.028549000	0.511847000
C	2.690421000	0.199001000	-0.345267000
C	1.389176000	-0.548470000	-0.304483000
C	0.188884000	0.381040000	-0.091386000

C	-1.143889000	-0.363761000	-0.086599000
C	-2.344382000	0.555634000	0.129274000
C	-3.670073000	-0.201302000	0.131988000
H	3.631048000	-0.703658000	1.313598000
H	4.608215000	0.607152000	0.445302000
H	2.786275000	0.945692000	-1.134834000
H	1.247545000	-1.094471000	-1.247969000
H	1.421289000	-1.299699000	0.494489000
H	0.316660000	0.918774000	0.856942000
H	0.176568000	1.145757000	-0.880365000
H	-1.264338000	-0.901542000	-1.037704000
H	-1.129179000	-1.131904000	0.699428000
H	-2.221584000	1.091322000	1.079300000
H	-2.357131000	1.322114000	-0.656300000
H	-3.687483000	-0.954244000	0.927060000
H	-4.518051000	0.471536000	0.288407000
H	-3.824438000	-0.720975000	-0.819598000
45			
Cycloheptane			
C	1.540218000	-0.757590000	0.103863000
C	1.539673000	0.758424000	-0.103985000
C	0.303129000	-1.503353000	-0.411665000
C	0.302232000	1.503480000	0.411742000
C	-0.956989000	-1.229545000	0.422263000
C	-1.774812000	-0.000626000	-0.000180000
C	-0.957879000	1.229151000	-0.421999000
H	2.436806000	-1.169628000	-0.374998000
H	1.640684000	-0.971628000	1.177230000
H	2.436076000	1.171097000	0.374675000
H	1.639780000	0.972488000	-1.177384000
H	0.123246000	-1.256849000	-1.467568000
H	0.520383000	-2.577146000	-0.382375000
H	0.122666000	1.256978000	1.467695000
H	0.518925000	2.577387000	0.382331000
H	-1.617911000	-2.103210000	0.393286000
H	-0.651897000	-1.123453000	1.471726000
H	-2.434456000	-0.274800000	-0.832574000
H	-2.435441000	0.272841000	0.831661000
H	-1.619386000	2.102348000	-0.392348000
H	-0.652910000	1.123927000	-1.471587000
46			

Cycloheptene			
C	0.939356000	−1.298189000	−0.289022000
C	−0.427770000	−1.524953000	0.375058000
C	1.639039000	−0.002500000	0.128026000
C	−1.537559000	−0.664007000	−0.178750000
C	0.943343000	1.295358000	−0.289111000
C	−0.423032000	1.526208000	0.375150000
C	−1.535477000	0.668765000	−0.178758000
H	1.595075000	−2.138227000	−0.030196000
H	0.816195000	−1.317336000	−1.379279000
H	−0.705382000	−2.578162000	0.268292000
H	−0.324350000	−1.344353000	1.455986000
H	1.756342000	−0.002621000	1.221614000
H	2.653598000	−0.004169000	−0.288485000
H	−2.393544000	−1.180120000	−0.609202000
H	1.601747000	2.133339000	−0.030454000
H	0.820180000	1.314701000	−1.379352000
H	−0.320020000	1.344939000	1.455997000
H	−0.697460000	2.580291000	0.268765000
H	−2.389773000	1.187633000	−0.609248000
47			
Cyclohepta-1,3-diene			
C	0.626434000	−1.333437000	−0.444722000
C	−0.687971000	−1.403822000	0.344298000
C	1.630982000	−0.320385000	0.096587000
C	−1.648946000	−0.291034000	0.029113000
C	1.200146000	1.118461000	0.116506000
C	−0.025181000	1.648909000	−0.008730000
C	−1.334932000	0.999430000	−0.140935000
H	1.102963000	−2.320040000	−0.433508000
H	0.400314000	−1.100786000	−1.491392000
H	−1.180706000	−2.359727000	0.138085000
H	−0.464456000	−1.405737000	1.421161000
H	1.933505000	−0.610052000	1.113718000
H	2.548954000	−0.385960000	−0.502840000
H	−2.694995000	−0.570273000	−0.079947000
H	2.019096000	1.825928000	0.241881000
H	−0.075849000	2.736268000	0.007137000
H	−2.152030000	1.681646000	−0.367001000
48			
Cyclohepta-1,3,5-triene			

C	0.964691000	1.217230000	−0.203092000
C	1.433199000	0.000827000	0.549650000
C	−0.341603000	1.525117000	−0.283706000
C	0.966111000	−1.216127000	−0.203079000
C	−1.419861000	0.678036000	0.190554000
C	−1.419069000	−0.679659000	0.190528000
C	−0.339831000	−1.525505000	−0.283710000
H	1.702040000	1.858591000	−0.679737000
H	2.518483000	0.001460000	0.668971000
H	0.977725000	0.000561000	1.549688000
H	−0.633152000	2.462759000	−0.752945000
H	1.704202000	−1.856672000	−0.679679000
H	−2.351095000	1.176801000	0.451907000
H	−2.349726000	−1.179516000	0.451856000
H	−0.630301000	−2.463496000	−0.752921000
49			
2,2-Dimethylpentane			
C	−2.154402000	−0.685199000	0.000000000
C	−0.621362000	−0.698299000	0.000000000
C	−0.131793000	0.762807000	0.000000000
C	1.381503000	0.980454000	0.000000000
C	1.737571000	2.466132000	0.000000000
C	−0.131793000	−1.435877000	1.251552000
C	−0.131793000	−1.435877000	−1.251552000
H	−2.541975000	−0.170102000	0.886403000
H	−2.541975000	−0.170102000	−0.886403000
H	−2.554471000	−1.705369000	0.000000000
H	−0.557966000	1.269257000	−0.878932000
H	−0.557966000	1.269257000	0.878932000
H	1.829251000	0.501703000	0.879010000
H	1.829251000	0.501703000	−0.879010000
H	1.326566000	2.965874000	0.883635000
H	2.820398000	2.620465000	0.000000000
H	1.326566000	2.965874000	−0.883635000
H	−0.433818000	−0.905544000	2.162348000
H	−0.557085000	−2.444993000	1.292827000
H	0.958268000	−1.536168000	1.262279000
H	−0.557085000	−2.444993000	−1.292827000
H	−0.433818000	−0.905544000	−2.162348000
H	0.958268000	−1.536168000	−1.262279000
50			

4,4-Dimethylpent-1-ene

C	−1.066700000	1.348704000	0.637920000
C	−0.793507000	−0.024821000	0.015959000
C	0.454353000	0.031139000	−0.897384000
C	1.710994000	0.497945000	−0.219693000
C	2.755100000	−0.281174000	0.049890000
C	−0.580273000	−1.058089000	1.125718000
C	−1.994208000	−0.437624000	−0.840752000
H	−0.263309000	1.646746000	1.319598000
H	−1.163915000	2.120188000	−0.135275000
H	−1.999296000	1.329605000	1.212801000
H	0.621989000	−0.968812000	−1.319260000
H	0.229350000	0.699988000	−1.740856000
H	1.749439000	1.549144000	0.066591000
H	3.642689000	0.098991000	0.546189000
H	2.757930000	−1.334164000	−0.223691000
H	0.284819000	−0.799812000	1.744369000
H	−1.462190000	−1.114986000	1.773679000
H	−0.406820000	−2.054409000	0.701931000
H	−2.900236000	−0.514094000	−0.229161000
H	−2.182008000	0.296370000	−1.632836000
H	−1.822997000	−1.411237000	−1.314032000

Author details

Ali Amir Khairbek
Physical Chemistry, Faculty of Science, Tishreen University, Lattakia, Syria

*Address all correspondence to: alikhairbek@gmail.com

IntechOpen

References

[1] Schleyer, P. v. R., Encyclopedia of computational chemistry. John Wiley & Sons: 1998.

[2] Feller, D.; Peterson, K. A., An examination of intrinsic errors in electronic structure methods using the Environmental Molecular Sciences Laboratory computational results database and the Gaussian-2 set. *The Journal of chemical physics* **1998,** *108* (1), 154–176.

[3] Klopper, W.; Bak, K. L.; Jørgensen, P.; Olsen, J.; Helgaker, T., Highly accurate calculations of molecular electronic structure. *Journal of Physics B: Atomic, Molecular and Optical Physics* **1999,** *32* (13), R103.

[4] Dunning, T. H., A road map for the calculation of molecular binding energies. *The Journal of Physical Chemistry A* **2000,** *104* (40), 9062–9080.

[5] Feller, D.; Sordo, J. A., A CCSDT study of the effects of higher order correlation on spectroscopic constants. I. First row diatomic hydrides. *The Journal of Chemical Physics* **2000,** *112* (13), 5604–5610.

[6] Feller, D.; Sordo, J. A., Performance of CCSDT for diatomic dissociation energies. *The Journal of Chemical Physics* **2000,** *113* (2), 485–493.

[7] Helgaker, T.; Jorgensen, P.; Olsen, J., *Molecular electronic-structure theory*. John Wiley & Sons: **2000**

[8] Feller, D.; Dixon, D. A., Extended benchmark studies of coupled cluster theory through triple excitations. *The Journal of Chemical Physics* **2001,** *115* (8), 3484–3496.

[9] Helgaker, T.; Klopper, W.; Halkier, H.; Bak, K.; Jørgensen, P.; Olsen, J., In Highly Accurate Ab Initio Computation

of Thermochemical Data, Cioslowski J. Kluwer: Dordrecht: 2001.

[10] Dixon, D. A.; De Jong, W. A.; Peterson, K. A.; Francisco, J. S., Heats of formation of CBr, CHBr, and CBr2 from ab initio quantum chemistry. *The Journal of Physical Chemistry A* **2002,** *106* (18), 4725–4728.

[11] Martin, J. M.; de Oliveira, G., Towards standard methods for benchmark quality ab initio thermochemistry—W1 and W2 theory. *The Journal of chemical physics* **1999,** *111* (5), 1843–1856.

[12] Parthiban, S.; Martin, J. M., Fully ab initio atomization energy of benzene via Weizmann-2 theory. *The Journal of chemical physics* **2001,** *115* (5), 2051–2054.

[13] de Oliveira, G.; Martin, J. M.; Silwal, I. K.; Liebman, J. F., Definitive heat of formation of methylenimine, CH2∙NH, and of methylenimmonium ion, CH2NH2+, by means of W2 theory. *Journal of Computational Chemistry* **2001,** *22* (13), 1297–1305.

[14] Parthiban, S.; Martin, J. M.; Liebman, J. F., The heats of formation of the haloacetylenes XCCY [X, Y= H, F, Cl]: basis set limit ab initio results and thermochemical analysis. *Molecular Physics* **2002,** *100* (4), 453–464.

[15] Martin, J. M.; Parthiban, S., W1 and W2 theories, and their variants: thermochemistry in the kJ/mol accuracy range. In *Quantum-Mechanical Prediction of Thermochemical Data*, Springer: 2001; pp 31–65.

[16] Feller, D.; Davidson, E. R., Basis sets for ab initio molecular orbital calculations and intermolecular interactions. *Reviews in computational chemistry* **1990**, 1–43.

[17] Helgaker, T.; Taylor, P. R., Gaussian basis sets and molecular integrals. In *Modern Electronic Structure Theory: Part II*, **1995**; pp 725–856.

[18] Dunning Jr, T.; Peterson, K.; Woon, D., Schleyer PvR, Allinger NL, Clark T, Gesteiger J, Kolman PA, Schaefer HF III (eds) In: Encyclopedia of computational chemistry. Wiley, Chichester: **1998**, 88–115.

[19] Dunning Jr, T., Rates of convergence and error estimation formulas for the Rayleigh– Ritz variational method. *J. Chem. Phys* **1989,** *90*, 1007–1023.

[20] Woon, D. E.; Dunning Jr, T. H., Gaussian basis sets for use in correlated molecular calculations. V. Core-valence basis sets for boron through neon. *The Journal of chemical physics* **1995,** *103* (11), 4572–4585.

[21] Feller, D., Application of systematic sequences of wave functions to the water dimer. *The Journal of chemical physics* **1992,** *96* (8), 6104–6114.

[22] Feller, D., The use of systematic sequences of wave functions for estimating the complete basis set, full configuration interaction limit in water. *The Journal of chemical physics* **1993,** *98* (9), 7059–7071.

[23] Martin, J. M., Ab initio total atomization energies of small molecules —towards the basis set limit. *Chemical physics letters* **1996,** *259* (5–6), 669–678.

[24] Martin, J. M., Benchmark ab initio calculations of the total atomization energies of the first-row hydrides AHn (A= Li•F). *Chemical physics letters* **1997,** *273* (1–2), 98–106.

[25] Martin, J. M., Coupling between the convergence behavior of basis set and electron correlation: a quantitative study. *Theoretical Chemistry Accounts* **1997,** *97* (1–4), 227–231.

[26] Martin, J. M., Very accurate ab initio binding energies—a comparison between empirical corrections and extrapolation methods. *Journal of Molecular Structure: THEOCHEM* **1997,** *398*, 135–144.

[27] Helgaker, T.; Klopper, W.; Koch, H.; Noga, J., Basis-set convergence of correlated calculations on water. *The Journal of chemical physics* **1997,** *106* (23), 9639–9646.

[28] Halkier, A.; Helgaker, T.; Jørgensen, P.; Klopper, W.; Koch, H.; Olsen, J.; Wilson, A. K., Basis-set convergence in correlated calculations on Ne, N2, and H2O. *Chemical Physics Letters* **1998,** *286* (3–4), 243–252.

[29] Klopper, W.; Helgaker, T., Extrapolation to the limit of a complete basis set for electronic structure calculations on the N2 molecule. *Theoretical Chemistry Accounts* **1998,** *99* (4), 265–271.

[30] Halkier, A.; Helgaker, T.; Klopper, W.; Jørgensen, P.; Csaszar, A. G., Comment on "Geometry optimization with an infinite basis set"w ž/x J. Phys. Chem. A 103 1999 651 and "Basis-set extrapolation"w ž//x Chem. Phys. Lett. 294 1998 45. *Chemical physics letters* **1999,** *310*, 385–389.

[31] Bak, K.; Halkier, A.; Jørgensen, P.; Olsen, J.; Helgaker, T.; Klopper, W., Chemical accuracy from 'Coulomb hole'extrapolated molecular quantum-mechanical calculations. *Journal of Molecular Structure* **2001,** *567*, 375–384.

[32] Bak, K. L.; Jørgensen, P.; Olsen, J.; Helgaker, T.; Klopper, W., Accuracy of atomization energies and reaction enthalpies in standard and extrapolated electronic wave function/basis set calculations. *The Journal of Chemical Physics* **2000,** *112* (21), 9229–9242.

[33] Rogers, D. W., *Heats of hydrogenation: experimental and*

computational hydrogen thermochemistry of organic compounds. World Scientific: 2006, or from website https://webbook.nist.gov/chemistry/.

[34] Zhao, Y.; Truhlar, D. G., The M06 suite of density functionals for main group thermochemistry, thermochemical kinetics, noncovalent interactions, excited states, and transition elements: two new functionals and systematic testing of four M06-class functionals and 12 other functionals. *Theoretical Chemistry Accounts* **2008,** *120* (1–3), 215–241.

[35] Frisch, M.; Trucks, G.; Schlegel, H. B.; Scuseria, G. E.; Robb, M. A.; Cheeseman, J. R.; Scalmani, G.; Barone, V.; Mennucci, B.; Petersson, G., gaussian 09, Revision d. 01, Gaussian. *Inc., Wallingford CT* **2009,** *201*.

[36] Vasilyev, V., Online complete basis set limit extrapolation calculator. *Computational and Theoretical Chemistry* **2017,** *1115*, 1–3. http://sf.anu.edu.au/∼vvv900/cbs/#ref_3.

[37] Wiberg, K. B., Accuracy of calculations of heats of reduction/hydrogenation: Application to some small ring systems. *The Journal of organic chemistry* **2012,** *77* (22), 10393–10398.

[38] Rogers, D. W.; McLafferty, F. J.; Podosenin, A. V., Ab Initio Calculations of Enthalpies of Hydrogenation and Isomerization of Cyclic C4 Hydrocarbons. *The Journal of Physical Chemistry* **1996,** *100* (43), 17148–17151.

[39] Rogers, D. W.; McLafferty, F. J.; Podosenin, A. V., G2 (MP2) and G2 (MP2, SVP) calculations of enthalpies of hydrogenation, isomerization, and formation of C5 hydrocarbons. 2. Substituted cyclobutenes, vinylcyclopropene, spiropentane, and methyltetrahedrane. *The Journal of Physical Chemistry A* **1998,** *102* (7), 1209–1213.

[40] Li, Z.; Rogers, D. W.; McLafferty, F. J.; Mandziuk, M.; Podosenin, A. V., Ab initio calculations of enthalpies of hydrogenation, isomerization, and formation of cyclic C6 hydrocarbons. Benzene isomers. *The Journal of Physical Chemistry A* **1999,** *103* (3), 426–430.

Edited by Luigi Cocco and Muhammad Aziz

The automobile industry is tremendously peculiar due to several strict requirements regarding functional reliability, safety standards, comfort level, high-volume production, and environmental limits. In addition, the industry is experiencing a disruptive evolution of modern vehicle research and design: electrification, connectivity, and autonomous driving. This book provides a robust overview of automotive engineering, including new proposals and the latest trends in road vehicle systems and sub-systems. Each chapter presents a rigorous analysis or a new solution in a clear and concise manner, such that professional and academic readers will appreciate both the theory dissertation and the industrial application.

IntechOpen